June 2021

Enhancing the Intracellular Availability of Protein Cargoes in Polymer-Mediated Delivery

Christopher R. Hango
University of Massachusetts Amherst

ENHANCING THE INTRACELLULAR AVAILABILITY OF PROTEIN CARGOES IN POLYMER-MEDIATED DELIVERY

A Dissertation Presented

by

CHRISTOPHER R. HANGO

Submitted to the Graduate School of the
University of Massachusetts Amherst in partial fulfillment
of the requirements for the degree of

DOCTOR OF PHILOSOPHY

May 2021

Polymer Science and Engineering

ENHANCING THE INTRACELLULAR AVAILABILITY OF PROTEIN CARGOES IN POLYMER-MEDIATED DELIVERY

A Dissertation Presented

by

CHRISTOPHER R. HANGO

Approved as to style and content by:

_____
Gregory N. Tew, Chair

_____
Maria M. Santore, Member

_____
Lisa M. Minter, Member

_____
David A. Hoagland, Department Head
Polymer Science and Engineering

DEDICATION

To my family.

ACKNOWLEDGMENTS

A majority of the text and figures in the following dissertation come directly from previously published work or articles that are currently in press or in review. The source of the text and figures is identified and credited at the start of the chapter in which it is used. This thesis contains work modified from an article published in ACS Applied Bio Materials, DOI: 10.1021/acsabm.9b00876.

The work presented here has been supported by a number of research grants over the past five years. In particular, I am grateful to the National Science Foundation (NSF) for funding through NSF DMR-1308123 and the NSF National Research Traineeship fellowship and travel grant (NRT-1545399). Additionally, I would like to thank the Department of Education for the funding through the Graduate Assistance in Areas of National Need (GAANN) fellowship (DoED P200A150276). I am also extremely grateful to the German Academic Exchange Service (DAAD) for the incredible opportunity to spend two months working in the group of Professor Pol Besenius at Johannes Gutenberg-Universität Mainz.

First and foremost, I would like to acknowledge my advisor, Professor Greg Tew, for his immeasurable role in my PhD and (perhaps more importantly) my development as a scientist. As a first-year student with little background in chemistry or biology, Greg welcomed me into his group and patiently provided me with the support and opportunity to develop an entirely new skillset. I have been fortunate to work with an advisor who always encouraged me to pursue the questions that interested me, even as I allocated far too much time toward the projects that ultimately never succeeded. I sincerely believe that I grew from the failures as much as from the successes that actually made it into this

document. Secondly, I need to thank my committee members, Professors Lisa Minter and Maria Santore. I had the unique experience of splitting my time between Greg's lab in Conte and Lisa's lab in ISB. The support and advice provided by Lisa and her group, as well as the Osborne and Pobezinsky research groups sharing the same lab space, greatly enhanced my graduate experience. Maria has always provided me with a critical engineering perspective to my research questions. She is an incredibly thorough scientist who truly invests herself in helping the students she mentors. She is an excellent resource and role model, and I only wish I had taken more time to absorb more of her expertise.

My graduate experience would not have been complete without all of the past and present members of the Tew group with whom I had the pleasure of working: Brittany deRonde, Joel Sarapas, Coralie Backlund, Ilker Ozay, Nick Posey, Kelly McLeod, Mike Kwasny, Megan Matta, Maren Schweitzer, Eva Morgenthaler, Jessica Erlenbusch, Hazel Davis, Ipek Sacligil, Brandon Clarke, Kayla Koch, Leah Caffrey, Carolyn Watkins, Gennifer Greenberg, Miguel Franco, and Esha Uddin. I chose the Tew group for the people just as much as the research. In particular, I cannot thank Coralie enough for her years of mentorship, friendship, and help throughout the cumulative exam process. I am likewise immensely grateful to Nick and Ilker for training me in polymer synthesis and cell culture, respectively, and to Hazel and my undergraduate students, Miguel and Esha, whose work was indispensable for the completion of my projects. I want to profusely thank Trouble Mandeson for her years of dedication to managing both our group and the NRT program: we all miss you so much. Lastly, I will be forever indebted to my German friends and the Besenius research group in Mainz, Germany, especially Ronja Otter, Kiki Berač, Maren Schweitzer, Yami Bülbül, Eva Morgenthaler, and Conny Meißner, who wholeheartedly

welcomed, trained, and took care of Hazel and I, making us feel perfectly at home (perhaps more at home than in Amherst?) in a foreign country.

The Polymer Science and Engineering (PSE) department at UMass is a special place. I chose to complete my PhD in PSE because it offered a uniquely welcoming and collaborative environment that I found nowhere else. In addition to all of the faculty, I am incredibly thankful for all of the current and past staff members, particularly Lisa Groth, Maria Farrington, Jack Hirsch, Cheryl Kehoe, Alyssa Kristek, Lisa McNamara, Andre Mel'cuk, and Jessica Skrocki, who have consistently gone above and beyond to help the department run smoothly. I want to extend a special thank you to Weiguo Hu for his management of the NMR facility, and Amy Burnside and Jim Chambers, who manage the Flow Cytometry and Light Microscopy Core Facilities, respectively, outside of PSE. My scientific discussions with these individuals and the use of their facilities were instrumental to my research.

I am additionally thankful to the broader UMass community, especially the Chemistry and MCB graduate programs, as well as the NRT, CBI, and BTP training programs, which all provided me the opportunity to meet people across campus and make lifelong friends. In particular, I need to thank Mikey Mingroni, for being such an excellent roommate and friend, Robert Enright, for being the best travel buddy, Francesca Anson, for sharing in all of the ups and downs of grad school while also being a great scientific resource, and Alexandria Wells, for being my closest friend in ISB and the life of our softball team.

I am extremely grateful for my formative experiences at Worcester Polytechnic Institute in making me the scientist and person I am today. In particular, Professors Stephen Kmiotek, Satya Shivkumar, and Terri Camesano have continuously inspired me follow my interests in polymers, drug delivery, food science, and basic research. Special thanks to Professor Nouceiba Adouani and Billy Homkey at l'École nationale supérieure des industries chimiques (ENSIC) at the University of Lorraine in Nancy, France for their mentoring of Laura and I during our two-month stay in Nancy working on our senior theses.

I am so fortunate to have such a loving and supportive family. To my immediate and extended family (especially to all of the engineers), thank you for inspiring me to explore all of my disparate passions in science, engineering, and music in an academic capacity from the beginning. To my parents, Lisa and John, and my siblings, Erika, Alex, and Melissa, thank you for the many years growing up together and the inspiration you've provided me in your own careers. Special thanks in particular to my grandparents, for creating the family we have today, including my grandfather, Roy Hango, for teaching me to be a hard worker and think like an engineer growing up.

I would like to thank my new work family at Incredible Foods. To Marty Kolewe, Kristen Enright, Kiersten Walker, Brandon Schaeffer, Jackson Hooks Davis, Belen Herrera, and Ana Secco: thank you for welcoming me into the company and supporting me for the last six months as I finished my PhD. I'm so excited to be entering the world of food science with such a great team of coworkers!

Finally, I need to thank the most important people in my life who haven't made it into this list yet. Thank you to my close friends, Saad Riaz, Zack Tripp, Tyler Miles, and

Joe Spina, for helping me to get through my PhD. And finally, to Melissa Dery, Laura Hart, and Alexander Thompson thank you for your love, patience, and most of all, for being there for me in my lowest moments. I couldn't have done this without you, and I love each of you more than I can describe.

ABSTRACT

ENHANCING THE INTRACELLULAR AVAILABILITY OF PROTEIN CARGOES IN POLYMER-MEDIATED DELIVERY

MAY 2021

CHRISTOPHER R. HANGO, B.S., WORCESTER POLYTECHNIC INSTITUTE

M.S., UNIVERSITY OF MASSACHUSETTS AMHERST

Ph.D., UNIVERSITY OF MASSACHUSETTS AMHERST

Directed by: Professor Gregory N. Tew

Protein drugs, including antibodies, are rapidly emerging as the top-selling pharmaceuticals worldwide owing to their unparalleled specificity and biocompatibility. However, none of the currently-approved protein therapeutics act intracellularly, despite the vast majority of potential drug targets residing within the cell. This is due mainly to the paramount challenge of transporting hydrophilic macromolecular cargoes across the plasma membrane. As such, effective protein carriers are essential for the advancement of modern medicine. Despite significant advances, many challenges still plague protein delivery. Following membrane transduction, delivery vectors must preserve the structure and activity of their cargoes while transporting them to the correct subcellular destination and release them in a pharmacokinetically appropriate manner. Ultimately, the intracellular availability (IA), or fraction of total internalized drug which reaches its target in an active state, must be maximized to achieve meaningful biological outcomes.

Our group has developed a library of synthetic cell-penetrating peptide mimics (CPPMs) for intracellular delivery. These polymers have enabled robust non-covalent binding and delivery of functional protein and nucleic acid cargoes, resulting in substantial

manipulation of cell biology. This dissertation comprises four studies wherein polymer structure is modulated to boost protein IA. First, CPPMs were directly compared to other non-covalent carriers for quantity of protein delivered and found to overwhelmingly outperform the others across all conditions tested, most significantly in particularly difficult-to-transfect T cells, neurons, and stem cells. In a second study, new block copolypeptide CPPs were reverse-engineered from optimized CPPM structures. Several of these new peptides were able to non-covalently bind and deliver proteins, a rare ability for CPPs, and hydrophobicity was revealed to universally predict IA. The next chapter documents the competing effects of polymer length on cargo uptake and function, revealing longer amphiphiles to exhibit greater IA. Finally, the effects of CPPM structure on subcellular protein delivery to the mitochondrion were investigated. This work was enabled by the simultaneous development of a new flow cytometry technique for rapid quantification of intra-organellular drug delivery. In general, these findings indicate that uptake-driven optimization is a gross oversimplification of the delivery process. Future studies should seek to better understand the mechanisms underlying IA.

TABLE OF CONTENTS

Page

LIST OF TABLES

Table Page

LIST OF FIGURES

LIST OF SCHEMES

Scheme Page

CHAPTER 1

1 INTRODUCTION

NOTE: This chapter contains excerpts adapted with permission from the following previously published article: Backlund, C. M.; Hango, C. R.; Minter, L. M.; Tew, G. N. Protein and Antibody Delivery into Difficult-to-Transfect Cells by Polymeric Peptide Mimics. *ACS Appl. Bio Mater.* **2020**, *3* (1), 180–185.

1.1 Overview and Significance of Protein Delivery

The human genome contains tens of thousands of genes, which are in turn responsible for an even greater number of distinct functional proteins when alternative splicing and post-translational modifications are considered.[1,2] Compounded with the precise spatial and temporal regulation of protein concentrations and interactions exhibited by the body, this extraordinarily diverse class of biomolecules is integral to virtually all biological processes.[2] Consequently, protein dysfunction caused by sequence mutations, inappropriate levels of expression, and improper post-translational modifications accounts for a large fraction of disease.[2,3] Newfound strategies to correct abnormalities at the protein level are thus being increasingly exploited for therapeutic applications.[4–6]

Rapid, efficient, and tailorable control over cellular processes using proteins is likewise expected to revolutionize our fundamental understanding of cellular biology.[7] Historically, manipulation of intracellular protein levels has been achieved by the delivery of exogenous DNA for constitutive expression or, more recently, the delivery of small interfering (si)RNA to reduce protein translation. Similarly, DNA delivery has been used to accomplish nuclease-based genome editing (e.g., by encoding ZFN, TALEN, or CRISPR-associated proteins), enabling complete protein knockout. In contrast, the ability to directly deliver proteins into the cytosol can be exploited to produce (or prevent) highly

specific intracellular interactions with spatial and temporal control.[8] Results from protein transduction can be extremely fast in comparison with traditional gene expression, as it does not require transcription or translation processes to occur.[9] Additionally, temporal control allows for the investigation of transient protein effects, while avoiding overexpression or random insertion of DNA into the target genome.[10] The delivery of proteins, and specifically antibodies, into the cytosol provides a platform to probe intracellular pathways involved in protein expression, transcriptional regulation, and cell cycle, along with many other applications.[11]

In comparison with conventional drugs, protein therapeutics offer several unique advantages. First, proteins are complex molecules capable of performing sophisticated tasks which are exceptionally difficult to replicate with traditional small molecule drugs.[2] Second, proteins exert their function on precise substrates, dramatically reducing of off-target activity and side effects.[4] Finally, proteins are inherently more biocompatible, although induction of undesired immune responses remains a concern. However, many of these issues can be overcome through recombinant protein engineering or by cloaking with stealth molecules, such as poly(ethylene glycol) (PEG).[12] Fortunately, recent advances in protein production systems, often involving engineering of bacterial or yeast cells, have made protein therapeutics significantly cheaper and more scalable.[2] Unsurprisingly, protein therapeutics now represent the largest fraction of pharmaceuticals by sale, and this is only expected to increase.[13] Still, substantial barriers remain in the delivery of proteins, ranging from protecting them from degradation and clearance from the body to targeting them to the required tissues and subcellular compartments.[1,12] Undoubtedly the largest challenge facing progress in protein delivery, however, is transport of these large, polar

macromolecules through the cellular membrane.[14] In fact, all currently approved protein pharmaceuticals act on extracellular targets, despite the vast majority of potential drug targets residing inside the cell.[15] As such, safe and effective carriers are urgently needed for the advancement of intracellular protein therapeutics.

1.2 Cell-Penetrating Peptides (CPPs) and Their Mimics (CPPMs)

1.2.1 Origins and Key Structure-Activity Relationships

Since the discovery of the first protein transduction domain (PTD), a short arginine-rich sequence responsible for rapid cellular uptake of the HIV-1 trans-activator of transcription (Tat) protein, researchers have been captivated by the vast research and therapeutic potential of cationic peptides for intracellular delivery (Figure 1.1).[16–18] Shortly after the discovery of Tat's transduction ability, cationic PTDs with added hydrophobic content were reported, like the third helix of the *Drosophila* homeoprotein Antennapedia (later named Penetratin), implying that hydrophobicity might enhance membrane transduction (Figure 1.1).[19,20] These two discoveries ushered in countless reports of new cell-penetrating peptide (CPP) sequences, both naturally and synthetically derived.[21–23]

Several fundamental findings have shaped our understanding of CPP activity. The initial replacement of all residues in $Tat_{49\text{-}57}$ (RKKRRQRRR) with arginine (R_9) afforded even greater cellular uptake (Figure 1.1).[24] In contrast, other cationic analogues (K_9 and H_9) exhibited a dramatic loss of activity, establishing arginine specifically as the key component of CPPs.[25] Likewise, the replacement of all seven cationic residues in the Penetratin sequence (RQIKIWFQNRRMKWKK) with arginine and lysine led to increased

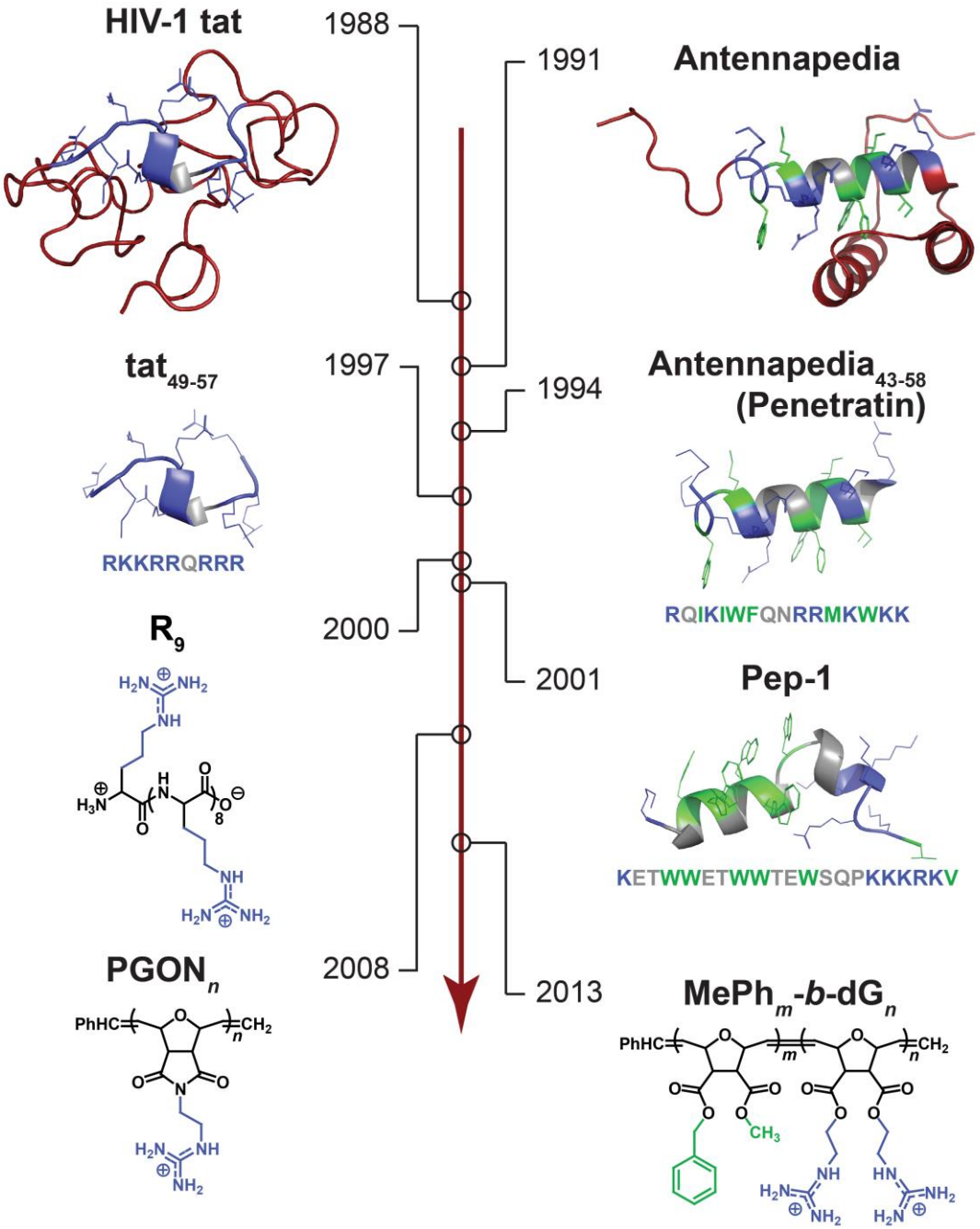

Figure 1.1: The evolution of cell-penetrating peptides (CPPs) and their mimics (CPPMs). Cationic residues and hydrophobic residues are highlighted in blue and green, respectively. 1988: The unexpected ability of several proteins to translocate across the cellular membrane is discovered. 1997: Translocation of these proteins is attributed to short, cation-rich sequences, termed protein transduction domains (PTDs). 2000: Peptides like nona-arginine are designed to maximize membrane activity and become known as cell-penetrating peptides (CPPs). Secondary structure found in PTDs is not required for activity. 2008: Synthetic guanidine-rich polymers are designed. Peptide backbone is not necessary for activity. These polymers become known as CPP mimics (CPPMs). 1991 & 1994: Simultaneously, cationic PTDs with significant hydrophobic content are discovered. 2001: Synthetic CPPs incorporating both cationic and hydrophobic residues are designed. 2013: Block copolymer CPPMs containing both cationic and hydrophobic functionalities show greatly enhanced protein delivery.

and decreased uptake, respectively.[26] The success of these arginine-rich variants implied that the secondary structures of Tat and Penetratin may not be essential for cell penetration. Intrigued by these findings, several groups began incorporating guanidine, the cationic head group of arginine, onto other scaffolds, ranging from closely-related β-peptides and peptoids to entirely distant synthetic polymers, demonstrating even the peptide backbone to be dispensable (Figure 1.1).[24,27,36–41,28–35] Collectively, these abiotic macromolecules have become interchangeably known as PTD or CPP mimics (PTDMs or CPPMs). The easily tunable chemistry enabled by these synthetic platforms encouraged deeper investigation of the role of hydrophobicity in cell penetration. Consistent with the linearly or facially segregated nature of several effective CPPs,[42–48] segregation of hydrophobic and cationic moieties into discrete domains (i.e., chimeric or blocky architectures) has also been shown to enhance CPPM performance in several cases Figure 1.1[29,49,50] Hydrophobicity also generally leads to higher uptake within a set of structurally similar carriers, although too much hydrophobicity can result in toxicity or insolubility, resulting in an optimal hydrophobic window.[51–56]

1.2.2 Non-Covalent Delivery with CPP(M)s

The anionic nature of nucleic acid cargoes often enables strong electrostatic-driven binding by cationic CPP(M)s, thus making a straightforward non-covalent delivery strategy possible.[57] Conversely, protein net charge can range from anionic to cationic. Furthermore, proteins feature patchy surfaces of locally anionic, cationic, and hydrophobic groups, regardless of their net charge or hydrophobicity, rendering them an incredibly diverse collection of cargoes with heterogenous surface properties.[58] Even the most anionic proteins lack the dense negative charge inherent to all nucleic acid cargoes. The

inability to consistently rely on electrostatic-driven binding poses a significant challenge for non-covalent carriers. As a result, a vast number of CPP(M)s are reliant on covalent conjugation, either via genetic or chemical means, to facilitate robust delivery of proteins.[40,59,60]

The desire for protein carriers capable of non-covalent delivery remains substantial given the immense workflow simplification afforded by a quick carrier-cargo mixing step, particularly when substituting new cargoes. While several such non-covalent carriers have recently been developed, they are often restricted to select cargoes, easily-transduced cell types, and serum-free conditions.[49,61–63] In pursuit of more broadly effective non-covalent carriers, our group has spent the last decade developing a library of polymeric CPPMs, mainly synthesized via the ring-opening metathesis polymerization (ROMP) of functionalized norbornene monomers.[49,51,52,54,64–66] These CPPMs have been shown to effectively bind and deliver a wide variety of protein and nucleic acid cargoes, including functional siRNA, antibodies, and enzymes.[63,67–69] Synthetic platforms afford rapid synthesis of large carrier libraries with access to a much broader chemical space. In particular, the living nature of ROMP allows for molecular weight control and synthesis of block copolymers. Working with this platform has enabled the elucidation of several fundamental structure-activity relationships (SARs).

1.3 Factors Driving Cargo Intracellular Availability

In Chapter 3, the concept of cargo intracellular availability (IA) is introduced and developed. This parameter was formalized to be distinct from bioavailability, which is most often defined as the fraction of drug which enters circulation upon administration.[6]

IA, a term which has also been informally referenced the literature, instead describes the fraction of total intracellular drug which reaches its molecular target without loss of function.[70–72] Whereas bioavailability summarizes the preliminary stage of *in vivo* drug delivery, IA seeks to describe the post-internalization capacity of a cargo to perform its intended function. Although absolute measurements of the numerator and denominator of IA are virtually impossible to achieve, indirect or relative tools can be adequately employed, such as fluorescence-based assays or downstream readouts of protein function. Provided that the methods used are consistent, simple and accurate comparisons can be made between a collection of carriers or delivery conditions.

Several conditions must be met for a cargo to be intracellularly available. Its carrier must not only transduce the plasma membrane and distribute within the correct subcellular compartment, but also function dually to protect the drug from degradation and denaturation during transport while facilitating its release upon reaching the target destination.[73] Thus, processes including carrier-cargo interactions, cellular entry mechanism, endosomal escape efficiency, subcellular trafficking patterns, and cargo release can each heavily influence a drug's ultimate IA (Figure 1.2). It is imperative that the next wave of drug delivery research seeks to better understand the mechanisms underlying each step of the delivery process in order to inform the intelligent design of new carriers.[4] The effects of CPPM structure on protein IA will be discussed throughout this dissertation. The remainder of this chapter will focus on the current strategies employed to maximize IA in polymer delivery systems.

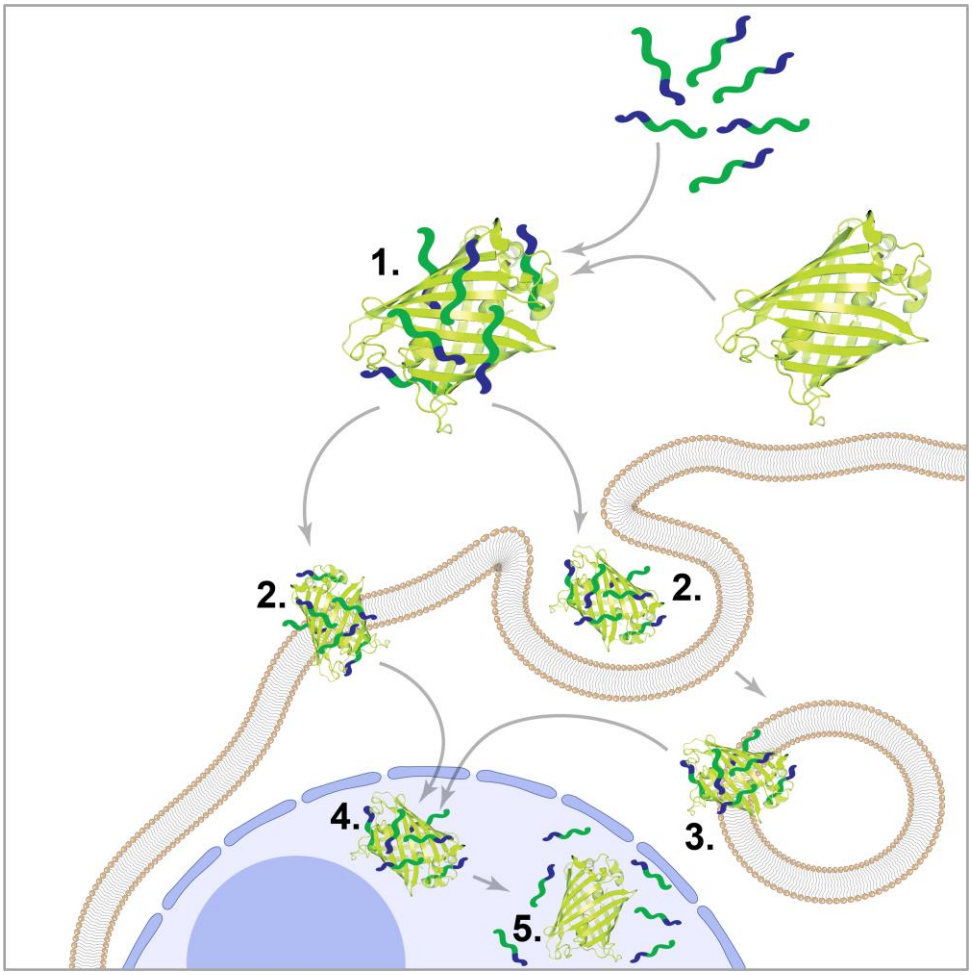

Figure 1.2: Stages in the non-covalent delivery landscape which influence drug intracellular availability: (1) carrier-cargo association, (2) cellular internalization via endocytosis or direct translocation, (3) endosomal escape, (4) subcellular localization, and (5) cargo release.

1.3.1 Carrier-Cargo Interactions: Binding and Release

In non-covalent systems, initial binding interactions are crucial for maintaining carrier-cargo association throughout the delivery process.[14] A careful balance is required: insufficient binding can result in premature cargo release, particularly in the presence of competing serum proteins, while particularly strong interactions may result in disturbance of protein structure or lack of release.[58,74] However, binding strength has not been found to correlate with quantity of cargo delivered, provided that some minimum threshold level of binding is achieved in order to transport the cargo intracellularly.[58,62,75,76] Drug carriers

must also protect their cargo from degradation, and proteins are particularly susceptible to omniprevalent enzymes (e.g., proteases, esterases, etc.) and environmental changes like pH.[2,12] This is of particular concern in the endocytic uptake pathway as pH is rapidly lowered.[77] For *in vivo* applications, delivery vehicles can also function to prolong the drug circulation and shield cargo from recognition by the immune system.[78]

Cargo release from polymeric nanoparticles can be accomplished in several manners, ranging from passive release to highly-engineered events. Non-covalently complexed polymer-protein systems are hypothesized to dissociate by protein displacement owing to the crowded environment of the cytoplasm.[14] Alternatively, cargo can slowly diffuse out of a polymeric nanoparticle over time. Control of mesh size in polymeric nanogels is an elegant method of tuning the drug release rate in nanoparticles. Polymers, especially biopolymers, can also be susceptible to degradation with time, allowing cargo to be slowly freed. More sophisticated systems include membrane fusion (with either the plasma or endosomal membranes) to directly empty the contents of polymeric micelles or polymersomes into the cytoplasm.[79] Finally, pH- or enzyme-responsive polymeric carriers can be utilized to release their cargo based on environmental factors.[70]

1.3.2 Cellular Uptake Efficiency and Mechanism

The most intuitive strategy to maximize drug efficacy is to increase intracellular concentration (i.e., maximize cellular uptake). Indeed, this model is reasonable provided that IA remains unchanged. Constant IA is a fair assumption when the key stages of the delivery process (e.g., carrier-cargo binding, cellular uptake mechanism, endosomal escape

efficiency, intracellular localization, and cargo release) are reasonably similar. Thus, optimizing cargo internalization remains a useful exercise, though it is too often used as the sole metric for screening libraries of diverse carriers. Relatively small quantities of delivered protein can substantially affect cell biology if IA is sufficiently high, while large quantities of cargo can be trapped within endosomes and subsequently degraded. Finally, it should be noted that non-linear or non-monotonic dose-response relationships may exist, depending on the biological system, meaning that higher intracellular drug concentrations are not always desired.[80]

The broad term "endocytosis" refers to a collection processes by which cells internalize material from their environment. Endocytosis can be divided into phagocytosis and pinocytosis, which refer to the uptake of large particles (typically > 1 μm) and solubilized materials, respectively. Whereas all cells exhibit pinocytosis, only specialized cells (e.g., macrophages, dendritic cells, monocytes, and neutrophils) perform phagocytosis. In one classification method, pinocytosis is further divided into fluid-phase, adsorptive, and receptor-mediated endocytosis. Fluid-phase endocytosis can be thought of as sampling the extracellular environment, with materials being internalized at the same concentrations at which they are present outside the cell. Adsorptive and receptor-mediated endocytosis, in contrast, involve uptake of materials attached to the cell surface, that is, in higher concentrations than they are present extracellularly. While the former involves non-specific adsorption, the latter is triggered by precise ligand-receptor binding.[71,72,81,82]

While this classification strategy can be useful, it is far more precise and informative to classify endocytosis by the proteins involved.[81] In this regard, pinocytosis

can be separated into clathrin-mediated endocytosis (CME), caveolae-mediated endocytosis (CvME), macropinocytosis, and clathrin- and caveolae-independent endocytosis (a catch-all category for minor endocytosis mechanisms mediated by other proteins). CME is considered the classical route of cellular entry and is active in all cell types. The protein clathrin-1 polymerizes on the cytosolic side of the membrane, creating a clathrin-coated pit, which becomes a clathrin-coated vesicle. These vesicles are ~100-150 nm and follow the traditional endo/lysosomal route, becoming early endosomes, late endosomes, and ultimately fusing with lysosomes, a process associated with rapid drop in pH and eventual degradation of the vesicle's contents. CME is responsible for internalization of iron via transferrin (Tf) and the Tf receptor. Thus, nanoparticles can be targeted for greater CME uptake by decoration with Tf. CvME is present in most (not all) cell types, but is much more abundant in endothelial cells. Unlike CME, this pathway is thought to evade the lysosomal pathway; rather, caveosomes (~50-100 nm) are trafficked to the Golgi apparatus or endoplasmic reticulum, though this remains debated.[71] Macropinosomes are characterized by their large size (~0.2-5 μm in diameter), actin-driven formation, and non-specific uptake of material. Macropinocytosis is typically induced following cellular stimulation by growth factors or other signals. The fate of macropinosomes in relation to the endo/lysosomal pathway appears to be cell-type dependent.[71,72,81,82]

Finally, some materials are capable of direct membrane translocation, thus avoiding the endocytic pathways and more straightforwardly accessing the cytosolic environment. The two major types of energy-independent uptake mechanisms are membrane fusion and direct penetration.[72] The mechanism of CPP(M) cellular internalization is highly debated

in the literature, though a combination of multiple pathways, including both energy-dependent and energy-independent processes, are likely to be present in many situations.[72,83] In general, it is not uncommon for nanoparticles to take advantage of multiple mechanisms of cellular entry simultaneously.[81]

1.3.3 Endosomal Escape

Most nanoparticles are internalized through endocytosis, yet most drugs require localization in another subcellular compartment.[70] Unsurprisingly, endosomal escape is one of the largest challenges facing drug delivery. Escape rates from the endosome may be as low as 1-2%, making this a critical bottleneck in the delivery process.[70,84] In addition to presenting a physical barrier to proper subcellular localization, the proteins are subjected to acidic pH. As a particle is internalized, the pH rapidly drops from 7.4 (extracellular pH) to ~6.0, ~6.5, and ~5 in the early endosome, late endosome, and lysosome, respectively, which can degrade or denature proteins that are poorly stabilized.[77]

Many delivery systems are designed to take advantage of this pH shift to promote endosomal escape. Three such proposed mechanisms for pH-dependent escape are the proton sponge effect, particle swelling, and membrane destabilization. In the first, cationic polymers like polyethylenimine (PEI) are thought to burst the endosome by increasing the osmotic pressure. Though this hypothesis remains highly debated in the literature, it states that, as the endosome is acidified, the polymer acts as a buffer, requiring more protons to be pumped in to lower the pH. This results in an influx of chloride counterions and water, and the pressure buildup ultimately ruptures the endosome, freeing the cargo.[70,77,82,85] Alternatively, polymeric nanoparticles which become positively charged just below

physiological pH can increasingly repel each other and become solvated, inducing swelling of up to several times the particle's initial diameter. Similar to the proton sponge effect, it is hypothesized that such swelling can rupture the endosome.[70,77,82] Nanoparticles containing polymers which are minimally membrane-active at physiological pH, but strongly membrane-active in slightly acidic environments, can selectively destabilize the endosomal membrane without rupturing plasma or organellular membranes, which would otherwise cause toxicity.[70,82] For example, cationic or anionic carriers which become increasingly protonated at lower pH can become more cationic or hydrophobic, respectively, either of which could result in stronger membrane interctions.[82]

Membrane fusion and pore formation are two mechanisms through which the endo/lysosome is not entirely destroyed. In membrane fusion, nanoparticles composed of lipids or amphiphilic polymers can fuse with the endosomal membrane, similar to the way that enveloped viruses escape endosomes, thus expelling their contents into the cytoplasm.[82] Fusion peptides directly derived from viruses have been used to accomplish this. Similarly, polymers and peptides can self-assemble across the endosomal membrane to create pores, which may cargo to diffuse out. However, such transmembrane pores are typically only ~1-2 nm in size, allowing only relatively small cargoes to escape.[82]

Finally, it should be noted that timing of endo/lysosomal escape can be a critical factor determining efficacy of the delivery system. Lysosome rupture can release proapoptotic molecules, such as cathepsins and calcium ions, resulting in cell death.[82] Thus, earlier escape is generally considered to be advantageous.

1.3.4 Subcellular Localization

Subcellular-targeting moieties are being increasingly integrated into delivery systems to assist in reaching the proper pharmacological site.[86,87] Carriers which can target drugs to a range of intracellular sites, including the cytoplasm, nucleus, endo/lysosomes, mitochondria, Golgi apparatus, and endoplasmic reticulum, must be developed.[88,89] Of these, strategies to reach the endo/lysosomal and cytoplasmic compartments have been indirectly addressed in the endosomal escape section. While some non-targeting delivery systems can rely on diffusion to gain access to the site of action, certain organelles cannot be reached in this manner, particularly when the cargo is restricted by a subcellular membrane.[86] To combat this issue, two main strategies are currently employed: alteration of carrier physiochemical properties and conjugation of localization peptides.

1.3.4.1 Delivery to the Nucleus

The nucleus is a key target for many gene therapies. The main entry route through the double-layered nuclear envelope is via the nuclear pore complexes (NPCs), though molecules larger than ~40 kDa are typically restricted, preventing the passage of intact nanoparticles.[86,90] The nuclear envelope breaks down during mitosis, allowing cytosolic cargoes to diffuse into the nucleus, but this phenomenon cannot be relied upon for delivery to primary cells.[88] Thus, active targeting strategies have been taken advantage of. The most popular method includes conjugation of nuclear localization signals (NLSs) derived from HIV-1 Tat and the SV40 large T-antigen (PKKKRKV) to the carrier or cargo.[88] An alternative strategy involves conjugating glucocorticoids (e.g., Dexamethasone) to nanoparticles, resulting in targeting and expansion of the NPCs by up to 60 nm and translocation across the nuclear envelope.[86]

1.3.4.2 Delivery to the Mitochondrion

The mitochondrion is an attractive drug target for neurological diseases and cancers, owing to its involvement in energy production and apoptosis, among other critical cellular processes. Additionally, the mitochondrion contains a set of DNA (mtDNA), whose associated mutations have been linked to various genetic diseases.[91,92] Mitochondria are surrounded by double membrane structures consisting of a porous outer membrane and a more impermeable inner membrane which exhibits a highly negative membrane potential.[92,93] To date, the most widely-adopted strategy for mitochondrial targeting is via the attachment of delocalized lipophilic cations, such as triphenylphosphonium (TPP) or rhodamine 123. Such moieties preferentially localize within the mitochondria due to its negative membrane potential.[86,92] Peptide sequences have also been heavily utilized for intramitochondrial transport, namely mitochondria-penetrating peptides (MPPs), Szeto-Schiller peptides, and mitochondrial targeting signals (MTSs), which are derived from proteins synthesized in the cytoplasm that traffic to the mitochondria.[86]

1.3.4.3 Delivery to the Golgi Apparatus and Endoplasmic Reticulum

The development Golgi apparatus- and endoplasmic reticulum (ER)-targeting functionalities remains in its infancy, though delivery to these organelles is certainly of great interest. Dysfunction of the Golgi apparatus has been liked to skin, muscular, skeletal, and nervous system disorders.[94] Several Golgi-localizing peptide sequences have been reported, offering a promising subcellular delivery strategy. The ER is critical for proper protein folding and is an important target for antifungal drugs and vaccines, since antigens are loaded onto major histocompatibility complex class I (MHC I) molecules in

this organelle.[93] One successful strategy for ER transport has been the conjugation of Shiga or cholera toxins, which target the ER in nature, onto therapeutic carriers or cargoes.[90]

1.4 References

(1) Vaishya, R.; Khurana, V.; Patel, S.; Mitra, A. K. Long-term delivery of protein therapeutics. *Expert Opin. Drug Deliv.* **2015**, *12* (3), 415–440.

(2) Leader, B.; Baca, Q. J.; Golan, D. E. Protein therapeutics: A summary and pharmacological classification. *Nat. Rev. Drug Discov.* **2008**, *7* (1), 21–39.

(3) Dalle-Donne, I.; Aldini, G.; Carini, M.; Colombo, R.; Rossi, R.; Milzani, A. Protein carbonylation, cellular dysfunction, and disease progression. *J. Cell. Mol. Med.* **2006**, *10* (2), 389–406.

(4) Ray, M.; Lee, Y. W.; Scaletti, F.; Yu, R.; Rotello, V. M. Intracellular delivery of proteins by nanocarriers. *Nanomedicine* **2017**, *12* (8), 941–952.

(5) Krejsa, C.; Rogge, M.; Sadee, W. Protein therapeutics: new applications for pharmacogenetics. *Nat. Rev. Drug Discov.* **2006**, *5* (6), 507–521.

(6) Cleland, J. L.; Daugherty, A.; Mrsny, R. Emerging protein delivery methods. *Curr. Opin. Biotechnol.* **2001**, *12* (2), 212–219.

(7) Marschall, A. L. J.; Frenzel, A.; Schirrmann, T.; Schüngel, M.; Dübel, S. Targeting antibodies to the cytoplasm. *mAbs* **2011**, *3* (1), 3–16.

(8) Stewart, M. P.; Sharei, A.; Ding, X.; Sahay, G.; Langer, R.; Jensen, K. F. *In vitro* and *ex vivo* strategies for intracellular delivery. *Nature* **2016**, *538* (7624), 183–192.

(9) Maeder, M. L.; Gersbach, C. A. Genome-editing Technologies for Gene and Cell Therapy. *Mol. Ther.* **2016**, *24* (3), 430–446.

(10) Gu, Z.; Biswas, A.; Zhao, M.; Tang, Y. Tailoring nanocarriers for intracellular protein delivery. *Chem. Soc. Rev.* **2011**, *40* (7), 3638.

(11) Todorova, R. Estimation of methods of protein delivery into mammalian cells--a comparative study by electroporation and bioporter assay. *Appl. Biochem. Microbiol.* **2009**, *45* (4), 493–496.

(12) Frokjaer, S.; Otzen, D. E. Protein drug stability: A formulation challenge. *Nat. Rev. Drug Discov.* **2005**, *4* (4), 298–306.

(13) Nongkhlaw, R.; Patra, P.; Chavrasiya, A.; Jayabalan, N.; Dubey, S. Biologics: Delivery options and formulation strategies. In *Drug Delivery Aspects*; Elsevier, 2020; pp 115–155.

(14) Posey, N. D.; Tew, G. N. Associative and Dissociative Processes in Non-Covalent Polymer-Mediated Intracellular Protein Delivery. *Chem. - An Asian J.* **2018**, *13* (22), 3351–3365.

(15) Carter, P. J. Introduction to current and future protein therapeutics: A protein engineering perspective. *Exp. Cell Res.* **2011**, *317* (9), 1261–1269.

(16) Frankel, A. D.; Pabo, C. O. Cellular uptake of the tat protein from human immunodeficiency virus. *Cell* **1988**, *55* (6), 1189–1193.

(17) Vivès, E.; Brodin, P.; Lebleu, B.; Vivè, E.; Brodin, P.; Lebleu, B. A Truncated HIV-1 Tat Protein Basic Domain Rapidly Translocates through the Plasma Membrane and Accumulates in the Cell Nucleus. *J. Biol. Chem.* **1997**, *272* (25), 16010–16017.

(18) Green, M.; Loewenstein, P. M. Autonomous functional domains of chemically synthesized human immunodeficiency virus tat trans-activator protein. *Cell* **1988**, *55* (6), 1179–1188.

(19) Joliot, A.; Pernelle, C.; Deagostini-Bazin, H.; Prochiantz, A. Antennapedia homeobox peptide regulates neural morphogenesis. *Proc. Natl. Acad. Sci.* **1991**, *88* (5), 1864–1868.

(20) Derossi, D.; Joliot, A. H.; Chassaing, G.; Prochiantz, A. The third helix of the Antennapedia homeodomain translocates through biological membranes. *J. Biol. Chem.* **1994**, *269* (14), 10444–10450.

(21) Milletti, F. Cell-penetrating peptides: classes, origin, and current landscape. *Drug Discov. Today* **2012**, *17* (15–16), 850–860.

(22) Koren, E.; Torchilin, V. P. Cell-penetrating peptides: breaking through to the other side. *Trends Mol. Med.* **2012**, *18* (7), 385–393.

(23) Lindgren, M.; Hällbrink, M.; Prochiantz, A.; Langel, Ü. Cell-penetrating peptides. *Trends Pharmacol. Sci.* **2000**, *21* (3), 99–103.

(24) Wender, P. A.; Mitchell, D. J.; Pattabiraman, K.; Pelkey, E. T.; Steinman, L.; Rothbard, J. B. The design, synthesis, and evaluation of molecules that enable or enhance cellular uptake: Peptoid molecular transporters. *Proc. Natl. Acad. Sci.* **2000**, *97* (24), 13003–13008.

(25) Mitchell, D. J.; Steinman, L.; Kim, D. T.; Fathman, C. G.; Rothbard, J. B. Polyarginine enters cells more efficiently than other polycationic homopolymers. *J. Pept. Res.* **2000**, *56* (5), 318–325.

(26) Åmand, H. L.; Fant, K.; Nordén, B.; Esbjörner, E. K. Stimulated endocytosis in penetratin uptake: Effect of arginine and lysine. *Biochem. Biophys. Res. Commun.* **2008**, *371* (4), 621–625.

(27) Kolonko, E. M.; Kiessling, L. L. A Polymeric Domain That Promotes Cellular Internalization. *J. Am. Chem. Soc.* **2008**, *130* (17), 5626–5627.

(28) Cooley, C. B.; Trantow, B. M.; Nederberg, F.; Kiesewetter, M. K.; Hedrick, J. L.; Waymouth, R. M.; Wender, P. A. Oligocarbonate Molecular Transporters: Oligomerization-Based Syntheses and Cell-Penetrating Studies. *J. Am. Chem. Soc.* **2009**, *131* (45), 16401–16403.

(29) Geihe, E. I.; Cooley, C. B.; Simon, J. R.; Kiesewetter, M. K.; Edward, J. A.; Hickerson, R. P.; Kaspar, R. L.; Hedrick, J. L.; Waymouth, R. M.; Wender, P. A. Designed guanidinium-rich amphipathic oligocarbonate molecular transporters complex, deliver and release siRNA in cells. *Proc. Natl. Acad. Sci.* **2012**, *109* (33), 13171–13176.

(30) Bang, E.-K.; Gasparini, G.; Molinard, G.; Roux, A.; Sakai, N.; Matile, S. Substrate-Initiated Synthesis of Cell-Penetrating Poly(disulfide)s. *J. Am. Chem. Soc.* **2013**, *135* (6), 2088–2091.

(31) Kim, T.; Ou, M.; Lee, M.; Kim, S. W. Arginine-grafted bioreducible poly(disulfide amine) for gene delivery systems. *Biomaterials* **2009**, *30* (4), 658–664.

(32) Wender, P. A.; Kreider, E.; Pelkey, E. T.; Rothbard, J.; VanDeusen, C. L. Dendrimeric Molecular Transporters: Synthesis and Evaluation of Tunable Polyguanidino Dendrimers That Facilitate Cellular Uptake. *Org. Lett.* **2005**, *7* (22), 4815–4818.

(33) Luedtke, N. W.; Carmichael, P.; Tor, Y. Cellular Uptake of Aminoglycosides, Guanidinoglycosides, and Poly-arginine. *J. Am. Chem. Soc.* **2003**, *125* (41), 12374–12375.

(34) Treat, N. J.; Smith, D.; Teng, C.; Flores, J. D.; Abel, B. A.; York, A. W.; Huang, F.; McCormick, C. L. Guanidine-Containing Methacrylamide (Co)polymers via a RAFT: Toward a Cell-Penetrating Peptide Mimic. *ACS Macro Lett.* **2012**, *1* (1), 100–104.

(35) Zhou, P.; Wang, M.; Du, L.; Fisher, G. W.; Waggoner, A.; Ly, D. H. Novel Binding and Efficient Cellular Uptake of Guanidine-Based Peptide Nucleic Acids (GPNA). *J. Am. Chem. Soc.* **2003**, *125* (23), 6878–6879.

(36) Wender, P. A.; Rothbard, J. B.; Jessop, T. C.; Kreider, E. L.; Wylie, B. L. Oligocarbamate Molecular Transporters: Design, Synthesis, and Biological Evaluation of a New Class of Transporters for Drug Delivery. *J. Am. Chem. Soc.* **2002**, *124* (45), 13382–13383.

(37) Umezawa, N.; Gelman, M. A.; Haigis, M. C.; Raines, R. T.; Gellman, S. H. Translocation of a β-Peptide Across Cell Membranes. *J. Am. Chem. Soc.* **2002**, *124* (3), 368–369.

(38) Futaki, S.; Nakase, I.; Suzuki, T.; Youjun, Z.; Sugiura, Y. Translocation of branched-chain arginine peptides through cell membranes: Flexibility in the spatial disposition of positive charges in membrane-permeable peptides. *Biochemistry* **2002**, *41* (25), 7925–7930.

(39) Maiti, K. K.; Jeon, O.-Y.; Lee, W. S.; Kim, D.-C.; Kim, K.-T.; Takeuchi, T.; Futaki, S.; Chung, S.-K. Design, Synthesis, and Membrane-Translocation Studies of Inositol-Based Transporters. *Angew. Chemie Int. Ed.* **2006**, *45* (18), 2907–2912.

(40) deRonde, B. M.; Tew, G. N. Development of protein mimics for intracellular delivery. *Biopolymers* **2015**, *104* (4), 265–280.

(41) Wender, P. A.; Galliher, W. C.; Goun, E. A.; Jones, L. R.; Pillow, T. H. The design of guanidinium-rich transporters and their internalization mechanisms. *Adv. Drug Deliv. Rev.* **2008**, *60* (4–5), 452–472.

(42) Morris, M. C.; Depollier, J.; Mery, J.; Heitz, F.; Divita, G. A peptide carrier for the delivery of biologically active proteins into mammalian cells. *Nat. Biotechnol.* **2001**, *19* (12), 1173–1176.

(43) Morris, M. C.; Vidal, P.; Chaloin, L.; Heitz, F.; Divita, G. A new peptide vector for efficient delivery of oligonucleotides into mammalian cells. *Nucleic Acids Res.* **1997**, *25* (14), 2730–2736.

(44) Pooga, M.; Hällbrink, M.; Zorko, M.; Langel, Ü. Cell penetration by transportan. *FASEB J.* **1998**, *12* (1), 67–77.

(45) Oehlke, J.; Scheller, A.; Wiesner, B.; Krause, E.; Beyermann, M.; Klauschenz, E.; Melzig, M.; Bienert, M. Cellular uptake of an α-helical amphipathic model peptide with the potential to deliver polar compounds into the cell interior non-endocytically. *Biochim. Biophys. Acta - Biomembr.* **1998**, *1414* (1–2), 127–139.

(46) Crombez, L.; Aldrian-Herrada, G.; Konate, K.; Nguyen, Q. N.; McMaster, G. K.; Brasseur, R.; Heitz, F.; Divita, G. A New Potent Secondary Amphipathic Cell–penetrating Peptide for siRNA Delivery Into Mammalian Cells. *Mol. Ther.* **2009**, *17* (1), 95–103.

(47) Elmquist, A.; Lindgren, M.; Bartfai, T.; Langel, Ü. VE-Cadherin-Derived Cell-Penetrating Peptide, pVEC, with Carrier Functions. *Exp. Cell Res.* **2001**, *269* (2), 237–244.

(48) El-Andaloussi, S.; Johansson, H. J.; Holm, T.; Langel, Ü. A Novel Cell-penetrating Peptide, M918, for Efficient Delivery of Proteins and Peptide Nucleic Acids. *Mol. Ther.* **2007**, *15* (10), 1820–1826.

(49) Sgolastra, F.; Backlund, C. M.; Ilker Ozay, E.; deRonde, B. M.; Minter, L. M.; Tew, G. N. Sequence segregation improves non-covalent protein delivery. *J. Control. Release* **2017**, *254*, 131–136.

(50) Sgolastra, F.; Minter, L. M.; Osborne, B. A.; Tew, G. N. Importance of Sequence Specific Hydrophobicity in Synthetic Protein Transduction Domain Mimics. *Biomacromolecules* **2014**, *15* (3), 812–820.

(51) deRonde, B. M.; Posey, N. D.; Otter, R.; Caffrey, L. M.; Minter, L. M.; Tew, G. N. Optimal Hydrophobicity in Ring-Opening Metathesis Polymerization-Based Protein Mimics Required for siRNA Internalization. *Biomacromolecules* **2016**, *17* (6), 1969–1977.

(52) Posey, N. D.; Caffrey, L. M.; Minter, L. M.; Tew, G. N. Protein Mimic Hydrophobicity Affects Intracellular Delivery but not Cargo Binding. *ChemistrySelect* **2016**, *1* (19), 6146–6150.

(53) Takayama, K.; Hirose, H.; Tanaka, G.; Pujals, S.; Katayama, S.; Nakase, I.; Futaki, S. Effect of the Attachment of a Penetration Accelerating Sequence and the Influence of Hydrophobicity on Octaarginine-Mediated Intracellular Delivery. *Mol. Pharm.* **2012**, *9* (5), 1222–1230.

(54) Backlund, C. M.; Sgolastra, F.; Otter, R.; Minter, L. M.; Takeuchi, T.; Futaki, S.; Tew, G. N. Increased hydrophobic block length of PTDMs promotes protein internalization. *Polym. Chem.* **2016**, *7* (48), 7514–7521.

(55) Som, A.; Tezgel, A. Ö.; Gabriel, G. J.; Tew, G. N. Self-Activation in De Novo Designed Mimics of Cell-Penetrating Peptides. *Angew. Chemie Int. Ed.* **2011**, *50* (27), 6147–6150.

(56) Martin, L.; Peltier, R.; Kuroki, A.; Town, J. S.; Perrier, S. Investigating Cell Uptake of Guanidinium-Rich RAFT Polymers: Impact of Comonomer and Monomer Distribution. *Biomacromolecules* **2018**, *19* (8), 3190–3200.

(57) Pack, D. W.; Hoffman, A. S.; Pun, S.; Stayton, P. S. Design and development of polymers for gene delivery. *Nat. Rev. Drug Discov.* **2005**, *4* (7), 581–593.

(58) Posey, N. D.; Hango, C. R.; Minter, L. M.; Tew, G. N. The Role of Cargo Binding Strength in Polymer-Mediated Intracellular Protein Delivery. *Bioconjug. Chem.* **2018**, *29* (8), 2679–2690.

(59) Deshayes, S.; Morris, M.; Heitz, F.; Divita, G. Delivery of proteins and nucleic acids using a non-covalent peptide-based strategy. *Adv. Drug Deliv. Rev.* **2008**, *60* (4–5), 537–547.

(60) Zorko, M.; Langel, Ü. Cell-penetrating peptides: mechanism and kinetics of cargo delivery. *Adv. Drug Deliv. Rev.* **2005**, *57* (4), 529–545.

(61) Backlund, C. M.; Hango, C. R.; Minter, L. M.; Tew, G. N. Protein and Antibody Delivery into Difficult-to-Transfect Cells by Polymeric Peptide Mimics. *ACS Appl. Bio Mater.* **2020**, *3* (1), 180–185.

(62) Kurzawa, L.; Pellerano, M.; Morris, M. C. PEP and CADY-mediated delivery of fluorescent peptides and proteins into living cells. *Biochim. Biophys. Acta - Biomembr.* **2010**, *1798* (12), 2274–2285.

(63) Tezgel, A. Ö.; Jacobs, P.; Backlund, C. M.; Telfer, J. C.; Tew, G. N. Synthetic Protein Mimics for Functional Protein Delivery. *Biomacromolecules* **2017**, *18* (3), 819–825.

(64) Sarapas, J. M.; Backlund, C. M.; DeRonde, B. M.; Minter, L. M.; Tew, G. N. ROMP- and RAFT-Based Guanidinium-Containing Polymers as Scaffolds for Protein Mimic Synthesis. *Chem. - A Eur. J.* **2017**, *23* (28), 6858–6863.

(65) Caffrey, L. M.; deRonde, B. M.; Minter, L. M.; Tew, G. N. Mapping Optimal Charge Density and Length of ROMP-Based PTDMs for siRNA Internalization. *Biomacromolecules* **2016**, *17* (10), 3205–3212.

(66) deRonde, B. M.; Birke, A.; Tew, G. N. Design of Aromatic-Containing Cell-Penetrating Peptide Mimics with Structurally Modified π Electronics. *Chem. - A Eur. J.* **2015**, *21* (7), 3013–3019.

(67) Ozay, E. I.; Gonzalez-Perez, G.; Torres, J. A.; Vijayaraghavan, J.; Lawlor, R.; Sherman, H. L.; Garrigan, D. T.; Burnside, A. S.; Osborne, B. A.; Tew, G. N.; Minter, L. M. Intracellular Delivery of Anti-pPKCθ (Thr538) via Protein Transduction Domain Mimics for Immunomodulation. *Mol. Ther.* **2016**, *24* (12), 2118–2130.

(68) Backlund, C. M.; Parhamifar, L.; Minter, L.; Tew, G. N.; Andresen, T. L. Protein Transduction Domain Mimics Facilitate Rapid Antigen Delivery into Monocytes. *Mol. Pharm.* **2019**, *16* (6), 2462–2469.

(69) Tezgel, A. Ö.; Gonzalez-Perez, G.; Telfer, J. C.; Osborne, B. A.; Minter, L. M.; Tew, G. N. Novel Protein Transduction Domain Mimics as Nonviral Delivery Vectors for siRNA Targeting *NOTCH1* in Primary Human T cells. *Mol. Ther.* **2013**, *21* (1), 201–209.

(70) Shete, H. K.; Prabhu, R. H.; Patravale, V. B. Endosomal Escape: A Bottleneck in Intracellular Delivery. *J. Nanosci. Nanotechnol.* **2014**, *14* (1), 460–474.

(71) Xiang, S.; Tong, H.; Shi, Q.; Fernandes, J. C.; Jin, T.; Dai, K.; Zhang, X. Uptake mechanisms of non-viral gene delivery. *J. Control. Release* **2012**, *158* (3), 371–378.

(72) Khalil, I. A.; Kogure, K.; Akita, H.; Harashima, H. Uptake Pathways and Subsequent Intracellular Trafficking in Nonviral Gene Delivery. *Pharmacol. Rev.* **2006**, *58* (1), 32–45.

(73) Fu, A.; Tang, R.; Hardie, J.; Farkas, M. E.; Rotello, V. M. Promises and Pitfalls of Intracellular Delivery of Proteins. *Bioconjug. Chem.* **2014**, *25* (9), 1602–1608.

(74) Du, J.; Jin, J.; Yan, M.; Lu, Y. Synthetic Nanocarriers for Intracellular Protein Delivery. *Curr. Drug Metab.* **2012**, *13* (1), 82–92.

(75) Backlund, C. M.; Takeuchi, T.; Futaki, S.; Tew, G. N. Relating structure and internalization for ROMP-based protein mimics. *Biochim. Biophys. Acta - Biomembr.* **2016**, *1858* (7), 1443–1450.

(76) Deshayes, S.; Heitz, A.; Morris, M. C.; Charnet, P.; Divita, G.; Heitz, F. Insight into the Mechanism of Internalization of the Cell-Penetrating Carrier Peptide Pep-1 through Conformational Analysis. *Biochemistry* **2004**, *43* (6), 1449–1457.

(77) Smith, S. A.; Selby, L. I.; Johnston, A. P. R. R.; Such, G. K. The Endosomal Escape of Nanoparticles: Toward More Efficient Cellular Delivery. *Bioconjug. Chem.* **2019**, *30* (2), 263–272.

(78) Mitragotri, S.; Burke, P. A.; Langer, R. Overcoming the challenges in administering biopharmaceuticals: Formulation and delivery strategies. *Nat. Rev. Drug Discov.* **2014**, *13* (9), 655–672.

(79) Salmaso, S.; Caliceti, P. Self assembling nanocomposites for protein delivery: Supramolecular interactions of soluble polymers with protein drugs. *Int. J. Pharm.* **2013**, *440* (1), 111–123.

(80) Hoffman, A. Pharmacodynamic aspects of sustained release preparations. *Adv. Drug Deliv. Rev.* **1998**, *33* (3), 185–199.

(81) Sahay, G.; Alakhova, D. Y.; Kabanov, A. V. Endocytosis of nanomedicines. *J. Control. Release* **2010**, *145* (3), 182–195.

(82) Selby, L. I.; Cortez-Jugo, C. M.; Such, G. K.; Johnston, A. P. R. Nanoescapology: progress toward understanding the endosomal escape of polymeric nanoparticles. *Wiley Interdiscip. Rev.: Nanomed. Nanobiotechnol.* **2017**, *9* (5), e1452.

(83) Madani, F.; Lindberg, S.; Langel, Ü.; Futaki, S.; Gräslund, A. Mechanisms of Cellular Uptake of Cell-Penetrating Peptides. *J. Biophys.* **2011**, *2011*, 1–10.

(84) Gilleron, J.; Querbes, W.; Zeigerer, A.; Borodovsky, A.; Marsico, G.; Schubert, U.; Manygoats, K.; Seifert, S.; Andree, C.; Stöter, M.; Epstein-Barash, H.; Zhang, L.; Koteliansky, V.; Fitzgerald, K.; Fava, E.; Bickle, M.; Kalaidzidis, Y.; Akinc, A.; Maier, M.; et al. Image-based analysis of lipid nanoparticle–mediated siRNA delivery, intracellular trafficking and endosomal escape. *Nat. Biotechnol.* **2013**, *31* (7), 638–646.

(85) Varkouhi, A. K.; Scholte, M.; Storm, G.; Haisma, H. J. Endosomal escape pathways for delivery of biologicals. *J. Control. Release* **2011**, *151* (3), 220–228.

(86) Jhaveri, A.; Torchilin, V. Intracellular delivery of nanocarriers and targeting to subcellular organelles. *Expert Opin. Drug Deliv.* **2016**, *13* (1), 49–70.

(87) Maity, A. R.; Stepensky, D. Delivery of drugs to intracellular organelles using drug delivery systems: Analysis of research trends and targeting efficiencies. *Int. J. Pharm.* **2015**, *496* (2), 268–274.

(88) Chen, W. H.; Luo, G. F.; Zhang, X. Z. Recent Advances in Subcellular Targeted Cancer Therapy Based on Functional Materials. *Adv. Mater.* **2019**, *31* (3), 1–39.

(89) Ma, X.; Gong, N.; Zhong, L.; Sun, J.; Liang, X.-J. Future of nanotherapeutics: Targeting the cellular sub-organelles. *Biomaterials* **2016**, *97*, 10–21.

(90) Guo, X.; Wei, X.; Chen, Z.; Zhang, X.; Yang, G.; Zhou, S. Multifunctional nanoplatforms for subcellular delivery of drugs in cancer therapy. *Prog. Mater. Sci.* **2020**, *107*, 100599.

(91) Hou, X.-S. S.; Wang, H.-S. S.; Mugaka, B. P.; Yang, G.-J. J.; Ding, Y. Mitochondria: Promising organelle targets for cancer diagnosis and treatment. *Biomater. Sci.* **2018**, *6* (11), 2786–2797.

(92) Ma, C.; Xia, F.; Kelley, S. O. Mitochondrial Targeting of Probes and Therapeutics to the Powerhouse of the Cell. *Bioconjug. Chem.* **2020**, *31* (12), 2650–2667.

(93) Yameen, B.; Choi, W. Il; Vilos, C.; Swami, A.; Shi, J.; Farokhzad, O. C. Insight into nanoparticle cellular uptake and intracellular targeting. *J. Control. Release* **2014**, *190*, 485–499.

(94) Louzoun-Zada, S.; Jaber, Q. Z.; Fridman, M. Guiding Drugs to Target-Harboring Organelles: Stretching Drug-Delivery to a Higher Level of Resolution. *Angew. Chemie Int. Ed.* **2019**, *58* (44), 15584–15594.

CHAPTER 2

2 PROTEIN AND ANTIBODY DELIVERY TO DIFFICULT-TO-TRANSFECT CELLS BY POLYMERIC PEPTIDE MIMICS

NOTE: This chapter has been adapted with permission from the following previously published article: Backlund, C. M.; Hango, C. R.; Minter, L. M.; Tew, G. N. Protein and Antibody Delivery into Difficult-to-Transfect Cells by Polymeric Peptide Mimics. *ACS Appl. Bio Mater.* **2020**, *3* (1), 180–185.

Polymer preparation and EGFP delivery experiments in HeLa, HUVEC, Jurkat, and MSC cells in this chapter were completed by Coralie M. Backlund.

2.1 Introduction

2.1.1 Summary

Intracellular protein delivery using simple non-covalent carriers is an emerging field advancing the study of intracellular pathways and novel therapeutics. Here, we directly compare GFP delivery using our recently-reported protein transduction domain mimic (PTDM) to delivery with four commercially-available, amphiphilic macromolecular carriers in five diverse cell types. While most carriers succeeded only in serum-free conditions, the PTDM maintained robust delivery in complete media, even when tasked with antibody delivery into difficult-to-transfect neurons for the first time. The broad effectiveness of this reagent establishes PTDMs as a promising strategy for the delivery of biologics into such sensitive and challenging cell types.

2.1.2 Background

To date, protein delivery has been predominantly addressed using virus-like particles, electroporation, liposomal carriers, and nanoparticles.[1] While effective in some cases, these techniques often face limitations including high toxicity and low efficiency,

which has led to the development of new synthetic carriers based primarily on cationic polymers.[2–4] Several such polymer systems are currently available commercially, but are often limited to select cargoes and easier-to-transfect cell types. For example, primary cells have traditionally proven much more challenging to transfect than immortalized cell lines.[5–7] Additionally, almost all of these delivery platforms require serum-free conditions, which is detrimental to cell viability, particularly when working with sensitive cultures like primary cells. These limitations underscore the importance of developing tools which can service a broader range of applications and are widely effective across all cell types, cargoes, and conditions.[1]

In an effort to address these needs, a unique library of bioinspired amphiphilic, polymeric protein transduction domain mimics (PTDMs) was developed using a ring-opening metathesis polymerization-based synthetic platform.[3,8–12] In contrast with protein transduction domains and cell-penetrating peptides, which usually require covalent attachment to their cargo, PTDMs bind their payload in a simple mixing and complexation step, without the need for cumbersome conjugation chemistry or protein engineering. The PTDM used in this study, **MePh$_{10}$-*b*-dG$_5$**, was designed to directly mimic cell-penetrating peptides, incorporating a dense block of guanidinium functionality (**dG)**, known for its ability to transition across cell membranes, attached to a hydrophobic block (**MePh**), which has been shown to enhance cargo delivery.[13–15] Details regarding the structure and synthesis of this polymer can be found in Figure 2.1. PTDMs including this one have successfully delivered a variety of proteins, peptides, and antibodies into several difficult-to-transfect cell types, including primary T cells.[8–10,12] The non-covalent complexes these

PTDMs form with the desired payload facilitate cargo transport across the cell membrane in both complete media and serum-free conditions with low cytotoxicity.

While countless isolated instances of carrier-mediated protein delivery have been reported, comprehensive side-by-side comparisons under application-relevant conditions are rare;[16] more are needed to eliminate experimental variation and directly assess a carrier's relative effectiveness for a given application. Given the remarkable ability of PTDMs to successfully deliver various functional proteins to challenging cell types, a direct comparison to other similar delivery platforms is needed. Herein, we compare the performance of **MePh$_{10}$-*b*-dG$_5$** (henceforth referred to as the PTDM) to four commercially available amphiphilic polymers or peptides: Chariot™ (also known as Pep-1), ProteoJuice™, PULSin™, and Xfect™. Each reagent was assessed for its ability to deliver the model cargo green fluorescent protein (GFP) in both serum-free and serum-containing conditions with HeLa cells, human umbilical vein endothelial cells (HUVECs), hTERT mesenchymal stem cells (MSCs), Jurkat T cells, and embryonic mouse hippocampal-18 cells (mHippoE). While HeLa cells are generally easily transfected, HUVECs, stem cells, immune cells, and neuron cells have traditionally proven particularly difficult-to-transfect.[1,5–7,17–20]

Examples of successful protein and antibody delivery to neurons are particularly scarce. To the best of our knowledge, only a few examples of intraneuronal antibody delivery exist, just one of which is polymer-mediated.[21–26] Because of this, antibody delivery was then assessed in neurons to evaluate the capacity of PTDMs as novel tools for elucidation and manipulation of biology in a presently inaccessible cell type.

Several cationic, macromolecular delivery vehicles were tested for their ability to deliver GFP into five disparate cell types. Specifically, the commercially available reagents Chariot™, ProteoJuice™, PULSin™, and Xfect™ were compared with our PTDM, in both complete and serum-free conditions. All purchased delivery reagents claim non-covalent interactions with their cargo and broad cell specificity. While most of the reagents reported here are proprietary, the descriptions of each of the carriers from their respective manufacturers are found in Section 2.2 Materials and Methods.

Several cell lines were chosen to demonstrate translation across cell type: HeLa cells, human umbilical vein endothelial cells (HUVECs), Jurkat T cells, hTERT mesenchymal stem cells (MSCs), and embryonic mouse hippocampal (mHippoE) cells. HeLa cells are the oldest, most common adherent cell line and are extensively used in many research fields due to their stability and relative ease of transfection. HUVECs are derived from the endothelium of veins from a human umbilical cord and have different cell surface properties than epithelial cells such as HeLas. Jurkats are a suspension immune cell line that have proven difficult for many transfection reagents. MSCs represent a cell type whose differentiation could be affected by protein delivery. mHippoE cells are derived from the murine hippocampus and represent a neural cell type, a class of cells for which many transfection reagents fall short. These cell types were specifically selected because immune cells, stem cells, and neurons are among the most notoriously challenging classes of cells to transfect.

2.2 Materials and Methods

2.2.1 Protein Carriers

2.2.1.1 Pep-1

Pep-1 was first reported by Morris *et al.* to deliver proteins intracellularly using non-covalent interactions with the macromolecule of interest.[27] Since then, Pep-1 and its derivatives have been patented and are now marketed by Active Motif® under the name Chariot™. Chariot™ reports delivery efficiency between 60-95% in less than two hours after delivery, at which time live cells can be assayed to determine the effects of the introduced material, without the need for fixing. According to Morris *et al.* and Active Motif®, the peptide stabilizes the protein, reducing degradation and preserving its natural characteristics during delivery.[27–29] After delivery, the complex dissociates, leaving the macromolecule biologically active and free to proceed to its target organelle. Previous reports indicate that delivery occurs in the presence or absence of serum and is independent of the endosomal pathway, which can modify macromolecules during internalization.[30] Additionally, Chariot™ boasts low toxicity to the cells being transfected.

2.2.1.2 PULSin

PULSin™ is a cationic amphiphilic reagent designed by Polyplus Transfection® for the delivery of peptides, antibodies and proteins into cells. The proprietary formulation claims efficient delivery of anionic proteins and antibodies into a large variety of eukaryotic cell lines and primary cells. PULSin™ is most efficient when able to interact with the protein by electrostatic and/or lipophilic interactions. According to Polyplus Transfection®, complexes are internalized via anionic cell-adhesion receptors and are

released into the cytoplasm where they disassemble. The process is non-toxic and delivers functional proteins, without the requirement of fixation.

2.2.1.3 ProteoJuice

ProteoJuice™ is a reagent produced by Novagen®, owned by MerckMillipore®, for the introduction of intact functional protein into mammalian cells. ProteoJuice™ forms non-covalent interactions with protein and has endosome-protective properties, ensuring delivery of intact protein within the cell. ProteoJuice™ is compatible with delivery of peptides and small proteins, large proteins, and even multimeric protein complexes with minimal toxicity and broad cell specificity. Live cells can be examined less than two hours after delivery to determine the effects of the introduced material without the need for cell fixation.

2.2.1.4 Xfect

The Xfect™ Protein Transfection Reagent uses a cell-penetrating peptide developed at Clontech® to bind and transport active proteins directly into a wide variety of mammalian cell types, including hard-to-transfect human suspension cell lines and mouse embryonic stem cells. Xfect™ is a modified peptide with cell-penetrating activity whose amino acid composition enables it to interact with a protein cargo and transport this protein across a cell membrane barrier within 2 hours.

2.2.1.5 $MePh_{10}$-*b*-dG_5 (PTDM)

The PTDM used in this chapter, **$MePh_{10}$-*b*-dG_5** (referred to simply as the PTDM in this study), was synthesized by the Tew Group for use in previous studies, where the full

synthetic procedure and characterization can be found.[11,31] The chemical structure of the PTDM is shown in Figure 2.1.

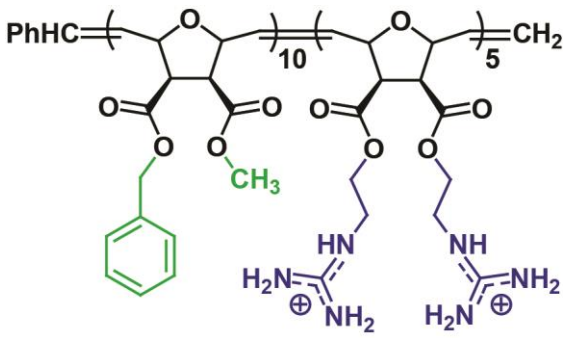

Figure 2.1: Chemical structure of **MePh$_{10}$-*b*-dG$_5$**, the PTDM used in Chapter 2. Hydrophobic and cationic functional groups are shown in green and blue, respectively.

2.2.2 Other Materials

All adherent cell lines were cultured in Gibco™ DMEM High Glucose GlutaMAX™ Supplement (Thermo Fisher Scientific), supplemented with 10% (v/v) FBS or EquaFETAL (Atlas Biologicals), 1% (v/v) 100 mM Sodium Pyruvate Solution (Lonza) or 100 mM HyClone™ Sodium Pyruvate Solution (Fisher Scientific), 1% (v/v) 100x MEM Non-Essential Amino Acid Solution (Lonza) or 100x HyClone™ Non-Essential Amino Acids NEAA (Fisher Scientific), and 1% (v/v) Penicillin-Streptomycin Mixture (10LK/10K) (Lonza). Jurkat T cells were cultured in Gibco™ RPMI 1640 High Glucose GlutaMAX™ Supplement (Thermo Fisher Scientific), supplemented with all of the previously-mentioned materials as well as 1% (v/v) HEPES (1 M) (Thermo Fisher Scientific). Serum-free DMEM and serum-free RPMI were formulated in the same manner, withholding the 10% FBS or EquaFETAL. Gibco™ 10X phosphate-buffered saline (PBS), pH 7.4 was diluted to 1X prior to use. Gibco™ 0.25% trypsin-EDTA (Thermo Fisher Scientific) was used to lift adherent cells prior to washing with heparin sodium salt from porcine intestinal mucosa (≥100 IU/mg) (Alfa Aesar/VWR) to remove

extracellular complexes from the cell surfaces. 7-aminoactinomycin D (7-AAD) Staining Solution (BD Biosciences/Fisher Scientific) was used to assess cellular viability in uptake experiments.

2.2.3 Instrumentation

Flow cytometry experiments for HeLa, HUVEC, Jurkat, and MSC cell lines were conducted using either a BD LSRII (HeLa, HUVEC, Jurkat, and MSC experiments) or a BD Dual LSRFortessa™ (mHippoE experiments). Analysis was performed using FlowJo software. Confocal microscopy images were collected using a Nikon A1 Spectral Detector Confocal with FLIM Module at 60x with immersion oil using the FITC channel for fluorescence detection.

2.2.4 GFP Delivery

2.2.4.1 Delivery with Pep-1

The lyophilized Pep-1 reagent was dissolved in sterile H_2O, aliquoted, and stored at -20 °C until needed, as described by the manufacturer. In the case of adherent cell lines, cells were seeded in 6-well plates in complete DMEM 24h prior to delivery at an appropriate density to achieve ~70-90% confluency by the time of transfection. Media was replaced with 0.8 mL of fresh DMEM, either serum-containing or serum-free (in this case, after washing once with 1X PBS to remove any traces of serum), depending on the experiment, at the time of transfection. In contrast, Jurkat T cells were harvested on the day of the experiment and seeded in 12-well plates at a density of 4×10^5 cells/0.8 mL of fresh RPMI, again either serum-containing or serum-free (800 μL per well). The GFP stock solution was diluted to a working concentration of 0.5 mg/mL with 1X phosphate-

buffered saline (PBS, pH ~7.4). Appropriate quantities of diluted GFP (corresponding to a final delivery concentration of 3 μg/mL) and Pep-1 (6 μL; see Section 2.2.5 Carrier Optimization) were brought to volumes of 100 μL in separate microcentrifuge tubes using 1X PBS and sterile H_2O, respectively. Pep-1:GFP complexes were formed by combining the two solutions to reach a total volume of 200 μL and mixing by pipette. These complexes were incubated in the dark at room temperature for 30 min prior to adding them dropwise to each well, resulting in final delivery volumes of 1 mL. The cells were incubated with the complexes for 4 h at 37°C in 5% CO_2. In serum-free experiments, 800 μL of complete media was added to each well halfway through the incubation, to help with cellular viability. After the incubation period, the cells were harvested (following treatment with 200 μL 0.25% trypsin-EDTA and neutralization with 800 μL DMEM, in the case of adherent cells), transferred to microcentrifuge tubes, centrifuged, and washed 3 times with 800 μL of heparin (20 U/mL in 1X PBS) to remove any extracellular or surface-bound complexes, in accordance with previously-published procedures. Cells were resuspended in 200 μL of FACS buffer (0.2% BSA in PBS) containing 5 μL of 7-aminoactinomycin D (7-AAD) stain prior to internalization and viability analysis by flow cytometry, in which data for 10,000 cells were collected.

2.2.4.2 Delivery with PULSin

Cellular uptake experiments for PULSin were performed in accordance with manufacturer guidelines. Specifically, transfections were performed as described for Pep-1, with the following exceptions. The PULSin reagent was used as received, without further dilution, and stored at 4 °C, as described by the manufacturer. PULSin:GFP complexes were formed by combining appropriate quantities of diluted GFP

(corresponding to a final delivery concentration of 3 μg/mL) and PULSin (3 μL; see Section 2.2.5 Carrier Optimization) in the supplied HEPES buffer to achieve a volume of 100 μL, followed by brief vortexing to mix. Following the 30-minute complexation period, 100 μL of serum-free media was added to reach a final complex volume of 200 μL.

2.2.4.3 Delivery with ProteoJuice

Cellular uptake experiments for ProteoJuice were performed in accordance with manufacturer guidelines. Specifically, transfections were performed as described for Pep-1, with the following exceptions. The ProteoJuice reagent was used as received, without further dilution, and stored at 4 °C, as described by the manufacturer. ProteoJuice:GFP complexes were formed by combining appropriate quantities of diluted GFP (corresponding to a final delivery concentration of 3 μg/mL) and ProteoJuice (3 μL; see Section 2.2.5 Carrier Optimization) in serum-free media to achieve a volume of 53 μL, followed by brief vortexing to mix. Following the 30-minute complexation period, 147 μL of serum-free media was added to reach a final complex volume of 200 μL.

2.2.4.4 Delivery with Xfect

Cellular uptake experiments for Xfect were performed in accordance with manufacturer guidelines. Specifically, transfections were performed as described for Pep-1, with the following exceptions. The lyophilized Xfect reagent was dissolved in sterile H_2O, aliquoted, and stored at -20 °C until needed, as described by the manufacturer. Appropriate quantities of diluted GFP (corresponding to a final delivery concentration of 3 μg/mL) and Xfect (15 μL; see Section 2.2.5 Carrier Optimization) were brought to volumes of 40 μL in separate microcentrifuge tubes using the supplied Protein Buffer and

sterile H_2O, respectively. Xfect:GFP complexes were formed by combining the two solutions to reach a total volume of 80 μL and mixing by pipette. Following the 30-minute complexation period, 120 μL of serum-free media was added to reach a final complex volume of 200 μL.

2.2.4.5 Delivery with $MePh_{10}$-*b*-dG_5 (PTDM)

The following general procedure for fluorescent protein uptake was based on previously-published procedures.[11,31] The PTDM was dissolved in DMSO to make a 1 mM stock solution and was stored at -20 °C. In the case of the adherent cell lines, cells were seeded in 12-well plates in complete DMEM 24h prior to delivery at an appropriate density to achieve ~70-90% confluency by the time of transfection. Media was replaced with 0.8 mL of fresh DMEM, either serum-containing or serum-free, depending on the experiment, at the time of transfection. In contrast, Jurkat T cells were harvested on the day of the experiment and seeded in 12-well plates at a density of 4 x 10^5 cells/0.8 mL of fresh RPMI, again either serum-containing or serum-free (800 μL per well). GFP and PTDM stock solutions were diluted to working concentrations with 1X phosphate-buffered saline (PBS, pH ~7.4). Carrier:protein complexes were prepared by mixing appropriate volumes of protein (corresponding to a final delivery concentration of 3 μg/mL GFP) and carrier (20:1 molar ratio of PTDM:GFP) in 1X PBS to achieve total volumes of 200 μL. These complexes were incubated in the dark at room temperature for 30 min prior to adding them dropwise to each well, resulting in final delivery volumes of 1 mL. The cells were incubated with the complexes for 4 h at 37°C in 5% CO_2. In serum-free experiments, 800 μL of complete media was added to each well halfway through the incubation, to help with cellular viability. After the incubation period, the cells were harvested (following

treatment with 0.25% trypsin-EDTA and neutralization with DMEM in the case of adherent cells), transferred to microcentrifuge tubes, centrifuged, and washed 3 times with 800 μL of heparin (20 U/mL in 1X PBS) to remove any extracellular or surface-bound complexes, in accordance with previously-published procedures.[32] Cells were resuspended in 200 μL of FACS buffer (0.2% BSA in PBS) containing 5 μL of 7-aminoactinomycin D (7-AAD) stain prior to internalization and viability analysis by flow cytometry, in which data for 10,000 cells were collected.

2.2.5 Carrier Optimization

For delivery of GFP into each cell line, the amount of each delivery reagent was tested at the suggested concentration, as well as 2- and 4-fold higher concentrations, in their respective diluents. Cells were treated independently in serum-free and serum-containing media to determine the optimal conditions for protein delivery. All conditions were assessed after a 4-6 hour incubation, according to the manufacturer's protocol, by lifting with trypsin followed by 3 washes using 20 μg/mL heparin and analysis by flow cytometry. The concentration of delivery vehicle that produced the highest GFP delivery with the lowest cytotoxic effect was selected.

2.2.6 Antibody Delivery

PTDM-mediated antibody delivery experiments were performed in a similar manner to PTDM-mediated GFP delivery experiments (Section 2.2.4.5) with the following exceptions. IgG, $F(ab')_2$, and PTDM stock solutions were diluted to working concentrations with 1X phosphate-buffered saline (PBS, pH ~7.4). Cells were plated in

12-well plates, rather than 6-well plates. Complexes were prepared at a concentration of 5 nM IgG-AF488 or F(ab')$_2$-AF488 and a molar ratio of 40:1 PTDM:antibody.

2.2.7 Confocal Microscopy

IgG-AF488 delivery for imaging by confocal microscopy was performed as described in Section 2.2.6 with the following variations. Cells were plated 48 hours prior to delivery at a density of 10,000 cells/well in 8-well microscopy slides. Following delivery, cells were washed three times by incubation with heparin (20 U/mL) for 5 minutes each. After the final wash, the heparin was replaced with fresh media and the cells were directly imaged.

2.3 Results and Discussion

To assess protein delivery with each reagent, GFP was chosen as a self-reporting cargo. The amount of protein used for delivery was held constant at 3 µg, allowing the different reagents to be compared with one another. As depicted in Figure 2.2, uptake was assessed by gain in cellular fluorescence, as monitored by flow cytometry after treatment

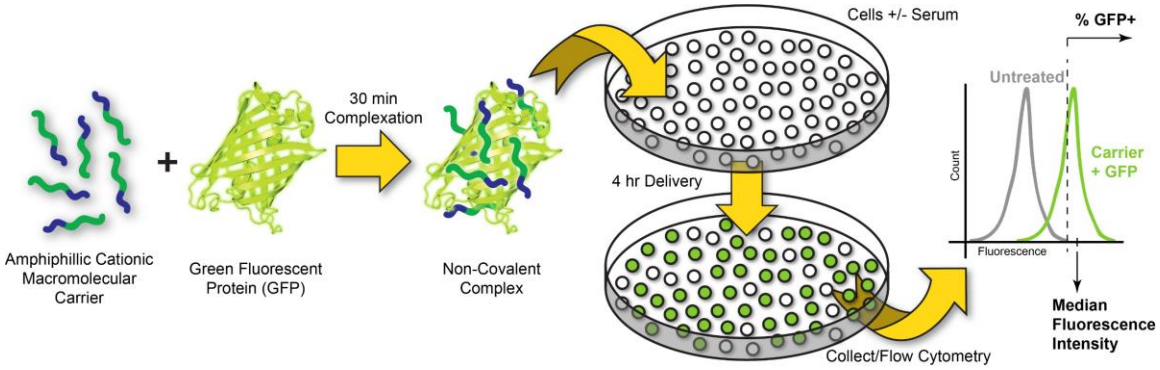

Figure 2.2: Workflow for side-by-side evaluation of protein delivery reagents. Briefly, each amphiphilic carrier (hydrophobic/hydrophilic functionalities represented in green/blue, respectively) was first mixed with green fluorescent protein (GFP) and allowed to incubate at room temperature for 30 minutes to form non-covalent complexes. These complexes were then introduced to cells in either serum-free or serum-containing media and allowed to incubate for 4 hours. Following delivery, the cells were washed with heparin to remove extracellular complexes and subsequently analyzed by flow cytometry to assess intracellular fluorescence.

with the complexes and subsequent washing of the cell surface with heparin (20 U/mL) to remove any surface-associated carrier:protein complexes, in accordance with previously-published methods.[32]

Importantly, commercial reagents were individually optimized to maximize their delivery ability in each cell line prior to comparison with the other reagents, as described in Section 2.2.5. Even though some of the reagents report the ability to deliver in complete media, most suggest removal of any exogenous protein during the actual transduction by washing with PBS. To accommodate this, delivery was performed on cells in serum-free media that had previously been washed twice with PBS to remove serum proteins. A comparison of the reagents was also made in complete media (containing 10% serum) to show the effect of serum on uptake.

When assessed by the percentage of cells positive for GFP, Xfect™ was the only commercial reagent able to deliver GFP into all five cell types under serum-free conditions, although neurons proved significantly more challenging than other cell lines (Figure 2.3A, C, E, G, I). Similarly, PULSin™ was able to deliver GFP in serum-free media to a significant percentage of every cell type except neurons. ProteoJuice™ only achieved moderate delivery (~20%) in one cell type (Jurkat T cells), while Chariot™ was unable to deliver GFP to any cell type. In almost all cases, a drastic reduction in effectiveness was observed when delivery was performed in complete media (red bars), as opposed to serum-free media (blue bars). In fact, the only example of significant GFP delivery in the presence of serum was PULSin with MSCs. In stark contrast to all commercial reagents, the PTDM performed exceptionally well in every cell type, both in the absence and the presence of serum. Unlike its commercial counterparts, the PTDM performed just as well in complete

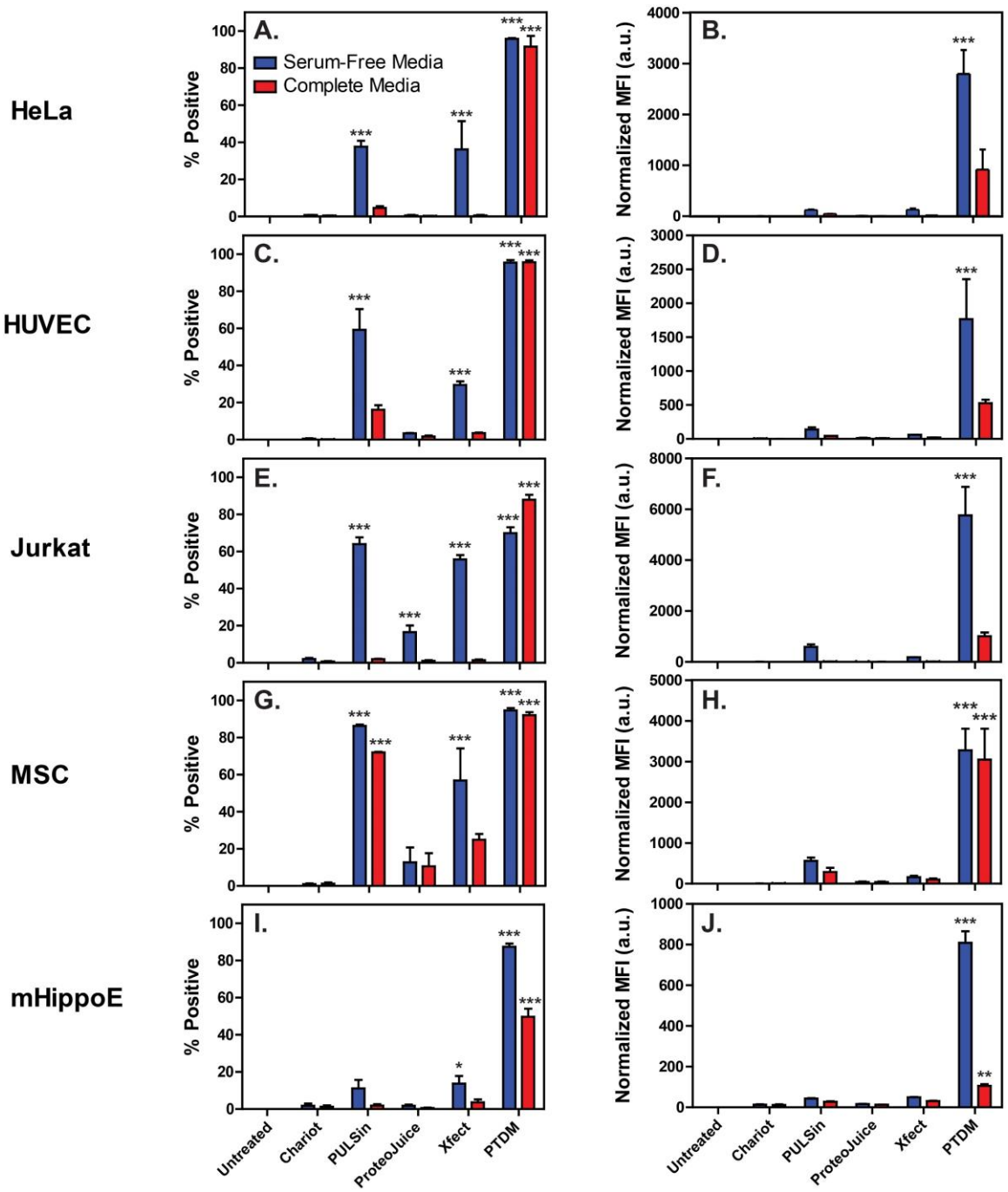

Figure 2.3: Uptake of 3 µg GFP into (A-B) HeLa cells, (C-D) human umbilical vein endothelial cells (HUVEC), (E-F) Jurkat T cells, (G-H) hTERT mesenchymal stem cells (MSC), and (I-J) embryonic mouse hippocampal cells (mHippoE) after treatment in either serum-free (blue bars) or complete media (red bars) using amphiphilic polymers designed for non-covalent protein delivery. The left-hand column indicates the percent of cells positive for the fluorescent cargo, while the right-hand column shows the median fluorescence intensity (MFI) of the entire population, proportional to the quantity of protein internalized. Data are displayed as the mean ± the standard error of the mean for three independent replicates. Statistics indicate significance in comparison with the untreated control: * = $p < 0.05$, ** = $p < 0.01$, *** = $p < 0.001$, no symbol = no significance, as determined by one-way ANOVA followed by a Tukey post-test.

media as in serum-free media, except with mHippoE cells (though delivery to half the population was still managed in this case).

When assessed by the median fluorescence intensity (MFI), which is directly proportional to the amount of protein delivered, delivery was exceptionally low for all commercial carriers in all cell types (Figure 2.3B, D, F, H, J). None of these carriers were able to deliver a statistically significant quantity of cargo into any cell types, even in the absence of serum. This indicates that, while some carriers were able to target a large fraction of the population, they were not able to deliver much protein into those cells. The PTDM, however, reliably delivered significant quantities of protein to every cell type in serum-free media. In the presence of serum, statistically significant amounts of GFP were only delivered to MSCs and neurons, although the MFIs for HeLa, Jurkat, and HUVEC cell lines still appear to be higher than the controls and might become significant if more than three replicates were collected.

Significant drops in cellular viability were observed for several cell type/carrier combinations under serum-free conditions: HeLa cells (PULSin), Jurkat T cells (PULSin, ProteoJuice, and PTDM) and mHippoE cells (PULSin and PTDM) (Figure 2.4). However, the use of serum-containing media eliminated these viability concerns in almost every case, highlighting the importance of developing serum-insensitive delivery vehicles, like the PTDM, for delivery to more fragile cell types like T cells and neurons.

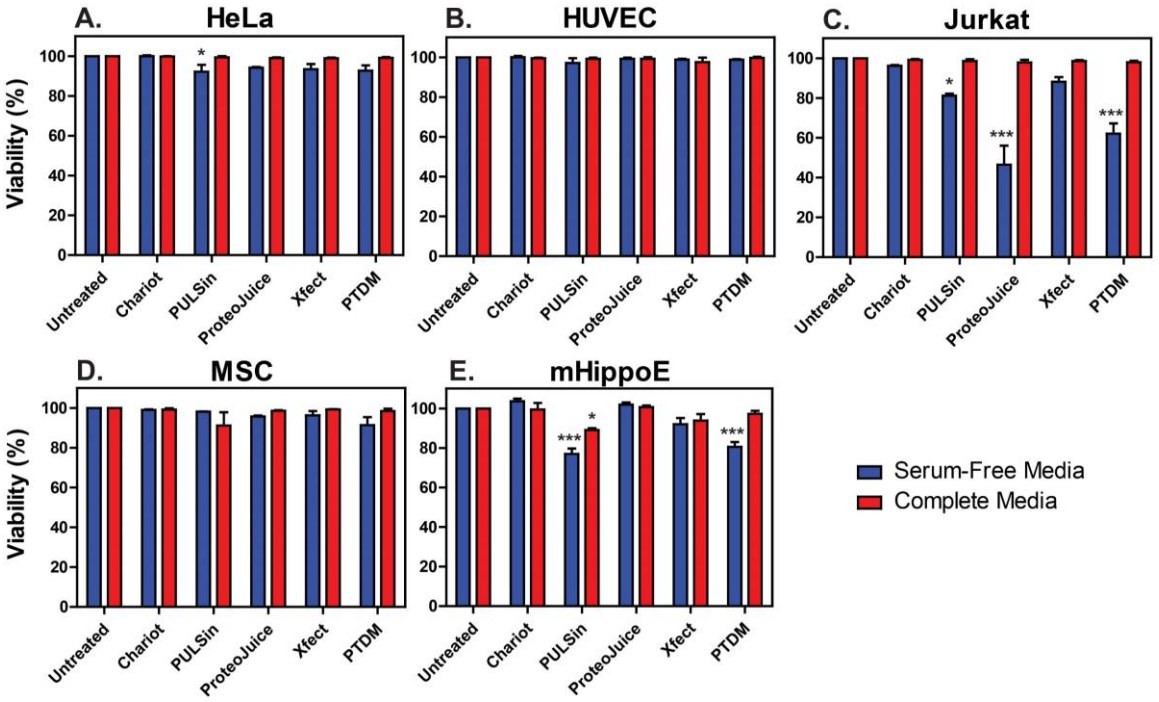

Figure 2.4: Viability as determined by 7-AAD staining of (A) HeLa, (B) HUVEC, (C) Jurkat, (D) MSC, and (E) mHippoE cell lines treated with the carrier:GFP complexes in serum-free (blue bars) or complete (red bars) media. Samples were normalized against the untreated control in which cells were treated with PBS only, and the mean ± SEM is shown for three separate experiments. Statistics indicate significance in comparison with the untreated control: * = $p < 0.05$, ** = $p < 0.01$, *** = $p < 0.001$, no symbol = no significance, as determined by one-way ANOVA followed by a Tukey post-test.

Taken altogether, GFP delivery by the PTDM in complete media consistently outperformed the optimized conditions of all other delivery reagents in serum-free conditions across all cell types surveyed. Significantly, the PTDM was able to successfully deliver to mHippoE cells, by far the most challenging cell type for all of the commercial reagents, indicating for the first time that PTDMs are a promising candidate for intraneuronal protein delivery, a need which is largely unmet in the field of neuron biology.[1,19,20]

Motivated by successful GFP delivery in the mHippoE cell line and the lack of efficient protein delivery carriers in the neuron literature, the utility of the reported PTDM was further explored using additional protein cargoes. Specifically, a polyclonal IgG antibody and a polyclonal $F(ab')_2$ antibody fragment, both fluorescently labelled with

Alexa Fluor 488® (AF488), were assessed for mHippoE internalization using the PTDM in serum-containing media (Figure 2.5). These antibody-based cargoes were selected to evaluate delivery of clinically-relevant biologics whose physical properties such as size and shape deviate greatly from those of other proteins, like GFP.

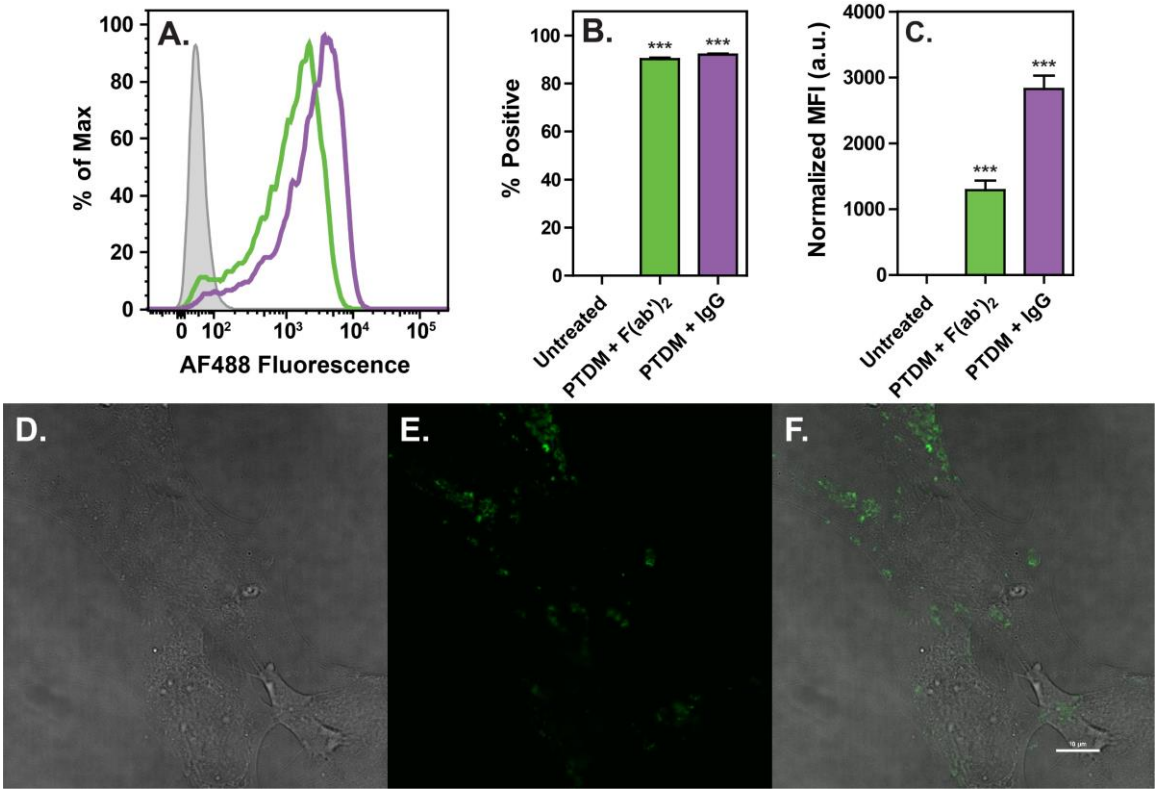

Figure 2.5: PTDM-mediated delivery of 5 nM antibody into embryonic mouse hippocampal cells, as assessed by flow cytometry (A-C) and confocal microscopy (D-F). Flow cytometry data show (A) representative fluorescence histograms, (B) percent of cells positive for the fluorescent cargo, and (C) normalized median fluorescence intensities (MFIs) for a polyclonal IgG-AF488 antibody (purple), polyclonal F(ab')$_2$-AF488 antibody fragment (green), and an untreated sample (grey) after 4 hours in complete media. Data are displayed as the mean ± the standard error of the mean for three independent replicates. Statistics indicate significance in comparison with the untreated control: * = $p < 0.05$, ** = $p < 0.01$, *** = $p < 0.001$, no symbol = no significance, as determined by one-way ANOVA followed by a Tukey post-test. Confocal data show the optical (D), fluorescence (E), and merged (F) channels of a representative microscope image following IgG-AF488 delivery for 4 hours in complete media. Scale bar represents 10 μm.

The successful delivery of both cargoes is evidenced by a dramatic fluorescence shift of virtually the entire population in the flow cytometry histograms (Figure 2.5A). In both cases, cargo was delivered to more than 90% of the population, with high MFI values relative to the untreated control (Figure 2.5B-C). Importantly, cellular viability data also

indicated no significant cytotoxicity of the PTDM for either whole antibody or antibody fragment delivery (Figure 2.6). The neurons were also visualized immediately following delivery of IgG-AF488 using confocal microscopy, confirming GFP uptake into most of the cell body, apart from the nucleus (Figure 2.5D-F).

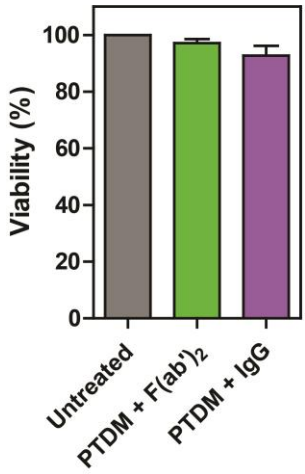

Figure 2.6: Viability as determined by 7-AAD staining of mHippoE cells treated with F(ab')$_2$-PTDM (green) or IgG-PTDM (purple) complexes in complete media. Samples were normalized against the untreated control (grey) in which cells were treated with PBS only, and the mean ± SEM is shown for three separate experiments. Statistics indicate significance in comparison with the untreated control: * = $p < 0.05$, ** = $p < 0.01$, *** = $p < 0.001$, no symbol = no significance, as determined by one-way ANOVA followed by a Tukey post-test.

Due to potential differences in dye-labeling of the two cargoes, no conclusion should be drawn from the differences in MFI values. Likewise, no quantitative comparison can be made between the antibodies and GFP, an entirely different chromophore. For this reason, no speculation as to the relative amounts of IgG, F(ab')$_2$, or GFP delivered are made; nonetheless, these data strongly suggest that PTDMs are a promising new class of carriers for the delivery of functional proteins, particularly antibody-based cargoes, into neurons.

2.4 Conclusions

While many products are being developed for protein delivery, all of the commercially available options within the class of cationic, amphiphilic polymers require

optimization, performing only in serum-free conditions and are unable to deliver large payloads into the cells of greatest interest. Here, we demonstrate the use of a bio-inspired polymeric peptide mimic that is capable of non-covalent protein and antibody into a variety of cell types in complete media. In all cases, the PTDM outperformed its commercially available counterparts within the same class of carriers. The PTDM was consistently able to deliver significantly higher amounts of protein into at least 50% of the population, both in serum-free and serum-containing conditions. Most significantly, the PTDM remained effective in difficult-to-transfect cell types, namely immune cells, stem cells, and neural cells, even when challenged with transporting significantly larger antibody-based cargoes. In other work, we have observed a correlation of PTDM membrane translocation with functional antibody and protein delivery in the cytosol.[8,11] Future work demonstrating functional protein and antibody delivery in neurons and other hard-to-transfect cell types will advance the field of transfection and establish protein delivery as an important tool in molecular biology.

2.5 References

(1) Stewart, M. P.; Sharei, A.; Ding, X.; Sahay, G.; Langer, R.; Jensen, K. F. *In vitro* and *ex vivo* strategies for intracellular delivery. *Nature* **2016**, *538* (7624), 183–192.

(2) Du, J.; Jin, J.; Yan, M.; Lu, Y. Synthetic Nanocarriers for Intracellular Protein Delivery. *Curr. Drug Metab.* **2012**, *13* (1), 82–92.

(3) Sgolastra, F.; deRonde, B. M.; Sarapas, J. M.; Som, A.; Tew, G. N. Designing mimics of membrane active proteins. *Acc. Chem. Res.* **2013**, *46* (12), 2977–2987.

(4) Gu, Z.; Biswas, A.; Zhao, M.; Tang, Y. Tailoring nanocarriers for intracellular protein delivery. *Chem. Soc. Rev.* **2011**, *40* (7), 3638.

(5) Shalek, A. K.; Gaublomme, J. T.; Wang, L.; Yosef, N.; Chevrier, N.; Andersen, M. S.; Robinson, J. T.; Pochet, N.; Neuberg, D.; Gertner, R. S.; Amit, I.; Brown, J. R.; Hacohen, N.; Regev, A.; Wu, C. J.; Park, H. Nanowire-mediated delivery enables functional interrogation of primary immune cells: Application to the analysis of chronic lymphocytic leukemia. *Nano Lett.* **2012**, *12* (12), 6498–6504.

(6) Jordan, E. T.; Collins, M.; Terefe, J.; Ugozzoli, L.; Rubio, T. Optimizing electroporation conditions in primary and other difficult-to-transfect cells. *J. Biomol. Tech.* **2008**, *19* (5), 328–334.

(7) Hamm, A.; Krott, N.; Breibach, I.; Blindt, R.; Bosserhoff, A. K. Efficient Transfection Method for Primary Cells. *Tissue Eng.* **2002**, *8* (2), 235–245.

(8) Ozay, E. I.; Gonzalez-Perez, G.; Torres, J. A.; Vijayaraghavan, J.; Lawlor, R.; Sherman, H. L.; Garrigan, D. T.; Burnside, A. S.; Osborne, B. A.; Tew, G. N.; Minter, L. M. Intracellular Delivery of Anti-pPKCθ (Thr538) via Protein Transduction Domain Mimics for Immunomodulation. *Mol. Ther.* **2016**, *24* (12), 2118–2130.

(9) Backlund, C. M.; Parhamifar, L.; Minter, L.; Tew, G. N.; Andresen, T. L. Protein Transduction Domain Mimics Facilitate Rapid Antigen Delivery into Monocytes. *Mol. Pharm.* **2019**, *16* (6), 2462–2469.

(10) Posey, N. D.; Hango, C. R.; Minter, L. M.; Tew, G. N. The Role of Cargo Binding Strength in Polymer-Mediated Intracellular Protein Delivery. *Bioconjug. Chem.* **2018**, *29* (8), 2679–2690.

(11) Sgolastra, F.; Backlund, C. M.; Ilker Ozay, E.; deRonde, B. M.; Minter, L. M.; Tew, G. N. Sequence segregation improves non-covalent protein delivery. *J. Control. Release* **2017**, *254*, 131–136.

(12) deRonde, B. M.; Torres, J. A.; Minter, L. M.; Tew, G. N. Development of Guanidinium-Rich Protein Mimics for Efficient siRNA Delivery into Human T Cells. *Biomacromolecules* **2015**, *16* (10), 3172–3179.

(13) Mitchell, D. J.; Steinman, L.; Kim, D. T.; Fathman, C. G.; Rothbard, J. B. Polyarginine enters cells more efficiently than other polycationic homopolymers. *J. Pept. Res.* **2000**, *56* (5), 318–325.

(14) Katayama, S.; Hirose, H.; Takayama, K.; Nakase, I.; Futaki, S. Acylation of octaarginine: Implication to the use of intracellular delivery vectors. *J. Control. Release* **2011**, *149* (1), 29–35.

(15) Gasparini, G.; Bang, E. K.; Montenegro, J.; Matile, S. Cellular uptake: lessons from supramolecular organic chemistry. *Chem. Commun.* **2015**, *51* (52), 10389–10402.

(16) Verdurmen, W. P. R.; Mazlami, M.; Plückthun, A. A quantitative comparison of cytosolic delivery via different protein uptake systems. *Sci. Rep.* **2017**, *7* (1), 13194.

(17) Fenton, M.; Bone, N.; Sinclair, A. J. The efficient and rapid import of a peptide into primary B and T lymphocytes and a lymphoblastoid cell line. *J. Immunol. Methods* **1998**, *212* (1), 41–48.

(18) Peer, D. A daunting task: Manipulating leukocyte function with RNAi. *Immunol. Rev.* **2013**, *253* (1), 185–197.

(19) Karra, D.; Dahm, R. Transfection Techniques for Neuronal Cells. *J. Neurosci.* **2010**, *30* (18), 6171–6177.

(20) Washbourne, P.; McAllister, A. K. Techniques for gene transfer into neurons. *Curr. Opin. Neurobiol.* **2002**, *12* (5), 566–573.

(21) Coulpier, M.; Anders, J.; Ibáñez, C. F. Coordinated activation of autophosphorylation sites in the RET receptor tyrosine kinase: Importance of tyrosine 1062 for GDNF mediated neuronal differentiation and survival. *J. Biol. Chem.* **2002**, *277* (3), 1991–1999.

(22) Raz-Prag, D.; Grimes, W. N.; Fariss, R. N.; Vijayasarathy, C.; Campos, M. M.; Bush, R. A.; Diamond, J. S.; Sieving, P. A. Probing potassium channel function *in vivo* by intracellular delivery of antibodies in a rat model of retinal neurodegeneration. *Proc. Natl. Acad. Sci.* **2010**, *107* (28), 12710–12715.

(23) Shea, T. B.; Perrone-Bizzozero, N. I.; Beermann, M. L.; Benowitz, L. I. Phospholipid-mediated delivery of anti-GAP-43 antibodies into neuroblastoma cells prevents neuritogenesis. *J. Neurosci.* **1991**, *11* (6), 1685–1690.

(24) Wang, Y.; Yang, Y.; Yan, L.; Kwok, S. Y.; Li, W.; Wang, Z.; Zhu, X.; Zhu, G.; Zhang, W.; Chen, X.; Shi, P. Poking cells for efficient vector-free intracellular delivery. *Nat. Commun.* **2014**, *5*, 1–9.

(25) Lu, Y. M. Src Activation in the Induction of Long-Term Potentiation in CA1 Hippocampal Neurons. *Science* **1998**, *279* (5355), 1363–1368.

(26) Hasadsri, L.; Kreuter, J.; Hattori, H.; Iwasaki, T.; George, J. M. Functional protein delivery into neurons using polymeric nanoparticles. *J. Biol. Chem.* **2009**, *284* (11), 6972–6981.

(27) Morris, M. C.; Depollier, J.; Mery, J.; Heitz, F.; Divita, G. A peptide carrier for the delivery of biologically active proteins into mammalian cells. *Nat. Biotechnol.* **2001**, *19* (12), 1173–1176.

(28) Morris, M. C.; Deshayes, S.; Heitz, F.; Divita, G. Cell-penetrating peptides: from molecular mechanisms to therapeutics. *Biol. Cell* **2008**, *100* (4), 201–217.

(29) Heitz, F.; Morris, M. C.; Divita, G. Twenty years of cell-penetrating peptides: from molecular mechanisms to therapeutics. *Br. J. Pharmacol.* **2009**, *157* (2), 195–206.

(30) Simeoni, F.; Morris, M. C.; Heitz, F.; Divita, G. Insight into the mechanism of the peptide-based gene delivery system MPG: Implications for delivery of siRNA into mammalian cells. *Nucleic Acids Res.* **2003**, *31* (11), 2717–2724.

(31) Backlund, C. M.; Sgolastra, F.; Otter, R.; Minter, L. M.; Takeuchi, T.; Futaki, S.; Tew, G. N. Increased hydrophobic block length of PTDMs promotes protein internalization. *Polym. Chem.* **2016**, *7* (48), 7514–7521.

(32) McNaughton, B. R.; Cronican, J. J.; Thompson, D. B.; Liu, D. R. Mammalian cell penetration, siRNA transfection, and DNA transfection by supercharged proteins. *Proc. Natl. Acad. Sci.* **2009**, *106* (15), 6111–6116.

CHAPTER 3

3 NON-COVALENT CARRIER HYDROPHOBICITY AS A UNIVERSAL PREDICTOR OF INTRACELLULAR PROTEIN ACTIVITY

NOTE: Polymers used in this chapter were prepared with the help of Nicholas D. Posey and Coralie M. Backlund. Homopolymer-mediated EGFP delivery experiments were performed in collaboration with Coralie M. Backlund. Binding assays were performed by Hazel C. Davis.

3.1 Introduction

3.1.1 Summary

Over the past decade, extensive optimization of polymeric cell-penetrating peptide (CPP) mimics (CPPMs) by our group has generated a substantial library of broadly effective carriers which circumvent the need for covalent conjugation often required by CPPs. In this study, design rules learned from CPPM development were applied to reverse-engineer the first library of simple amphiphilic block copolypeptides for non-covalent protein delivery, namely poly(alanine-*block*-arginine), poly(phenylalanine-*block*-arginine), and poly(tryptophan-*block*-arginine). This new CPP library was screened for EGFP and Cre recombinase delivery alongside a library of CPPMs featuring equivalent side-chain configurations. Due to the added hydrophobicity imparted by the polymer backbone as compared to the polypeptide backbone, side-chain functionality was not a universal predictor of carrier performance. Rather, overall carrier hydrophobicity predicted the top performers for both internalization and activity of protein cargo, regardless of backbone identity. Furthermore, comparison of protein uptake and function revealed carriers which facilitated high gene recombination despite remarkably low Cre internalization, leading us to formalize the loosely-used term “intracellular availability”

(IA). IA, a measure of cargo activity per quantity of cargo internalized, provides valuable insight into the physical relationship between cellular internalization and bioavailability, which can be affected by bottlenecks such as endosomal escape and cargo release. Importantly, carriers with maximal IA existed within a narrow hydrophobicity window, more hydrophilic than those exhibiting maximal cargo uptake. Hydrophobicity may be used as a scaffold-independent predictor of protein uptake, function, and IA, enabling identification of new, effective carriers which would be overlooked by uptake-based screening methods.

3.1.2 Background

Polymeric materials are being increasingly utilized for delivery of drugs, including proteins, intracellularly.[1–3] This has been enabled in large part by recent advances in polymer chemistry, for example the introduction of living polymerizations which allow for synthesis of precisely-tuned polymer structures with narrow molecular weight distributions.[4] While synthetic polymers offer many advantages, peptides have their own unique and desirable properties, such as discrete molecular weights and biodegradability. In order to further advance the field of non-covalent protein delivery, it is important to study both natural and synthetic materials in ways which complement one another. In this study, the SARs gained from working with CPPMs were applied to inform the intelligent design of novel CPP sequences, which were then evaluated for their ability to facilitate non-covalent protein delivery alongside their CPPM counterparts.

Given the sequence simplicity of our optimized block copolymers, consisting of at most two distinct comonomers, we sought to design a series of equally simple block

copolypeptides. Within our CPPM library, carriers featuring a hydrophobic block of all-phenyl side chains yielded higher EGFP delivery than those of greater (e.g., all-naphthyl) or lower (e.g., all-methyl) hydrophobicity.[5] Conveniently, both the methyl and phenyl side chains appear on natural amino acids (alanine and phenylalanine), providing a straightforward opportunity to directly compare top-performing and poorer-performing polymers with their analogous peptide counterparts. Notably, however, tryptophan (the most hydrophobic natural amino acid[6–8]) has frequently been used to introduce hydrophobicity into CPPs[9–20] and other membrane-active peptides.[9,21–25] In fact, replacement of both tryptophan residues in the Penetratin sequence with phenylalanine resulted in dramatically reduced cellular uptake.[26] Despite the prevalence of tryptophan-rich CPPs, very few indole-containing synthetic carriers have been reported to date.[27–29] For this reason, we synthesized two new indole-containing polymeric mimics and included their tryptophan-rich peptide counterparts for comparison in this study. Based on previous findings that an increased hydrophobic:cationic block ratio (2:1 vs. 1:1) results in enhanced protein delivery,[30] each carrier in this study was evaluated at both ratios to determine if this CPPM finding translates back to CPPs as well.

Carriers were evaluated for delivery into Jurkat T cells, widely recognized as a challenging cell type for intracellular delivery,[31,32] using two protein cargoes: enhanced green fluorescent protein (EGFP) and Cre recombinase (Cre). The two proteins are similar in size (33 and 40 kDa, respectively), but the high isoelectric point (pI) of Cre (around 9.2) contrasts well with the low pI of EGFP (6.2). At physiological pH, the net negative charge of EGFP should allow for electrostatic attraction to a CPP(M), while binding to the net positive surface of Cre may pose more of a challenge.[33] Although EGFP's post-delivery

fluorescence implies preservation of protein structure, Cre delivery provides a route to explicitly probe the biological function of delivered cargo. Gene recombination, which can only occur following nuclear localization and tetrameric assembly of Cre,[34] offers a simple readout of activity for elucidation of relationships between carrier structure and cargo function.

Despite their structural simplicity, block copolypeptides like the ones presented here are surprisingly absent in the field of CPPs. To the best of our knowledge, the only similar block CPPs previously reported are $F_{2,4,6}GR_8$,[35] $F_6G_6(rR)_3R_2$,[36] $F_{3,5}GR_8$,[37] and $W_{1\text{-}4}R_{7\text{-}8}$.[9,12,13] The former two were investigated for delivery of model cargoes (covalently) and fluorescent probes (non-covalently), respectively, while the latter two were only screened for cellular uptake. Several more distantly related peptides include pH-responsive block CPPs (containing H and R),[38] self-assembling block peptides for drug encapsulation (combinations of M, L, F, H, K, and R),[39–45] block peptides for membrane insertion (containing A and K),[46,47] and antimicrobial peptides end-tagged with hydrophobic stretches of oligopeptides (including A, F, and W).[21–24] Thus, while a few related materials have been studied for similar applications, all of the amphiphilic peptides presented in this study are new and represent the first use of simple block copolypeptides for non-covalent protein delivery. In this work, we identify carrier hydrophobicity as universal predictor of a protein cargo's internalization, activity, and intracellular availability (IA), regardless of the carrier's macromolecular scaffold.

3.2 Materials and Methods

3.2.1 Materials

3.2.1.1 Synthesis

Chemicals and solvents were obtained as reagent grade from Millipore Sigma, Alfa Aesar, Fisher Scientific, Fluka, BDH, or Acros Organics and used as received unless otherwise noted. Grubbs 3rd generation catalyst (Dichloro-di(3-bromopyridino)-N,N'-Dimesitylenoimidazolino-Ru=CHPh; G3) was synthesized as described previously.[48] Deuterated NMR solvents were obtained from Cambridge Isotope Laboratories. Polymers were dialyzed using Spectra/Por® dialysis membranes with molecular weight cutoffs (MWCOs) ranging from 0.5-1 kDa.

Cre recombinase was fluorescently labelled for uptake studies using the Alexa Fluor™ 647 Protein Labeling Kit purchased from Thermo Fisher Scientific (product code A20173) to create the Cre-AF647 conjugate. Dialysis of Cre-AF647 was performed using a Tube-O-DIALYZER micro dialysis kit with 1 kDa MWCO membranes purchased from VWR/G-Biosciences (product code 95057-588).

3.2.1.2 Peptides and Proteins

Peptides were purchased by custom order from GenScript with no end group modifications. Recombinant enhanced green fluorescent protein (EGFP) with both an N-terminal and a C-terminal 6XHis tag was purchased from BioVision (product code 4999), reconstituted to a concentration of 1 mg/mL in 1x PBS, and stored at -20 ºC, per manufacturer recommendations. The isoelectric point (pI) of this EGFP variant is 6.2.[33] Recombinant Cre recombinase with an N-terminal 6XHis tag and NLS sequence

(PKKKRKV) was purchased from Excellgen (HNC form, old product code RP-7, new product code EG-1067) and stored at -20 ºC, per manufacturer recommendations. The pI of this Cre variant was estimated to be ~9.23 by entering the following amino acid sequence into a web-based calculator:[49]

MGSSHHHHHHPKKKRKVSNLLTVHQNLPALPVDATSDEVRKNLMDMFRDRQA
FSEHTWKMLLSVCRSWAAWCKLNNRKWFPAEPEDVRDYLLYLQARGLAVKTI
QQHLGQLNMLHRRSGLPRPSDSNAVSLVMRRIRKENVDAGERAKQALAFERTD
FDQVRSLMENSDRCQDIRNLAFLGIAYNTLLRIAEIARIRVKDISRTDGGRMLIHIG
RTKTLVSTAGVEKALSLGVTKLVERWISVSGVADDPNNYLFCRVRKNGVAAPS
ATSQLSTRALEGIFEATHRLIYGAKDDSGQRYLAWSGHSARVGAARDMARAGV
SIPEIMQAGGWTNVNIVMNYIRNLDSETGAMVRLLEDGD

3.2.1.3 Reporter Jurkat T Cell Line

The Jurkat reporter cell line was created by stably transfecting Jurkat T cells with the pWPT-GFP plasmid. pWPT-GFP was a gift from Didier Trono (Addgene plasmid # 12255; http://n2t.net/addgene:12255; RRID:Addgene_12255). A single cell containing one copy of the *EGFP* gene was then identified, isolated, and expanded to create the monoclonal cell line used for Cre and Cre-AF647 delivery.

3.2.1.4 Cell Culture Reagents

Jurkat T cells and the modified reporter Jurkat T cells were cultured in Gibco™ RPMI 1640 High Glucose GlutaMAX™ Supplement (Thermo Fisher Scientific), supplemented with 10% (v/v) EquaFETAL (Atlas Biologicals), 1% (v/v) 100 mM Sodium Pyruvate Solution (Lonza) or 100 mM HyClone™ Sodium Pyruvate Solution (Fisher

Scientific), 1% (v/v) 100x MEM Non-Essential Amino Acid Solution (Lonza) or 100x HyClone™ Non-Essential Amino Acids NEAA (Fisher Scientific), 1% (v/v) HEPES (1 M) (Thermo Fisher Scientific), and 1% (v/v) Penicillin-Streptomycin Mixture (10K/10K) (Lonza). Serum-free RPMI was formulated in the same manner, withholding the 10% EquaFETAL. Gibco™ 10X phosphate-buffered saline (PBS), pH 7.4 was diluted to 1X prior to use. Heparin sodium salt from porcine intestinal mucosa (≥100 IU/mg) (Alfa Aesar/VWR) was used to remove extracellular complexes from the cell surfaces. 7-aminoactinomycin D (7-AAD) Staining Solution (BD Biosciences/Fisher Scientific) or the Zombie Violet Fixable Viability Kit (BioLegend) was used to assess cellular viability in flow cytometry experiments.

3.2.2 Instrumentation and Software

^{1}H nuclear magnetic resonance (NMR) spectra were recorded for all monomers and polymers at 500 MHz using a Bruker Ascend Nuclear Magnetic Resonance Spectrometer retrofitted with a cryoprobe. Chemical shifts (δ) are listed in ppm and coupling constants (*J*) in Hz. Splitting patterns were described as either s, singlet; d, doublet; dd, doublet of doublets; t, triplet; tt triplet of triplets; dt, doublet of triplets; q, quartet; or m, multiplet; or br, broad. Analysis of NMR spectra was performed using MestReNova v. 6.1.0-6224 (Mestrelab Research).

A CombiFlash R_f 200 automated chromatography system (Teledyne ISCO) with 120 g RediSep R_f silica disposable columns was used to purify the **dIn** monomer. The other monomers and intermediates were purified by standard silica gel chromatography methods.

Gel permeation chromatography (GPC) chromatograms were recorded for all polymers using an Agilent Technologies 1260 Infinity series system equipped with refractive index (RI) and ultraviolet (UV) detectors, a PL Gel 5 μm guard column, two PL Gel 5 μm analytical Mixed-C columns, and a PL Gel 5 μm analytical Mixed-D column. These columns were connected in series and incubated at 40 ºC. THF was used as the eluent at a flow rate of 1 mL/min. Toluene was used as the flow marker. The instrument was calibrated with both poly(methyl methacrylate) and polystyrene standards. All samples were prepared at ~3 mg/mL and filtered into Agilent Technologies autosampler vials using 0.45 μm PTFE syringe filters prior to injection.

Flow cytometry experiments were conducted using a BD Dual LSRFortessa™ flow cytometer and FACSDiva as the acquisition software. Zombie Violet, EGFP, Alexa Fluor™ 647 (AF647), and 7-aminoactinomycin D (7-AAD) were excited with 405 nm, 488 nm, 640 nm, and 488 nm lasers, respectively. Fluorescence emission for the dyes were collected using 450/50, 530/30, 670/30, and 710/50 band pass filters, respectively. Fluorescence signals of 10,000 cells were collected for every sample. Analysis was performed using FlowJo v. 10.0.7r2 (Tree Star).

Cre concentrations and degree of fluorescent labelling were determined using a BioDrop μLite instrument with a pathlength of 5 mm. Cre-AF647 binding curves were collected for all carriers using a BioTek Instruments Synergy Mx plate reader and Gen5 1.10 as the acquisition software. Samples were measured at 25 °C in Ultra Cruz 96 well sterile poly(styrene) black tissue culture plates with clear flat bottoms purchased from Santa Cruz Biotechnology, Inc.

Hydrophobicity was predicted for all model carriers using a combination of software packages. Chemical structures were drawn in ChemDraw Ultra v. 8.0.3 (CambridgeSoft). Octanol-water partition coefficients (LogP) were predicted using the KOWWIN v. 1.68 module of EPI Suite v. 4.1 (United States Environmental Protection Agency). Connolly molecular surface area values (SA) were predicted using Chem3D Ultra v. 8.0.3 (CambridgeSoft).

3.2.3 Methods

3.2.3.1 Synthesis

The following polymeric carriers were previously reported and characterized: **dG$_5$**, **dG$_{10}$**, **dMe$_5$-*b*-dG$_5$**, **dMe$_{10}$-*b*-dG$_5$**, **dPh$_5$-*b*-dG$_5$**, and **dPh$_{10}$-*b*-dG$_5$**.[30,50] **MePh$_{10}$-*b*-dG$_5$**, while reported several times before, was resynthesized for this study, necessitating the synthesis of both the **MePh** and the **dG** monomers. Synthesis and characterization of this polymer and its constituent monomers are presented here. The **dIn** monomer and its two resulting polymers, **dIn$_5$-*b*-dG$_5$** and **dIn$_{10}$-*b*-dG$_5$**, are reported here for the first time.

3.2.3.1.1 Monomer Synthesis

In general, all monomers were prepared following previously reported procedures.[51] A brief overview is provided here (Figure 3.1 and Figure 3.2).

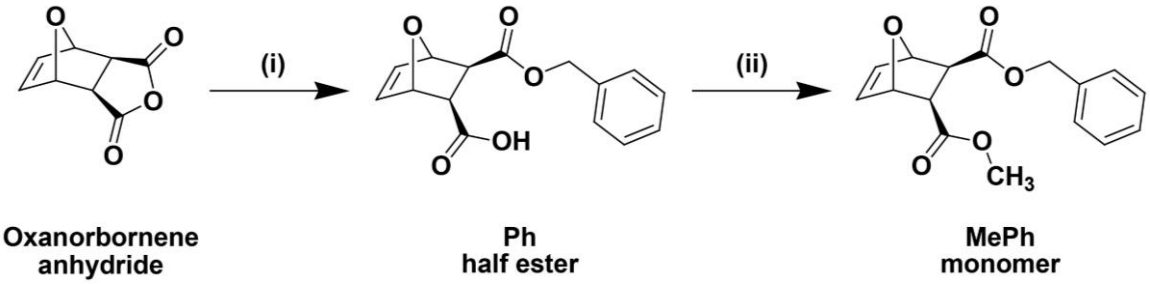

Figure 3.1: Synthesis of the asymmetric **MePh** monomer. (i) Methanol, DMAP, CH_2Cl_2, room temperature, overnight; (ii) benzyl alcohol, DMAP, EDC, CH_2Cl_2, 0 °C to room temperature, overnight.

Ph half ester: One molar equivalent of **oxanorbornene anhydride** and 0.1 molar equivalents of 4-dimethylaminopyridine (DMAP) were added to an oven dried two-neck round bottom flask under nitrogen gas and dissolved in sufficient freshly distilled CH_2Cl_2 dried over CaH_2. One molar equivalent of benzyl alcohol was added via syringe. The reaction was stirred overnight under nitrogen at room temperature. As the half ester product formed, it precipitated out overnight. The precipitate was isolated by vacuum filtration, washing with cold CH_2Cl_2, and then dried under vacuum.

56% yield

^{1}H NMR (500 MHz, DMSO) δ 12.45 (s, 1H), 7.41 – 7.28 (m, 5H), 6.50 – 6.42 (m, 2H), 5.11 (d, *J* = 5.8 Hz, 2H), 5.08 – 4.91 (m, 2H), 2.81 – 2.73 (m, 2H).

MePh monomer: One molar equivalent of the **Ph half ester** and 0.1 molar equivalents of DMAP were added to an oven dried two-neck round bottom flask under nitrogen gas and dissolved in sufficient freshly distilled CH_2Cl_2 dried over CaH_2. One molar equivalent of methanol was added via syringe. The solution was then cooled down to 0 °C in an ice bath and 1.2 molar equivalents of 1-ethyl-3-(3-dimethylaminopropyl)carbodiimide (EDC) were added. The solution was allowed to stir overnight under nitrogen and gradually return to room temperature. The diester product was isolated by normal phase flash chromatography with silica using a 90/10 (v/v) mixture of CH_2Cl_2/ethyl acetate (EtOAc) as the eluent. Pure fractions were combined and concentrated using rotary evaporation. The sample was dried under vacuum overnight at room temperature to obtain a white solid.

69% yield

^{1}H NMR (500 MHz, $CDCl_3$) δ 7.40 – 7.29 (m, 5H), 6.47 – 6.42 (m, 2H), 5.28 (d, *J* = 3.4 Hz, 2H), 5.18 – 5.10 (m, 2H), 3.55 (s, 3H), 2.88 – 2.79 (m, 2H).

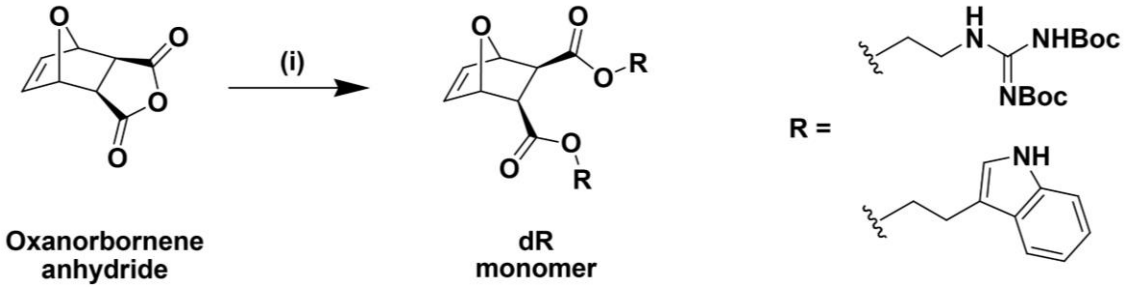

Figure 3.2: Synthesis of the symmetric **dG** and **dIn** monomers. (i) R-OH, DMAP, EDC, CH_2Cl_2, 0 °C to room temperature, overnight.

dG: One molar equivalent of oxanorbornene anhydride, two molar equivalents of 1,3,-di-boc-2-(2-hydroxyethyl)guanidine, and 0.1 molar equivalents of DMAP were dissolved in freshly distilled CH_2Cl_2 dried over CaH_2 and stirred at room temperature under nitrogen. The solution was then cooled down to 0 °C in an ice bath and 1.2 molar equivalents of EDC were added. The solution was allowed to stir overnight under nitrogen and gradually return to room temperature. The diester product was isolated by normal phase flash chromatography using silica using a 70/30 (v/v) mixture of CH_2Cl_2/EtOAc as the eluent. Pure fractions were combined and concentrated using rotary evaporation. The sample was dried under vacuum overnight at room temperature to obtain a white solid.

71% yield

^{1}H NMR (500 MHz, $CDCl_3$) δ 11.49 (br, 2H), 8.56 (br, 2H), 6.47 (br, 2H), 5.35 – 5.27 (m, 2H), 4.33 – 4.19 (m, 4H), 3.83 – 3.61 (m, 4H), 2.85 (br, 2H), 1.69 – 1.39 (m, 36H).

dIn: One molar equivalent of oxanorbornene anhydride, two molar equivalents of tryptophol, and 0.1 molar equivalents of DMAP were dissolved in CH_2Cl_2 and stirred at room temperature under nitrogen. The solution was then cooled down to 0 °C in an ice

bath and 1.5 molar equivalents of EDC were added. The solution was allowed to stir overnight under nitrogen and gradually return to room temperature. The reaction mixture was then concentrated using rotary evaporation and purified by normal phase, flash chromatography using a 120 g silica column and a solvent gradient from pure hexanes to pure ethyl acetate as the eluent. Pure fractions were combined and then concentrated using rotary evaporation. The sample was dried under vacuum overnight at room temperature to obtain a white solid.

44% yield

^{1}H NMR (500 MHz, $CDCl_3$) δ 7.96 (s, 2H), 7.60 (d, *J* = 7.9 Hz, 2H), 7.33 (d, *J* = 8.1 Hz, 2H), 7.18 (t, *J* = 7.6 Hz, 2H), 7.10 (t, *J* = 7.5 Hz, 2H), 7.00 (d, *J* = 2.1 Hz, 2H), 6.41 (s, 2H), 5.19 (s, 2H), 4.40 – 4.26 (m, 4H), 3.07 (t, *J* = 7.1 Hz, 4H), 2.79 (s, 2H).

3.2.3.1.2 Polymer Synthesis

All polymers were prepared according to previously reported procedures (Figure 3.3).[51]

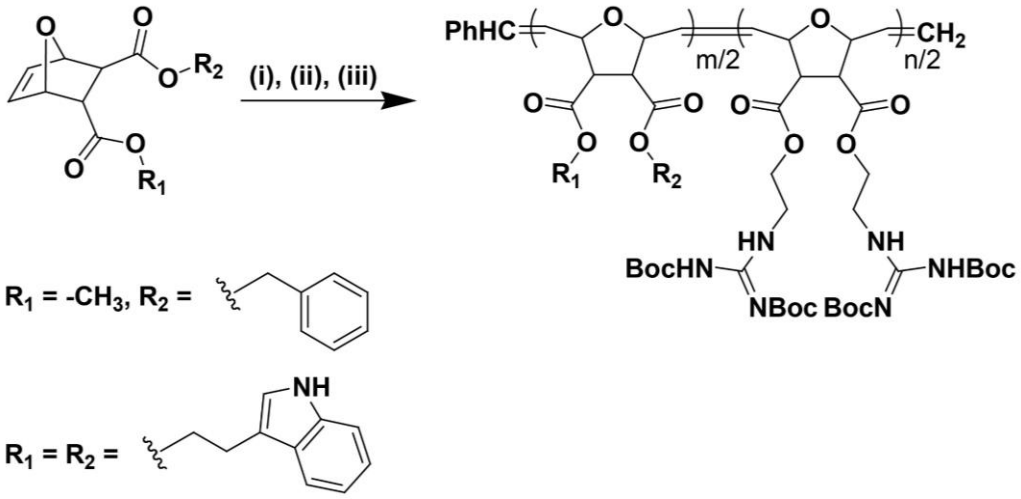

Figure 3.3: Synthesis of Boc-protected block copolymers used in Chapter 3. (i) G3, CH_2Cl_2, room temperature, 10 min; (ii) **dG**, CH_2Cl_2, room temperature, 90 min; (iii) ethyl vinyl ether, room temperature, overnight.

In brief, 1 molar equivalent of G3, 5 or 10 molar equivalents of the hydrophobic block monomer (depending on the target length of the hydrophobic block), and 5 molar equivalents of the **dG** monomer were each dissolved in separate oven dried Schlenk flasks using freshly distilled CH_2Cl_2 dried over CaH_2. The contents of all Schlenk flasks were put through a minimum of 3 freeze, pump, thaw (FPT) cycles to rigorously degas the monomer and catalyst solutions. After the final FPT cycle, the contents of the flask containing the hydrophobic monomer were cannulated into the flask containing the stirring G3 solution. This monomer was allowed to polymerize for about 10 minutes, at which time a crude aliquot was taken and dried using compressed air for analysis by ^{1}H NMR and THF GPC. The NMR spectrum was used to confirm monomer consumption by a complete upfield shift of the alkene protons in the oxanorbornene-based monomer. The GPC chromatogram was used to calculate the molecular weight and dispersity of the hydrophobic block. The **dG** monomer was then cannulated into the G3 flask and allowed to polymerize for approximately 90 minutes. Upon completion, 2-3 mL of ethyl vinyl ether (EVE) was injected into the Schlenk flask to terminate the polymerization. A crude aliquot was taken at this point and dried using compressed air for analysis by ^{1}H NMR and THF GPC. As with the first aliquot, this NMR spectrum was used to confirm complete consumption of the second monomer. The GPC chromatogram was used to confirm successful chain extension by comparison with the first chromatogram. After stirring overnight with EVE, the crude reaction mixture was concentrated to a solid using rotary evaporation before it was redissolved in 1 mL of tetrahydrofuran (THF). This solution was then precipitated dropwise into cold, stirring pentane. The precipitated polymers in their Boc-protected forms were recovered using vacuum filtration and dried under high vacuum

overnight, at which point they were again characterized by ^{1}H NMR and THF GPC. The final NMR spectrum was used to calculate the relative block composition using integrations of diagnostic peaks from each of the respective blocks (Table 3.1). For **MePh$_{10}$-*b*-dG$_5$**, the **MePh** block CH_3 protons at 3.45 ppm were compared to the **dG** block CH_2 protons at 4.21 ppm. For the indole-containing polymers, the **dG** block NH protons at ~8.5 ppm were compared to the **dIn** block aromatic CH protons at ~7.5 ppm. The final GPC chromatogram was used to determine the approximate molecular weight (MW) and dispersity of each polymer, also reported in Table 3.1.

Table 3.1: Characterization summary for PTDMs used in Chapter 3 based on ^{1}H NMR and THF GPC analysis.

Polymer	Block 1: Block 2[a]	Theoretical MW (g/mol)[b]	M_p (g/mol)[c]	M_n (g/mol)[c]	M_w (g/mol)[c]	Đ[c]
MePh$_{10}$-*b*-dG$_5$	66:33	6,761	8,149	7,119	7,780	1.1
dIn$_5$-*b*-dG$_5$	48:52	6,231	5,790	5,150	5,620	1.1
dIn$_{10}$-*b*-dG$_5$	69:31	8,584	7,660	6,930	7,620	1.1

[a]Relative block incorporation as calculated by ^{1}H NMR. [b]Theoretical molecular weight based on polymer structure shown in Figure 3.3. [c]Calculated by GPC in THF, 40ºC, flow rate 1 mL/min with polystyrene standards and toluene as the flow marker.

The ^{1}H NMR chemical shifts for each precipitated, Boc-protected polymer are below. Overlays of the three GPC chromatograms taken for each polymer can be found in Figure 3.4, Figure 3.5, and Figure 3.6.

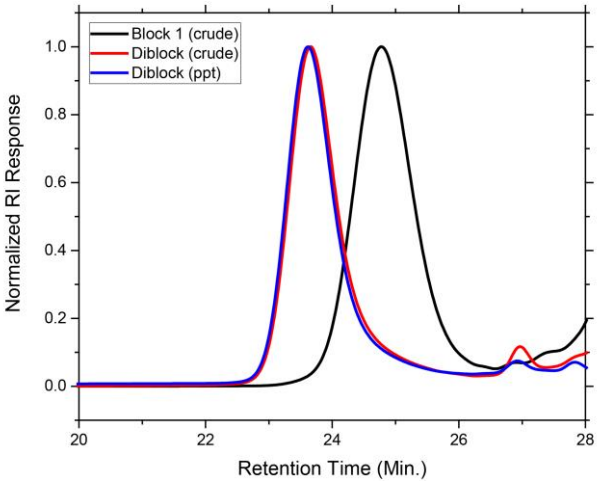

Figure 3.4: GPC traces illustrating the increase in molecular weight upon chain extension of the first block (containing just the **MePh** monomer) to create the Boc-protected copolymer (**MePh$_{10}$-*b*-dG$_5$**), shown here before and after purification by precipitation.

MePh$_{10}$-*b*-dG$_5$: ^{1}H NMR (500 MHz, $CDCl_3$) δ 11.47 (br, 2H), 8.48 (br, 2H), 7.32 (br, 11H), 5.84 (*trans*) and 5.57 (*cis*) (br, 6H total), 5.09 (br, 4H), 5.09 (*cis*) and 4.68 (*trans*) (br, 6H total), 4.21 (br, 4H), 3.68 (br, 4H), 3.45 (br, 6H), 3.08 (br, 6H), 1.56 (s, 18H), 1.47 (s, 18H).

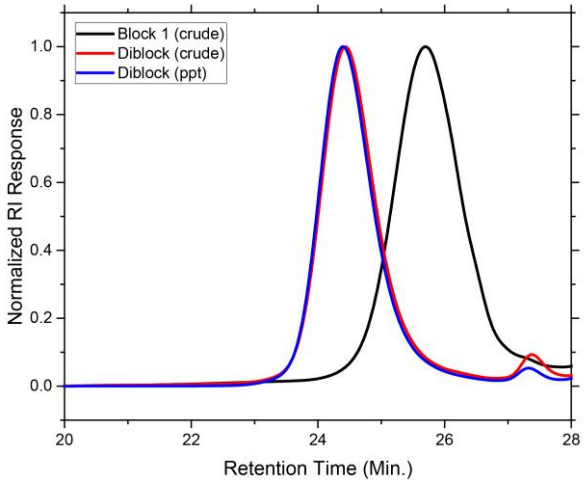

Figure 3.5: GPC traces illustrating the increase in molecular weight upon chain extension of the first block (containing just the **dIn** monomer) to create the Boc-protected copolymer (**dIn$_5$-*b*-dG$_5$**), shown here before and after purification by precipitation.

dIn$_5$-*b*-dG$_5$: ^{1}H NMR (500 MHz, $CDCl_3$) δ 11.47 (br, 2H), 8.49 (br, 2H), 8.09 (br, 2H), 7.47 (br, 2H), 7.14 (br, 7H), 6.77 (br, 2H), 5.84 (*trans*) and 5.51 (*cis*) (br, 4H total), 5.10 (*cis*) and 4.61 (*trans*) (br, 4H total), 4.20 (br, 8H), 3.59 (br, 4H), 2.98 (br, 8H), 1.57 (s, 18H), 1.47 (s, 18H).

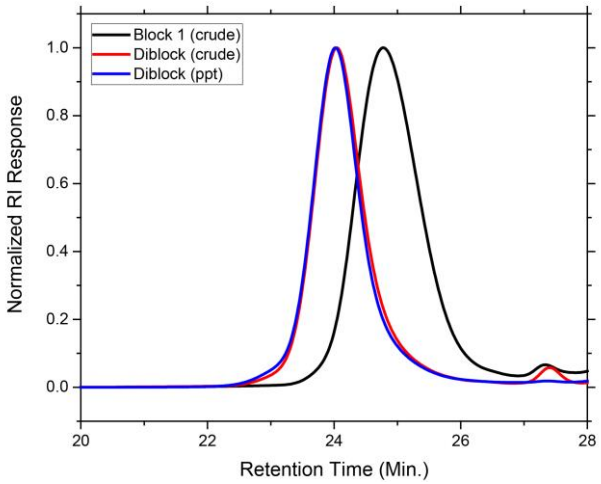

Figure 3.6: GPC traces illustrating the increase in molecular weight upon chain extension of the first block (containing just the **dIn** monomer) to create the Boc-protected copolymer (**dIn$_{10}$-*b*-dG$_5$**), shown here before and after purification by precipitation.

dIn$_{10}$-*b*-dG$_5$: ^{1}H NMR (500 MHz, $CDCl_3$) δ 11.48 (br, 2H), 8.49 (br, 2H), 8.10 (br, 4H), 7.46 (br, 4H), 7.11 (br, 13H), 6.74 (br, 4H), 5.85 (*trans*) and 5.49 (*cis*) (br, 6H total), 5.10 (*cis*) and 4.64 (*trans*) (br, 6H total), 4.20 (br, 12H), 3.63 (br, 4H), 2.91 (br, 14H), 1.64 (s, 18H), 1.47 (s, 18H).

3.2.3.1.3 Polymer Deprotection

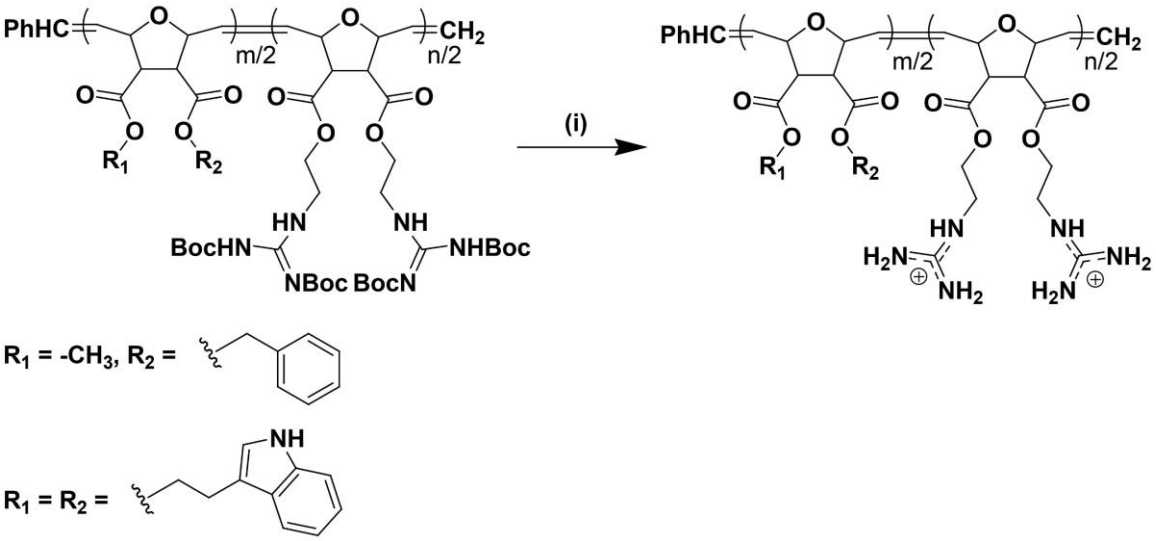

Figure 3.7: Deprotection of Boc-protected block copolymers used in Chapter 3 to yield cationic guanidinium groups. (i) TFA/CH_2Cl_2 (1:1), room temperature, overnight.

To remove the Boc protecting groups, each polymer was dissolved in a 4 mL solution of 1:1 CH_2Cl_2:trifluoroacetic acid (TFA) and stirred in a scintillation vial overnight (Figure 3.7). The scintillation vials were filled to halfway with methanol and concentrated using rotary evaporation. This process was repeated up to 7 times to remove traces of TFA by azeotropic distillation. The deprotected polymers were then dissolved in a minimal volume of methanol, diluted in approximately 10 mL of reverse osmosis (RO) water, and loaded into hydrated dialysis membrane tubing (MWCO = 500-1000 Da). All polymers were dialyzed against RO water until the conductivity of the solution outside the bag reached 0.3 μS or lower. Once dialysis was completed, polymer solutions were flash

frozen in plastic cups by submerging them in liquid nitrogen. Frozen water was then removed by lyophilization *in vacuo* over the course of 3-5 days.

3.2.3.2 Fluorescent Labelling of Cre-AF647

Cre was gradually dialyzed at 4 °C into a buffer containing ~15 % (v/v) glycerol in PBS to remove arginine and reduce the glycerol level (from 50%), according to Thermo Fisher Scientific's recommendations, since the NHS ester dye in the protein labelling kit reacts with primary amines and the reaction rate is slowed by viscous solvents like glycerol. Dialysis was performed using a Tube-O-DIALYZER micro dialysis kit with 1 kDa MWCO membranes for ~24 h at a sample to buffer ratio of ~1:1000. The buffer was replaced several times throughout dialysis and stirred continuously. The final protein solution was passed through a 0.45 μm PTFE filter to ensure the removal of any aggregated protein. Dialyzed Cre was stored at 4 °C.

Concentration of the dialyzed Cre was determined from the absorbance of 280 nm wavelength light (A_{280}), using distilled water as the reference solution, as recommended by Excellgen. The extinction coefficient of Cre at 280 nm (ε_{280}) was estimated from the number of strongly absorbing residues (tryptophan, tyrosine, and cysteine) using the following equation:[52]

$$\varepsilon_{280} \approx (5500\ M^{-1}cm^{-1})W + (1490\ M^{-1}cm^{-1})Y + (125\ M^{-1}cm^{-1})C$$

For a protein with W = 7, Y = 7, and C = 4, this becomes $\varepsilon_{280} \approx$ 49,430 $M^{-1}cm^{-1}$. Knowing the light pathlength within the BioDrop (l = 0.05 cm), Cre concentration was then determined using Beer's Law:

$$c = \frac{A_{280}}{\varepsilon_{280} l}$$

Approximately 1.4 mL of 1.4 mg/mL Cre was labelled with the contents of two AF647 NHS ester dye tubes and subsequently separated from the excess unreacted dye by size exclusion chromatography according to manufacturer guidelines.

The concentration of the Cre-AF647 conjugate was determined from its absorbance at 280 nm and 650 nm (A_{650}) using a modified version of Beer's Law, in which the factor of 0.03 corrects for the added absorbance of the dye molecule at 280 nm:

$$c = \frac{A_{280} - 0.03A_{650}}{\varepsilon_{280} l}$$

The conjugate's degree of labelling (DOL), or average number of dye molecules per protein, was then calculated as the ratio of molar AF647 concentration to molar Cre concentration:

$$DOL = \frac{c_{AF647}}{c_{Cre}} = \frac{A_{650}/\varepsilon_{650} l}{c_{Cre}} = \frac{A_{650}}{\varepsilon_{650} c_{Cre} l}$$

By this method, Cre-AF647 DOL was found to be approximately 0.78.

3.2.3.3 Delivery

3.2.3.3.1 EGFP Internalization

EGFP delivery was based on previously published protocols.[5,27,30,32,33,50,53] Peptides were received as lyophilized powders, dissolved in DMSO to make 1-5 mM stock solutions, and stored at -20 °C. Polymers were dissolved in DMSO to make 1 mM stock

solutions and stored at -20 °C. Jurkat T cells were harvested on the day of the experiment and seeded in 12-well plates at a density of 4 x 10^5 cells/0.8 mL of fresh serum-containing RPMI (800 μL per well). Stock EGFP (1 mg/mL) was diluted 1:10 in 1X phosphate-buffered saline (PBS, pH ~7.4) to achieve a working concentration of 0.1 mg/mL. Peptide and polymer stock solutions were diluted appropriately in PBS to achieve working concentrations of 0.1 mM. Carrier:protein complexes were prepared by mixing appropriate volumes of EGFP (corresponding to a final delivery concentration of 3 μg/mL) and carrier (corresponding to a final delivery concentration of 2 μM, yielding a 20:1 molar ratio of carrier:cargo) in PBS to achieve total volumes of 200 μL. These complexes were incubated in the dark at room temperature for 30 min prior to adding them dropwise to each well, resulting in final delivery volumes of 1 mL. The cells were incubated with the complexes for 4 h at 37 °C in 5% CO_2. After the incubation period, the cells were harvested, transferred to microcentrifuge tubes, collected by centrifugation at 400 x g, and washed 3 times with 800 μL of heparin (20 U/mL in PBS) to remove any extracellular or surface-bound complexes, in accordance with previously published procedures.[54] Cells were resuspended in 200 μL of FACS buffer (0.2% bovine serum albumin in PBS) containing 5 μL of 7-aminoactinomycin D (7-AAD) stain prior to internalization and viability analysis by flow cytometry, in which data for 10,000 cells were collected.

3.2.3.3.2 Cre-AF647 Internalization

Cre-AF647 delivery was performed in much the same way as EGFP delivery, with the following exceptions. In order to match the functional Cre delivery experiments as closely as possible, Cre-AF647 internalization was performed with the same EGFP-expressing modified Jurkat T cell line. Cells were seeded in 24-well plates at a density of

2 x 10^5 cells/0.4 mL of fresh serum-free RPMI (400 μL per well). Stock Cre-AF647 (20 μM) was not further diluted in PBS to a working concentration, since it was already dilute enough to use directly for complexation. Carrier:protein complexes were prepared by mixing appropriate volumes of Cre-AF647 (corresponding to a final delivery concentration of 560 nM) and carrier (corresponding to a final delivery concentration of 3 μM, yielding a molar ratio of carrier:cargo of around 5:1) in PBS to achieve total volumes of 100 μL. The cells were incubated with the complexes for 4 h at 37 °C in 5% CO_2. Halfway through the 4 h incubation, 500 μL of complete RPMI was added to each well to assist with cellular viability. To avoid the large spectral overlap of 7-AAD with AF647, cells were instead stained with Zombie Violet. The lyophilized Zombie Violet dye was reconstituted by dissolving in anhydrous DMSO and stored at -20 °C according to manufacturer guidelines. Zombie Violet was diluted 1:1000 in PBS, and each cell sample was stained with 100 μL for 15 min in the dark at room temperature. Following staining, the dye was diluted by adding 700 μL of PBS on top of each sample and removed by centrifugation. Samples were then resuspended in 200 μL of FACS buffer prior to internalization and viability analysis by flow cytometry, in which data for 10,000 cells were collected.

3.2.3.3.3 Functional Cre Delivery

Cre delivery was performed in an identical manner to Cre-AF647 delivery, with the following exceptions. The very high concentration stock Cre (70 μM) was first diluted 1:10 in PBS to a working concentration of 7 μM prior to complexation. The final delivery concentration of 3 μM remained the same as for Cre-AF647. Following the 4h delivery incubation, cells were centrifuged, resuspended in fresh serum-containing RPMI, and cultured for 6 days to allow for intracellular EGFP expressed prior to gene recombination

to be degraded. On this day, the cells were harvested, transferred to microcentrifuge tubes, collected by centrifugation, and washed once with PBS to remove the culture medium. Cells were resuspended in 200 μL of FACS buffer containing 5 μL of 7-AAD (as done with EGFP delivery, since the AF647 fluorophore was absent from this assay), to exclude dead cells from the analysis, prior to gene recombination by flow cytometry, in which data for 10,000 cells were collected.

3.2.3.4 Hydrophobicity Calculations

3.2.3.4.1 Model Carrier Design

Theoretical hydrophobicity was calculated for each carrier according to a method reported by Magenau *et al*.[55] Although the peptides and polymers used here were relatively short, they were still too large to be processed by the software utilized for octanol-water partition coefficient (LogP) prediction. Instead, a series of shorter model carriers, each containing the same comonomer ratio as their respective full-length polymers, were used. The model carrier degrees of polymerization (DPs) were dictated by the maximum DP of the highest-molecular weight carrier accepted by EPI Suite, keeping in mind that these numbers needed to be divisible by either 2 (homopolymers/homopeptides) or 3 (copolymers/copolypeptides) to accurately capture various carrier lengths. The highest molecular weight carriers were therefore $\mathbf{R_6}$ for the homopolypeptides, $\mathbf{dG_4}$ for the homopolymers, $\mathbf{W_6R_3}$ for the copolypeptides, and $\mathbf{dIn_2}$-***b***-$\mathbf{dG_1}$ for the copolymers. A full list of the model carriers used can be found in Figure 3.14.

Magenau *et al*. found that, because large end groups can have a disproportionately large effect on hydrophobicity at lower DPs, omitting them in model molecules led to the

most accurate prediction of full-length polymer hydrophobicity. In reality, something has to be attached as an end group on the model molecules. The small, hydrophilic NH_3^+ and COO^- end groups were retained on the model peptides, as their presence would not significantly affect overall hydrophobicity or surface area of a net-hydrophilic peptide at low DP. The full-length ROMP polymers, however, contain a bulky phenyl group at one end. Since retaining such a large, hydrophobic end group on the net-hydrophilic model carriers would cause the carriers to be represented as unfairly hydrophobic and large at low DPs, the smaller, less hydrophobic $-CH_2$ group (already found on the opposite end of the polymer) was used for the polymer models instead.

3.2.3.4.2 LogP

The chemical structure of each model was drawn in ChemDraw Ultra v. 8.0.3. The SMILES code was then obtained by selecting the molecule and navigating to "File", "Edit", "Copy As", "SMILES". EPI Suite v. 4.1 was launched and the KOWWIN v. 1.68 module was opened. The SMILES code was pasted into the "Enter SMILES" field, and the estimated LogP (Log K_{ow}) value was obtained by clicking "Calculate" and recording the value displayed in the pop-up window.

3.2.3.4.3 Surface Area and Hydrophobicity

The surface areas of the model peptide carriers were relatively straightforward to model, given their precise and unambiguous stereochemical structure. The chemical structures were copied from ChemDraw Ultra v. 8.0.3 and pasted into Chem3D Ultra v. 8.0.3, at which point an MM2 energy minimization was performed by navigating to "MM2", "Minimize Energy", and clicking "Run". The molecular surface area (SA) was obtained by navigating to "Analyze", "Compute Properties", selecting "Connolly Molecular Area", clicking "Add", "Ok", and recording the value displayed on the message bar at the bottom of the screen. The probe size used was the default of 1.4 Å. Carrier hydrophobicity was then predicted by normalizing the LogP value by the molecular surface area (LogP/SA). A summary of these values for the peptide carriers, ranked from most hydrophilic to most hydrophobic, can be found in Table 3.2.

Table 3.2: Summary of hydrophobicity parameters calculated for model peptide carriers. Carriers are ranked in order of increasing predicted hydrophobicity.

Full-Length Carrier	Model Carrier	Octanol-Water Partition Coefficient (LogP)[a]	Molecular Surface Area (SA) (nm^2)[b]	LogP/SA (nm^{-2})
R_9	R_3	-20.54	4.62	-4.44
R_{20}	R_6	-38.31	9.18	-4.17
$A_{10}R_{10}$	A_3R_3	-21.78	6.65	-3.28
$A_{20}R_{10}$	A_6R_3	-23.01	8.69	-2.65
$F_{10}R_{10}$	F_3R_3	-16.65	8.05	-2.07
$W_{10}R_{10}$	W_3R_3	-16.47	8.83	-1.87
$F_{20}R_{10}$	F_6R_3	-12.76	11.45	-1.11
$W_{20}R_{10}$	W_6R_3	-6.48	13.24	-0.49

[a]LogP values calculated using the KOWWIN tool in EPI Suite v. 4.1. [b]Surface area is the Conolly molecular area, calculated in Chem3D Ultra 8.0 using a probe size of 1.4 Å after performing a MM2 energy minimization.

Modelling the surface areas of the polymers was complicated by the mixture of polymer microstructures afforded by ROMP, arising from the double bonds and chiral carbons inherent to the poly(oxanorbornene) backbone. Specifically, the polymers can contain varying amounts of isoselectivity (*cis* or *trans* monomer addition), stereoselectivity

(preference for isotactic, syndiotactic, or atactic monomer addition), and regioselectivity (head-to-tail [HT], head-to-head [HH], and tail-to-tail [TT] monomer addition).[56,57] Combinations of these parameters within the same polymer chain lead to an immense number of unique possible configurations. If we simplify the situation by assuming the entire polymer chain has double bonds of the same isomer (all *cis* or all *trans* bonds), is tactic (isotactic or syndiotactic, not atactic), and has a single regiochemistry (only HT-HT, HH-TT, TH-TH, or TT-HH monomer addition) there are only 12 unique polymer configurations. Furthermore, for polymers built from symmetric monomers (i.e., featuring the same functional groups on both arms), the regioisomers become redundant, reducing the number of possible configurations to just four: (1) all-*cis*, isotactic, (2) all-*cis*, syndiotactic, (3), all-*trans*, isotactic, and (4) all-*trans*, syndiotactic. This is a reasonable simplification given that only one of the nine polymers contains an asymmetric monomer (**MePh**). The *cis*:*trans* ratio of ROMP polymers is easily quantified through ^{1}H NMR. For our oxanorbornene-based CPPMs, this ratio is typically close to 50:50.[58] The catalyst used to produce the ROMP polymers, Grubbs third generation catalyst, is known to produce polynorbornenes with a mixture of stereoisomers. In fact, highly specialized catalysts must be designed to obtain syndiotactic or isotactic macromolecules. Thus, it is entirely reasonable to assume our CPPMs are atactic in nature, and that any given repeat unit has an equal chance of being positioned either "syndiotactic" or "isotactic" relative to its preceding neighbor.[59]

Based on the assumptions outlined above, polymers were modeled in each of the four simplified configurations (*cis*/isotactic, *cis*/syndiotactic, *trans*/isotactic, and *trans*/syndiotactic) and equal weight was given to each possible configuration in

calculating an average surface area of the model molecule. For simplicity, **MePh$_{10}$-*b*-dG$_5$** (modeled as **MePh$_2$-*b*-dG$_1$**), the only carrier in which regioisomers were also possible, was only modeled in the HT-HT configuration. As is evident from the SA values for each configuration (Table 3.3) and the virtually invisible LogP/SA x-axis error bars (Figure 3.12, Figure 3.13, and Figure 3.16B, D), the various polymer configurations had little effect on the final predicted surface area and hydrophobicity.

Table 3.3: Summary of hydrophobicity parameters calculated for model polymer carriers. Carriers are ranked in order of increasing predicted hydrophobicity.

Full-Length Carrier	Model Carrier[a]	LogP[b]	Trial	*cis*, iso SA[c] (nm^2)	*cis*, syndio SA[c] (nm^2)	*trans*, iso SA[c] (nm^2)	*trans*, syndio SA[c] (nm^2)	Avg. SA[d] (nm^2)	Avg. LogP/ SA (nm^{-2})
dG$_{10}$	dG$_4$	-45.70	1	13.05	13.07	12.94	13.25	12.93	-3.53
			2	12.99	13.00	12.78	12.68		
			3	12.49	12.95	12.94	13.01		
dG$_5$	dG$_2$	-22.22	1	6.65	6.80	6.81	6.84	6.77	-3.28
			2	6.48	6.86	6.88	6.64		
			3	6.82	6.78	6.80	6.85		
dMe$_5$-*b*-dG$_5$	dMe$_1$-*b*-dG$_1$	-10.33	1	5.18	5.32	5.22	5.18	5.20	-1.99
			2	5.15	5.09	5.16	5.13		
			3	5.17	5.44	5.26	5.14		
dMe$_{10}$-*b*-dG$_5$	dMe$_2$-*b*-dG$_1$	-10.18	1	6.46	6.90	6.84	6.83	6.77	-1.50
			2	6.70	6.70	6.82	6.87		
			3	6.78	6.83	6.95	6.63		
dPh$_5$-*b*-dG$_5$	dPh$_1$-*b*-dG$_1$	-6.91	1	6.30	6.21	6.33	5.90	6.20	-1.11
			2	6.11	6.38	6.28	5.97		
			3	6.28	6.41	6.28	5.99		
MePh$_{10}$-*b*-dG$_5$	MePh$_2$-*b*-dG$_1$	-6.76	1	7.59	7.88	8.12	7.30	7.67	-0.88
			2	7.51	7.70	7.86	7.41		
			3	7.16	7.98	8.07	7.41		
dIn$_5$-*b*-dG$_5$	dIn$_1$-*b*-dG$_1$	-5.80	1	6.50	6.96	6.97	6.39	6.70	-0.87
			2	6.50	6.95	6.94	6.47		
			3	6.22	6.92	6.97	6.61		
dPh$_{10}$-*b*-dG$_5$	dPh$_2$-*b*-dG$_1$	-3.34	1	8.29	8.93	9.00	8.73	8.81	-0.38
			2	8.36	8.86	9.06	8.88		
			3	8.76	8.93	9.17	8.79		
dIn$_{10}$-*b*-dG$_5$	dIn$_2$-*b*-dG$_1$	-1.13	1	9.16	10.32	10.23	9.30	9.67	-0.12
			2	9.17	9.77	10.25	9.41		
			3	9.11	9.80	10.24	9.24		

[a]Polymer structures modelled with a -CH_2 end group rather than the phenyl end group. [b]Octanol-water partition coefficient (LogP) values calculated using the KOWWIN v. 1.68 tool in EPI Suite v. 4.1. [c]Surface area (SA) is the Conolly molecular area, calculated in Chem3D Ultra 8.0.3 using a probe size of 1.4 Å after performing a MM2 energy minimization. [d]Average SA values represent equally weighted averages of all three trials of each of the four polymer configurations modelled.

Because the energy minimization function in Chem3D Ultra v. 8.0.3 could only find a local energy minimum (not the global minimum), the surface area of the optimized structure was dependent on the starting positions of the molecule's atoms and bonds. Thus, rather than pasting the entire model polymer structure from ChemDraw (which often resulted in a very messy, tangled molecule), the repeat units were individually pasted from ChemDraw, then arranged and connected in Chem3D in a logical, consistent manner. This process is illustrated in below for each microstructure of the model carrier **dG$_4$** (Figure 3.8).

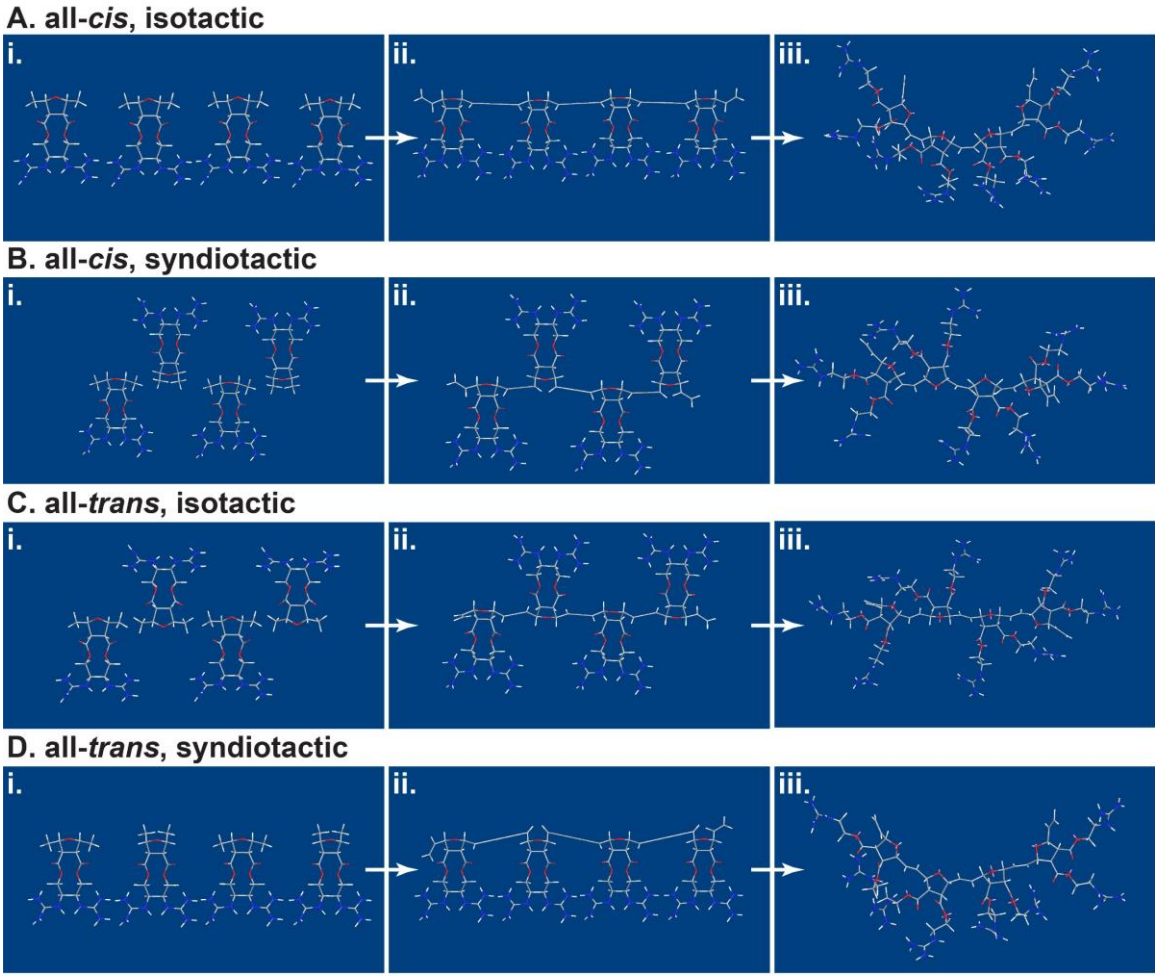

Figure 3.8: Representative trial of energy minimization prior to surface area calculation for a model polymeric carrier (**dG$_4$**) in the *cis*/isotactic (A), *cis*/syndiotactic (B), *trans*/isotactic (C), and *trans*/syndiotactic configurations. In each case the process involved (i) copying the appropriate repeat-unit stereoisomers from ChemDraw Ultra, pasting them into Chem3D Ultra, and arranging them in the appropriate orientations, (ii) connecting the repeat units with double bonds, and (iii) performing a MM2 energy minimization to obtain the optimized structure.

Each configuration was modelled three times, resulting in a total of 12 SA values which were averaged to achieve the final SA value. LogP values (which are unaffected by stereochemistry) were divided by SA values to obtain the hydrophobicity parameter, LogP/SA. A summary of these values can be found in Table 3.3.

3.2.3.5 Cre-AF647 Fluorescence-Based Equilibrium Binding Assays

To determine the binding behavior for various carrier:Cre complexes, equilibrium fluorescence quenching assays were conducted according to previously published procedures.[5,33,53] These assays were conducted at 25 °C in PBS at pH ~7.2 and the fluorescence of Cre-AF647 was monitored and recorded as a function of increasing carrier concentration (from 0 up to 10 μM, depending on the carrier). These experiments were conducted in a 96-well polystyrene plate, where each well had black opaque sides and flat clear bottoms. In general, each well in the titration was designed to contain 200 nM Cre-AF647, the respective carrier concentration, and remaining PBS to reach a total volume of 200 μL. A stock concentration of 0.8 mg/mL was used for Cre-AF647, where aliquots were removed and subsequently diluted to yield a working solution of dye-labelled protein. Carrier stock concentrations were either at 1 or 2 mM in pure DMSO and were serially diluted in PBS to produce subsequent stock solutions of 100 μM (10% v/v DMSO), 10 μM (1% v/v DMSO), or 2 μM (0.2% v/v DMSO). Variable volumes from any of these less concentrated stocks were added to the wells such that each subsequent well in the series contained an increasing amount of carrier. As the use of different carrier stock solutions introduced DMSO in varying amounts, additional DMSO was added to each well such that all wells for a contained the same concentration (v/v) of DMSO. Once all wells had received the calculated volumes of PBS, DMSO, Cre-AF647 and the appropriate carrier,

they were gently mixed by pipetting up and down and stirring with the tip of the pipet. The 96-well plate was allowed to incubate in the dark (covered by the plastic lid and under foil) at room temperature for 30 min to achieve equilibrium prior to fluorescence measurements. Samples were excited at 650 nm and emission was read at 670 nm with a BioTek Mx plate reader. During the binding experiments, the fluorescence intensity of each well in the titration for a given protein was measured. The background noise of a negative control (containing only PBS and DMSO) was first subtracted from these measurements. Next, the values were normalized by the fluorescence intensity of a positive control (containing only 200 nM protein, PBS, and DMSO) to yield a curve of normalized fluorescence intensity vs. carrier concentration. The binding experiments were repeated in duplicate for each carrier. In some cases, the second replicate included additional data points at new concentrations to provide more information in critical parts of the binding curves. In the case of **MePh$_{10}$-*b*-dG$_5$**, the data were also converted to fractional saturation and the equilibrium dissociation constant (K_d) was calculated as reported previously.[33]

3.3 Results and Discussion

3.3.1 Macromolecular Carrier Design

Two groups of macromolecular carriers, CPPs (purple) and polymeric CPPMs (red), were designed to feature equivalent arrangements of *m* cationic (blue) and *n* hydrophobic (green) side-chains (Scheme 3.1). The peptides were built from the $_L$-amino acids arginine (**R**), alanine (**A**), phenylalanine (**F**), and tryptophan (**W**), while the polymers were synthesized from di-guanidine (**dG**), di-methyl (**dMe**), di-phenyl (**dPh**), and di-indole (**dIn**) functionalized ring-opening metathesis polymerization (ROMP) monomers.

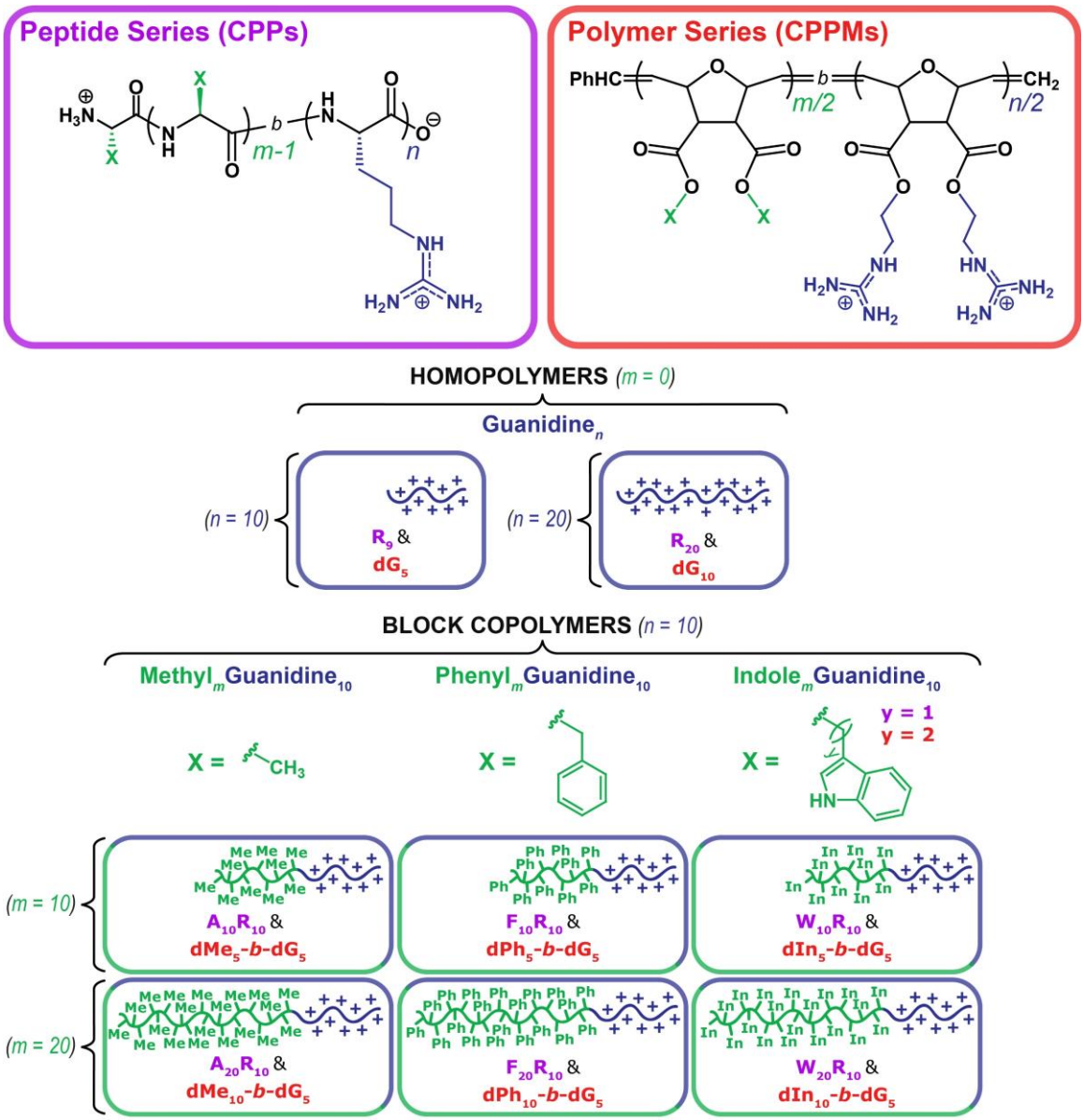

Scheme 3.1: Peptides (purple) and their polymeric mimics (red) selected for use in Chapter 3. Each of the eight polymer/peptide pairs was designed to contain an equal number of cationic (blue) and hydrophobic (green) functional groups (denoted by *n* and *m*, respectively). The homopolymer/peptide pairs ($m \equiv 0$, n = 10 or 20) feature only a cationic guanidinium functional groups (blue "+"), conferred by either the amino acid arginine (**R**) or its ROMP monomer mimic, di-guanidine (**dG**). The block copolymer/peptide pairs (m = 10 or 20, $n \equiv 10$) contain an added hydrophobic block consisting of either methyl (Me), phenyl (Ph), or indole (In) functional groups. This was accomplished by incorporating either hydrophobic amino acids (alanine [**A**], phenylalanine [**F**], tryptophan [**W**]) or their ROMP monomer mimics (di-methyl [**dMe**], di-phenyl [**dPh**], di-indole [**dIn**]).

Dual-functional ROMP monomers were selected over monofunctional ones with the intention of more closely matching the functional group density of the peptide series (two side chains for every six CPP or five CPPM backbone atoms).[60] Additionally, increased

CPPM functional group density has been shown to enhance protein delivery.[30] In order to compensate for the dual-functionality of these monomers, the degree of polymerization of each peptide was designed to be exactly double that of its polymeric counterpart, with the minor exception of employing **R$_9$** in lieu of **R$_{10}$**, due to its historical significance and widespread prevalence in the field of CPPs.[61] Within each macromolecular scaffold, four combinations of monomers were utilized: guanidine homopolymers (**R$_n$** and **dG$_n$**), methyl/guanidine copolymers (**A$_m$R$_{10}$** and **dMe$_{m/2}$-*b*-dG$_5$**), phenyl/guanidine copolymers (**F$_m$R$_{10}$** and **dPh$_{m/2}$-*b*-dG$_5$**), and indole/guanidine copolymers, (**W$_m$R$_{10}$** and **dIn$_{m/2}$-*b*-dG$_5$**). Each functional group combination was evaluated at two different degrees of polymerization (*n* or *m* = 10, 20). Carriers were compared to a positive control CPPM, **MePh$_{10}$-*b*-dG$_5$**, which has previously been reported to robustly deliver both EGFP and Cre.[5,27,30,32,33,50] The hydrophobic monomer incorporated in this polymer (**MePh**) features one methyl and one phenyl substituent. In total, 17 carriers including the positive control were used to deliver each cargo.

3.3.2 EGFP Internalization

The two macromolecular series were compared side-by-side for their abilities to facilitate EGFP delivery into Jurkat T cells (Figure 3.9). Cargo uptake is presented using two metrics: the percentage of live cells positive for EGFP (Figure 3.9A) and the median fluorescence intensity (MFI) of the entire live cell population (Figure 3.9B). Because these simple metrics lack information regarding the more complicated fluorescence profiles from which they are derived, a representative flow cytometry histogram has also been included for each carrier (Figure 3.9C-F). The positive control CPPM, **MePh$_{10}$-*b*-dG$_5$**, was also

used to deliver EGFP (and Cre recombinase). For comparison, the raw uptake histograms have been provided here as well (Figure 3.10A).

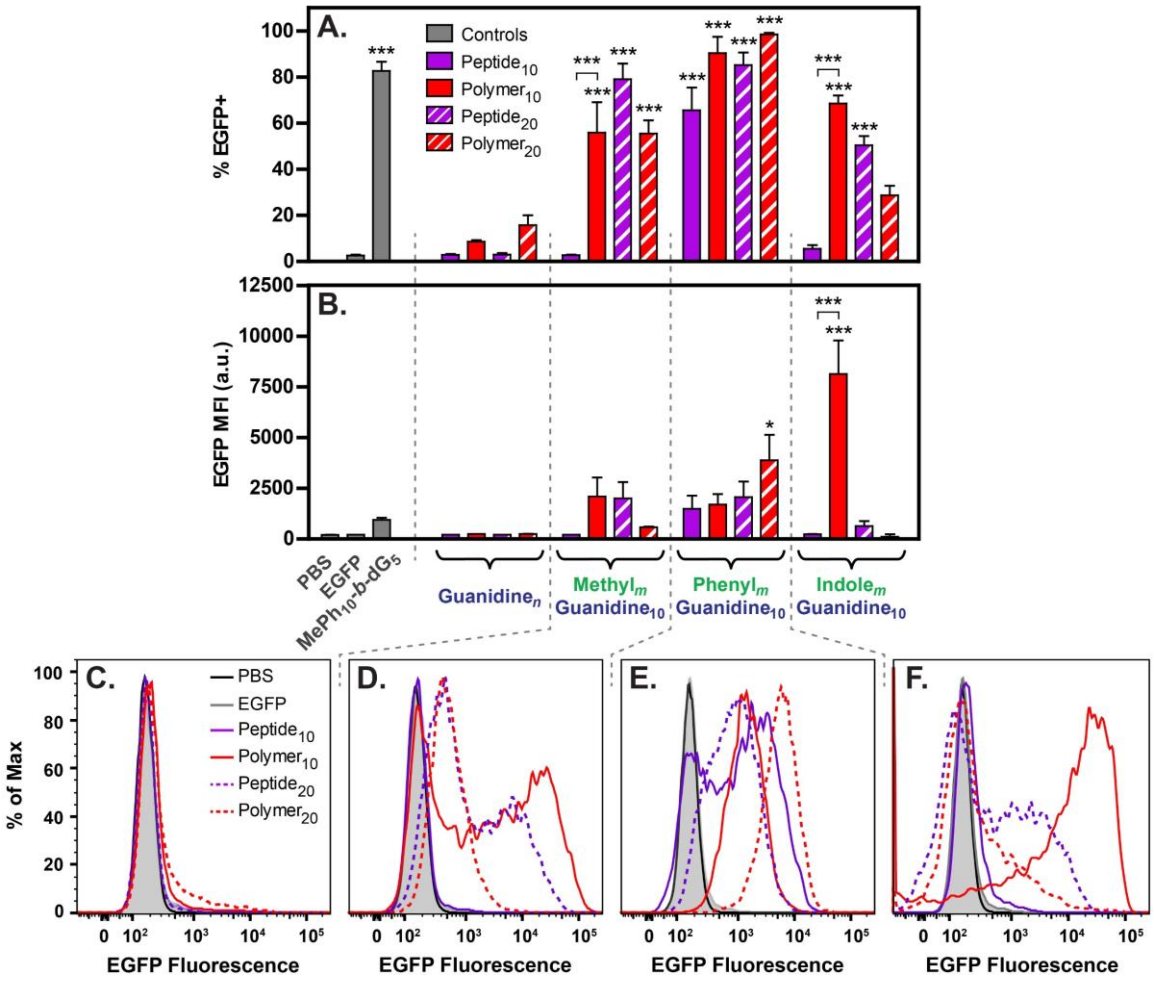

Figure 3.9: EGFP uptake in Jurkat T cells mediated by peptide carriers (purple) and their polymeric mimics (red). Within each functional group category, delivery with the shorter carriers (*n* or *m* = 10) is distinguished from delivery with the longer carriers (*n* or *m* = 20) by solid and hatched bars (or solid and dotted lines), respectively. Thus, each pair of adjacent bars represents the direct comparison of a peptide to its equivalent polymeric mimic, both possessing the same number, identity, and arrangement of side-chain functional groups. Internalization is presented as (A) percentage of the live-cell population positive for EGFP, (B) median fluorescence intensity (MFI) of the entire live-cell population, and (C-F) a representative flow cytometry histogram for each carrier overlaid with control samples containing only either PBS (black) or EGFP (grey). Uptake values (A and B) are displayed as the mean ± the standard error of the mean for three independent replicates of 10,000 cells each. Unless otherwise specified with a bracket, all statistical comparisons are between the indicated data and the EGFP control: * = $p < 0.05$, ** = $p < 0.01$, *** = $p < 0.001$, no symbol = no significance, as determined by one-way ANOVA followed by a Tukey post-test.

Whether compared by percent positive or MFI, the homopolymers/peptides all failed to deliver substantial amounts of EGFP. The block copolymers/peptides were far

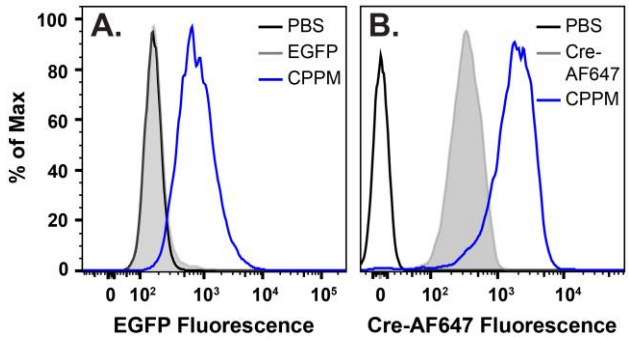

Figure 3.10: Representative fluorescence histograms for cellular internalization of (A) EGFP and (B) Cre-AF647 mediated by the positive control CPPM, **MePh$_{10}$-*b*-dG$_5$** (blue), overlaid with the relevant PBS (black) and protein-only (grey) controls.

more successful, though the extent of this success is dependent on the uptake metric considered. From the perspective of percent positive, only three amphiphilic carriers failed to deliver EGFP to a significant fraction of the population (**A$_{10}$R$_{10}$**, **W$_{10}$R$_{10}$**, and **dIn$_{10}$-*b*-dG$_5$**). Interestingly, their macromolecular counterparts (**dMe$_5$-*b*-dG$_5$**, **dIn$_5$-*b*-dG$_5$**, and **W$_{20}$R$_{10}$**) were all successful, suggesting that side-chain functionality does not predict delivery outcome in every case. Analysis by MFI, however, softens these differences, portraying only one of these polymer/peptide pairs (**W$_{10}$R$_{10}$** & **dIn$_5$-*b*-dG$_5$**) as performing significantly different from each other. Notably, **dIn$_5$-*b*-dG$_5$**, one of the new CPPMs reported here, facilitated significantly higher levels of EGFP delivery than any other carrier, making it a strong candidate for future studies.

The discrepancies between percent positive and MFI can be reconciled by understanding that the shape of the population distribution heavily affects which measure of delivery more accurately represent the actual outcomes.[62–64] This can be illustrated using several of the histograms in Figure 3.9. Two monomodal distributions (e.g., **dPh$_5$-*b*-dG$_5$** [solid red] and **dPh$_{10}$-*b*-dG$_5$** [dotted red] in Figure 3.9E) can be fairly compared by MFI, but not percent positive. This is because, while one carrier delivered a much higher quantity of cargo, both delivered to the entire population. Thus, MFI captures the delivery

differences while percent positive depicts them as equal. In contrast, two bimodal populations (e.g., **$W_{20}R_{10}$** [dotted purple] and EGFP [filled grey] in Figure 3.9F) can be accurately compared by percent positive, but not MFI. In this case, since the carrier delivered to less than half of the cells, its MFI lies in its negative mode, nearly equivalent to the MFI of the EGFP control. Thus, MFI portrays this carrier as facilitating no delivery, while percent positive accurately summarizes its success in nearly 50% of the population. Unfortunately, the carriers in this series produced a mixture of monomodal and bimodal fluorescence distributions, meaning neither percent positive nor MFI alone can fairly compare them all. For this reason, both metrics have been presented, as well as the raw data for one representative trial, to prevent misinterpretation of the data.

In summary, whether compared by percent positive or MFI, most of the amphiphilic carriers performed at similar levels. Although this means that many CPPs performed at the same level as their CPPM counterparts, it also implies that identity and arrangement of hydrophobic pendant groups are not the most critical design parameters. The stark differences within the **$Methyl_{10}Guanidine_{10}$** and **$Indole_{10}Guanidine_{10}$** pairs further suggest that side-chain functionality is an unsatisfactory predictor of performance.

3.3.3 Cre Recombinase Internalization

The CPP(M) series was also screened for Cre delivery to evaluate whether the results from EGFP delivery extrapolated to an oppositely charged protein. Function of the delivered Cre was quantified by loss of EGFP fluorescence six days post-delivery into a reporter Jurkat T cell line modified to stably express a floxed *EGFP* gene and will be discussed in a later section (Figure 3.11C, H-K). Cre internalization was assessed by

delivering Cre fluorescently labelled with Alexa Fluor 647 (Cre-AF647) into the same cell line (Figure 3.11A-B, D-G). The raw uptake histogram for the positive control CPPM, **MePh$_{10}$-*b*-dG$_5$**, is provided in Figure 3.10B for comparison.

The control sample containing only Cre-AF647 exhibited unusually high fluorescence compared to the PBS control. For reference, the control sample containing only EGFP in Figure 3.9 had essentially the same MFI as its respective PBS control. Since Cre is unable to facilitate its own delivery (evidenced by lack of gene recombination in the Figure 3.11C control), it can be inferred that Cre interacted particularly strongly with the cell surface. Cationic proteins, particularly those containing a cluster of positive charges (e.g., a Tat or NLS sequence, like the Cre used here) can commonly associate with anionic membranes via non-specific electrostatic interactions.[65,66] In fact, at least one previous study observed remarkable membrane adherence of fluorescently-labelled Tat-Cre.[67] Typically, washing the cell surface with heparin removes all extracellular protein, as was the case for EGFP.[54] Since extracellular Cre-AF647 could not be completely removed with multiple heparin washes in this case, only fluorescence intensities above this control were considered to be positive for intracellular Cre-AF647 (illustrated by black arrows in Figure 3.11D-G).

The heparin washes were, however, able to remove extracellular carrier:Cre complexes. This becomes evident when considering the carriers with fluorescence profiles lower than that of the Cre-AF647 control, like **dG$_5$** (red solid line, Figure 3.11D). While guanidine-rich ROMP homopolymers like **dG$_5$** have been shown to bind proteins, they are typically unable to facilitate significant protein internalization, as seen with EGFP (red

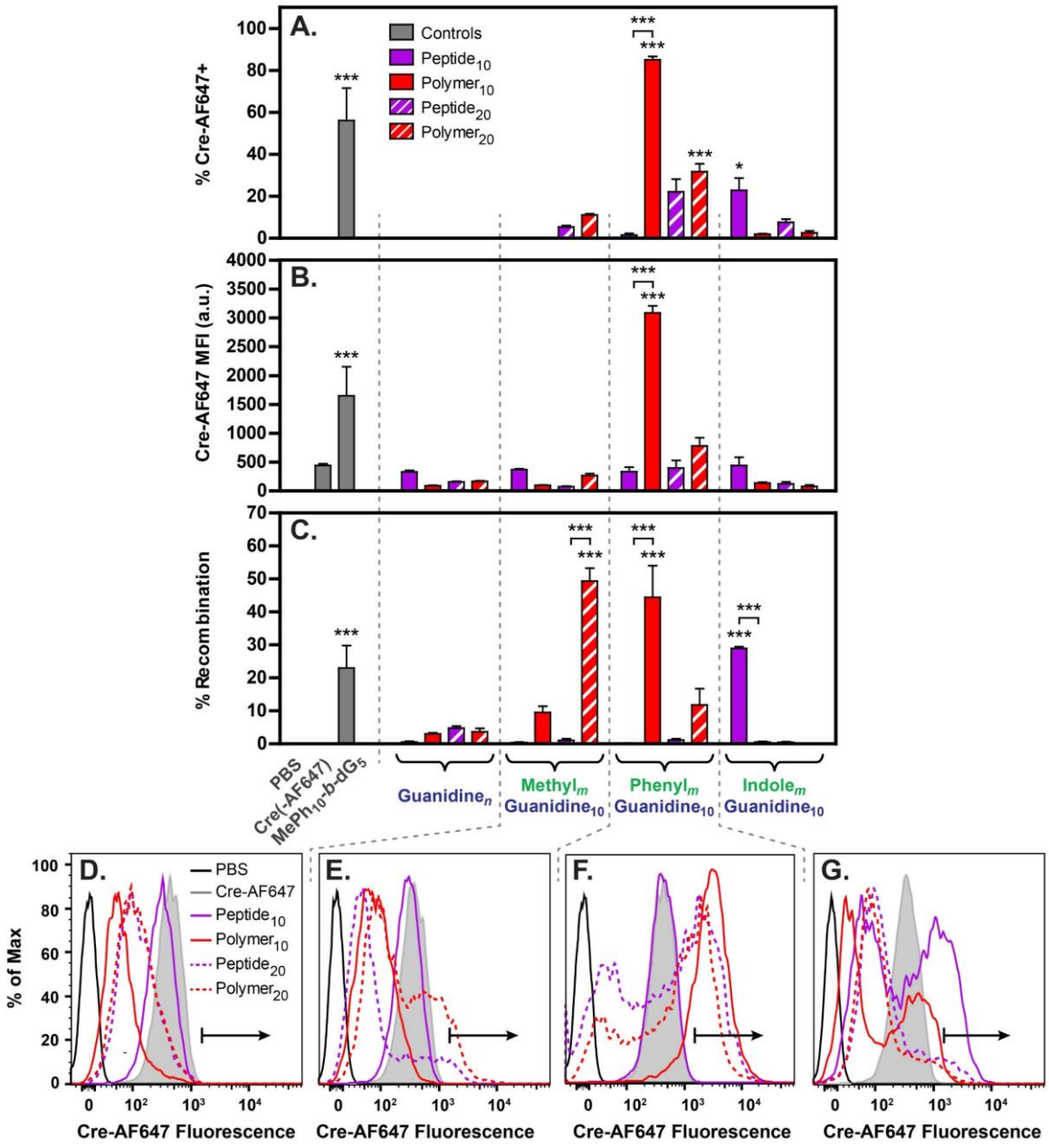

Figure 3.11: Uptake (A-B, D-G) and function (C) of Cre recombinase delivered with peptide carriers (purple) and their polymeric mimics (red) in a reporter Jurkat T cell line, modified to express a floxed *EGFP* gene. Within each functional group category, delivery with the shorter carriers (*n* or *m* = 10) is distinguished from delivery with the longer carriers (*n* or *m* = 20) by solid and hatched bars (or solid and dotted lines), respectively. Thus, each pair of adjacent bars represents the direct comparison of peptide to its equivalent polymeric mimic, which possesses the same number, identity, and arrangement of side-chain functional groups. Internalization of Cre, fluorescently labelled with Alexa Fluor 647 (Cre-AF647), is presented as (A) percentage of the live-cell population positive for Cre-AF647, (B) median fluorescence intensity (MFI) of the entire live-cell population, and (D-G) a representative flow cytometry histogram for each carrier overlaid with control samples containing either only PBS (black) or only Cre-AF647 (grey). Activity of Cre is displayed as (C) percentage of gene recombination (i.e., percentage of EGFP negative cells). Bars (A-C) are displayed as the mean ± the standard error of the mean for three independent replicates of 10,000 cells each. Unless otherwise specified with a bracket, all statistical comparisons are between the indicated data and the Cre or Cre-AF647 control: * = $p < 0.05$, ** = $p < 0.01$, *** = $p < 0.001$, no symbol = no significance, as determined by one-way ANOVA followed by a Tukey post-test.

solid line, Figure 3.9C).[53] Thus, when complexed with a carrier that is unable to facilitate delivery, Cre is no longer free to associate as strongly with the cell membrane. As a result, the heparin washes are more effective, and the fluorescence profile is lower than that of the Cre-AF647 control. In contrast, some carriers are altogether incapable of binding to proteins, like **R$_9$** (purple solid line, Figure 3.11D), explaining their need for covalent attachment.[50,68] In this case, Cre-AF647 is free to associate with the cell membrane and produces a nearly identical fluorescence profile to that of Cre-AF647 alone. In order to further explore this possibility, binding of another carrier with a similar fluorescence profile, **A$_{10}$R$_{10}$**, to Cre was measured using a previously reported equilibrium fluorescence quenching assay (Figure 3.18B).[5,33,53] As expected, **A$_{10}$R$_{10}$** was unable to bind Cre-AF647 at the low carrier:cargo ratio used in these experiments. Extrapolating this finding tells us that **F$_{10}$R$_{10}$** was also likely to have failed in binding Cre-AF647, given its fluorescence profile and lack of gene recombination.

Because of the competing effects of carrier binding and carrier-mediated internalization on fluorescence, it is unclear whether fluorescence intensities between **dG$_5$** and the Cre-AF647 control indicate (1) complete cargo binding and low cargo internalization, (2) partial cargo binding and low cargo-membrane adherence, or (3) partial cargo binding and a mixture of low cargo internalization combined with low cargo-membrane adherence. Despite ambiguity within the poorly performing carriers, the overwhelming quantity of Cre internalized by **dPh$_5$-*b*-dG$_5$** is undeniable. Interestingly, the complete failure of its peptide counterpart, **F$_{10}$R$_{10}$**, provides another explicit example of a polymer/peptide pair with dissimilar activity, likely due to discrepancies in cargo binding ability.

3.3.4 Differences in EGFP and Cre Internalization

Perhaps the most noticeable differences between EGFP and Cre delivery were the sheer number of carriers successful for EGFP internalization, including more methyl- and indole-containing carriers, and the identity of the top-performing carriers in each case (Figure 3.12). While **dIn$_5$-*b*-dG$_5$** was the overwhelming victor for EGFP internalization, it was among the worst performers for Cre uptake. Similarly, **dPh$_5$-*b*-dG$_5$** was by far the most successful carrier for Cre internalization, but only an average performer for EGFP delivery. The number of effective carriers for each cargo is addressed in later sections from the perspective of hydrophobicity.

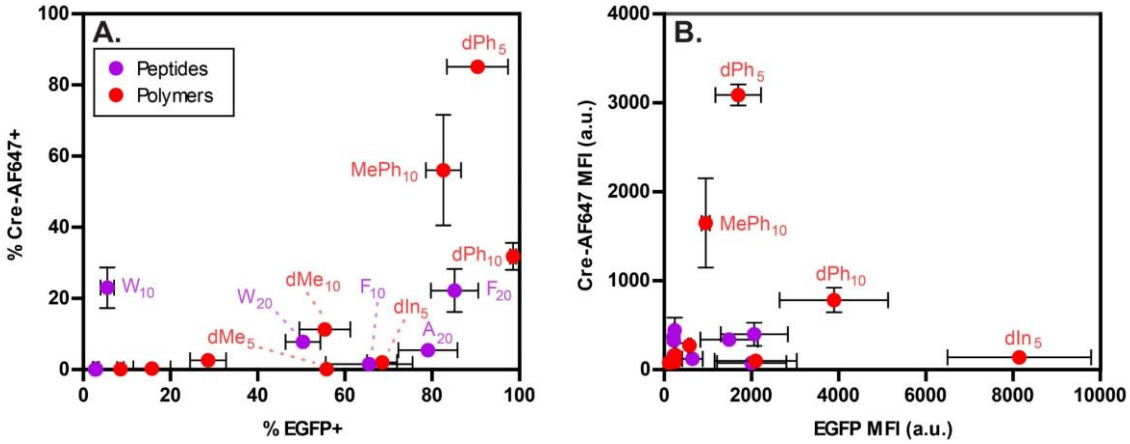

Figure 3.12: Relationship between Cre-AF647 and EGFP internalization for all peptide (purple) and polymer (red) carriers. For clarity, only data points representing statistically significant levels of uptake are accompanied by labels indicating the carrier's hydrophobic block. Internalization is compared by (A) percent positive and (B) median fluorescence intensity (MFI), demonstrating a lack of correlation between delivery of the two cargoes.

3.3.5 Differences in Cre Recombinase Activity

A comparison of the polymer/peptide pairs for intracellular Cre activity provides even more examples of performance discrepancies (Figure 3.13C, H-K). In fact, each carrier which facilitated significant gene recombination (**dMe$_{10}$-*b*-dG$_5$**, **dPh$_5$-*b*-dG$_5$**, and **W$_{10}$R$_{10}$**) had a polymer or peptide counterpart which entirely failed to achieve functional delivery (**A$_{20}$R$_{10}$**, **F$_{10}$R$_{10}$**, and **dIn$_5$-*b*-dG$_5$**). This finding further reinforces the suspicion

that carrier side-chain functionality is a poor-predictor of delivery outcomes. Furthermore, despite the dramatically higher internalization facilitated by **dPh$_5$-*b*-dG$_5$** over **dMe$_{10}$-*b*-dG$_5$**, they both yielded the same level of gene recombination (Figure 3.13).

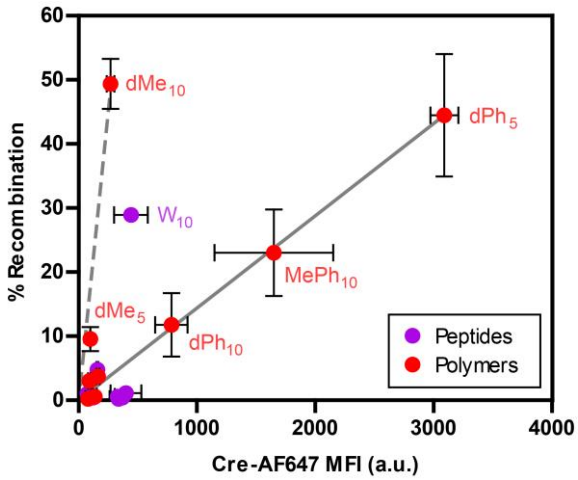

Figure 3.13: Relationships between Cre uptake and function for all peptide (purple) and polymer (red) carriers. Within the successful carriers, the phenyl-containing and methyl-only CPPMs both exhibit linear relationships between uptake and function (illustrated by solid grey and dotted grey lines, respectively). Such linear relationships between dose of intracellular cargo and cargo activity are intuitive, although it is interesting to note that three carriers in particular (**dMe$_5$-*b*-dG$_5$**, **W$_{10}$R$_{10}$**, and **dMe$_{10}$-*b*-dG$_5$**) facilitate much higher Cre activity considering their levels of uptake.

Closer analysis of the data reveals that the phenyl-containing CPPMs, including the positive control (**dPh$_{10}$-*b*-dG$_5$**, **MePh$_{10}$-*b*-dG$_5$**, and **dPh$_5$-*b*-dG$_5$**), follow a linear relationship between uptake and function (illustrated by the solid grey line). A linear dependence of intracellular dose and biological activity is intuitive; however, it is interesting to note that the methyl-only CPPMs (**dMe$_5$-*b*-dG$_5$** and **dMe$_{10}$-*b*-dG$_5$**) exhibit a different linear intracellular dose dependence (illustrated by the dashed grey line). The only successful CPP for Cre delivery (**W$_{10}$R$_{10}$**) appears to resemble the methyl-only CPPMs. Together, these three carriers (**dMe$_5$-*b*-dG$_5$**, **W$_{10}$R$_{10}$**, and **dMe$_{10}$-*b*-dG$_5$**) demonstrate that high levels of internalization are not necessarily required to achieve heightened cargo activity. It is possible that the uptake-function relationship differences are explained by the relative abilities of each carrier to facilitate release or endosomal

escape of its cargo. Although such differences should be explored in future studies, it is nonetheless clear that optimizing for maximum uptake can overlook carriers which are just as effective at delivering functional cargo.

3.3.6 Optimal Carrier Hydrophobicity for Protein Internalization

Several previous reports have revealed an optimal window in carrier hydrophobicity for enhanced uptake of CPP(M)s and their cargoes, however, these studies have been restricted to carriers of the same macromolecular scaffold.[5,30,35,58,69,70] Designing the polymer/peptide pairs to contain identical side chain arrangements allowed the effect of backbone identity on delivery outcomes to be isolated. Considering that the poly(oxanorbornene) backbone of the polymer series is considerably more hydrophobic than the more polar polyamide backbone of the peptide series, it is not entirely unexpected that carriers with different backbones would perform differently. Within a pair of carriers with equivalent side chains, significant differences in overall carrier hydrophobicity could still be imparted by the identity of the backbone, in turn causing performance discrepancies. Therefore, we sought to reorganize the carriers by hydrophobicity to see if this parameter was better correlated with delivery. Given that CPPMs have been shown not to self-assemble in solution[71] (which could alter the apparent hydrophobicity of the complexes experienced by the cell), single-chain hydrophobicity was taken as a reasonable predictor of complex hydrophobicity for this analysis.

Quantifying the hydrophobicity of macromolecules has been a challenge historically. While molecules with discrete molecular weights (e.g., peptides) can be evaluated by methods like HPLC, polymers with molecular weight distributions make this

much more difficult.[55] Constituent monomer hydrophobicity can sometimes be used as a convenient substitute for polymer hydrophobicity, however, this strategy is insufficient when polymers are built from dissimilar backbones (e.g., ROMP polymers and peptides).[5,30,69] Even within the same synthetic platform, predicting polymer hydrophobicity from monomer hydrophobicity is further complicated when considering copolymers. In the past, our group has successfully ranked copolymers by monomer hydrophobicity when either the identity of one monomer[5,69] or the comonomer ratio[30] was varied. This study varies both comonomer identity (**MePh**, **dMe**, **dPh**, and **dIn**) and ratio (1:1 and 2:1) simultaneously, rendering monomer hydrophobicity inadequate for prediction of polymer hydrophobicity. As a result, we have employed a theoretical method developed by Magenau *et al*. for calculating macromolecular hydrophobicity using shorter, model oligomers which capture the correct comonomer identities and ratios.[55]

In this method, the theoretical octanol-water partition coefficient (LogP), which has been shown to correlate well with experimentally measured hydrophobicity,[5,55,69] is normalized by the molecular surface area (SA) of the molecule to account for differences in polymer length. The resulting hydrophobicity parameter (LogP/SA) is presented for all carriers, ranked from most hydrophilic to most hydrophobic (Figure 3.14). The relative positions of the peptides of equal length in this table are consistent with reports that tryptophan is more hydrophobic than phenylalanine, which is in turn more hydrophobic than alanine, providing additional support for the validity of this hydrophobicity model.[6–8] Accordingly, the relative positions of the polymers in this list are also logical in terms of relative side-chain hydrophobicity (indole > phenyl > methyl). The hydrophobicity

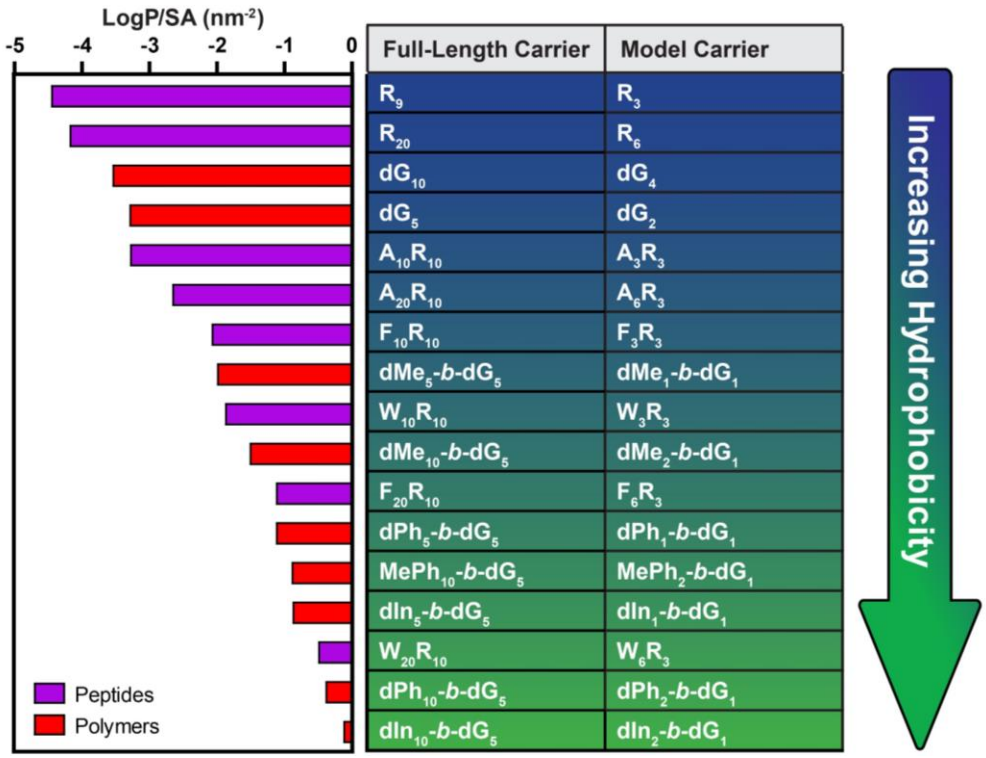

Figure 3.14: Predicted hydrophobicity of carriers used for EGFP and Cre delivery. Hydrophobicity was calculated as the ratio of the octanol-water partition coefficient (LogP) to molecular surface area (SA) for a series of shorter model molecules which simply capture the correct identity and ratio of hydrophobic to hydrophilic functional groups. LogP was calculated using the KOWWIN tool in EPI Suite v. 4.1, and SA is the Connolly molecular area, calculated in Chem3D Ultra 8.0 using a probe size of 1.4 Å after performing a MM2 energy minimization. Importantly, polymer structures were modelled with a $-CH_2$ end group in place of the actual phenyl end group, as this would disproportionately affect the overall hydrophobicity of such a small model molecule. Given the relatively short length of the full-length carriers, it is possible that the omission of the phenyl end groups resulted in representation of the polymers as slightly more hydrophilic than they are in reality, though this difference is likely very small.

ranking makes it clear that the ROMP polymer and polypeptide backbones are of sufficiently disparate hydrophobicity to skew the peptide series (purple) toward the more hydrophilic end of the scale and the polymer series (red) to the more hydrophobic end. In fact, ten alanine residues must be appended to R_{10} to impart it with the same hydrophobicity as the dG_5 homopolymer. Likewise, CPPMs with ten methyl and ten phenyl groups are just as hydrophobic as CPPs with ten phenyl and twenty phenyl groups, respectively.

Replotting internalization of both cargoes by hydrophobicity does in fact reveal windows for optimal performance, in accordance with previous studies, although the EGFP window appears to be much wider than that of Cre (Figure 3.15). Thus, neither carrier side-chain functionality nor backbone alone dictate cargo internalization; rather, the overall hydrophobicity resulting from the combination of these two design parameters predicts uptake for a given cargo.

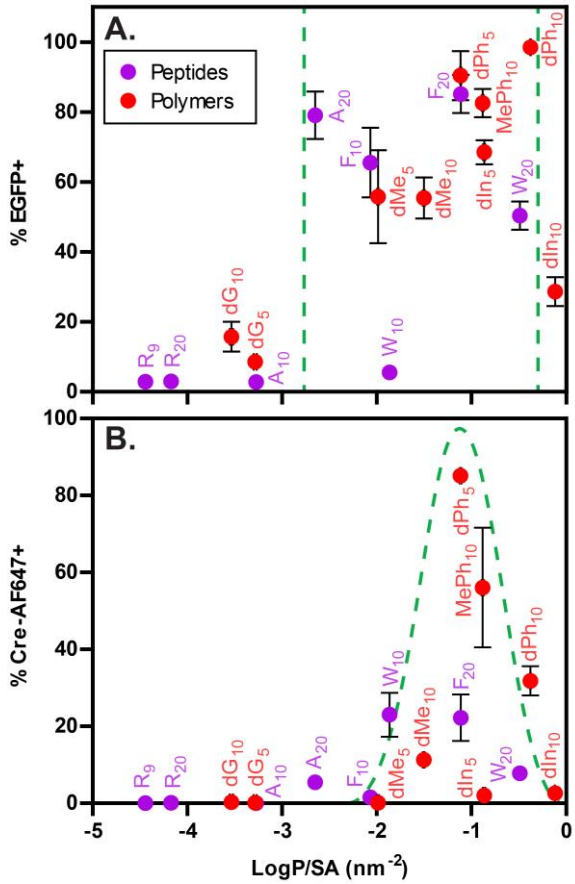

Figure 3.15: Optimal hydrophobic windows for (A) EGFP and (B) Cre-AF647 internalization mediated by all polymer (red) and peptide (purple) carriers as quantified by percent positive cells. Hydrophobicity is represented by the ratio of the theoretical octanol-water partition coefficient to molecular surface area (LogP/SA). The optimal hydrophobicity windows are illustrated by green dashed lines.

Comparison of EGFP and Cre-AF647 delivery through the lens of hydrophobicity supports the hypothesis that protein pI is largely responsible for the differences in uptake. Whereas EGFP can rely on both electrostatics and hydrophobics for complex formation, Cre is much more restricted to hydrophobics. Therefore, carriers of lower hydrophobicity likely struggle to bind (and deliver) Cre without the help of the electrostatic attraction present in EGFP binding. Differences in high hydrophobicity carriers were mostly due to toxicity. Whereas a loss in viability was only observed for the most hydrophobic carrier during EGFP delivery, several of the more hydrophobic carriers exhibited toxicity following Cre-AF647 delivery (Figure 3.16). The dead cells, which were excluded from the uptake analysis, were often those with high levels of internalized Cre-AF647.

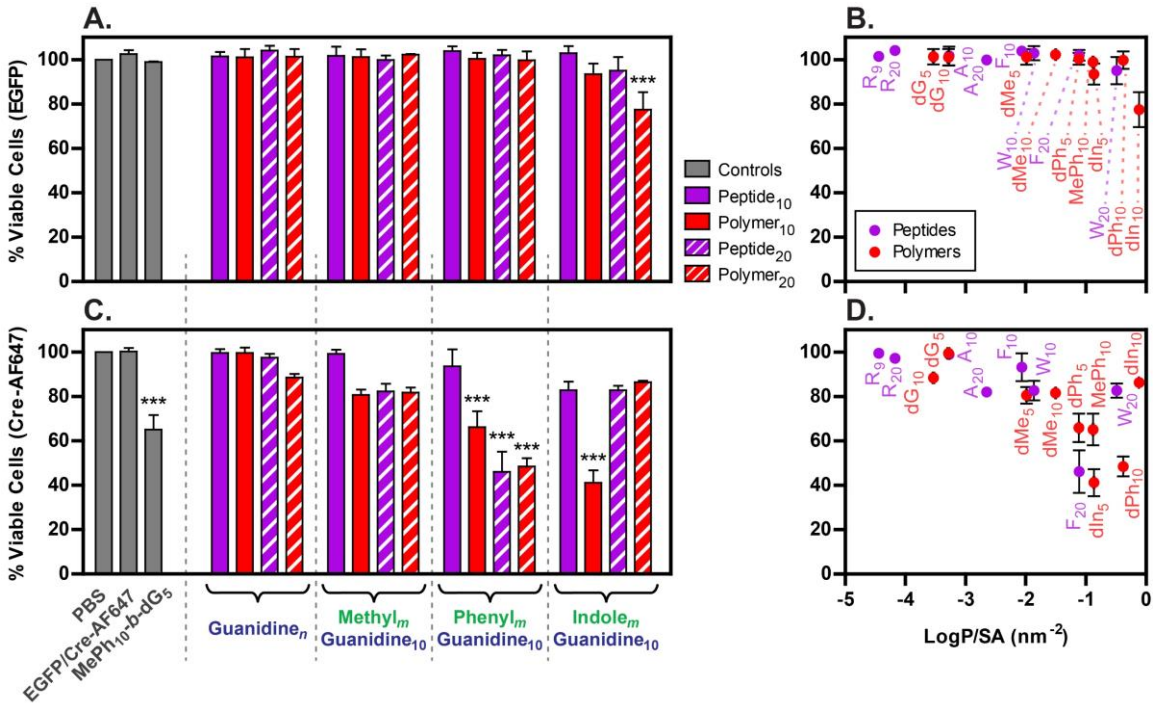

Figure 3.16: Cellular viability immediately following delivery of (A-B) EGFP and (C-D) Cre-AF647 with peptides (purple) and their corresponding polymeric mimics (red), compared with control samples (grey). Carriers are grouped by both side-chain functional group arrangement (A, C) and hydrophobicity (B, D) to illustrate the dependence of cytotoxicity on overall carrier hydrophobicity, rather than specific identity of the side-chain functional groups. Data are displayed as the mean ± the standard error of the mean for three independent replicates of 10,000 cells each. All statistical comparisons are between the indicated data and the appropriate PBS control: * = $p < 0.05$, ** = $p < 0.01$, *** = $p < 0.001$, no symbol = no significance, as determined by one-way ANOVA followed by a Tukey post-test.

Therefore, if both live and dead cells had been included in the analysis, there would be fewer differences between delivery of the two cargoes with the most hydrophobic carriers.

3.3.7 Optimal Carrier Hydrophobicity for Intracellular Availability (IA) of Cre

Replotting Cre activity as a function of hydrophobicity exposes a similar window containing the top performers for functional delivery (Figure 3.17A). Interestingly, the window for optimal Cre function extends further in the hydrophilic direction than the window for optimal Cre uptake. Closer examination reveals that the three carriers causing the broadening of this window (**dMe$_5$-*b*-dG$_5$**, **W$_{10}$R$_{10}$**, and **dMe$_{10}$-*b*-dG$_5$**) are the same

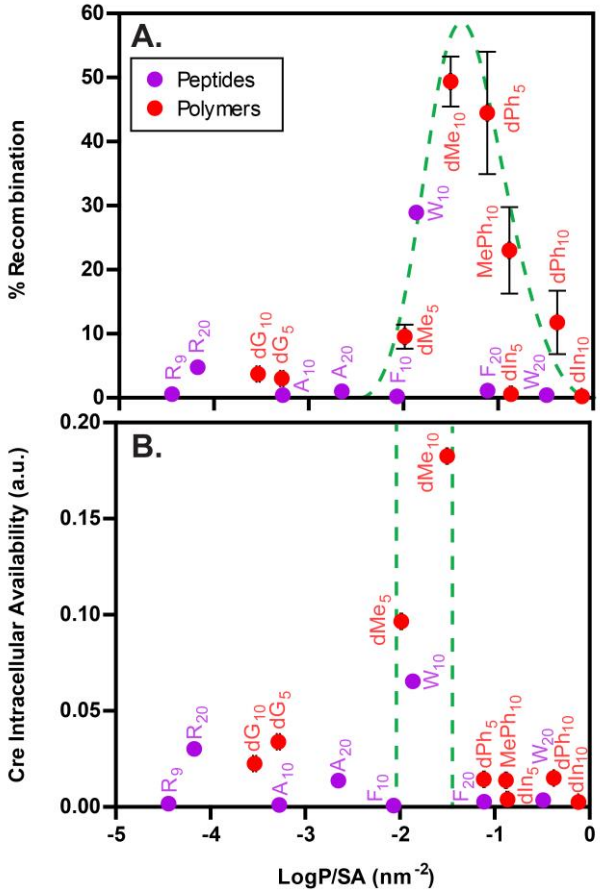

Figure 3.17: Optimal hydrophobic windows for (A) maximum intracellular activity of delivered Cre and (B) maximum intracellular availability (IA) of Cre for all polymer (red) and peptide (purple) carriers. IA values were calculated as the ratio of intracellular activity to protein uptake (recombination/Cre-AF647 MFI), with higher values representing relatively fewer internalized Cre molecules required to edit each cell. Hydrophobicity is represented by the ratio of the theoretical octanol-water partition coefficient to molecular surface area (LogP/SA). Optimal hydrophobic windows are illustrated with dashed green lines.

three which exhibited higher than expected Cre activity, given their low uptake. That is, these three relatively hydrophilic carriers appear strikingly more successful through the lens of cargo function than they did with cargo uptake. This phenomenon can be quantified by formally defining the intracellular availability (IA) of the cargo to denote the ratio of biologically active cargo to cellularly internalized cargo. For Cre delivery, IA can be calculated for each carrier by normalizing percent gene recombination by Cre-AF647 MFI, which is directly proportional to the quantity of intracellular Cre. The IA provides valuable insight into the physical differences between delivery with various carriers, effectively describing how efficient a carrier is at making its cargo available after promoting its internalization. While it is possible that all CPP(M)s behave similarly enough to directly associate the IA with the ability of a carrier to release its cargo, there are a number of steps in the complex delivery landscape that could influence this process. In particular, carrier-dependent cellular entry mechanisms and protein denaturation, as well as spatial and temporal differences surrounding intracellular trafficking, may all contribute to differences in IA. Nonetheless, IA appears to be strongly correlated with hydrophobicity (Figure 3.17B).

Importantly, differences in IA mean that not all carriers facilitating high cargo activity also exhibit high uptake. Thus, optimizing for maximum cargo uptake may fail to identify the carriers which are more effective at making their delivered cargo bioavailable. For example, past uptake-focused studies in our group painted **dMe$_{10}$-*b*-dG$_5$** as a relatively underwhelming carrier, resulting in its exclusion from functional delivery studies until now.[33,50] Additionally, a statistically significant loss of cellular viability was observed for the high uptake carriers (**MePh$_{10}$-*b*-dG$_5$** and **dPh$_5$-*b*-dG$_5$**), but not for the high IA carriers

(**dMe$_{10}$-*b*-dG$_5$** and **W$_{10}$R$_{10}$**), providing further incentive to identify and take advantage of such CPP(M)s (Figure 3.16).

3.3.8 Potential Relationship Between Binding and IA

Upon observation that high IA correlated with low hydrophobicity (within the optimal window), it was hypothesized that this heightened cargo availability might be due to increased ability of the carriers to facilitate intracellular cargo release, specifically as a result of relatively weaker carrier-cargo associations. Perhaps a carrier facilitating low uptake (e.g., **dMe$_{10}$-*b*-dG$_5$**) would yield the same level of activity as one with very high uptake (e.g., **dPh$_5$-*b*-dG$_5$**) if the former was more weakly bound to its cargo. This hypothesis of hydrophobicity-driven binding strength dictating intracellular release would be consistent with the idea that CPP(M):Cre binding relies heavily on hydrophobic interactions, given the lack of electrostatic attraction.

To test this hypothesis, previously reported fluorescence-based, equilibrium binding assays[5,33,53] were performed using Cre-AF647 and the five carriers which facilitated significant levels of either gene recombination or uptake: **MePh$_{10}$-*b*-dG$_5$**, **dMe$_{10}$-*b*-dG$_5$**, **dPh$_5$-*b*-dG$_5$**, **dPh$_{10}$-*b*-dG$_5$**, and **W$_{10}$R$_{10}$** (Figure 3.18A). Two additional carriers, one more hydrophilic (**A$_{10}$R$_{10}$**) and one more hydrophobic (**W$_{20}$R$_{10}$**) than any contained within this set, were studied as well to probe the effect of more dramatic shifts in hydrophobicity as well as to include more peptides (Figure 3.18B).

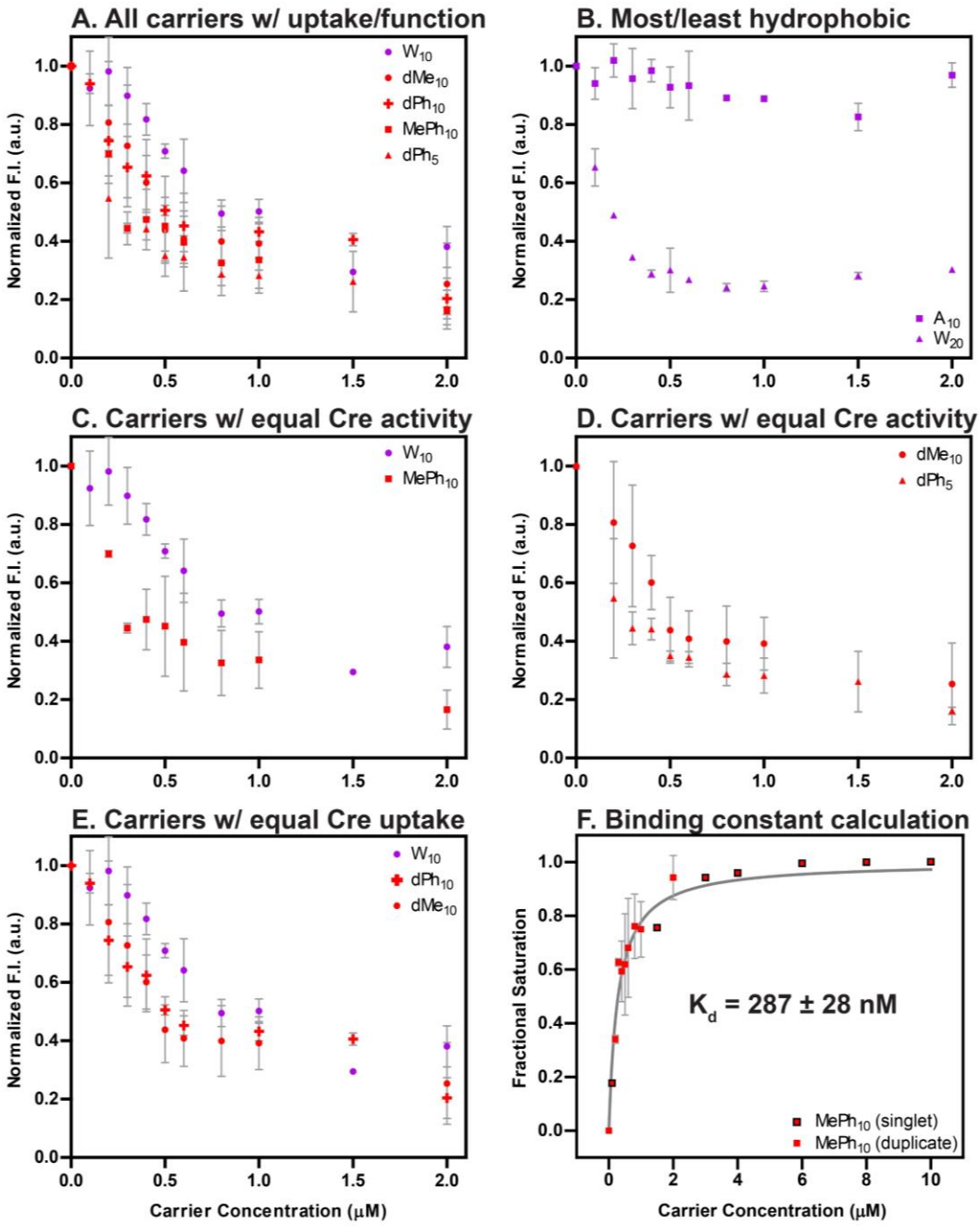

Figure 3.18: Peptide (purple) and polymer (red) carrier binding to Cre-AF647 as measured by equilibrium fluorescence quenching assays. (A) Overlay of binding curves for all carriers which facilitated statistically significant Cre uptake and/or function. (B) Overlay of binding curves for two additional carriers, one more hydrophilic (**$A_{10}R_{10}$**) and one more hydrophobic (**$W_{20}R_{10}$**) than any of the other carriers. (C) Overlay of **$W_{10}R_{10}$** and **$MePh_{10}$-*b*-dG_5**, two carriers which facilitated similar levels of gene recombination, despite the latter transporting significantly more Cre intracellularly. (D) Overlay of **dMe_{10}-*b*-dG_5** and **dPh_5-*b*-dG_5**, two carriers which facilitated similar levels of gene recombination, despite the latter transporting significantly more Cre intracellularly. (E) Overlay of **$W_{10}R_{10}$**, **dPh_{10}-*b*-dG_5**, **dMe_{10}-*b*-dG_5**, three carriers which facilitated significantly different levels of gene recombination, despite all transporting similar quantities of Cre intracellularly. (F) Fractional saturation plot of **$MePh_{10}$-*b*-dG_5** used to calculate the dissociation constant (K_d) between this carrier and Cre. Data are displayed as the mean ± the standard deviation of two independent replicates, except in (F), where singlet data for several additional concentrations (outlined in black) were added to improve the accuracy of the fractional saturation fit and binding constant (K_d) calculation.

Globally, increased hydrophobicity undoubtedly drove tighter Cre binding. A dramatic difference was observed between the most hydrophobic carrier (**$W_{20}R_{10}$**) and the least hydrophobic carrier (**$A_{10}R_{10}$**), which were the tightest and weakest binders, respectively (Figure 3.18B). The carriers of intermediate hydrophobicity, however, performed similar to one another. All of these intermediate hydrophobicity carriers achieved complete cargo binding at very low CPP(M) concentrations, on par with the lowest seen for any previously-studied CPPM:protein pairs.[5,33]

Though many of the binding curves were clearly overlapping, they were nonetheless replotted in groups of fewer carriers to make the comparisons originally proposed. Two individual pairs of carriers represent similar levels gene recombination despite different levels of uptake (Figure 3.18C-D). In both cases, it was predicted that the carriers with more uptake (**$MePh_{10}$-*b*-dG_5** and **dPh_5-*b*-dG_5**) would be hampered by tighter binding (leading to less cargo release), explaining the reason for their low IAs. Although the curves were not dramatically different from each other in either case, the predicted trend (tighter binding correlating with lower IA) did hold from a qualitative standpoint.

From the opposite perspective, three carriers facilitated similar uptake levels but different levels of gene recombination (Figure 3.18E). In this case, it was predicted that higher gene recombination (**dMe_{10}-*b*-dG_5** > **$W_{10}R_{10}$** > **dPh_{10}-*b*-dG_5**) would be accompanied by weaker binding, thus explaining the high IAs observed. This time, the trend did not hold. Specifically, **dMe_{10}-*b*-dG_5** had much tighter binding than expected, on par with **dPh_{10}-*b*-dG_5**, providing more evidence that binding tightness is not the only important parameter for intracellular activity.

While qualitative comparisons of binding curves suggested there might be correlations between binding tightness and relative Cre activity (Figure 3.18C-E), the curves were not well enough resolved to say this with any certainty. Despite the inability to rank these intermediate carriers, it can be definitively said that any potential differences are minor, given the much more substantial differences observed between previously-studied binding pairs.[33] Such small differences in Cre binding would be unlikely to explain the dramatic disparities in gene recombination. Future work investigating the forces underlying post-delivery cargo release may be a worthwhile endeavor, as it remains plausible that the complicated interactions surrounding intracellular unbinding differ significantly from those driving the complex formation event modeled by these assays.

Finally, for comparison with our previous report, which surveyed **MePh$_{10}$-*b*-dG$_5$** binding to seven unique proteins, the binding curve for **MePh$_{10}$-*b*-dG$_5$**:Cre-AF647 was converted into fractional saturation and the equilibrium dissociation constant (K_d) was calculated using the methodology presented in that study (Figure 3.18F).[33] To improve the quality of the fit (in particular, to ensure that saturation was achieved) a single replicate of additional data points was added to the binding curve prior to conversion to fractional saturation. These additional data points were measured at concentrations of 0.1 µM, 1.5 µM, and 3-10 µM, and are indicated with black outlines and no error bars. As expected, the K_d found for Cre (287 ± 28 nM) correlates well with the predicted K_d for a protein with a pI of about 9.2, further supporting the conclusion that pI drives CPPM binding tightness.

3.4 Conclusions

Optimized hydrophobic side-chain arrangements cannot be directly translated from one macromolecular platform to another with the expectation of equivalent delivery performance. This is because discrepancies in backbone hydrophobicity significantly impact the carrier's overall hydrophobicity. The overall hydrophobicity, which can be adequately predicted using theoretical methods, can instead be used to inform the design of new carriers with different backbones, thus increasing the chance of success. In this work, the relatively hydrophobic poly(oxanorbornene) CPPM backbone was found to generally improve polymer delivery outcomes as compared to their equivalent peptide counterparts, possessing hydrophilic polar backbones. This meant that CPPs generally required the incorporation of either a longer hydrophobic block, side chains of greater hydrophobicity, or a combination of the two to compete with polymer performance. Thus, the CPPMs were more often able to facilitate high levels of uptake and function, since relatively few of the CPPs were hydrophobic enough to fall within the optimal performance windows. Furthermore, the inherent heterogeneity afforded by synthetic methods (i.e., mixtures of molecules with slight variations in overall length, monomer ratio, and stereochemistry) may actually be advantageous for intracellular delivery, allowing for a broader range of unique interactions between carrier, cargo, and membrane to occur. Combined with their ease of synthesis and access to a broader chemical space, these results further validate the continued study of biomimetic materials in combination with peptides.

The utility of carrier hydrophobicity extends beyond what has been reported previously. While these studies were restricted to prediction of uptake within a specific carrier scaffold, our findings generalize this to more universally predict both uptake and

intracellular cargo activity, despite multiple carrier backbones. Furthermore, carrier hydrophobicity was also found to strongly correlate with the intracellular availability (IA) of the cargo, defined as the ability of a carrier to make its cargo available to perform its biological function. Despite their low cellular internalization, two carriers with high IAs were just as effective at gene recombination as carriers with the highest uptake, yet resulted in lower cell death, making them highly attractive from a functional delivery standpoint. Within the CPPM series, the more hydrophobic phenyl-containing carriers tended to internalize more cargo, while the cargo delivered by the less hydrophobic methyl-containing carriers was more intracellularly available. Importantly, the high IA carriers would have been overlooked if screened for uptake alone. From a practical standpoint, however, it is reassuring to note that there were no cases of high uptake without high activity, providing evidence that optimizing for high uptake remains a useful tool for rapid screening of large libraries of new carriers. While carrier-cargo association strength does not appear to drive IA, it remains possible that hydrophobicity-driven differences in endosomal escape, cargo release kinetics, or even cargo denaturation are responsible for the observed phenomenon. It should be noted that the predictive capabilities of carrier hydrophobicity may be limited to assessing carriers of the same architecture (i.e., diblock copolymers), as two studies of macromolecular isomers have explicitly shown that statistical and block copolymers facilitate different levels of delivery, despite being of similar expected hydrophobicity.[53,70]

Carrier success was also dependent on inherent cargo properties. As a result of both electrostatic and hydrophobic driving forces, low pI proteins (like EGFP) are expected to be successfully delivered with a wider hydrophobic range of cationic carriers than high

pI proteins (like Cre), which cannot rely on electrostatics to compensate for a lack of hydrophobicity when it comes to cargo binding. This highlights the importance of designing chemically rich and versatile carriers, i.e., those which can interact with their cargoes in more than one manner, for the delivery of heterogeneous proteins. Additionally, the effectiveness of a carrier at delivering one cargo may not translate to delivery of other cargoes, a long-standing problem in the field of protein delivery.

In summary, we have reported the first series of simple block copolypeptides capable of binding and transporting proteins intracellularly without the need for covalent attachment. In studying these carriers and their synthetic mimics, we have also established macromolecular hydrophobicity as a universal parameter to predict protein uptake, function, and intracellular availability, regardless of carrier backbone.

3.5 References

(1) Ray, M.; Lee, Y. W.; Scaletti, F.; Yu, R.; Rotello, V. M. Intracellular delivery of proteins by nanocarriers. *Nanomedicine* **2017**, *12* (8), 941–952.

(2) Zhao, H.; Lin, Z. Y.; Yildirimer, L.; Dhinakar, A.; Zhao, X.; Wu, J. Polymer-based nanoparticles for protein delivery: design, strategies and applications. *J. Mater. Chem. B* **2016**, *4* (23), 4060–4071.

(3) Du, J.; Jin, J.; Yan, M.; Lu, Y. Synthetic Nanocarriers for Intracellular Protein Delivery. *Curr. Drug Metab.* **2012**, *13* (1), 82–92.

(4) Kowalski, P. S.; Bhattacharya, C.; Afewerki, S.; Langer, R. Smart Biomaterials: Recent Advances and Future Directions. *ACS Biomater. Sci. Eng.* **2018**, *4* (11), 3809–3817.

(5) Posey, N. D.; Caffrey, L. M.; Minter, L. M.; Tew, G. N. Protein Mimic Hydrophobicity Affects Intracellular Delivery but not Cargo Binding. *ChemistrySelect* **2016**, *1* (19), 6146–6150.

(6) Nozaki, Y.; Tanford, C. The solubility of amino acids and two glycine peptides in aqueous ethanol and dioxane solutions: establishment of a hydrophobicity scale. *J. Biol. Chem.* **1971**, *246* (7), 2211–2217.

(7) Wimley, W. C.; White, S. H. Experimentally determined hydrophobicity scale for proteins at membrane interfaces. *Nat. Struct. Mol. Biol.* **1996**, *3* (10), 842–848.

(8) Schmidt, S.; Adjobo-Hermans, M. J. W.; Kohze, R.; Enderle, T.; Brock, R.; Milletti, F. Identification of Short Hydrophobic Cell-Penetrating Peptides for Cytosolic Peptide Delivery by Rational Design. *Bioconjug. Chem.* **2017**, *28* (2), 382–389.

(9) Rydberg, H. A.; Carlsson, N.; Nordén, B. Membrane interaction and secondary structure of *de novo* designed arginine-and tryptophan peptides with dual function. *Biochem. Biophys. Res. Commun.* **2012**, *427* (2), 261–265.

(10) Walrant, A.; Bauzá, A.; Girardet, C.; Alves, I. D.; Lecomte, S.; Illien, F.; Cardon, S.; Chaianantakul, N.; Pallerla, M.; Burlina, F.; Frontera, A.; Sagan, S. Ionpair-π interactions favor cell penetration of arginine/tryptophan-rich cell-penetrating peptides. *Biochim. Biophys. Acta - Biomembr.* **2020**, *1862* (2), 183098.

(11) Bechara, C.; Pallerla, M.; Zaltsman, Y.; Burlina, F.; Alves, I. D.; Lequin, O.; Sagan, S. Tryptophan within basic peptide sequences triggers glycosaminoglycan-dependent endocytosis. *FASEB J.* **2013**, *27* (2), 738–749.

(12) Thorén, P. E. G.; Persson, D.; Esbjörner, E. K.; Goksör, M.; Lincoln, P.; Nordén, B. Membrane Binding and Translocation of Cell-Penetrating Peptides. *Biochemistry* **2004**, *43* (12), 3471–3489.

(13) Rydberg, H. A.; Matson, M.; Åmand, H. L.; Esbjörner, E. K.; Nordén, B. Effects of Tryptophan Content and Backbone Spacing on the Uptake Efficiency of Cell-Penetrating Peptides. *Biochemistry* **2012**, *51* (27), 5531–5539.

(14) Maiolo, J. R.; Ferrer, M.; Ottinger, E. A. Effects of cargo molecules on the cellular uptake of arginine-rich cell-penetrating peptides. *Biochim. Biophys. Acta - Biomembr.* **2005**, *1712* (2), 161–172.

(15) Thorén, P. E. G.; Persson, D.; Isakson, P.; Goksör, M.; Önfelt, A.; Nordén, B. Uptake of analogs of penetratin, Tat(48–60) and oligoarginine in live cells. *Biochem. Biophys. Res. Commun.* **2003**, *307* (1), 100–107.

(16) Delaroche, D.; Aussedat, B.; Aubry, S.; Chassaing, G.; Burlina, F.; Clodic, G.; Bolbach, G.; Lavielle, S.; Sagan, S. Tracking a New Cell-Penetrating (W/R) Nonapeptide, through an Enzyme-Stable Mass Spectrometry Reporter Tag. *Anal. Chem.* **2007**, *79* (5), 1932–1938.

(17) Lécorché, P.; Walrant, A.; Burlina, F.; Dutot, L.; Sagan, S.; Mallet, J.-M.; Desbat, B.; Chassaing, G.; Alves, I. D.; Lavielle, S. Cellular uptake and biophysical properties of galactose and/or tryptophan containing cell-penetrating peptides. *Biochim. Biophys. Acta - Biomembr.* **2012**, *1818* (3), 448–457.

(18) Walrant, A.; Correia, I.; Jiao, C.-Y.; Lequin, O.; Bent, E. H.; Goasdoué, N.; Lacombe, C.; Chassaing, G.; Sagan, S.; Alves, I. D. Different membrane behaviour and cellular uptake of three basic arginine-rich peptides. *Biochim. Biophys. Acta - Biomembr.* **2011**, *1808* (1), 382–393.

(19) Farkhani, S. M.; Johari-ahar, M.; Zakeri-Milani, P.; Shahbazi Mojarrad, J.; Valizadeh, H. Enhanced cellular internalization of CdTe quantum dots mediated by arginine- and tryptophan-rich cell-penetrating peptides as efficient carriers. *Artif. Cells, Nanomedicine, Biotechnol.* **2015**, 1–5.

(20) Witte, K.; Olausson, B. E. S.; Walrant, A.; Alves, I. D.; Vogel, A. Structure and dynamics of the two amphipathic arginine-rich peptides RW9 and RL9 in a lipid environment investigated by solid-state NMR and MD simulations. *Biochim. Biophys. Acta - Biomembr.* **2013**, *1828* (2), 824–833.

(21) Pasupuleti, M.; Chalupka, A.; Mörgelin, M.; Schmidtchen, A.; Malmsten, M. Tryptophan end-tagging of antimicrobial peptides for increased potency against Pseudomonas aeruginosa. *Biochim. Biophys. Acta - Gen. Subj.* **2009**, *1790* (8), 800–808.

(22) Strömstedt, A. A.; Pasupuleti, M.; Schmidtchen, A.; Malmsten, M. Oligotryptophan-tagged antimicrobial peptides and the role of the cationic sequence. *Biochim. Biophys. Acta - Biomembr.* **2009**, *1788* (9), 1916–1923.

(23) Schmidtchen, A.; Pasupuleti, M.; Mörgelin, M.; Davoudi, M.; Alenfall, J.; Chalupka, A.; Malmsten, M. Boosting Antimicrobial Peptides by Hydrophobic Oligopeptide End Tags. *J. Biol. Chem.* **2009**, *284* (26), 17584–17594.

(24) Pasupuleti, M.; Schmidtchen, A.; Chalupka, A.; Ringstad, L.; Malmsten, M. End-Tagging of Ultra-Short Antimicrobial Peptides by W/F Stretches to Facilitate Bacterial Killing. *PLoS One* **2009**, *4* (4), e5285.

(25) Chan, D. I.; Prenner, E. J.; Vogel, H. J. Tryptophan- and arginine-rich antimicrobial peptides: Structures and mechanisms of action. *Biochim. Biophys. Acta - Biomembr.* **2006**, *1758* (9), 1184–1202.

(26) Derossi, D.; Joliot, A. H.; Chassaing, G.; Prochiantz, A. The third helix of the Antennapedia homeodomain translocates through biological membranes. *J. Biol. Chem.* **1994**, *269* (14), 10444–10450.

(27) Tezgel, A. Ö.; Jacobs, P.; Backlund, C. M.; Telfer, J. C.; Tew, G. N. Synthetic Protein Mimics for Functional Protein Delivery. *Biomacromolecules* **2017**, *18* (3), 819–825.

(28) Vezenkov, L. L.; Martin, V.; Bettache, N.; Simon, M.; Messerschmitt, A.; Legrand, B.; Bantignies, J.-L.; Subra, G.; Maynadier, M.; Bellet, V.; Garcia, M.; Martinez, J.; Amblard, M. Ribbon-like Foldamers for Cellular Uptake and Drug Delivery. *ChemBioChem* **2017**, *18* (21), 2110–2114.

(29) Cokca, C.; Zartner, L.; Tabujew, I.; Fischer, D.; Peneva, K. Incorporation of Indole Significantly Improves the Transfection Efficiency of Guanidinium-Containing Poly(Methacrylamide)s. *Macromol. Rapid Commun.* **2020**, *41* (6), 1900668.

(30) Backlund, C. M.; Sgolastra, F.; Otter, R.; Minter, L. M.; Takeuchi, T.; Futaki, S.; Tew, G. N. Increased hydrophobic block length of PTDMs promotes protein internalization. *Polym. Chem.* **2016**, *7* (48), 7514–7521.

(31) Jordan, E. T.; Collins, M.; Terefe, J.; Ugozzoli, L.; Rubio, T. Optimizing electroporation conditions in primary and other difficult-to-transfect cells. *J. Biomol. Tech.* **2008**, *19* (5), 328–334.

(32) Backlund, C. M.; Hango, C. R.; Minter, L. M.; Tew, G. N. Protein and Antibody Delivery into Difficult-to-Transfect Cells by Polymeric Peptide Mimics. *ACS Appl. Bio Mater.* **2020**, *3* (1), 180–185.

(33) Posey, N. D.; Hango, C. R.; Minter, L. M.; Tew, G. N. The Role of Cargo Binding Strength in Polymer-Mediated Intracellular Protein Delivery. *Bioconjug. Chem.* **2018**, *29* (8), 2679–2690.

(34) Guo, F.; Gopaul, D. N.; Van Duyne, G. D. Structure of Cre recombinase complexed with DNA in a site-specific recombination synapse. *Nature* **1997**, *389* (6646), 40–46.

(35) Takayama, K.; Hirose, H.; Tanaka, G.; Pujals, S.; Katayama, S.; Nakase, I.; Futaki, S. Effect of the Attachment of a Penetration Accelerating Sequence and the Influence of Hydrophobicity on Octaarginine-Mediated Intracellular Delivery. *Mol. Pharm.* **2012**, *9* (5), 1222–1230.

(36) Zhu, Z.; Tian, D.; Gao, P.; Wang, K.; Li, Y.; Shu, X.; Zhu, J.; Zhao, Q. Cell-Penetrating Peptides Transport Noncovalently Linked Thermally Activated Delayed Fluorescence Nanoparticles for Time-Resolved Luminescence Imaging. *J. Am. Chem. Soc.* **2018**, *140* (50), 17484–17491.

(37) Matsumoto, R.; Okochi, M.; Shimizu, K.; Kanie, K.; Kato, R.; Honda, H. Effects of the properties of short peptides conjugated with cell-penetrating peptides on their internalization into cells. *Sci. Rep.* **2015**, *5* (1), 12884.

(38) Jiang, T.; Zhang, Z.; Zhang, Y.; Lv, H.; Zhou, J.; Li, C.; Hou, L.; Zhang, Q. Dual-functional liposomes based on pH-responsive cell-penetrating peptide and hyaluronic acid for tumor-targeted anticancer drug delivery. *Biomaterials* **2012**, *33* (36), 9246–9258.

(39) Yoo, J.; Sanoj Rejinold, N.; Lee, D.; Jon, S.; Kim, Y.-C. Protease-activatable cell-penetrating peptide possessing ROS-triggered phase transition for enhanced cancer therapy. *J. Control. Release* **2017**, *264*, 89–101.

(40) Holowka, E. P.; Pochan, D. J.; Deming, T. J. Charged Polypeptide Vesicles with Controllable Diameter. *J. Am. Chem. Soc.* **2005**, *127* (35), 12423–12428.

(41) Hanson, J. A.; Chang, C. B.; Graves, S. M.; Li, Z.; Mason, T. G.; Deming, T. J. Nanoscale double emulsions stabilized by single-component block copolypeptides. *Nature* **2008**, *455* (7209), 85–88.

(42) Holowka, E. P.; Sun, V. Z.; Kamei, D. T.; Deming, T. J. Polyarginine segments in block copolypeptides drive both vesicular assembly and intracellular delivery. *Nat. Mater.* **2007**, *6* (1), 52–57.

(43) Sun, J.; Chen, X.; Deng, C.; Yu, H.; Xie, Z.; Jing, X. Direct Formation of Giant Vesicles from Synthetic Polypeptides. *Langmuir* **2007**, *23* (16), 8308–8315.

(44) Rodriguez, A. R.; Choe, U.-J.; Kamei, D. T.; Deming, T. J. Blending of Diblock and Triblock Copolypeptide Amphiphiles Yields Cell Penetrating Vesicles with Low Toxicity. *Macromol. Biosci.* **2015**, *15* (1), 90–97.

(45) Song, S. J.; Lee, S.; Ryu, K.-S.; Choi, J. S. Amphiphilic Peptide Nanorods Based on Oligo-Phenylalanine as a Biocompatible Drug Carrier. *Bioconjug. Chem.* **2017**, *28* (9), 2266–2276.

(46) Bechinger, B. Membrane Insertion and Orientation of Polyalanine Peptides: A ^{15}N Solid-State NMR Spectroscopy Investigation. *Biophys. J.* **2001**, *81* (4), 2251–2256.

(47) Chung, L. A.; Thompson, T. E. Design of Membrane-Inserting Peptides: Spectroscopic Characterization with and without Lipid Bilayers. *Biochemistry* **1996**, *35* (35), 11343–11354.

(48) Love, J. A.; Morgan, J. P.; Trnka, T. M.; Grubbs, R. H. A Practical and Highly Active Ruthenium-Based Catalyst that Effects the Cross Metathesis of Acrylonitrile. *Angew. Chemie Int. Ed.* **2002**, *41* (21), 4035–4037.

(49) Kozlowski, L. P. IPC – Isoelectric Point Calculator. *Biol. Direct* **2016**, *11* (1), 55.

(50) Backlund, C. M.; Takeuchi, T.; Futaki, S.; Tew, G. N. Relating structure and internalization for ROMP-based protein mimics. *Biochim. Biophys. Acta - Biomembr.* **2016**, *1858* (7), 1443–1450.

(51) Lienkamp, K.; Madkour, A. E.; Musante, A.; Nelson, C. F.; Nüsslein, K.; Tew, G. N. Antimicrobial Polymers Prepared by ROMP with Unprecedented Selectivity: A Molecular Construction Kit Approach. *J. Am. Chem. Soc.* **2008**, *130* (30), 9836–9843.

(52) Gill, S. C.; von Hippel, P. H. Calculation of protein extinction coefficients from amino acid sequence data. *Anal. Biochem.* **1989**, *182* (2), 319–326.

(53) Sgolastra, F.; Backlund, C. M.; Ilker Ozay, E.; deRonde, B. M.; Minter, L. M.; Tew, G. N. Sequence segregation improves non-covalent protein delivery. *J. Control. Release* **2017**, *254*, 131–136.

(54) McNaughton, B. R.; Cronican, J. J.; Thompson, D. B.; Liu, D. R. Mammalian cell penetration, siRNA transfection, and DNA transfection by supercharged proteins. *Proc. Natl. Acad. Sci.* **2009**, *106* (15), 6111–6116.

(55) Magenau, A. J. D.; Richards, J. A.; Pasquinelli, M. A.; Savin, D. A.; Mathers, R. T. Systematic Insights from Medicinal Chemistry To Discern the Nature of Polymer Hydrophobicity. *Macromolecules* **2015**, *48* (19), 7230–7236.

(56) Hamilton, J. G. The determination and interpretation of tacticity in ring-opening metathesis polymerization. *Polymer* **1998**, *39* (8–9), 1669–1689.

(57) Chang, A. B.; Miyake, G. M.; Grubbs, R. H. Sequence-Controlled Polymers by Ruthenium-Mediated Ring-Opening Metathesis Polymerization. *ACS Symp. Ser.* **2014**, *1170*, 161–188.

(58) Som, A.; Tezgel, A. Ö.; Gabriel, G. J.; Tew, G. N. Self-Activation in De Novo Designed Mimics of Cell-Penetrating Peptides. *Angew. Chemie Int. Ed.* **2011**, *50* (27), 6147–6150.

(59) Ilker, M. F.; Nüsslein, K.; Tew, G. N.; Coughlin, E. B. Tuning the Hemolytic and Antibacterial Activities of Amphiphilic Polynorbornene Derivatives. *J. Am. Chem. Soc.* **2004**, *126* (48), 15870–15875.

(60) Schmidt, N. W.; Lis, M.; Zhao, K.; Lai, G. H.; Alexandrova, A. N.; Tew, G. N.; Wong, G. C. L. Molecular Basis for Nanoscopic Membrane Curvature Generation from Quantum Mechanical Models and Synthetic Transporter Sequences. *J. Am. Chem. Soc.* **2012**, *134* (46), 19207–19216.

(61) Wender, P. A.; Mitchell, D. J.; Pattabiraman, K.; Pelkey, E. T.; Steinman, L.; Rothbard, J. B. The design, synthesis, and evaluation of molecules that enable or enhance cellular uptake: Peptoid molecular transporters. *Proc. Natl. Acad. Sci.* **2000**, *97* (24), 13003–13008.

(62) Selby, L. I.; Kongkatigumjorn, N.; Such, G. K.; Johnston, A. P. R. HD Flow Cytometry: An Improved Way to Quantify Cellular Interactions with Nanoparticles. *Adv. Healthc. Mater.* **2016**, *5* (18), 2333–2338.

(63) Moloney, M.; Shreffler, W. G. Basic science for the practicing physician: flow cytometry and cell sorting. *Ann. Allergy, Asthma Immunol.* **2008**, *101* (5), 544–549.

(64) Lampariello, F. Ratio analysis of cumulatives for labeled cell quantification from immunofluorescence histograms derived from cells expressing low antigen levels. *Cytom. Part A* **2009**, *75A* (8), 665–674.

(65) Mulgrew-Nesbitt, A.; Diraviyam, K.; Wang, J.; Singh, S.; Murray, P.; Li, Z.; Rogers, L.; Mirkovic, N.; Murray, D. The role of electrostatics in protein–membrane interactions. *Biochim. Biophys. Acta - Mol. Cell Biol. Lipids* **2006**, *1761* (8), 812–826.

(66) Gump, J. M.; June, R. K.; Dowdy, S. F. Revised Role of Glycosaminoglycans in TAT Protein Transduction Domain-mediated Cellular Transduction. *J. Biol. Chem.* **2010**, *285* (2), 1500–1507.

(67) Wadia, J. S.; Stan, R. V; Dowdy, S. F. Transducible TAT-HA fusogenic peptide enhances escape of TAT-fusion proteins after lipid raft macropinocytosis. *Nat. Med.* **2004**, *10* (3), 310–315.

(68) Kurzawa, L.; Pellerano, M.; Morris, M. C. PEP and CADY-mediated delivery of fluorescent peptides and proteins into living cells. *Biochim. Biophys. Acta - Biomembr.* **2010**, *1798* (12), 2274–2285.

(69) deRonde, B. M.; Posey, N. D.; Otter, R.; Caffrey, L. M.; Minter, L. M.; Tew, G. N. Optimal Hydrophobicity in Ring-Opening Metathesis Polymerization-Based Protein Mimics Required for siRNA Internalization. *Biomacromolecules* **2016**, *17* (6), 1969–1977.

(70) Martin, L.; Peltier, R.; Kuroki, A.; Town, J. S.; Perrier, S. Investigating Cell Uptake of Guanidinium-Rich RAFT Polymers: Impact of Comonomer and Monomer Distribution. *Biomacromolecules* **2018**, *19* (8), 3190–3200.

(71) Posey, N. D.; Tew, G. N. Protein Transduction Domain Mimic (PTDM) Self-Assembly? *Polymers* **2018**, *10* (9), 1039.

CHAPTER 4

4 INCREASED BLOCK COPOLYMER LENGTH IMPROVES INTRACELLULAR AVAILABILITY OF PROTEIN CARGO

NOTE: Polymers used in this chapter were prepared with the help of Hazel C. Davis, Leah M. Caffrey, and Brittany M. deRonde. Optimization of delivery conditions was done with the help of Esha A. Uddin. Binding assays and dynamic light scattering were performed by Hazel C. Davis.

4.1 Introduction

4.1.1 Summary

Amphiphilic protein transduction domain mimics (PTDMs) of various lengths were studied for their abilities to non-covalently deliver proteins into Jurkat T cells. While shorter PTDMs facilitated greater EGFP and IgG internalization, longer block copolymers promoted heightened activity of Cre recombinase post-delivery. Notably, the highest molecular weight PTDM facilitated robust gene recombination even at exceptionally low concentrations (approximately one polymer molecule per protein). Dynamic light scattering revealed that longer polymers formed considerably smaller nanoparticles upon protein complexation. Moreover, while increasing the carrier to cargo ratio produced larger aggregates for short PTDMs (up to a micron in diameter), an eight-fold increase in ratio yielded no change in nanoparticle size for the longest amphiphile, implying a fundamentally different mechanism of assembly. The greater intracellular cargo availability exhibited by these markedly smaller nanoparticles implies that limiting complex size may be more beneficial than simply boosting cargo internalization. The structural and dimensional differences in these polymer-protein complexes likely influence

cargo protection, cellular uptake mechanism, intracellular trafficking, or dissociation kinetics, all of which are critical to on-target, functional delivery.

4.1.2 Background

Formation of polymer-protein complexes via non-covalent interactions offers distinct advantages over covalent carrier-cargo attachment. In particular, such assemblies can be formed via a simple mixing step, analogous to polyplex formation in nucleic acid delivery, which circumvents the need for laborious coupling and purification steps.[1–3] Moreover, polymer-protein conjugation must typically be performed under mild aqueous conditions, greatly limiting the available synthetic routes, and frequently leads to substantial reduction in protein activity.[1,4–7] Owing to the immense heterogeneity in composition, structure, and stability of proteins, successful strategies for conjugate preparation are also challenging to broadly apply to other protein cargoes. In contrast, non-covalent delivery offers flexibility in that carriers and cargoes can be easily substituted or combined in any proportion, enabling rapid screening of libraries for elucidation of structure-activity relationships. Polymer-protein complexes are distinct from other polymer nanoparticle systems, such as those employing carrier self-assembly (e.g., polymeric micelles and polymersomes) or physical methods (e.g., nanoprecipitation and emulsions) to produce delivery vehicles. Instead, complexation is induced by strong carrier-cargo associations, including electrostatic, hydrophobic, and hydrogen bonding interactions.[2,8] Although the homogenous, colloidal aggregates formed by non-covalent complexation lack the precise order that is characteristic of self-assembling carrier systems, a wider range of macromolecular structures can be employed, given that ability to self-assemble is not a requirement.

While a number of natural and synthetic polymeric carriers have been reported to deliver proteins via complexation, optimization has focused largely on chemical modifications rather degree of polymerization (DP).[3,9,10] Prominent examples in which DP has been explicitly modulated in the context of protein complexation and delivery have primarily focused on cationic homopolymers of chitosan[11–16] and polyethylenimine (PEI)[17,18] complexed with model proteins, such as bovine serum albumin (BSA), human serum albumin (HSA), and insulin. The cationic nature of both chitosan and PEI enables strong interactions with anionic cargoes and cellular membranes, making them highly popular choices for a range of delivery applications. Although not applied to intracellular delivery, the effect of molecular weight on BSA and HSA complexation by poly(ethylene glycol) (PEG), modified to contain hydrophobic end groups, has also been investigated.[19] Altogether, these studies have explored polymer-protein binding, complex size, complex stability, protein release, and retention of protein structure and activity as a function of polymer DP. Though results were sometimes conflicting, longer polymers generally appeared to strengthen carrier-cargo interactions and retard protein release at the cost of increasingly altered protein conformation.[11,13–15,18,19] The effects of DP on block copolymer-protein complexation are severely understudied. Block copolymers typically combine disparate chemical properties, resulting in fundamentally different interactions with both proteins and lipid membranes. In particular, lengthening amphiphilic block copolymers would be expected to increase their surfactant-like character, potentially giving rise to self-assembly, cargo denaturation, enhanced endosomal escape, or increased cellular toxicity.[20–24]

Our group has developed a library of synthetic guanidine-rich polymers known as protein transduction domain mimics (PTDMs) which resemble the membrane-transducing peptide sequences found in HIV-1 Tat and Antennapedia.[25–29] The effects of DP and charge density on siRNA delivery have been thoroughly explored using both cationic homopolymers and cationic-hydrophobic block copolymers, however, such optimization has thus far not been extended to protein delivery.[30–32] To date, ring-opening metathesis polymerization-based PTDMs have been used at a maximum length of just 20 repeat units with protein cargoes.[33,34]

Block copolymer PTDMs have consistently outperformed their homopolymer counterparts for protein delivery, likely due to insufficient hydrophobicity and poor cargo binding of homopolymers (demonstrated in Chapter 3).[33,35,36] However, as with the aforementioned carriers, homopolymer chain extension might be expected to enhance carrier-cargo binding, preserve native protein structure, and ultimately boost internalization. Likewise, given that variation in cationic charge density of chitosan altered protein encapsulation efficiency in one study, there is motivation to modulate this parameter in PTDMs as well.[15] Accordingly, EGFP delivery has been explored here using PTDMs comprising 20-60 repeat units with charge densities of one or two guanidine groups per monomer (7-22 kDa and 12-35 kDa in size, respectively). Past optimization of block copolymers indicated that incorporation of hydrophobic and hydrophilic monomers at a 2:1 ratio maximizes both protein internalization and function.[34,37] Additionally, PTDMs constructed from a hydrophobic monomer featuring methyl and phenyl substituents (**MePh**) and a cationic monomer containing two guanidine groups (**dG**) have demonstrated robust delivery of several functional proteins, including antibodies and

enzymes.[37–41] Thus, these carriers were synthesized with DPs of 15-120 (6-46 kDa in size), at a consistent 2:1 ratio of **MePh** to **dG**. This series of block copolymers has been used here to deliver EGFP, IgG, and Cre recombinase to elucidate the impact of molecular weight on both internalization and protein activity.

4.2 Materials and Methods

4.2.1 Materials

4.2.1.1 Synthesis

Chemicals and solvents were obtained as reagent grade from Millipore Sigma, Alfa Aesar, Fisher Scientific, Fluka, BDH, or Acros Organics and used as received unless otherwise noted. Grubbs 3rd generation catalyst (Dichloro-di(3-bromopyridino)-N,N'-Dimesitylenoimidazolino-Ru=CHPh; G3) was synthesized as described previously.[42] Deuterated NMR solvents were obtained from Cambridge Isotope Laboratories. Polymers were dialyzed using Spectra/Por® dialysis membranes with molecular weight cutoffs (MWCOs) ranging from 0.5-1 kDa.

4.2.1.2 Protein Cargoes

Recombinant enhanced green fluorescent protein (EGFP) with both an N-terminal and a C-terminal 6XHis tag was purchased from BioVision (product code 4999), reconstituted to a concentration of 1 mg/mL in 1x PBS, and stored at -20 ºC, per manufacturer recommendations. Cross-adsorbed goat anti-rabbit immunoglobulin G, fluorescently labelled with Alexa Fluor 488 (herein referred to as "IgG-AF488"), was purchased from ThermoFisher Scientific (product number A-11008) and stored in the dark

at 4 ºC upon receipt, per manufacturer recommendations. Bovine serum albumin fluorescently labelled with fluorescein isothiocyanate (herein referred to as "BSA-FITC") was purchased from Millipore Sigma (product number A9771) and stored in the dark at 4 ºC upon receipt, per manufacturer recommendations. Unlabeled immunoglobulin G from goat serum (herein referred to as "IgG") was purchased from Millipore Sigma (product number I5256) and stored at 4 ºC upon receipt, per manufacturer recommendations. Recombinant Cre recombinase with an N-terminal 6XHis tag and NLS sequence (PKKKRKV) was purchased from Excellgen (HNC form, old product code RP-7, new product code EG-1067) and stored at -20 ºC, per manufacturer recommendations.

4.2.1.3 Reporter Jurkat T Cell Line

The Jurkat reporter cell line (herein referred to as "Jurkat-GFP") was created by stably transfecting Jurkat T cells with the pWPT-GFP plasmid. pWPT-GFP was a gift from Didier Trono (Addgene plasmid # 12255; http://n2t.net/addgene:12255; RRID:Addgene_12255). A single cell containing one copy of the *EGFP* gene was then identified, isolated, and expanded to create the monoclonal cell line used for Cre delivery.

4.2.1.4 Cell Culture Reagents

Jurkat T cells and the modified Jurkat-GFP cell line were cultured in Gibco™ RPMI 1640 High Glucose GlutaMAX™ Supplement (Thermo Fisher Scientific), supplemented with 10% (v/v) EquaFETAL (Atlas Biologicals), 1% (v/v) 100 mM Sodium Pyruvate Solution (Lonza) or 100 mM HyClone™ Sodium Pyruvate Solution (Fisher Scientific), 1% (v/v) 100x MEM Non-Essential Amino Acid Solution (Lonza) or 100x HyClone™ Non-Essential Amino Acids NEAA (Fisher Scientific), 1% (v/v) HEPES (1

M) (Thermo Fisher Scientific), and 1% (v/v) Penicillin-Streptomycin Mixture (10K/10K) (Lonza). Serum-free RPMI was formulated in the same manner, withholding the 10% EquaFETAL. Gibco™ 10X phosphate-buffered saline (PBS), pH 7.4 was diluted to 1X prior to use. The embryonic mouse hippocampal-18 (mHippoE) cell line was cultured in Gibco™ DMEM High Glucose GlutaMAX™ Supplement (Thermo Fisher Scientific), supplemented with 10% (v/v) FBS or EquaFETAL (Atlas Biologicals), 1% (v/v) 100 mM Sodium Pyruvate Solution (Lonza) or 100 mM HyClone™ Sodium Pyruvate Solution (Fisher Scientific), 1% (v/v) 100x MEM Non-Essential Amino Acid Solution (Lonza) or 100x HyClone™ Non-Essential Amino Acids NEAA (Fisher Scientific), and 1% (v/v) Penicillin-Streptomycin Mixture (10LK/10K) (Lonza). Heparin sodium salt from porcine intestinal mucosa (≥100 IU/mg) (Alfa Aesar/VWR) was used to remove extracellular complexes from the cell surfaces. 7-aminoactinomycin D (7-AAD) Staining Solution (BD Biosciences/Fisher Scientific) was used to assess cellular viability in flow cytometry experiments. Bovine serum albumin, standard heat shock (Rocky Mountain Biologicals, Inc.) was used in FACS buffer preparation.

4.2.2 Instrumentation and Software

^{1}H nuclear magnetic resonance spectra were recorded for all monomers and polymers at 500 MHz using a Bruker Ascend Nuclear Magnetic Resonance Spectrometer retrofitted with a cryoprobe. Chemical shifts (δ) are listed in ppm and coupling constants (*J*) in Hz. Splitting patterns were described as either s, singlet; d, doublet; dd, doublet of doublets; t, triplet; tt triplet of triplets; dt, doublet of triplets; q, quartet; or m, multiplet; or br, broad. Analysis of NMR spectra was performed using MestReNova v. 6.1.0-6224 (Mestrelab Research).

Gel permeation chromatography (GPC) chromatograms were recorded for all polymers using an Agilent Technologies 1260 Infinity series system equipped with refractive index (RI) and ultraviolet (UV) detectors, a PL Gel 5 μm guard column, two PL Gel 5 μm analytical Mixed-C columns, and a PL Gel 5 μm analytical Mixed-D column. These columns were connected in series and incubated at 40 ºC. THF was used as the eluent at a flow rate of 1 mL/min. Toluene was used as the flow marker. The instrument was calibrated with both poly(methyl methacrylate) and polystyrene standards. All samples were prepared at ~3 mg/mL and filtered into Agilent Technologies autosampler vials using 0.45 μm PTFE syringe filters prior to injection.

Flow cytometry experiments were conducted using a BD Dual LSRFortessa™ flow cytometer and FACSDiva acquisition software. EGFP, AF488, and 7-AAD were all excited with a 488 nm laser. Fluorescence emission was collected using 530/30 (for EGFP and 7-AAD) and 710/50 band pass filters. Fluorescence signals were recorded for 10,000 cells in all samples. Analysis was performed using FlowJo v. 10.0.7r2 (Tree Star).

Fluorescence data for equilibrium binding assays were collected using a BioTek Instruments Synergy Mx plate reader and Gen5 1.10 acquisition software. Samples were measured at 25 °C in Ultra Cruz 96 well sterile poly(styrene) black tissue culture plates with clear flat bottoms purchased from Santa Cruz Biotechnology, Inc.

Dynamic light scattering experiments were conducted using a Malvern Instruments Zetasizer Nano Series Nano-ZS and Zetasizer software (v. 8.00.4813) for analysis. The standard operating procedure (SOP) used for all DLS experiments included the use of the instrument default “protein” as the material with a refractive index (RI) of 1.450 and

absorption of 0.001. The dispersant selected in the SOP was a "complex solvent", 1x PBS, (RI = 1.3317, viscosity = 0.9051 cP), where the primary component selected was water and the minor components consisted of sodium chloride (0.1551 M), sodium phosphate dibasic (0.0030 M), and potassium bicarbonate (0.0010 M) as a substitute for potassium phosphate monobasic, which was the actual component in the 1x PBS used. Measurement temperature was set at 25°C with an equilibration time of 120 seconds between measurements. The disposable cuvette option DTS0012 (for PTDM:IgG samples) or ZEN0040 (for PTDM:Cre samples) was also selected in the SOP. Light scattering was measured at a back-scattering angle of 173° with the number of runs per measurement set to automatic, 11 runs per measurement, and a run duration of 10 seconds. Each DLS trial consisted of 3 measurements. Finally, for data processing, the analysis model was a general purpose (normal resolution) model. Disposable polystyrene cuvettes with a volume capacity of 4.5 mL or 1.5 mL were purchased from Fisher Scientific. Poly(ethersulfone) (PES) syringe filters were purchased from the Restek Corporation.

4.2.3 Methods

4.2.3.1 Synthesis

The **PGON$_n$** and **dG$_n$** series of carriers studied have been previously characterized.[30,31] Although the **MePh$_{10}$-*b*-dG$_5$** carrier has also been reported previously, it was resynthesized for these studies. The following carriers are reported here for the first time: **MePh$_{20}$-*b*-dG$_{10}$**, **MePh$_{30}$-*b*-dG$_{15}$**, **MePh$_{40}$-*b*-dG$_{20}$**, and **MePh$_{80}$-*b*-dG$_{40}$**. Synthetic protocols and characterization data for the **MePh$_{2n}$-*b*-dG$_n$** series and its constituent monomers are detailed in the subsequent sections.

4.2.3.1.1 Monomer Synthesis

In general, the **dG** and **MePh** monomers were prepared following previously reported procedures.[43] A brief overview is provided here (Figure 4.1 and Figure 4.2).

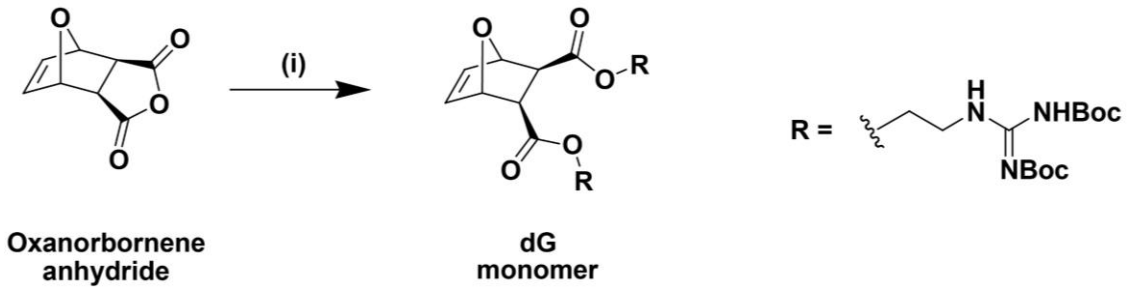

Figure 4.1: Synthesis of the symmetric **dG** monomer. (i) R-OH, DMAP, EDC, CH_2Cl_2, 0 °C to room temperature, overnight.

dG monomer: One molar equivalent of oxanorbornene anhydride, two molar equivalents of 1,3,-di-boc-2-(2-hydroxyethyl)guanidine, and 0.1 molar equivalents of DMAP were dissolved in freshly distilled CH_2Cl_2 dried over CaH_2 and stirred at room temperature under nitrogen. The solution was then cooled down to 0 °C in an ice bath and 1.2 molar equivalents of EDC were added. The solution was allowed to stir overnight under nitrogen and gradually return to room temperature. The diester product was isolated by normal phase flash chromatography using silica using a 70/30 (v/v) mixture of CH_2Cl_2/ethyl acetate (EtOAc) as the eluent. Pure fractions were combined and concentrated using rotary evaporation. The sample was dried under vacuum overnight at room temperature to obtain a white solid.

71% yield

^{1}H NMR (500 MHz, $CDCl_3$) δ 11.49 (br, 2H), 8.56 (br, 2H), 6.47 (br, 2H), 5.35 – 5.27 (m, 2H), 4.33 – 4.19 (m, 4H), 3.83 – 3.61 (m, 4H), 2.85 (br, 2H), 1.69 – 1.39 (m, 36H).

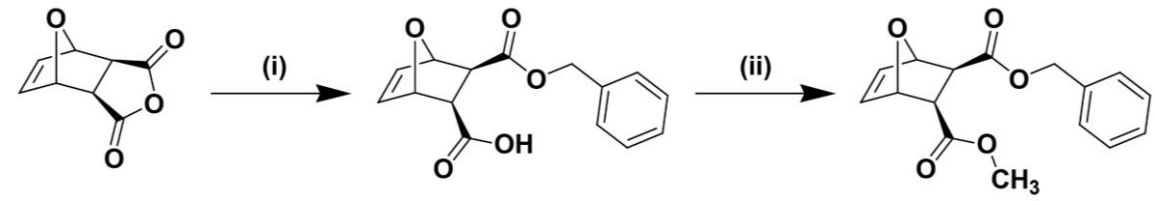

Figure 4.2: Synthesis of the asymmetric **MePh** monomer. (i) Methanol, DMAP, CH_2Cl_2, room temperature, overnight; (ii) benzyl alcohol, DMAP, EDC, CH_2Cl_2, 0 °C to room temperature, overnight.

Ph half ester: One molar equivalent of **oxanorbornene anhydride** and 0.1 molar equivalents of 4-dimethylaminopyridine (DMAP) were added to an oven dried two-neck round bottom flask under nitrogen gas and dissolved in sufficient freshly distilled CH_2Cl_2 dried over CaH_2. One molar equivalent of benzyl alcohol was added via syringe. The reaction was stirred overnight under nitrogen at room temperature. As the half ester product formed, it precipitated out overnight. The precipitate was isolated by vacuum filtration, washing with cold CH_2Cl_2, and then dried under vacuum.

56% yield

^{1}H NMR (500 MHz, DMSO) δ 12.45 (s, 1H), 7.41 – 7.28 (m, 5H), 6.50 – 6.42 (m, 2H), 5.11 (d, J = 5.8 Hz, 2H), 5.08 – 4.91 (m, 2H), 2.81 – 2.73 (m, 2H).

MePh monomer: One molar equivalent of the **Ph half ester** and 0.1 molar equivalents of DMAP were added to an oven dried two-neck round bottom flask under nitrogen gas and dissolved in sufficient freshly distilled CH_2Cl_2 dried over CaH_2. One molar equivalent of methanol was added via syringe. The solution was then cooled down to 0 °C in an ice bath and 1.2 molar equivalents of 1-ethyl-3-(3-dimethylaminopropyl)carbodiimide (EDC) were added. The solution was allowed to stir overnight under nitrogen and gradually return to room temperature. The diester product was isolated by normal phase flash chromatography

with silica using a 90/10 (v/v) mixture ofCH_2Cl_2/EtOAc as the eluent. Pure fractions were combined and concentrated using rotary evaporation. The sample was dried under vacuum overnight at room temperature to obtain a white solid.

69% yield

^{1}H NMR (500 MHz, $CDCl_3$) δ 7.40 – 7.29 (m, 5H), 6.47 – 6.42 (m, 2H), 5.28 (d, *J* = 3.4 Hz, 2H), 5.18 – 5.10 (m, 2H), 3.55 (s, 3H), 2.88 – 2.79 (m, 2H).

4.2.3.1.2 Polymer Synthesis

All polymers were prepared according to previously reported procedures (Figure 4.3).[43]

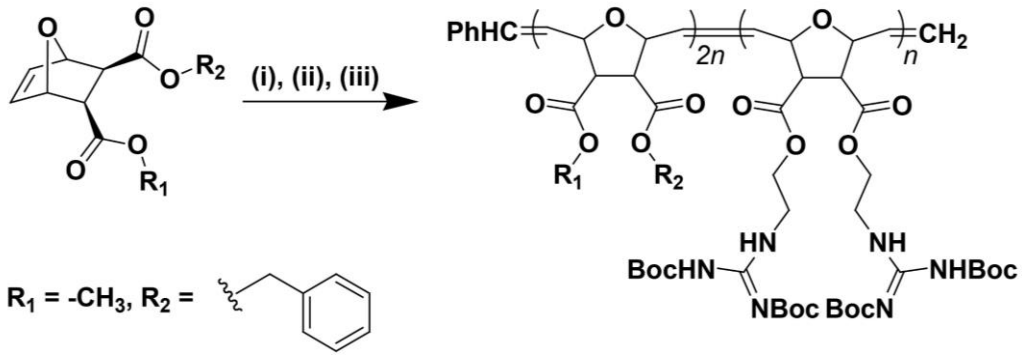

Figure 4.3: Synthesis of Boc-protected block copolymers used in Chapter 4. (i) G3, CH2Cl2, room temperature, 10 min; (ii) dG, CH2Cl2, room temperature, 90 min; (iii) ethyl vinyl ether, room temperature, overnight.

In brief, 1 molar equivalent of G3, 10-80 molar equivalents of the **MePh** monomer (depending on the target length of the hydrophobic block), and 5-40 molar equivalents of the **dG** monomer (depending on the target length of the cationic block) were each dissolved in separate oven dried Schlenk flasks using freshly distilled CH_2Cl_2 dried over CaH_2. The contents of all Schlenk flasks were put through a minimum of 3 freeze, pump, thaw (FPT) cycles to rigorously degas the monomer and catalyst solutions. After the final FPT cycle,

the contents of the flask containing the hydrophobic monomer were cannulated into the flask containing the stirring G3 solution. This monomer was allowed to polymerize for about 10 minutes, at which time a crude aliquot was taken and dried using compressed air for analysis by ^{1}H NMR and THF GPC. The NMR spectrum was used to confirm monomer consumption by a complete upfield shift of the alkene protons in the oxanorbornene-based monomer. The GPC chromatogram was used to calculate the molecular weight and dispersity of the hydrophobic block. The **dG** monomer was then cannulated into the G3 flask and allowed to polymerize for approximately 90 minutes. Upon completion, 2-3 mL of ethyl vinyl ether (EVE) was injected into the Schlenk flask to terminate the polymerization. A crude aliquot was taken at this point and dried using compressed air for analysis by ^{1}H NMR and THF GPC. As with the first aliquot, this NMR spectrum was used to confirm complete consumption of the second monomer. The GPC chromatogram was used to confirm successful chain extension by comparison with the first chromatogram. After stirring overnight with EVE, the crude reaction mixture was concentrated to a solid using rotary evaporation before it was redissolved in 1 mL of tetrahydrofuran (THF). This solution was then precipitated dropwise into cold, stirring pentane. The precipitated polymers in their Boc-protected forms were recovered using vacuum filtration and dried under high vacuum overnight, at which point they were again characterized by ^{1}H NMR and THF GPC. The final NMR spectrum was used to calculate the relative block composition using integrations of diagnostic peaks from each of the respective blocks (Table 4.1). For this analysis, the oxanorbornene backbone -CH protons at ~3.15-3.13 ppm were compared to the **dG** block -CH_2 protons at ~4.22-4.16 ppm. The

final GPC chromatogram was used to determine the molecular weight (MW) averages and dispersity (Đ) of each polymer, reported in Table 4.1.

Table 4.1: Characterization summary for PTDMs used in Chapter 4 based on ^{1}H NMR and THF GPC analysis.

Polymer	Block 1: Block 2[a]	Theoretical MW (kDa)[b]	M_p (kDa)[c]	M_n (kDa)[c]	M_w (kDa)[c]	Đ[c]
PGON$_{20}$[d]	--	9.11	11.2	9.56	10.5	1.1
PGON$_{40}$[d]	--	18.1	19.0	17.3	18.4	1.1
PGON$_{80}$[d]	--	36.1	44.2	34.4	38.4	1.1
dG$_{20}$[d]	--	15.2	13.5	12.7	13.4	1.1
dG$_{40}$[d]	--	30.3	30.5	23.6	27.2	1.2
dG$_{80}$[d]	--	60.5	71.0	50.2	59.2	1.2
MePh$_{10}$-*b*-dG$_5$	67:33	6.76	7.73	6.65	7.39	1.1
MePh$_{20}$-*b*-dG$_{10}$	69:31	13.4	15.4	12.4	14.2	1.1
MePh$_{30}$-*b*-dG$_{15}$	69:31	20.1	22.2	17.6	20.2	1.1
MePh$_{40}$-*b*-dG$_{20}$	68:32	26.7	27.3	23.0	25.1	1.1
MePh$_{80}$-*b*-dG$_{40}$	68:32	53.4	54.2	40.3	46.9	1.2

[a]Relative block incorporation as calculated by ^{1}H NMR. [b]Theoretical molecular weight based on polymer structure shown in Figure 4.3. [c]Calculated by GPC in THF, 40ºC, flow rate 1 mL/min with polystyrene (**PGON$_n$** and **MePh$_{2n}$-*b*-dG$_n$**) or poly(methyl methacrylate) (**dG$_n$**) standards and toluene as the flow marker. [d]Data summarized from previous reports.[30,31]

The ^{1}H NMR chemical shifts for each precipitated, Boc-protected polymer are below. Overlays of the intermediate and final GPC chromatograms taken for each polymer can be found in Figure 4.4, Figure 4.5, Figure 4.6, Figure 4.7, and Figure 4.8. An overlay of the final chromatograms for all block copolymers can be found in Figure 4.9.

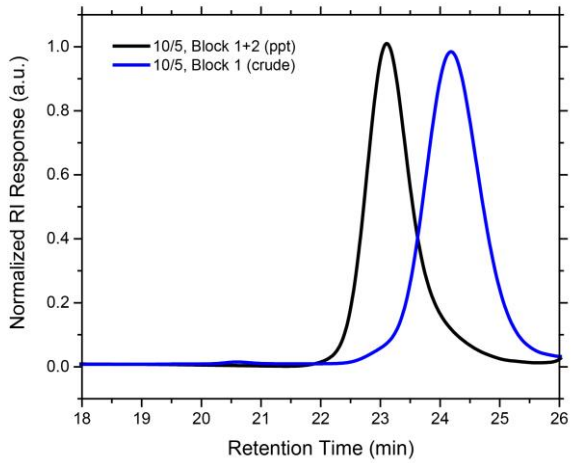

Figure 4.4: GPC traces illustrating the increase in molecular weight upon chain extension of the first block (containing just the **MePh** monomer) to create the Boc-protected copolymer (**MePh$_{10}$-*b*-dG$_5$**), shown here after purification by precipitation.

MePh$_{10}$-*b*-dG$_5$: ^{1}H NMR (500 MHz, CD_3CN) δ 11.52 (br, 2H), 8.35 (br, 2H), 7.34 (br, 10H), 5.84 (*trans*) and 5.59 (*cis*) (br, 6H total), 5.09 (br, 4H), 5.09 (*cis*) and 4.62 (*trans*) (br, 6H total), 4.22 (br, 4H), 3.55 (br, 4H), 3.47 (br, 6H), 3.13 (br, 6H), 1.47 (s, 18H), 1.41 (s, 18H).

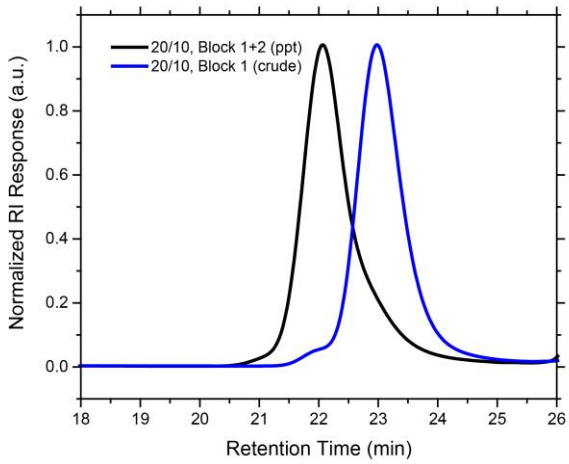

Figure 4.5: GPC traces illustrating the increase in molecular weight upon chain extension of the first block (containing just the **MePh** monomer) to create the Boc-protected copolymer (**MePh$_{20}$-*b*-dG$_{10}$**), shown here after purification by precipitation.

MePh$_{20}$-*b*-dG$_{10}$: ^{1}H NMR (500 MHz, CD_3CN) δ 11.53 (br, 2H), 8.35 (br, 2H), 7.33 (br, 10H), 5.84 (*trans*) and 5.58 (*cis*) (br, 6H total), 5.03 (br, 4H), 5.03 (*cis*) and 4.60 (*trans*) (6H total), 4.16 (br, 4H), 3.55 (br, 4H), 3.46 (br, 6H), 3.13 (br, 6H), 1.47 (s, 18H), 1.41 (s, 18H).

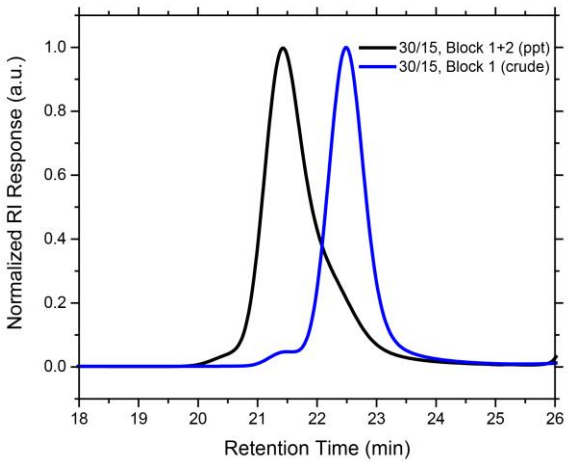

Figure 4.6: GPC traces illustrating the increase in molecular weight upon chain extension of the first block (containing just the **MePh** monomer) to create the Boc-protected copolymer (**MePh$_{30}$-*b*-dG$_{15}$**), shown here after purification by precipitation.

MePh$_{30}$-*b*-dG$_{15}$: ^{1}H NMR (500 MHz, CD_3CN) δ 11.53 (br, 2H), 8.35 (br, 2H), 7.33 (br, 10H), 5.83 (*trans*) and 5.58 (*cis*) (br, 6H total), 5.01 (br, 4H), 5.01 (*cis*) and 4.60 (*trans*) (br, 6H total), 4.16 (br, 4H), 3.55 (br, 4H), 3.46 (br, 6H), 3.13 (br, 6H), 1.47 (s, 18H), 1.41 (s, 18H).

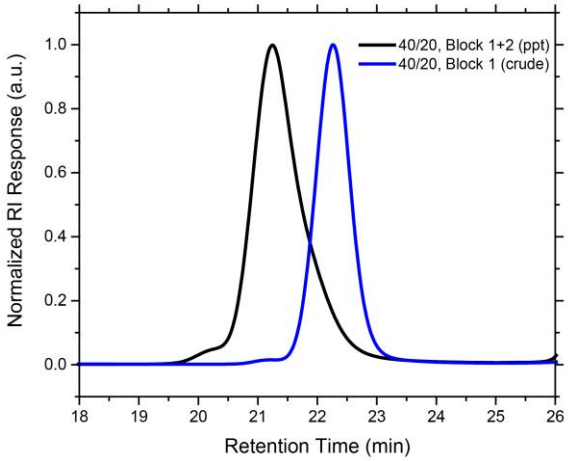

Figure 4.7: GPC traces illustrating the increase in molecular weight upon chain extension of the first block (containing just the **MePh** monomer) to create the Boc-protected copolymer (**MePh$_{40}$-*b*-dG$_{20}$**), shown here after purification by precipitation.

MePh$_{40}$-*b*-dG$_{20}$: ^{1}H NMR (500 MHz, CD_3CN) δ 11.53 (br, 2H), 8.35 (br, 2H), 7.33 (br, 10H), 5.83 (*trans*) and 5.58 (*cis*) (br, 6H total), 5.03 (br, 4H), 5.03 (*cis*) and 4.60 (*trans*) (br, 6H total), 4.17 (br, 4H), 3.55 (br, 4H), 3.46 (br, 6H), 3.13 (br, 6H), 1.47 (s, 18H), 1.41 (s, 18H).

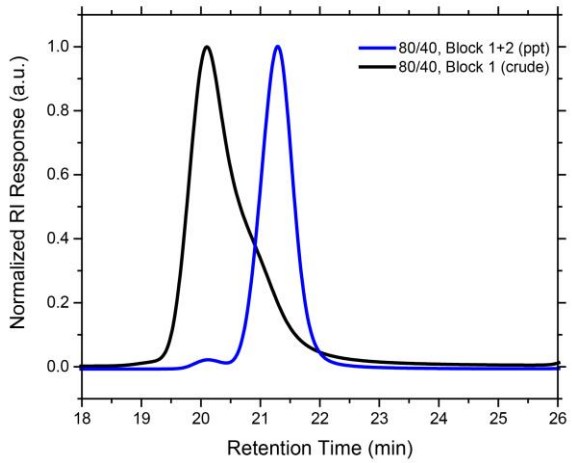

Figure 4.8: GPC traces illustrating the increase in molecular weight upon chain extension of the first block (containing just the **MePh** monomer) to create the Boc-protected copolymer (**MePh$_{80}$-*b*-dG$_{40}$**), shown here after purification by precipitation.

MePh$_{80}$-*b*-dG$_{40}$: ^{1}H NMR (500 MHz, CD_3CN) δ 11.53 (br, 2H), 8.35 (br, 2H), 7.33 (br, 10H), 5.84 (*trans*) and 5.58 (*cis*) (br, 6H total), 5.01 (br, 4H), 5.01 (*cis*) and 4.60 (*trans*) (br, 6H total), 4.17 (br, 4H), 3.61 (br, 4H), 3.46 (br, 6H), 3.15 (br, 6H), 1.48 (s, 18H), 1.42 (s, 18H).

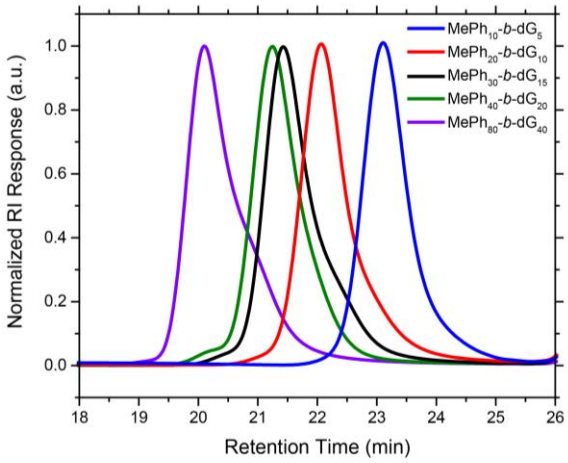

Figure 4.9: Overlay of all GPC traces for the purified, Boc-protected polymers in the **MePh$_{2n}$-*b*-dG$_n$** series, illustrating the differences in molecular weight distributions obtained.

4.2.3.1.3 Polymer Deprotection

To remove the Boc protecting groups, each polymer was dissolved in a 4 mL solution of 1:1 CH_2Cl_2:trifluoroacetic acid (TFA) and stirred in a scintillation vial overnight. The scintillation vials were then filled to halfway with methanol and concentrated using rotary evaporation. This process was repeated up to 7 times to remove traces of TFA by azeotropic distillation. The deprotected polymers were then dissolved in a minimal volume of methanol, diluted in approximately 10 mL of reverse osmosis (RO) water, and loaded into hydrated dialysis membrane tubing (MWCO = 500-1000 Da). All polymers were dialyzed against RO water until the conductivity of the solution outside the bag reached 0.3 μS or lower. Once dialysis was completed, polymer solutions were flash frozen in plastic cups by submerging them in liquid nitrogen. Frozen water was then removed by lyophilization *in vacuo* over the course of 3-5 days. ^{1}H NMR was used to

confirm complete removal of the Boc groups to yield the deprotected guanidinium functional groups.

4.2.3.2 Protein Delivery

4.2.3.2.1 Homopolymer-Mediated EGFP Delivery

EGFP delivery followed previously published protocols.[34–37,44–46] PTDMs were dissolved in DMSO to make 1 mM stock solutions and stored at -20 °C. Jurkat T cells were harvested on the day of the experiment and seeded in 12-well plates at a density of 4 x 10^5 cells/0.8 mL of fresh serum-containing RPMI (800 µL per well). Stock EGFP (1 mg/mL) was diluted 1:21 in 1X phosphate-buffered saline (PBS, pH ~7.4) to make a less concentrated working solution. Polymer stock solutions were diluted 1:20 in PBS to create working solutions of 50 µM. Polymer:protein complexes were prepared by combining appropriate volumes of PBS, EGFP, and PTDM (in that order) to achieve 200 µL solutions whose final delivery concentrations (after combining with the 0.8 mL cell solutions in a later step) were 60 nM EGFP and 1.2, 0.6, or 0.3 µM PTDM (*n* = 20 ,40, or 80, respectively). Resulting molar ratios of PTDM:protein were thus 20:1, 10:1, or 5:1, respectively. Inequal polymer:protein ratios were selected in order to maintain equivalent polymer repeat unit:protein ratios (400:1) across all samples, successfully isolating the effect of increased monomer connectivity on delivery. Thus, while molar concentration was varied based on PTDM DP, weight concentration remained at ~14 µg/mL **dG*n*** or ~0.9 µg/mL **PGON*n*** regardless of PTDM DP. The solutions were incubated in the dark at room temperature for 30 minutes to allow complexation, then added dropwise to each well containing cells, resulting in final delivery volumes of 1 mL. The cells were incubated

with the complexes for 4 h at 37 °C in 5% CO_2. After the incubation period, the cells were harvested, transferred to microcentrifuge tubes, collected by centrifugation for 5 min at 400 x g, and washed 3 times with 800 µL heparin (20 U/mL in PBS) to remove any extracellular or surface-bound complexes, in accordance with previously published procedures.[47] Cells were resuspended in 200 µL of FACS buffer (0.2% [w/w] bovine serum albumin in PBS) containing 2.5% (v/v) of 7-aminoactinomycin D (7-AAD) stain prior to internalization and viability analysis by flow cytometry, in which data for 10,000 cells were collected.

4.2.3.2.2 Block Copolymer-Mediated EGFP Delivery

Block copolymer-mediated EGFP delivery was performed in an identical manner to the above-described homopolymer-mediated EGFP delivery with the following modifications. Stock EGFP (1 mg/mL) was diluted 1:37 in PBS to achieve an appropriate working solution. Polymer stock solutions (1 mM) were diluted in 1:10 in PBS to achieve working solutions of 100 µM. Final delivery concentrations were 50 nM EGFP and 2, 0.5, or 0.25 µM PTDM (*2n*/*n* = 10/5, 40/20, and 80/40, respectively). Resulting molar ratios of PTDM:protein were thus 40:1, 10:1, and 5:1, respectively. Inequal polymer:protein ratios were selected in order to maintain equivalent polymer repeat unit:protein ratios (600:1) across all samples, successfully isolating the effect of increased monomer connectivity on delivery. Thus, while molar concentration was varied based on PTDM DP, weight concentration remained at ~12 µg/mL **MePh$_{2n}$-*b*-dG$_n$** regardless of PTDM DP.

4.2.3.2.3 Block Copolymer-Mediated IgG Delivery in Jurkat T Cells

Block copolymer-mediated IgG-AF488 delivery in Jurkat T cells was performed in an identical manner to the above-described homopolymer-mediated EGFP delivery

(substituting IgG for EGFP) with the following modifications. Stock IgG was received as 2 mg/mL and diluted 1:20 in PBS to make a working solution of 0.1 mg/mL. Polymer stock solutions (1 mM) were diluted 1:50 in PBS to make working solutions of 20 µM. Final delivery concentrations were 50 nM IgG-AF488 and 1, 0.5, 0.333, 0.25, or 0.125 µM PTDM (*2n*/*n* = 10/5, 20/10, 30/15, 40/20, and 80/40, respectively). Resulting molar ratios of PTDM:protein were thus 20:1, 10:1, 6.7:1, 5:1, and 2.5:1, respectively. Inequal polymer:protein ratios were selected in order to maintain equivalent polymer repeat unit:protein ratios (300:1) across all samples, successfully isolating the effect of increased monomer connectivity on delivery. Thus, while molar concentration was varied based on PTDM DP, weight concentration remained at ~6 µg/mL **MePh$_{2n}$-*b*-dG$_n$** regardless of PTDM DP.

4.2.3.2.4 Block Copolymer-Mediated IgG Delivery in mHippoE-18 Cells

Block copolymer-mediated IgG-AF488 delivery in mHippoE-18 cells was performed in an identical manner to the above-described homopolymer-mediated EGFP delivery (substituting IgG for EGFP) with the following modifications. mHippoE cells were harvested 24 h prior to the experiment and seeded in 12-well plates at a density of 7.5 x 10^4 cells/well. Stock IgG (2 mg/mL) was diluted 1:1000 in PBS to achieve a working concentration of 0.1 µM. Polymer stock solutions (1 mM) were serially diluted 1:10,000 in PBS to achieve 100 nM working concentrations. Final delivery concentrations were 1 nM IgG-AF488 and 5, 2.5, 1.667, or 1.25 nM PTDM (*2n*/*n* = 10/5, 20/10, 30/15, and 40/20, respectively). Resulting molar ratios of PTDM:protein were thus 5:1, 3:1, 2:1, and 1:.25:1, respectively. Inequal polymer:protein ratios were selected in order to maintain equivalent polymer repeat unit:protein ratios (75:1) across all samples, successfully isolating the effect

of increased monomer connectivity on delivery. Thus, while molar concentration was varied based on PTDM DP, weight concentration remained at ~29 pg/mL **MePh$_{2n}$-*b*-dG$_n$** regardless of PTDM DP. Immediately prior to treatment with the complexes, the medium was aspirated from each well and replaced with 800 µL of fresh, serum-containing DMEM. Following the incubation period, the medium was aspirated from each well, and the cells were rinsed with PBS, lifted with 0.25% trypsin-EDTA, diluted with DMEM (5x volume of trypsin), and collected by centrifugation for 5 min at 400 x g. After washing with heparin, cells were resuspended in 100% FACS buffer (viability was not assessed in these experiments).

4.2.3.2.5 Cre Delivery: PTDM Molecular Weight Comparison

Block copolymer-mediated Cre delivery in Jurkat-GFP cells was performed in an identical manner to the above-described homopolymer-mediated EGFP delivery (substituting Cre for EGFP) with the following modifications. Jurkat-GFP cells were seeded in a 24-well plates at a density of 2 x 10^5 cells/0.4 mL (400 µL total) of serum-free RPMI. Stock Cre was received as 60 µM and diluted 1:24 in PBS to achieve a working concentration of 2.5 µM. Polymer stock solutions (1 mM) were diluted 1:64 in PBS to create working solutions. Complexes were prepared in volumes of 100 µL (0.5 mL final delivery volume) with final delivery concentrations of 125 nM Cre and 0.625, 0.313, 0.208, 0.156, or 0.078 µM PTDM (*2n*/*n* = 10/5, 20/10, 30/15, 40/20, and 80/40, respectively). Resulting molar ratios of PTDM:protein were thus 5:1, 2.5:1, 1.667:1, 1.25:1, and 0.625:1, respectively. Inequal polymer:protein ratios were selected in order to maintain equivalent polymer repeat unit:protein ratios (75:1) across all samples, successfully isolating the effect of increased monomer connectivity on delivery. Thus, while molar concentration was

varied based on PTDM DP, weight concentration remained at 3.6 ng/mL **MePh$_{2n}$-*b*-dG$_n$** regardless of PTDM DP. Halfway through the 4h incubation of complexes with cells, 500 µL of serum-containing RPMI was added on top of wells to aid with cellular viability. At the end of the incubation, 10 µL was taken from each well, stained with trypan blue, and counted on a hemocytometer to assess cellular viability. The remainder of the sample was centrifuged for 5 min at 400 x g, resuspended in fresh serum-containing RPMI, and replated. The cells were cultured for 5 days, at which point they were harvested by centrifugation and washed once with PBS. Cells were then directly stained with 7-AAD to exclude dead cells from analysis during flow cytometry.

4.2.3.2.6 Cre Delivery: PTDM Molar Ratio Comparison

Block copolymer-mediated Cre delivery in Jurkat-GFP cells was performed in an identical manner to the above-described Cre molecular weight comparison experiment with the following modifications. **MePh$_{2n}$-*b*-dG$_n$** polymers were used at PTDM:Cre molar ratios of 0.625:1, 1.25:1, 2.5:1, and 5:1 (0.078, 0.156, 0.313, and 0.625 µM, respectively, for *2n*/*n* = 10/5, 20/10, 30/15, 40/20, and 80/40). These molar concentrations were selected such that the highest ratio (5:1) of **MePh$_{10}$-*b*-dG$_5$** had approximately the same weight concentration (~3.6 ng/mL) of polymer as the lowest ratio (0.625:1) of **MePh$_{80}$-*b*-dG$_{40}$**, as in the molecular weight comparison experiments.

4.2.3.3 Dynamic Light Scattering

Dynamic light scattering measurement procedures were adapted from a previously published report.[21] Prior to polymer:protein complexation, all microcentrifuge vials (used to prepare solutions) and cuvettes were rinsed 3 times with filtered methanol and allowed

to dry in a covered box that allowed for filtered air to pass through. Cuvettes and microcentrifuge vials were allowed to dry up to overnight to ensure complete drying and prevent dust accumulation.

Measurements were collected for solutions containing PTDM:protein complexes in 1x PBS. Protein concentrations were held constant at 50 nM and 125 nM for IgG and Cre, respectively. For experiments examining the effect of PTDM DP on complex size, **MePh$_{2n}$-*b*-dG$_n$** polymers were used at molar ratios of PTDM:IgG = 20:1, 10:1, 6.67:1, 5:1, and 2.5:1 and PTDM:Cre ratios = 5:1, 2.5:1, 1.67:1, 1.25:1, and 0.625:1 for $2n/n$ = 10/5, 20/10, 30/15, 40/20, and 80/40, respectively. For experiments examining the effect of PTDM:protein ratio on complex size, additional samples were prepared at molar ratios of PTDM:IgG = 2.5:1 and 20:1 for $2n/n$ = 10/5 and 80/40, respectively.

For IgG DLS samples, 1 mM stock solutions of PTDM were prepared by dissolving solid polymer in DMSO that had been filtered through 0.45 µM PES filters. 1x PBS was then filtered through 0.45 µM PES filters and subsequently used to prepare working solutions of both PTDM (10 µM) and protein. Appropriate volumes of PTDM and protein were then combined in 1.5 mL microcentrifuge tubes containing appropriate volumes of 1x PBS to achieve the final desired concentrations. Samples were mixed by gently pipetting up and down, incubated for 30 min at room temperature to allow complexes to form, and then carefully transferred to polystyrene cuvettes for analysis.

For Cre DLS samples, PTDM stock solutions were prepared in DMSO that had not been filtered previously, though filtered 1x PBS was used to create working solutions of both PTDM and Cre. Samples were prepared directly in cuvettes, mixed by gently

pipetting up and down, and then covered with a small slip of aluminum foil for 30 min prior to analysis.

It is important to note that the assumed RI value used in the SOP and absorbance of the material were used to convert the raw intensity-based size data to the number-based size data which have been reported in the main text. The distribution most closely related to the raw data is the intensity data, though the trends reported can be observed in either the intensity- or number-based analysis of particle size.

4.2.3.4 Fluorescence-Based Equilibrium Binding Assays

To isolate the effect of increasing PTDM degree of polymerization on protein binding, equilibrium fluorescence quenching assays were conducted according to previously published procedures using BSA-FITC as a model cargo.[35,44,45] These assays were conducted at 25 °C in 1x PBS at pH ~7.2, and the fluorescence of BSA-FITC was monitored and recorded as a function of increasing PTDM concentration from 0 to 8 μM (corresponding to ~ 47, 94, 140, and 186 mg/mL for the *2n*/*n* = 10/5, 20/10, 30/15, and 40/20 polymers, respectively). These experiments were conducted in a 96-well polystyrene plate, where each well had black opaque sides and flat clear bottoms. In general, each well in the titration was designed to contain 200 nM BSA-FITC, the appropriate carrier concentration, and PBS to reach a total volume of 200 μL. A stock solution of 1 mg/mL BSA-FITC in 1x PBS was prepared and used to prepare more dilute working solutions of dye-labelled protein. PTDM stock concentrations of 1 mM in pure DMSO were serially diluted in PBS to obtain working solutions of 100 μM (10% v/v DMSO) and 10 μM (1% v/v DMSO. Variable volumes from these working solutions were added to the wells such

that each subsequent well in the series contained an increasing final concentration of carrier. Since the use of different carrier stock solutions introduced DMSO in varying amounts, additional volumes of pure DMSO were added to each well such that all wells contained the same final concentration (v/v) of DMSO. Once all wells had received the appropriate volumes of PBS, BSA-FITC, DMSO, and PTDM, in that order, they were gently mixed by pipetting up and down and stirring with the tip of the pipet. The 96-well plate was incubated in the dark (covered by the plastic lid and under foil) at room temperature for 30 min to achieve equilibrium prior to fluorescence measurements. Samples were excited at 495 nm and emission was read at 523 nm with a BioTek Mx plate reader. During the binding experiments, the fluorescence intensity of each well in the titration was measured. The background fluorescence of a negative control (containing only PBS and the appropriate DMSO concentration) was first subtracted from these measurements. Next, the values were normalized by the fluorescence intensity of a positive control (containing only 200 nM BSA-FITC in PBS and the appropriate DMSO concentration) to yield a plot of normalized FITC fluorescence intensity vs. PTDM concentration. The binding experiments were repeated in triplicate for each PTDM. In certain cases, follow-up experiments consisting of three additional replicates at additional PTDM concentrations were performed in order to provide more data in critical regions of the binding curves.

4.3 Results and Discussion

4.3.1 PTDM Design

In an effort to isolate the effects of polymer length and charge density on protein delivery, homopolymers were synthesized with targeted DPs of 20, 40, and 80 repeat units and containing either one (poly[guanidinium oxanorbornene], or **PGON**) or two (diGuanidine, or **dG**) positive charges (Scheme 4.1). Given the well-established importance of hydrophobicity in non-covalent protein delivery, a series of block copolymers were synthesized consisting of a hydrophobic block (featuring methyl and phenyl substituents, or **MePh**) and a cationic block (**dG**).[1,33,35,36] These carriers were designed to contain a 2:1 ratio of hydrophobic to cationic repeat units (**MePh$_{2n}$-*b*-dG$_n$**) at DPs of 15, 30, 45, 60, and 120 (*2n*/*n* = 10/5, 20/10, 30/15, 40/20, and 80/40) to assess the impact of carrier length on both cargo uptake and biological activity.

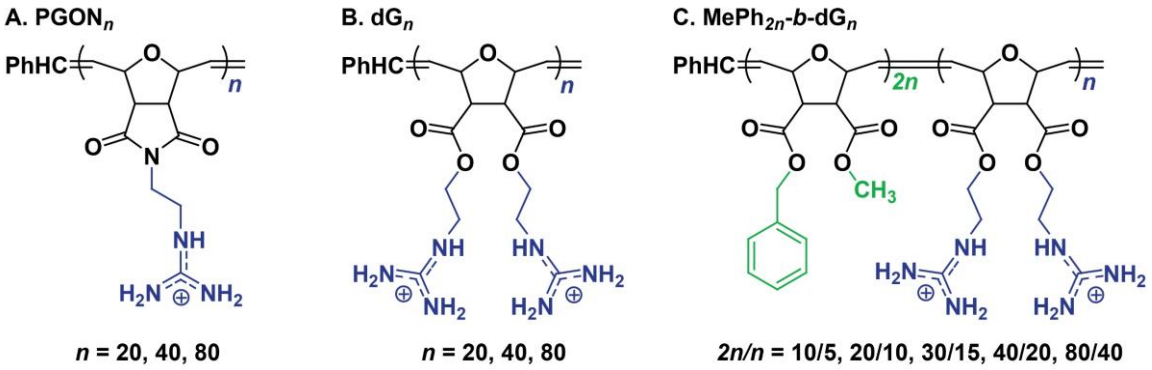

Scheme 4.1: Protein transduction domain mimic (PTDM) carriers selected for use in Chapter 4, comprising various charge densities, macromolecular architectures, and chain lengths. (A) Poly(guanidinium oxanorbornene) (**PGON$_n$**) homopolymers featuring one cationic charge per repeat unit. (B) Diguanidine (**dG$_n$**) homopolymers containing two cationic charges per repeat unit. (C) Block copolymers of hydrophobic (methyl/phenyl substituents, green) and cationic (guanidine substituents, blue) monomers incorporated at a constant 2:1 ratio (**MePh$_{2n}$-*b*-dG$_n$**). **PGON$_n$**, **dG$_n$**, and **MePh$_{2n}$-*b*-dG$_n$** homopolymers consisted of 20-80 repeat units (20-80 and 40-160 cationic charges per polymer for the **PGON$_n$** and **dG$_n$** series, respectively), while block copolymers were synthesized with 15-120 repeat units (10-80 cationic charges).

4.3.2 Impact of Homopolymer Length and Charge Density on Internalization

Homopolymers were complexed with 60 nM EGFP and incubated with Jurkat T cells for 4 hours to allow for cellular internalization (Figure 4.10). In much the same way

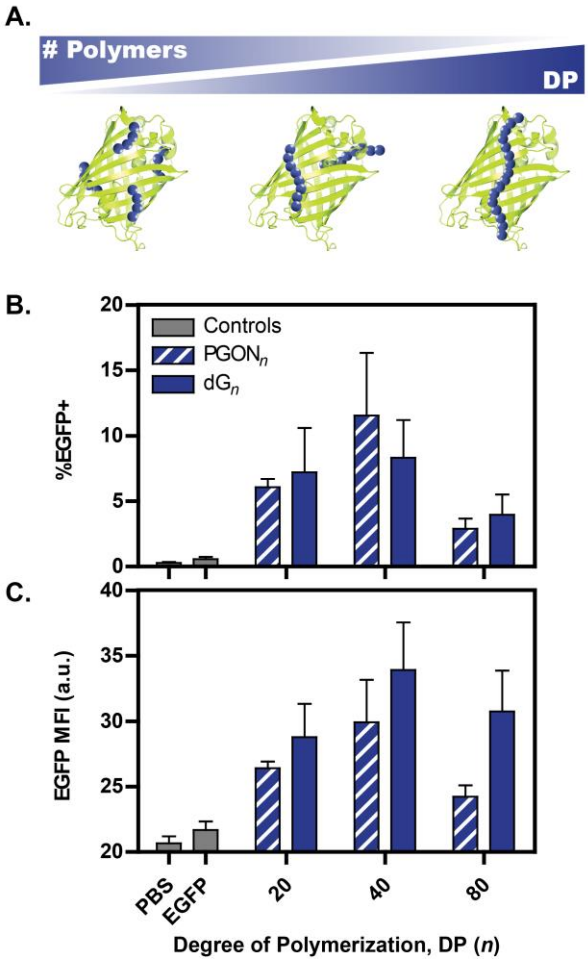

Figure 4.10: EGFP internalization in Jurkat T cells as a function of both homopolymer PTDM degree of polymerization (DP) and cationic charge density. (A) Illustration of the inverse relationship between DP and number of polymer molecules in the system given that the total number of polymer repeat units in the system is universally conserved. As shorter polymers are linked together to form longer ones, fewer independent chains remain, allowing for a direct assessment of the impact of monomer connectivity on delivery. The impact of charge density is observed by comparing polymers with one (hatched blue bars) and two (solid blue bars) charges per repeat unit at equal DPs (each pair of adjacent bars). EGFP internalization is quantified as (B) percentage of live cells positive for EGFP and (C) median fluorescence intensity (MFI) of the entire live-cell population. Data are displayed as the mean ± the standard error of the mean for four independent replicates of 10,000 cells each. Statistical analysis of the dataset was done by one-way ANOVA followed by a Tukey post-test. For all samples, p values were > 0.05 when compared to the PBS and EGFP controls (grey).

that N:P ratio is been held constant when optimizing the length of polymeric carriers for nucleic acid delivery, the ratio of polymer repeat units to protein molecules was maintained at 400:1 for all carriers.[30,32] As a result, the number of polymer chains in the system is decreased with increasing polymer length, effectively isolating the effect of monomer connectivity on carrier performance.

EGFP internalization was assessed by flow cytometry using two metrics: percentage of the cellular population positive for cargo in any quantity and median EGFP fluorescence intensity (MFI) of the population, a gauge of quantity delivered per cell. Not unlike past siRNA studies, both metrics suggested marginally better delivery with polymers of intermediate length, however, the differences here were insignificant owing to consistently poor internalization by all carriers. Likewise, charge density had no appreciable impact on delivery, suggesting that number of cations is perhaps less important for delivery of proteins than nucleic acids.[30]

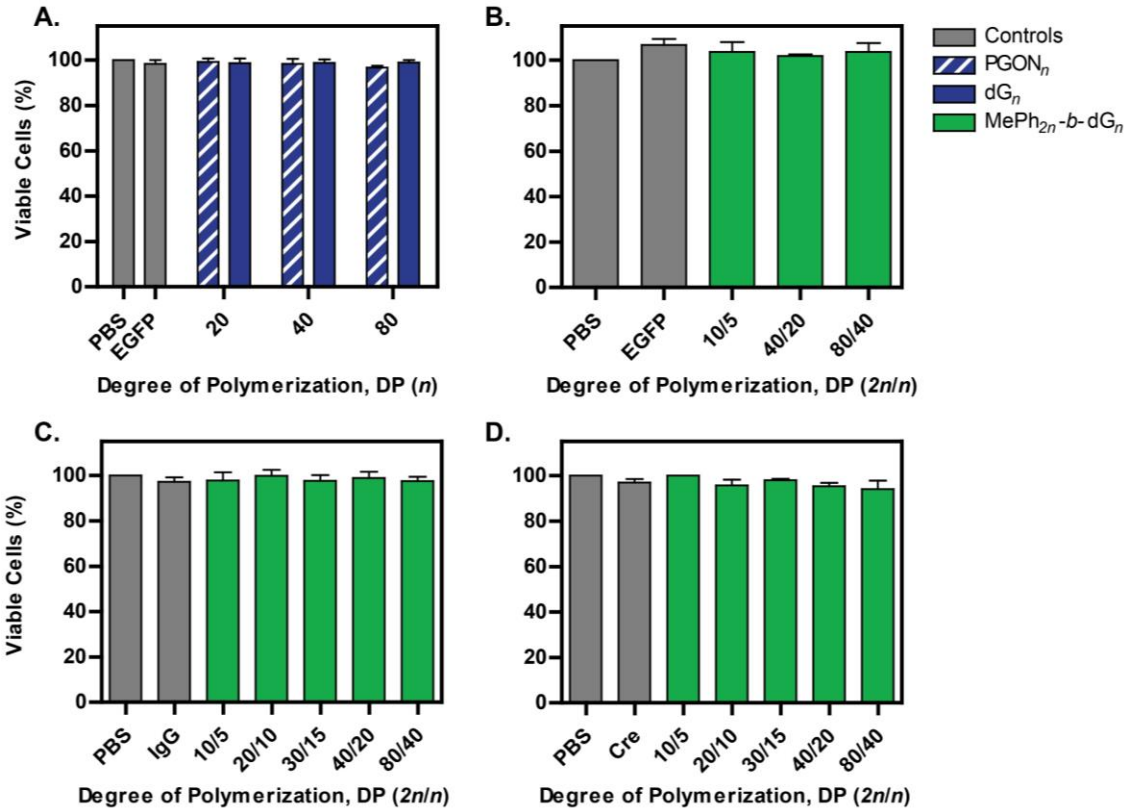

Figure 4.11: Cellular viability for EGFP (A-B), IgG (C), and Cre (D) delivery using PTDMs in the **PGON$_n$** (hatched blue bars), **dG$_n$** (solid blue bars), and **MePh$_{2n}$-*b*-dG$_n$** (solid green bars) series to accompany Figure 4.10, Figure 4.12, Figure 4.13, and Figure 4.15. Viability was determined by either 7-AAD (A-C) or trypan blue (D) staining immediately following delivery. 7-AAD data (A-C), obtained by flow cytometry, are displayed as the mean ± the standard error of the mean (SEM) for three (B) or four (A, C) independent replicates of 10,000 cells each. Trypan blue data (D), obtained by manual count with a hemocytometer, are displayed as the mean ± the SEM for three independent replicates. Statistical analyses of the datasets were done by one-way ANOVA followed by a Tukey post-test. For all samples, p values were > 0.05 when compared to their respective PBS and EGFP controls (grey).

7-AAD staining was used to assess viability following homopolymer-mediated EGFP delivery to Jurkat T cells (as well as for all other delivery experiments in Jurkat and Jurkat-GFP cell lines). Experiments for which no significant cellular toxicity was observed for any of the experimental conditions is presented here (Figure 4.11). Viability for the final experiment is presented alongside delivery data (Figure 4.16).

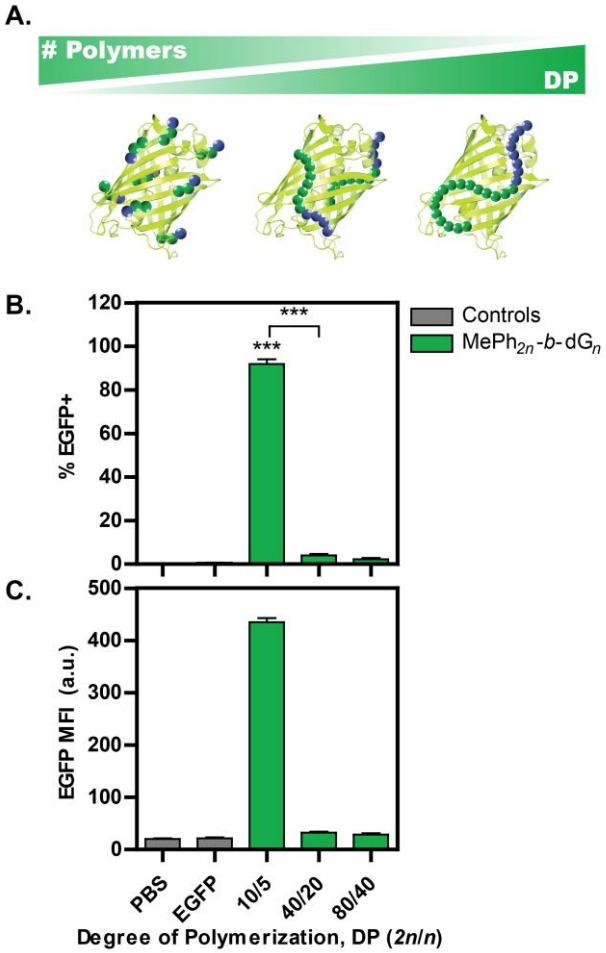

Figure 4.12: EGFP internalization in Jurkat T cells as a function of block copolymer PTDM degree of polymerization (DP). (A) Illustration of the inverse relationship between DP and number of polymer molecules in the system given that the total number of polymer repeat units in the system is universally conserved. As shorter polymers are linked together to form longer ones, fewer independent chains remain, allowing for a direct assessment of the impact of monomer connectivity on delivery. EGFP internalization is quantified as (B) percentage of live cells positive for EGFP and (C) median fluorescence intensity (MFI) of the entire live-cell population. Data are displayed as the mean ± the standard error of the mean for three independent replicates of 10,000 cells each. Statistics indicate significance in comparison with the PBS and EGFP controls (grey), unless otherwise noted: * = $p < 0.05$, ** = $p < 0.01$, *** = $p < 0.001$, no symbol = no significance, as determined by one-way ANOVA followed by a Tukey post-test.

4.3.3 Impact of Block Copolymer Length on Internalization and Activity

In a similar experiment, delivery of 50 nM EGFP was compared three lengths of **MePh$_{2n}$-*b*-dG$_n$** carriers at a ratio of 600 polymer repeat units per protein (Figure 4.12). In sharp contrast with homopolymer-mediated delivery, the shortest polymer facilitated EGFP internalization in virtually the entire cell population, while the longer two polymers failed entirely.

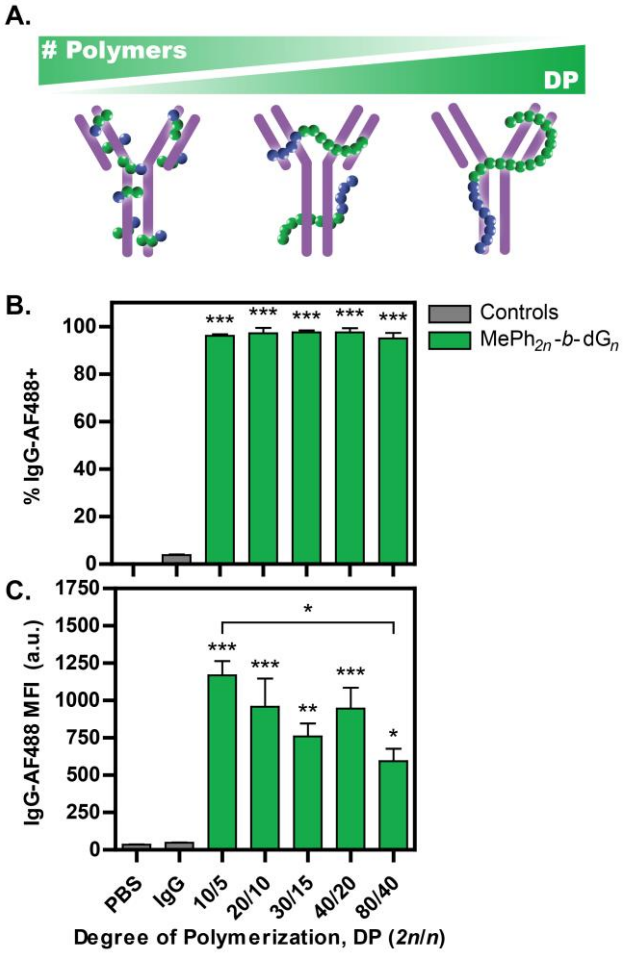

Figure 4.13: AlexaFluor (AF)488 conjugated IgG internalization in Jurkat T cells as a function of PTDM degree of polymerization (DP). (A) Illustration of the inverse relationship between DP and number of polymer molecules in the system given that the total number of polymer repeat units in the system is universally conserved. As shorter polymers are linked together to form longer ones, fewer independent chains remain, allowing for a direct assessment of the impact of monomer connectivity on delivery. IgG internalization is quantified as (B) percentage of live cells positive for AF488 and (C) median fluorescence intensity (MFI) of the entire live-cell population. Data are displayed as the mean ± the standard error of the mean for four independent replicates of 10,000 cells each. Statistics indicate significance in comparison with the PBS and IgG controls (grey), unless otherwise noted: * = $p < 0.05$, ** = $p < 0.01$, *** = $p < 0.001$, no symbol = no significance, as determined by one-way ANOVA followed by a Tukey post-test.

Although fluorescence is typically directly correlated with concentration of delivered protein, it is possible that the longer, more surfactant-like amphiphiles denatured EGFP, destroying its fluorophore. If true, lower fluorescence would be observed regardless of internalization level. To test this possibility, a second protein cargo was delivered, this time labelled with a small molecule dye whose fluorescence is independent of protein conformation. In this experiment, 50 nM of an AlexaFluor 488 conjugated antibody (IgG-

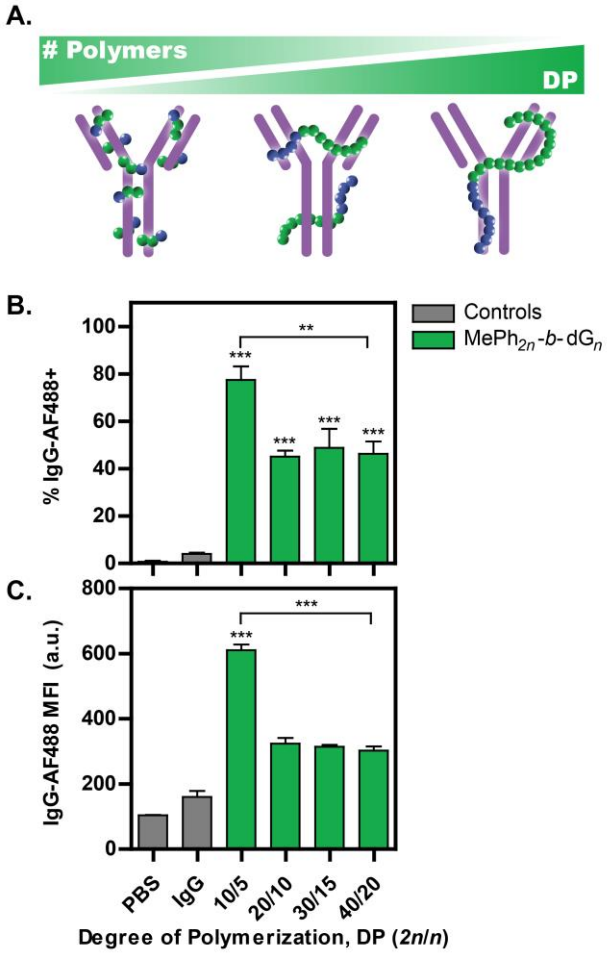

Figure 4.14: AlexaFluor (AF)488 conjugated IgG internalization in embryonic mouse hippocampal-18 (mHippoE-18) cells as a function of PTDM degree of polymerization (DP). (A) Illustration of the inverse relationship between DP and number of polymer molecules in the system given that the total number of polymer repeat units in the system is universally conserved. As shorter polymers are linked together to form longer ones, fewer independent chains remain, allowing for a direct assessment of the impact of monomer connectivity on delivery. IgG internalization is quantified as (B) percentage of live cells positive for AF488 and (C) median fluorescence intensity (MFI) of the entire live-cell population. Data are displayed as the mean ± the standard error of the mean for four independent replicates of 10,000 cells each. Statistics indicate significance in comparison with the PBS and IgG controls (grey), unless otherwise noted: * = $p < 0.05$, ** = $p < 0.01$, *** = $p < 0.001$, no symbol (or ns) = no significance, as determined by one-way ANOVA followed by a Tukey post-test.

AF488) was delivered into Jurkat T cells at a ratio of 300 polymer repeat units per protein (Figure 4.13). Similar to EGFP, IgG-AF488 internalization was significantly diminished when delivered with longer PTDMs. However, these longer polymers nonetheless delivered some IgG-AF488. This trend was replicated in a second cell line, embryonic mouse hippocampal-18 (mHippoE-18) cells (Figure 4.14). Thus, while it remains possible that protein denaturation contributed in part to the dramatic reduction in EGFP delivery, it appears that many, shorter PTDMs are more effective at maximizing protein internalization.

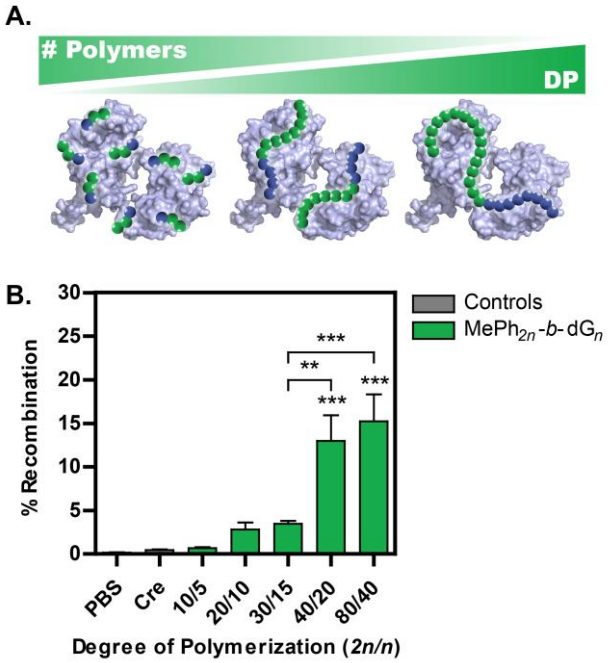

Figure 4.15: Functional delivery of Cre recombinase in Jurkat T cells, modified to express a floxed *EGFP* gene, as a function of PTDM degree of polymerization (DP). (A) Illustration of the inverse relationship between DP and number of polymer molecules in the system given that the total number of polymer repeat units in the system is universally conserved. As shorter polymers are linked together to form longer ones, fewer independent chains remain, allowing for a direct assessment of the impact of monomer connectivity on delivery. Functional Cre delivery is quantified as (B) percentage of cells negative for EGFP fluorescence 6 days post-delivery. Data are displayed as the mean ± the standard error of the mean for four independent replicates of 10,000 cells each. Statistics indicate significance in comparison with the PBS and Cre controls (grey), unless otherwise noted: * = $p < 0.05$, ** = $p < 0.01$, *** = $p < 0.001$, no symbol = no significance, as determined by one-way ANOVA followed by a Tukey post-test.

As demonstrated with this PTDM system in Chapter 3, high cargo activity can be achieved despite low internalization. That is, maximized internalization is not necessarily

associated with heightened cargo intracellular availability. For this reason, the block copolymers series was further screened for ability to deliver a model bioactive cargo, Cre recombinase, into a reporter Jurkat T cell line at a ratio of 75 polymer repeat units per protein (Figure 4.15). On-target delivery of structurally uncompromised Cre resulted in recombination of the *EGFP* gene and subsequent loss of cellular fluorescence. In stark contrast with internalization experiments, maximal protein activity was achieved with the longest carriers, **MePh$_{40}$-*b*-dG$_{20}$** and **MePh$_{80}$-*b*-dG$_{40}$**. This finding was particularly intriguing considering that the longest carrier, **MePh$_{80}$-*b*-dG$_{40}$**, was used at a ratio of less than one polymer molecule per protein. Considering that a large excess of carrier to cargo is almost always used in non-covalent delivery, the potency of this carrier is remarkable.

Although **MePh$_{80}$-*b*-dG$_{40}$** achieved the highest Cre activity at the conditions selected, the gene recombination rate was fairly low (~15%) in comparison with past studies (see Chapter 3) using this cargo.[35,37,48] Given that increasing PTDM:Cre ratio has been shown to elevate activity, ratios between 0.625:1 and 5:1 (the ratios used for **MePh$_{80}$-*b*-dG$_{40}$** and **MePh$_{10}$-*b*-dG$_{5}$** in Figure 4.15, respectively) were surveyed for the shortest and longest PTDMs (Figure 4.16).[48] Importantly, the ratio of polymer repeat units to protein molecules was not maintained in this case. In fact, each new condition tested represented either lower or higher ratios for **MePh$_{10}$-*b*-dG$_{5}$** and **MePh$_{80}$-*b*-dG$_{40}$**, respectively, compared with Figure 4.15 conditions. As expected, increasing polymer:protein ratio promoted higher gene recombination. It is worth noting, however, that at the highest mass of polymer used (i.e., **MePh$_{80}$-*b*-dG$_{40}$** with a 5:1 ratio), a slight drop in performance was observed. This reduction in activity coincided with severe cytotoxicity (~25% viable cells), suggesting that many of the cells receiving large quantities of protein did not survive.

Overall, the contrast between the different length polymers was clear: for the conditions evaluated, **MePh$_{10}$-*b*-dG$_5$** was unable to facilitate any notable gene recombination whereas **MePh$_{80}$-*b*-dG$_{40}$** modified 60% of the cellular population.

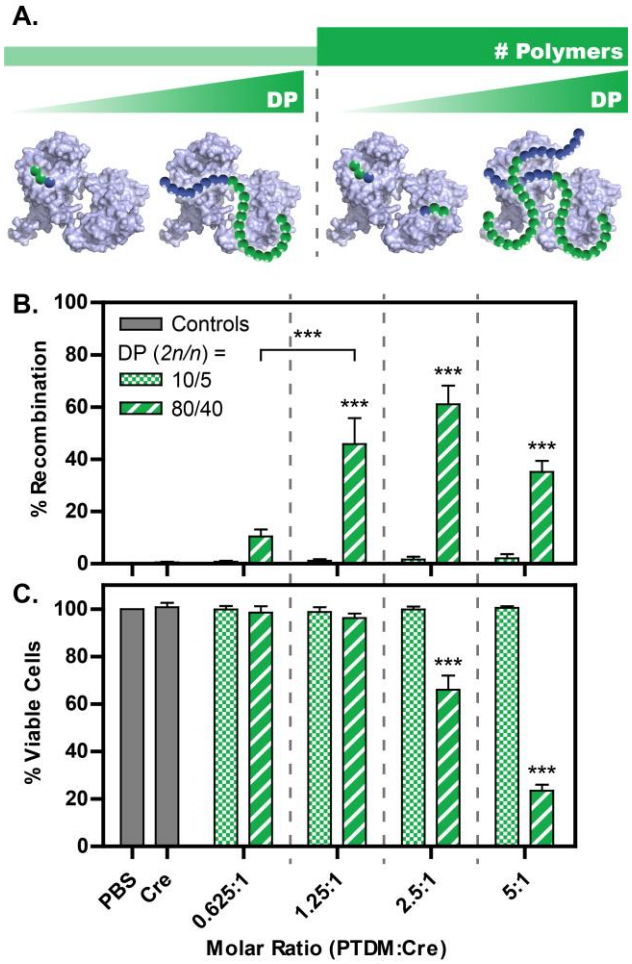

Figure 4.16: Functional delivery of Cre recombinase in Jurkat T cells, modified to express a floxed *EGFP* gene, as a function of both PTDM degree of polymerization (DP) and number of polymer chains in the system (i.e., molar ratio of PTDM:Cre). (A) Illustration of the experimental design, in which PTDMs with two different DPs (**MePh$_{10}$-*b*-dG$_5$** and **MePh$_{80}$-*b*-dG$_{40}$**) were studied at increasing ratios of PTDM chains to Cre molecules. Results are presented as (B) percentage of cells negative for EGFP fluorescence 6 days post-delivery and (C) cellular viability immediately following delivery. Each pair of bars represents delivery at equal polymer chain concentration, but unequal polymer repeat unit concentration (**MePh$_{10}$-*b*-dG$_5$** << **MePh$_{80}$-*b*-dG$_{40}$**). Data are displayed as the mean ± the standard error of the mean for four independent replicates of 10,000 cells each. Statistics indicate significance in comparison with the PBS and Cre controls (grey), unless otherwise noted: * = $p < 0.05$, ** = $p < 0.01$, *** = $p < 0.001$, no symbol = no significance, as determined by one-way ANOVA followed by a Tukey post-test.

4.3.4 Impact of Block Copolymer Length on Binding

The dramatic differences in cargo functionality when delivered with different length PTDMs, particularly considering the contradictory trend in internalization data, prompted speculation that there may be similarly large physical disparities in the polymer:protein complexes. Carrier-cargo association strength was probed using a model protein cargo, BSA-FITC, in a previously-established fluorescence-based binding assay (Figure 4.17).[35,44,45]

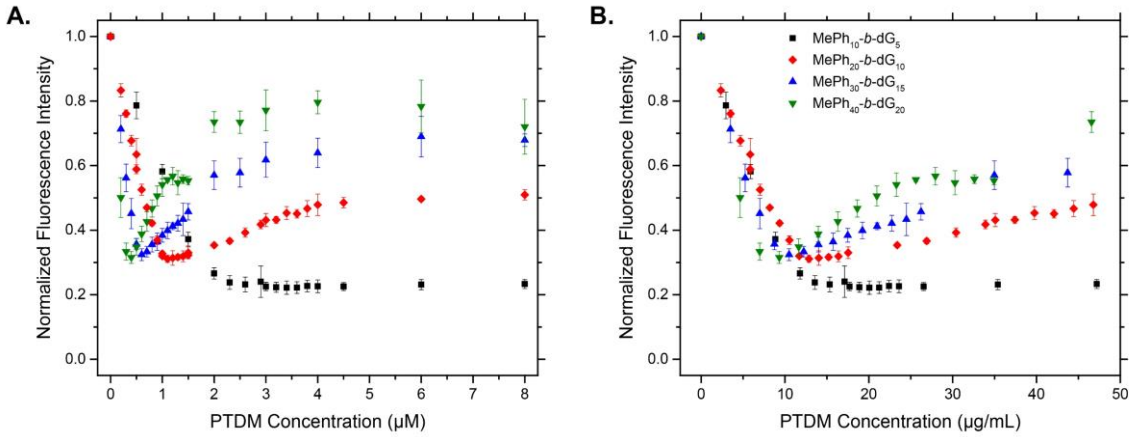

Figure 4.17: Fluorescence-quenching binding curves for PTDM:BSA-FITC pairs plotted by (A) PTDM molar concentration and (B) PTDM weight concentration. Replotting the data by weight concentration accounts for longer PTDMs containing more pendant functional groups, essentially normalizing to isolate the effect of increasing the concentration of repeat units in the system. Data points represent the mean normalized fluorescence intensity from three independent replicates ± the standard deviation.

Given that the binding regions of the curves (initial negative slope) collapsed onto each other when plotted by weight concentration (Figure 4.17B), but not when plotted by molar concentration (Figure 4.17A), cargo binding appeared to be driven by the polymer repeat unit to protein ratio (i.e., mass concentration of polymer in the system) rather than PTDM DP. This finding suggests that, in all experiments exploring the effect of increased monomer connectivity, proteins were bound with similar strengths by their carriers. It is interesting to note that after fluorescence quenching (i.e., binding) is achieved, the addition of more polymer into the system results in return of cargo fluorescence for polymers longer

than $2n/n = 10/5$. This phenomenon becomes progressively more pronounced as degree of polymerization increases. While it is not known whether this is due to a rearrangement event (e.g., cargo release, PTDM micellization, etc.), or simply an artifact of a smaller change in local fluorophore environment, these conditions are well above concentrations used in delivery experiments and have not been pursued in this study. Future studies may elucidate whether the more amphiphilic nature of these longer PTDMs results in self-assembly, for example micelle formation, above certain concentrations.

4.3.5 Impact of Block Copolymer Length on Complex Size

Dynamic light scattering (DLS) was subsequently used to probe the physical size of PTDM:IgG nanoparticles as a function of DP (Figure 4.18A-B). Complex size decreased dramatically with increasing polymer length, from ~1 μm to 50 nm in diameter, which represents nearly four orders of magnitude in particle volume reduction. To gain more insight into the complex formation process, the shortest and longest polymers were studied further by DLS at two PTDM:IgG ratios, 2.5:1 and 20:1, spanning the range of ratios employed in Figure 4.13 (Figure 4.18C-D). Consistent with previous findings, **MePh$_{10}$-*b*-dG$_5$**:IgG nanoparticles grew substantially in size as more polymer was introduced into the system.[21] In contrast, **MePh$_{80}$-*b*-dG$_{40}$**:IgG nanoparticles remained the same size despite the eight-fold increase in polymer concentration. This suggests higher molecular weight amphiphiles may form protein complexes via an entirely different mechanism than traditional PTDMs. The increased surfactant character of these long PTDMs may aid in complex stability at smaller sizes or even induce micellization. Regardless of the formation mechanism, complex size almost certainly impacts myriad

aspects of delivery, such as cellular internalization mechanism, endosomal escape, intracellular trafficking, and complex dissociation kinetics.[49–54]

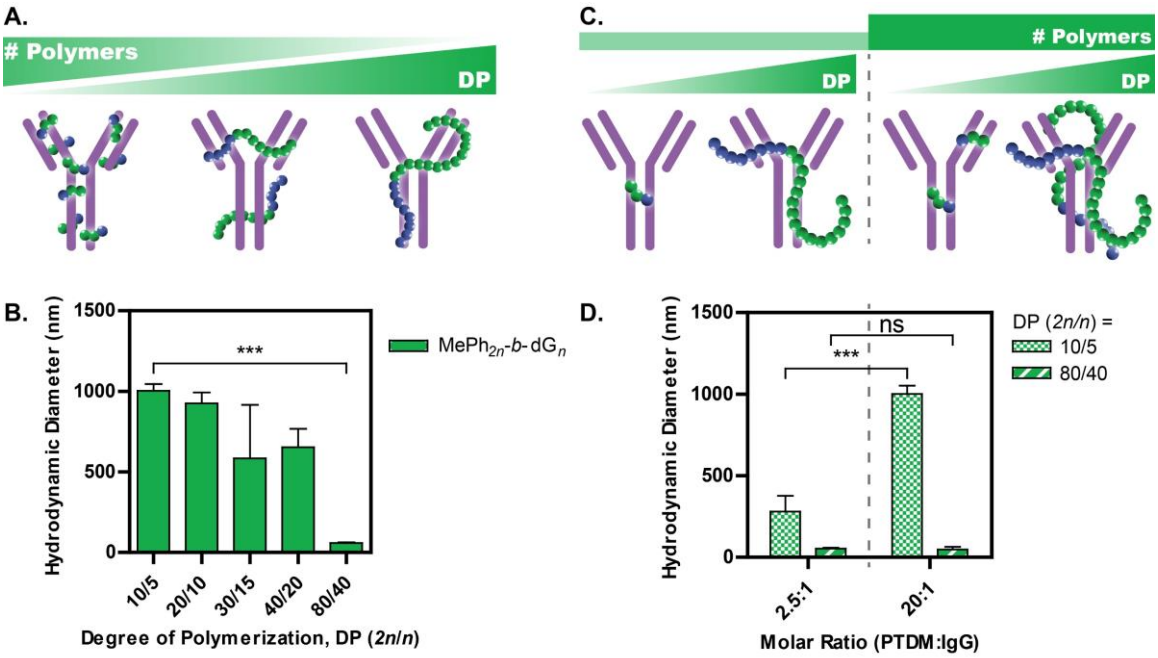

Figure 4.18: PTDM:IgG complex size as a function of (A-B) PTDM degree of polymerization (DP) and (C-D) number of polymer chains in the system (i.e., molar ratio of PTDM:IgG). (A) Illustration of the inverse relationship between DP and number of polymer molecules in the system in the first experiment, given that the total number of polymer repeat units in the system is universally conserved. As shorter polymers are linked together to form longer ones, fewer independent chains remain, allowing for a direct assessment of the impact of monomer connectivity on complex size. (B) PTDM:IgG complex diameter as measured by dynamic light scattering (DLS) for increasing PTDM DP. (C) Illustration of the second experimental design, in which PTDMs with two different DPs (**MePh$_{10}$-*b*-dG$_5$** and **MePh$_{80}$-*b*-dG$_{40}$**) were studied at increasing ratios of PTDM chains to Cre molecules. (D) PTDM:IgG complex diameter as determined by DLS, where each pair of bars represents complex size at equal polymer chain concentration, but unequal polymer repeat unit concentration (**MePh$_{10}$-*b*-dG$_5$** << **MePh$_{80}$-*b*-dG$_{40}$**). Data are presented as the mean size (by number) of the most populous distribution (when multimodal) ± the standard deviation for two (D) or three (B) independent replicates, each comprising three individual measurements of the same sample. In the case that a weak correlation curve was obtained, no meaningful data was obtained and the measurement was omitted. Further details regarding data analysis can be found in Section 4.2.3.3 Dynamic Light Scattering. Statistics indicate significance between the two data points indicated by brackets: * = $p < 0.05$, ** = $p < 0.01$, *** = $p < 0.001$, ns = no significance, as determined by one-way ANOVA followed by a Tukey post-test.

The DLS data in Figure 6B and Figure 6D were derived from the raw curves shown in Figure 4.19-Figure 4.22. Figure 4.19 and Figure 4.21 contain the intensity-based particle size distributions, while Figure 4.20 and Figure 4.22 display number-based population distributions. While the number distributions are of greater interest for the purposes of this study, it is important to recognize that they are derived directly from the intensity

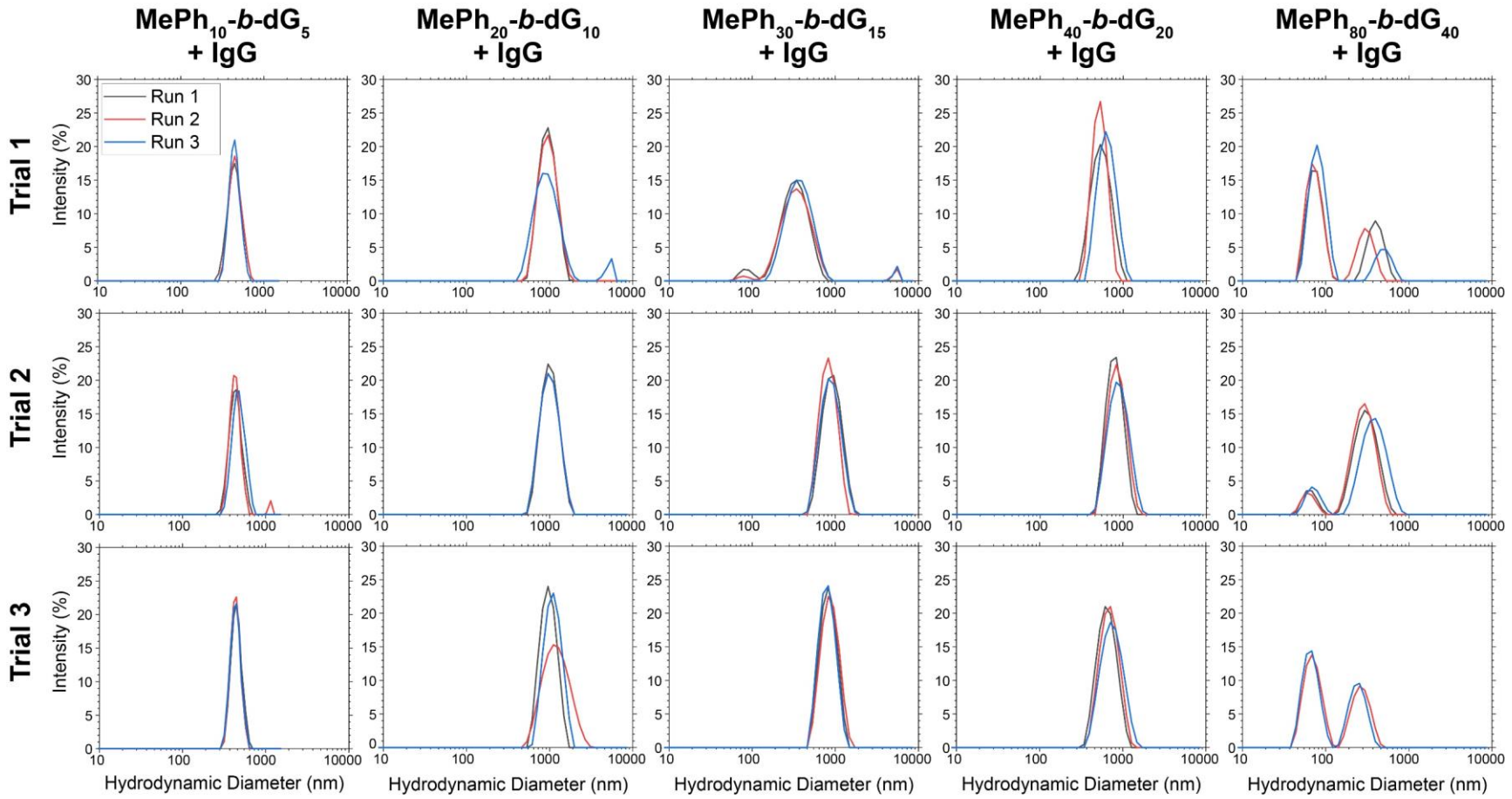

Figure 4.19: Raw DLS curves for **MePh$_{2n}$-*b*-dG$_n$**:IgG complexes plotted as percentage of total signal intensity as a function of diameter. Samples contained 50 nM IgG and PTDM:IgG molar ratios of 20:1, 10:1, 6.67:1, 5:1, and 2.5:1, respectively, for *2n*/*n* = 10/5, 20/10, 30/15, 40/20, and 80/40. Each individual plot contains overlaid data from three scans of the same sample. One run with a poor correlation function (Trial 3, Run 1 of **MePh$_{80}$-*b*-dG$_{40}$**) has been omitted.

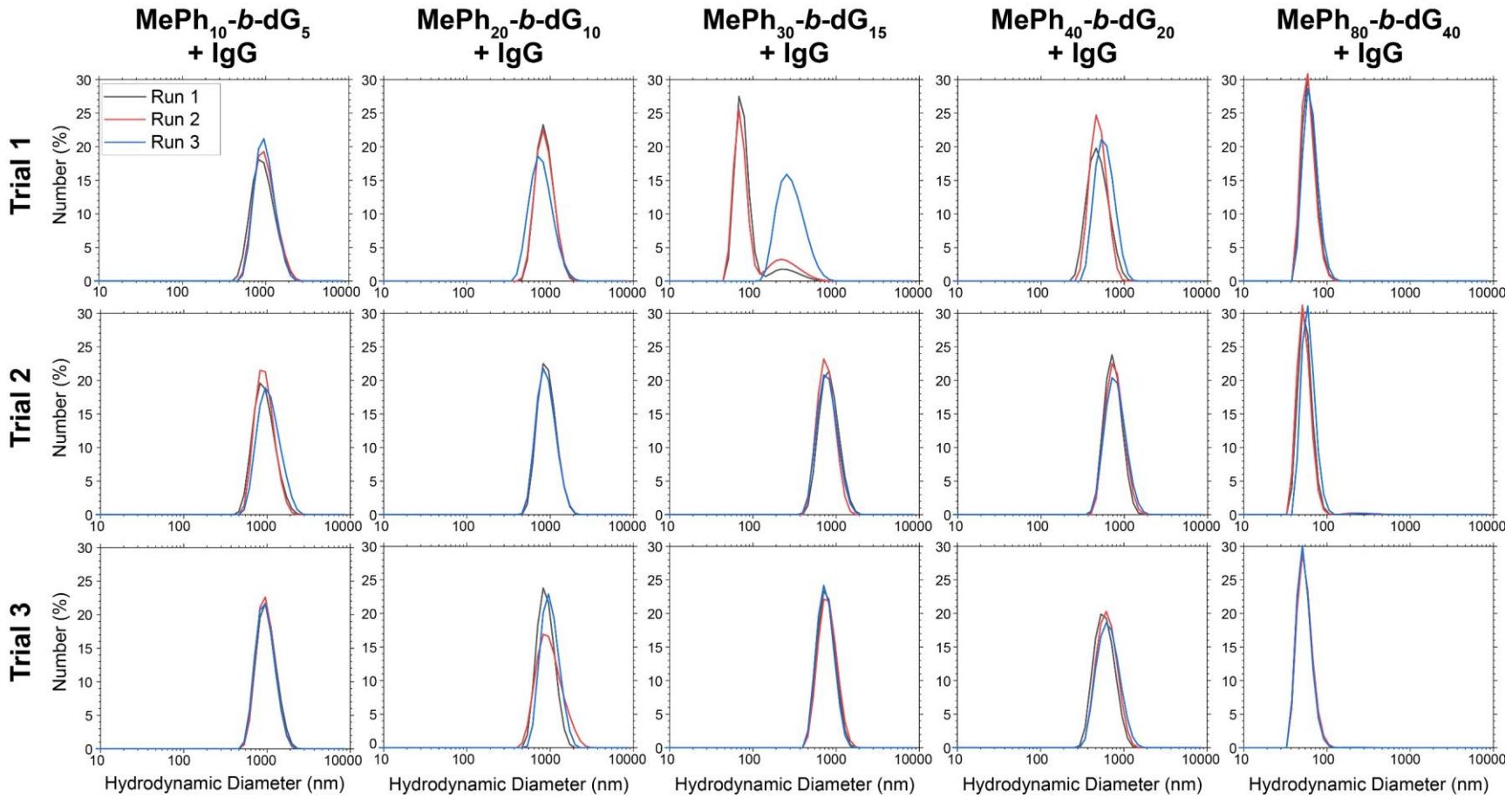

Figure 4.20: Raw DLS curves for **MePh$_{2n}$-*b*-dG$_n$**:IgG complexes plotted as percentage of total number of particles as a function of diameter. Samples contained 50 nM IgG and PTDM:IgG molar ratios of 20:1, 10:1, 6.67:1, 5:1, and 2.5:1, respectively, for *2n*/*n* = 10/5, 20/10, 30/15, 40/20, and 80/40. Each individual plot contains overlaid data from three scans of the same sample. One run with a poor correlation function (Trial 3, Run 1 of **MePh$_{80}$-*b*-dG$_{40}$**) has been omitted.

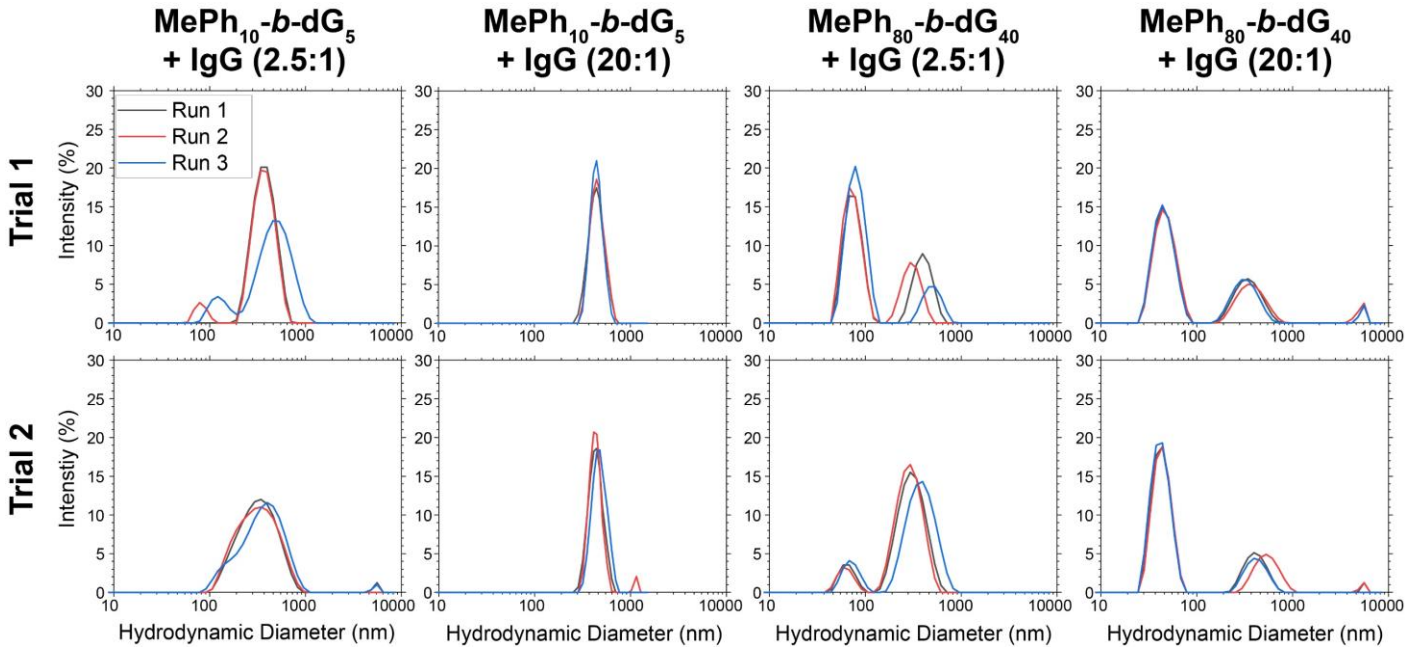

Figure 4.21: Raw DLS curves for **MePh$_{2n}$-*b*-dG$_n$**:IgG complexes plotted as percentage of total signal intensity as a function of diameter. Samples contained 50 nM IgG and various PTDM:IgG molar ratios as indicated at the top of each column. Each individual plot contains overlaid data from three scans of the same sample. Note that data contained within the middle two columns was included in Figure 4.20 but has been copied here for ease of comparison.

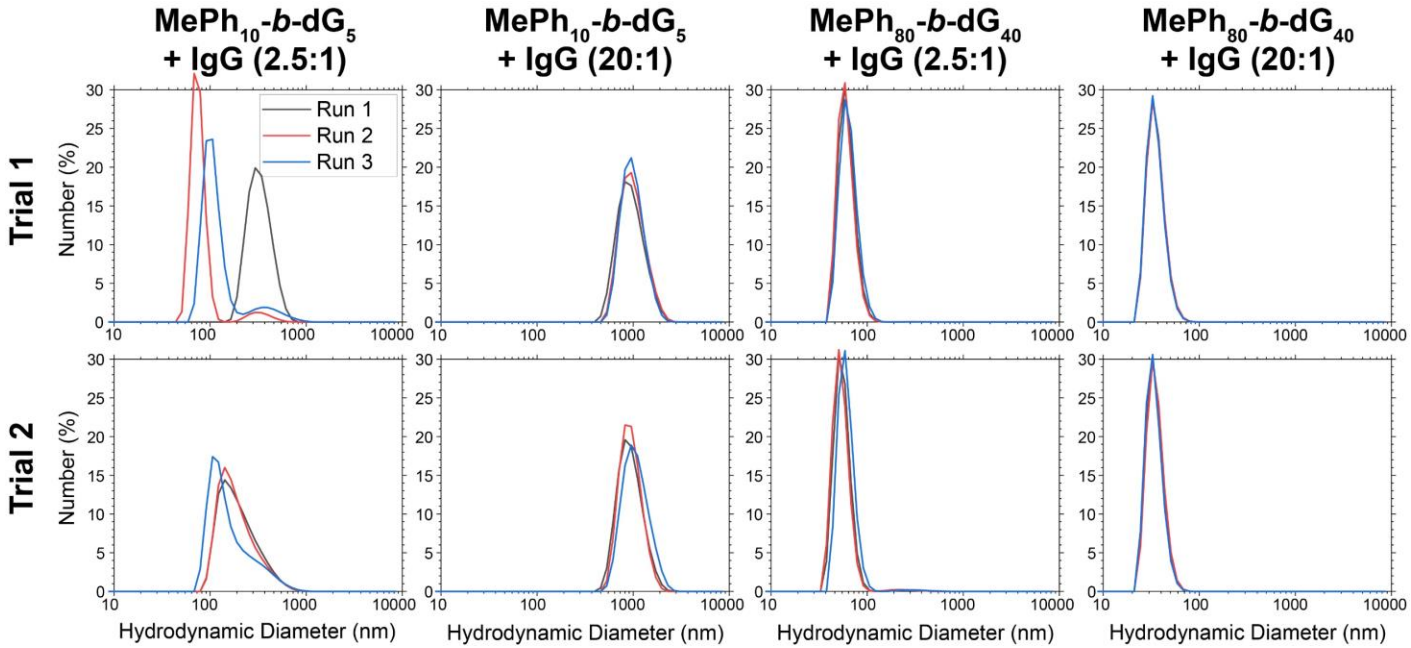

Figure 4.22: Raw DLS curves for **MePh$_{2n}$-*b*-dG$_n$**:IgG complexes plotted as percentage of total number of particles as a function of diameter. Samples contained 50 nM IgG and various PTDM:IgG molar ratios as indicated at the top of each column. Each individual plot contains overlaid data from three scans of the same sample. Note that data contained within the middle two columns was included in Figure 4.20 but has been copied here for ease of comparison.

distributions using the estimated RI value entered in the SOP. Though redundant, plots for samples which were used to isolate the effects of both PTDM DP and PTDM:IgG molar ratio on particle size (i.e., **MePh$_{10}$-*b*-dG$_5$** at a ratio of 20:1 and **MePh$_{80}$-*b*-dG$_{40}$** at 2.5:1) have been included in both sets of figures for ease of comparison.

Given that PTDM:IgG complex size dramatically decreased with increasing polymer length, a similar experiment was conducted using PTDM:Cre complexes in order to probe whether this phenomenon extended to Cre and might provide insight into the differences in biological activity observed (Figure 4.23). PTDM:Cre complexes did behave similarly, though the magnitude of size reduction was not as large (~50% decrease

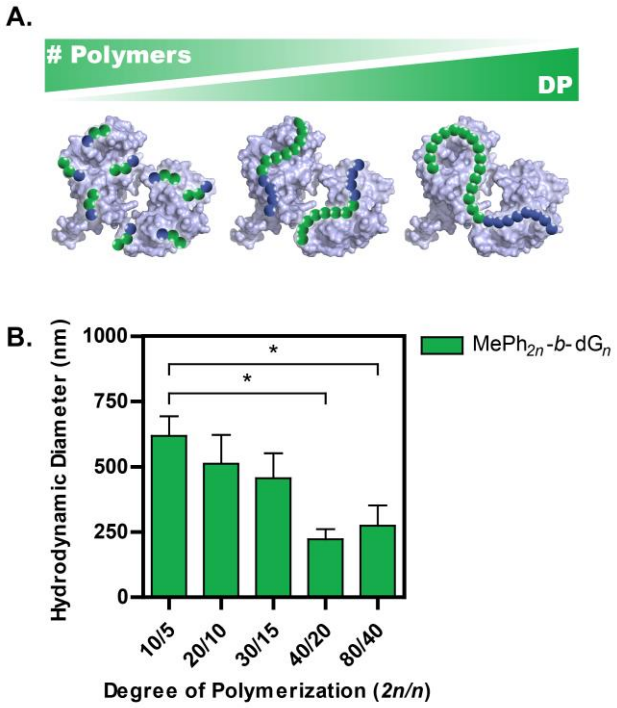

Figure 4.23: PTDM:Cre complex size as a function of PTDM degree of polymerization (DP). (A) Illustration of the inverse relationship between DP and number of polymer molecules in the system, given that the total number of polymer repeat units in the system is universally conserved. As shorter polymers are linked together to form longer ones, fewer independent chains remain, allowing for a direct assessment of the impact of monomer connectivity on complex size. (B) PTDM:Cre complex diameter as measured by dynamic light scattering (DLS) for increasing PTDM DP. Data are presented as the mean size (by number) of the most populous distribution (when multimodal) ± the standard deviation for three (C) independent replicates, each comprising three individual measurements of the same sample. In the case that a weak correlation curve was obtained, no meaningful data was obtained and the measurement was omitted. Statistics indicate significance between the two data points indicated by brackets: * = $p < 0.05$, ** = $p < 0.01$, *** = $p < 0.001$, no symbol = no significance, as determined by one-way ANOVA followed by a Tukey post-test.

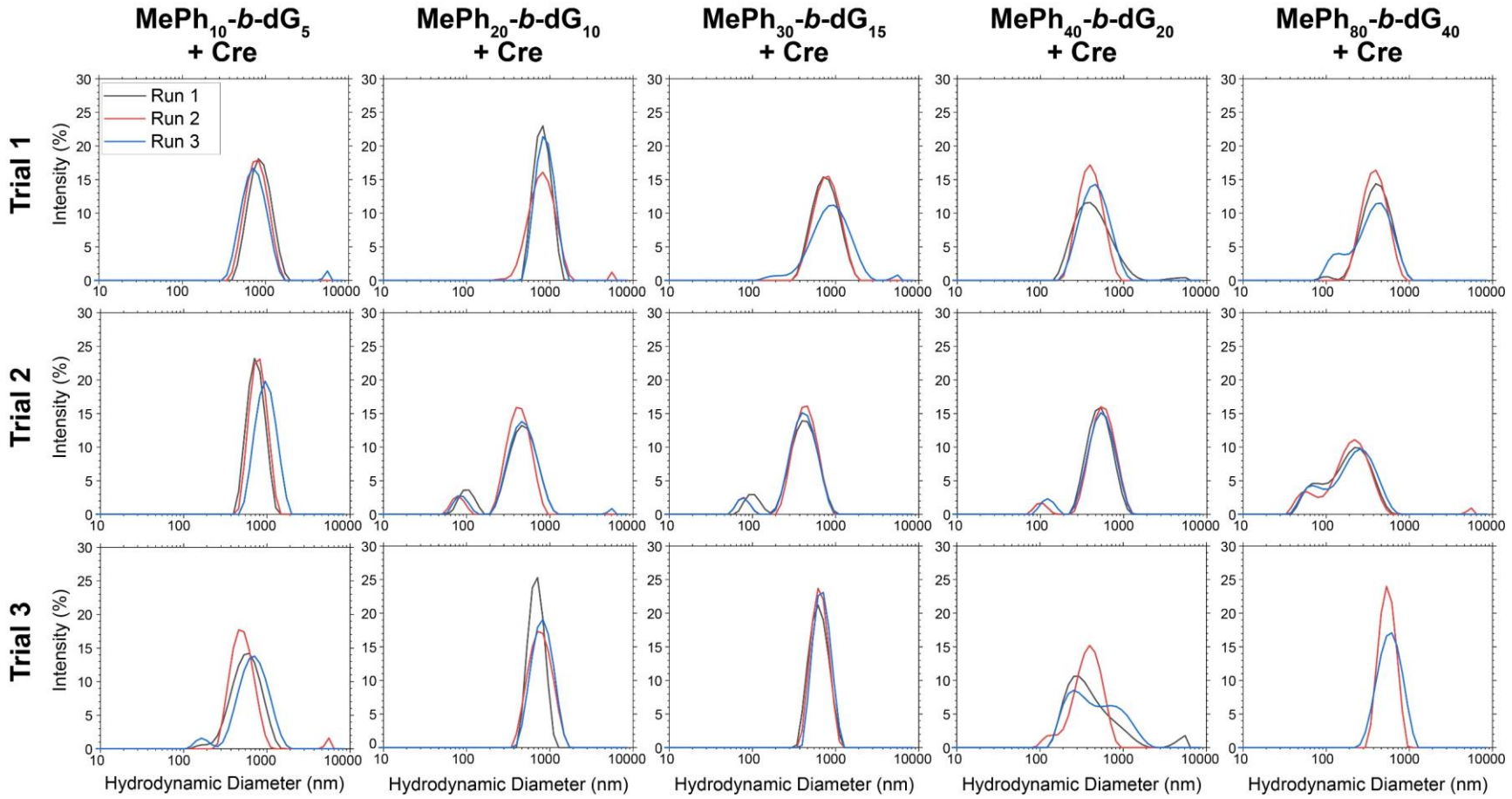

Figure 4.24: Raw DLS curves for **MePh$_{2n}$-*b*-dG$_n$**:Cre complexes plotted as percentage of total signal intensity as a function of diameter. Samples contained 125 nM Cre and PTDM:Cre molar ratios of 5:1, 2.5:1, 1.67:1, 1.25:1, and 0.625:1, respectively, for *2n*/*n* = 10/5, 20/10, 30/15, 40/20, and 80/40. Each individual plot contains overlaid data from three scans of the same sample. One run with a poor correlation function (Trial 1, Run 1 of **MePh$_{80}$-*b*-dG$_{40}$**) has been omitted.

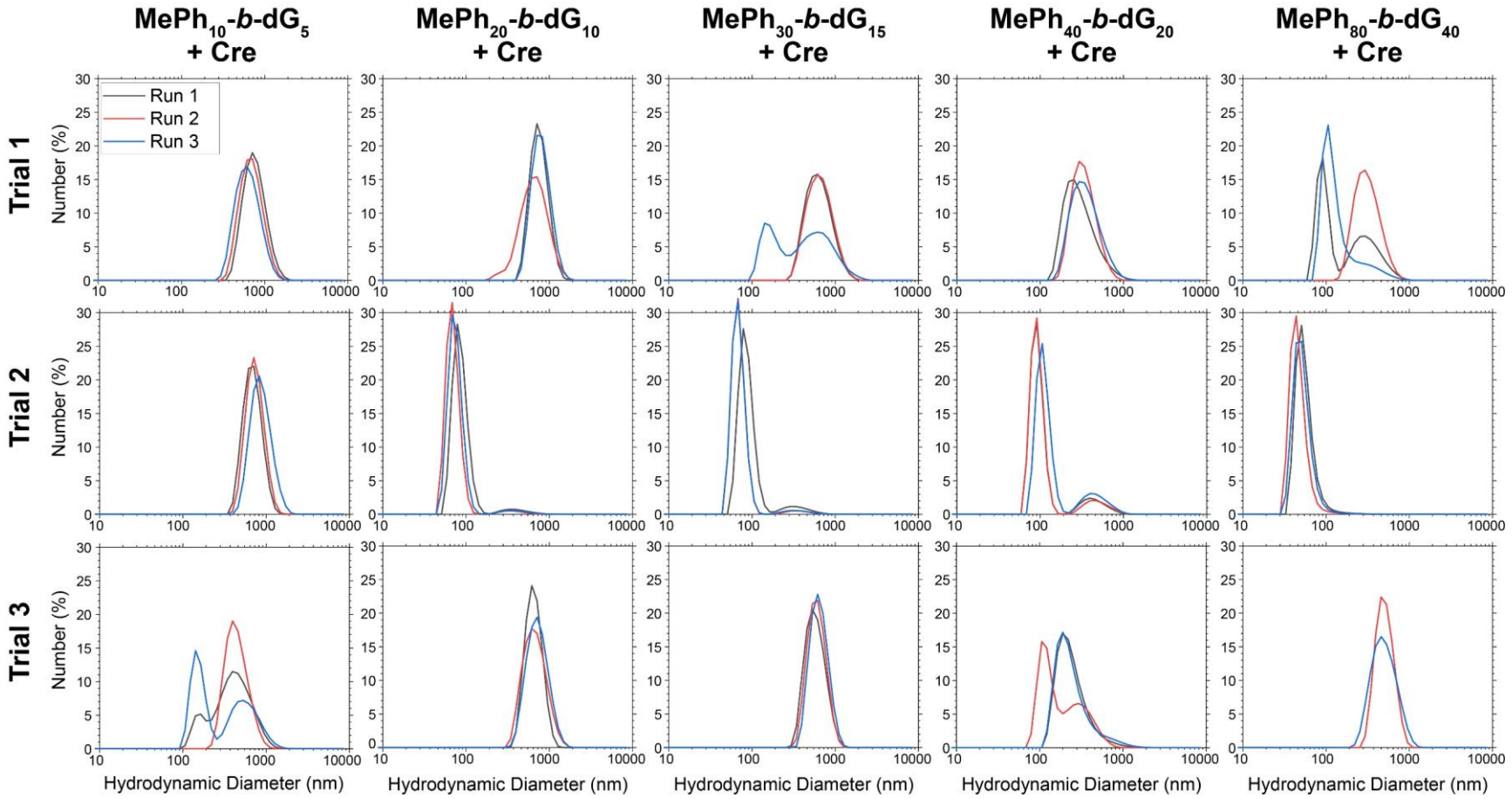

Figure 4.25: Raw DLS curves for **MePh$_{2n}$-*b*-dG$_n$**:Cre complexes plotted as percentage of total number of particles as a function of diameter. Samples contained 125 nM Cre and PTDM:Cre molar ratios of 5:1, 2.5:1, 1.67:1, 1.25:1, and 0.625:1, respectively, for *2n*/*n* = 10/5, 20/10, 30/15, 40/20, and 80/40. Each individual plot contains overlaid data from three scans of the same sample. One run with a poor correlation function (Trial 1, Run 1 of **MePh$_{80}$-*b*-dG$_{40}$**) has been omitted.

in diameter from **MePh$_{10}$-*b*-dG$_5$** to **MePh$_{80}$-*b*-dG$_{40}$** for Cre compared to almost an order of magnitude for IgG). However, a 50% decrease in nanoparticle diameter still represents about an order of magnitude reduction in volume. The raw intensity- and number-based particle size distributions from which Figure 4.23 was derived can be found in Figure 4.24 and Figure 4.25, respectively.

4.4 Conclusions

Whereas siRNA cargoes can be adequately delivered with homopolymer PTDMs,[30] these polymers are poor protein carriers, regardless of polymer length, charge density, or anionic nature of the cargo. This is consistent with previous findings that, although cationic homopolymers struggle to bind and deliver proteins, the simple addition of a hydrophobic block dramatically improves protein internalization.[35,36] Block copolymer degree of polymerization was found to affect protein delivery in competing ways. Although shortening these PTDMs maximized protein internalization, arranging the same number of monomers into fewer, longer polymer chains greatly improved functional delivery. This suggests that longer amphiphiles promote higher intracellular availability of their protein cargo even when minimal protein is delivered. Importantly, higher DP PTDMs with more surfactant-like character do not seem to significantly denature protein cargo. In contrast, they facilitate greater functional delivery. Taken together, these data reinforce the inconvenient reality that screening for maximal internalization alone is a gross oversimplification of the delivery process and can overlook highly effective carriers.

In order to understand the cause of intracellular availability differences, carrier-cargo binding and complex size were studied. Measured carrier-cargo binding interactions

were similar for various length PTDMs, however, complex size varied immensely. For PTDM:IgG complexes, particles ranged from 50 nm (DP = 120) to 1 μm (DP = 15) in diameter. Furthermore, unlike **MePh$_{10}$-*b*-dG$_5$** complexes, the size of **MePh$_{80}$-*b*-dG$_{40}$** complexes was independent of polymer concentration, indicating that they were particularly stable. While there is evidence in the literature of longer polymeric carriers protecting protein activity, the differences in intracellular availability seen here are likely due, at least in part, to differences in nanoparticle size. Cargoes contained within smaller nanoparticles may be more intracellularly available due variations in cellular uptake mechanism, nanoparticle surface area, or release kinetics. It is also possible, however, that the structures of these polymer-protein assemblies are fundamentally different. Future studies will be necessary to more thoroughly characterize the complexation mechanism, nanoparticle structure, and potential micellization of these high molecular weight PTDMs.

4.5 References

(1) Deshayes, S.; Morris, M.; Heitz, F.; Divita, G. Delivery of proteins and nucleic acids using a non-covalent peptide-based strategy. *Adv. Drug Deliv. Rev.* **2008**, *60* (4–5), 537–547.

(2) Posey, N. D.; Tew, G. N. Associative and Dissociative Processes in Non-Covalent Polymer-Mediated Intracellular Protein Delivery. *Chem. - An Asian J.* **2018**, *13* (22), 3351–3365.

(3) Herrera Estrada, L. P.; Champion, J. A. Protein nanoparticles for therapeutic protein delivery. *Biomater. Sci.* **2015**, *3* (6), 787–799.

(4) González-Toro, D. C.; Thayumanavan, S. Advances in polymer and polymeric nanostructures for protein conjugation. *Eur. Polym. J.* **2013**, *49* (10), 2906–2918.

(5) Pasut, G. Polymers for Protein Conjugation. *Polymers* **2014**, *6* (1), 160–178.

(6) Fu, A.; Tang, R.; Hardie, J.; Farkas, M. E.; Rotello, V. M. Promises and Pitfalls of Intracellular Delivery of Proteins. *Bioconjug. Chem.* **2014**, *25* (9), 1602–1608.

(7) Gong, Y.; Leroux, J. C.; Gauthier, M. A. Releasable Conjugation of Polymers to Proteins. *Bioconjugate Chemistry*. 2015, pp 1179–1181.

(8) Rao, J. P.; Geckeler, K. E. Polymer nanoparticles: Preparation techniques and size-control parameters. *Prog. Polym. Sci.* **2011**, *36* (7), 887–913.

(9) Zhao, H.; Lin, Z. Y.; Yildirimer, L.; Dhinakar, A.; Zhao, X.; Wu, J. Polymer-based nanoparticles for protein delivery: design, strategies and applications. *J. Mater. Chem. B* **2016**, *4* (23), 4060–4071.

(10) Hamid Akash, M. S.; Rehman, K.; Chen, S. Natural and Synthetic Polymers as Drug Carriers for Delivery of Therapeutic Proteins. *Polym. Rev.* **2015**, *55* (3), 371–406.

(11) Bekale, L.; Agudelo, D.; Tajmir-Riahi, H. A. Effect of polymer molecular weight on chitosan–protein interaction. *Colloids Surfaces B Biointerfaces* **2015**, *125*, 309–317.

(12) Sabnis, S.; Block, L. H. Chitosan as an enabling excipient for drug delivery systems I. Molecular modifications. *Int. J. Biol. Macromol.* **2000**, *27*, 181–186.

(13) Long, J.; Xu, E.; Li, X.; Wu, Z.; Wang, F.; Xu, X.; Jin, Z.; Jiao, A.; Zhan, X. Effect of chitosan molecular weight on the formation of chitosan-pullulanase soluble complexes and their application in the immobilization of pullulanase onto Fe_3O_4-κ-carrageenan nanoparticles. *Food Chem.* **2016**, *202*, 49–58.

(14) Gan, Q.; Wang, T. Chitosan nanoparticle as protein delivery carrier—Systematic examination of fabrication conditions for efficient loading and release. *Colloids Surfaces B Biointerfaces* **2007**, *59* (1), 24–34.

(15) Xu, Y.; Du, Y. Effect of molecular structure of chitosan on protein delivery properties of chitosan nanoparticles. *Int. J. Pharm.* **2003**, *250* (1), 215–226.

(16) Janes, K. A.; Alonso, M. J. Depolymerized chitosan nanoparticles for protein delivery: Preparation and characterization. *J. Appl. Polym. Sci.* **2003**, *88* (12), 2769–2776.

(17) Wang, F.; Mo, J.; Huang, A.; Zhang, M.; Ma, L. Effects of interaction with gene carrier polyethyleneimines on conformation and enzymatic activity of pig heart lactate dehydrogenase. *Spectrochim. Acta - Part A Mol. Biomol. Spectrosc.* **2018**, *204*, 217–224.

(18) Guo, Z.; Kong, Z.; Wei, Y.; Li, H.; Wang, Y.; Huang, A.; Ma, L. Effects of gene carrier polyethyleneimines on the structure and binding capability of bovine serum albumin. *Spectrochim. Acta - Part A Mol. Biomol. Spectrosc.* **2017**, *173*, 783–791.

(19) Bekale, L.; Agudelo, D.; Tajmir-Riahi, H. A. The role of polymer size and hydrophobic end-group in PEG–protein interaction. *Colloids Surfaces B Biointerfaces* **2015**, *130*, 141–148.

(20) Jain, S.; Bates, F. S. On the origins of morphological complexity in block copolymer surfactants. *Science* **2003**, *300* (5618), 460–464.

(21) Posey, N. D.; Tew, G. N. Protein Transduction Domain Mimic (PTDM) Self-Assembly? *Polymers* **2018**, *10* (9), 1039.

(22) Reynhout, I. C.; Cornelissen, J. J. L. M.; Nolte, R. J. M. Synthesis of Polymer−Biohybrids: From Small to Giant Surfactants. *Acc. Chem. Res.* **2009**, *42* (6), 681–692.

(23) Mai, Y.; Eisenberg, A. Self-assembly of block copolymers. *Chem. Soc. Rev.* **2012**, *41* (18), 5969.

(24) Raffa, P.; Wever, D. A. Z.; Picchioni, F.; Broekhuis, A. A. Polymeric Surfactants: Synthesis, Properties, and Links to Applications. *Chem. Rev.* **2015**, *115* (16), 8504–8563.

(25) Frankel, A. D.; Pabo, C. O. Cellular uptake of the tat protein from human immunodeficiency virus. *Cell* **1988**, *55* (6), 1189–1193.

(26) Green, M.; Loewenstein, P. M. Autonomous functional domains of chemically synthesized human immunodeficiency virus tat trans-activator protein. *Cell* **1988**, *55* (6), 1179–1188.

(27) Vivès, E.; Brodin, P.; Lebleu, B.; Vivè, E.; Brodin, P.; Lebleu, B. A Truncated HIV-1 Tat Protein Basic Domain Rapidly Translocates through the Plasma Membrane and Accumulates in the Cell Nucleus. *J. Biol. Chem.* **1997**, *272* (25), 16010–16017.

(28) Joliot, A.; Pernelle, C.; Deagostini-Bazin, H.; Prochiantz, A. Antennapedia homeobox peptide regulates neural morphogenesis. *Proc. Natl. Acad. Sci.* **1991**, *88* (5), 1864–1868.

(29) Derossi, D.; Joliot, A. H.; Chassaing, G.; Prochiantz, A. The third helix of the Antennapedia homeodomain translocates through biological membranes. *J. Biol. Chem.* **1994**, *269* (14), 10444–10450.

(30) Caffrey, L. M.; deRonde, B. M.; Minter, L. M.; Tew, G. N. Mapping Optimal Charge Density and Length of ROMP-Based PTDMs for siRNA Internalization. *Biomacromolecules* **2016**, *17* (10), 3205–3212.

(31) deRonde, B. M.; Torres, J. A.; Minter, L. M.; Tew, G. N. Development of Guanidinium-Rich Protein Mimics for Efficient siRNA Delivery into Human T Cells. *Biomacromolecules* **2015**, *16* (10), 3172–3179.

(32) deRonde, B. M.; Posey, N. D.; Otter, R.; Caffrey, L. M.; Minter, L. M.; Tew, G. N. Optimal Hydrophobicity in Ring-Opening Metathesis Polymerization-Based Protein Mimics Required for siRNA Internalization. *Biomacromolecules* **2016**, *17* (6), 1969–1977.

(33) Sarapas, J. M.; Backlund, C. M.; DeRonde, B. M.; Minter, L. M.; Tew, G. N. ROMP- and RAFT-Based Guanidinium-Containing Polymers as Scaffolds for Protein Mimic Synthesis. *Chem. - A Eur. J.* **2017**, *23* (28), 6858–6863.

(34) Backlund, C. M.; Sgolastra, F.; Otter, R.; Minter, L. M.; Takeuchi, T.; Futaki, S.; Tew, G. N. Increased hydrophobic block length of PTDMs promotes protein internalization. *Polym. Chem.* **2016**, *7* (48), 7514–7521.

(35) Sgolastra, F.; Backlund, C. M.; Ilker Ozay, E.; deRonde, B. M.; Minter, L. M.; Tew, G. N. Sequence segregation improves non-covalent protein delivery. *J. Control. Release* **2017**, *254*, 131–136.

(36) Backlund, C. M.; Takeuchi, T.; Futaki, S.; Tew, G. N. Relating structure and internalization for ROMP-based protein mimics. *Biochim. Biophys. Acta - Biomembr.* **2016**, *1858* (7), 1443–1450.

(37) Tezgel, A. Ö.; Jacobs, P.; Backlund, C. M.; Telfer, J. C.; Tew, G. N. Synthetic Protein Mimics for Functional Protein Delivery. *Biomacromolecules* **2017**, *18* (3), 819–825.

(38) Backlund, C. M.; Parhamifar, L.; Minter, L.; Tew, G. N.; Andresen, T. L. Protein Transduction Domain Mimics Facilitate Rapid Antigen Delivery into Monocytes. *Mol. Pharm.* **2019**, *16* (6), 2462–2469.

(39) Ozay, E. I.; Gonzalez-Perez, G.; Torres, J. A.; Vijayaraghavan, J.; Lawlor, R.; Sherman, H. L.; Garrigan, D. T.; Burnside, A. S.; Osborne, B. A.; Tew, G. N.; Minter, L. M. Intracellular Delivery of Anti-pPKCθ (Thr538) via Protein Transduction Domain Mimics for Immunomodulation. *Mol. Ther.* **2016**, *24* (12), 2118–2130.

(40) Ozay, E. I.; Shanthalingam, S.; Sherman, H. L.; Torres, J. A.; Osborne, B. A.; Tew, G. N.; Minter, L. M. Cell-Penetrating Anti-Protein Kinase C Theta Antibodies Act Intracellularly to Generate Stable, Highly Suppressive Regulatory T Cells. *Mol. Ther.* **2020**, *28* (8), 1987–2006.

(41) Ozay, E. I.; Shanthalingam, S.; Torres, J. A.; Osborne, B. A.; Tew, G. N.; Minter, L. M. Protein Kinase C Theta Modulates PCMT1 through hnRNPL to Regulate FOXP3 Stability in Regulatory T Cells. *Mol. Ther.* **2020**, *28* (10), 1–17.

(42) Love, J. A.; Morgan, J. P.; Trnka, T. M.; Grubbs, R. H. A Practical and Highly Active Ruthenium-Based Catalyst that Effects the Cross Metathesis of Acrylonitrile. *Angew. Chemie Int. Ed.* **2002**, *41* (21), 4035–4037.

(43) Lienkamp, K.; Madkour, A. E.; Musante, A.; Nelson, C. F.; Nüsslein, K.; Tew, G. N. Antimicrobial Polymers Prepared by ROMP with Unprecedented Selectivity: A Molecular Construction Kit Approach. *J. Am. Chem. Soc.* **2008**, *130* (30), 9836–9843.

(44) Posey, N. D.; Hango, C. R.; Minter, L. M.; Tew, G. N. The Role of Cargo Binding Strength in Polymer-Mediated Intracellular Protein Delivery. *Bioconjug. Chem.* **2018**, *29* (8), 2679–2690.

(45) Posey, N. D.; Caffrey, L. M.; Minter, L. M.; Tew, G. N. Protein Mimic Hydrophobicity Affects Intracellular Delivery but not Cargo Binding. *ChemistrySelect* **2016**, *1* (19), 6146–6150.

(46) Backlund, C. M.; Hango, C. R.; Minter, L. M.; Tew, G. N. Protein and Antibody Delivery into Difficult-to-Transfect Cells by Polymeric Peptide Mimics. *ACS Appl. Bio Mater.* **2020**, *3* (1), 180–185.

(47) McNaughton, B. R.; Cronican, J. J.; Thompson, D. B.; Liu, D. R. Mammalian cell penetration, siRNA transfection, and DNA transfection by supercharged proteins. *Proc. Natl. Acad. Sci.* **2009**, *106* (15), 6111–6116.

(48) Sgolastra, F.; Kuksin, C. A. A.; Gonzalez-Perez, G.; Minter, L. M.; Tew, G. N. Enhanced TAT-Cre Protein Transduction for Efficient Gene Recombination in T cells. *ACS Appl. Bio Mater.* **2018**, *1*, 444–451.

(49) Kettler, K.; Veltman, K.; van de Meent, D.; van Wezel, A.; Hendriks, A. J. Cellular uptake of nanoparticles as determined by particle properties, experimental conditions, and cell type. *Environ. Toxicol. Chem.* **2014**, *33* (3), 481–492.

(50) Yameen, B.; Choi, W. Il; Vilos, C.; Swami, A.; Shi, J.; Farokhzad, O. C. Insight into nanoparticle cellular uptake and intracellular targeting. *J. Control. Release* **2014**, *190*, 485–499.

(51) Selby, L. I.; Cortez-Jugo, C. M.; Such, G. K.; Johnston, A. P. R. Nanoescapology: progress toward understanding the endosomal escape of polymeric nanoparticles. *Wiley Interdiscip. Rev.: Nanomed. Nanobiotechnol.* **2017**, *9* (5), e1452.

(52) Smith, S. A.; Selby, L. I.; Johnston, A. P. R. R.; Such, G. K. The Endosomal Escape of Nanoparticles: Toward More Efficient Cellular Delivery. *Bioconjug. Chem.* **2019**, *30* (2), 263–272.

(53) Yus, C.; Irusta, S.; Sebastian, V.; Arruebo, M. Controlling Particle Size and Release Kinetics in the Sustained Delivery of Oral Antibiotics Using pH-Independent Mucoadhesive Polymers. *Mol. Pharm.* **2020**, *17* (9), 3314–3327.

(54) Guo, X.; Wei, X.; Chen, Z.; Zhang, X.; Yang, G.; Zhou, S. Multifunctional nanoplatforms for subcellular delivery of drugs in cancer therapy. *Prog. Mater. Sci.* **2020**, *107*, 100599.

CHAPTER 5

5 RAPID QUANTIFICATION OF SUBCELLULAR DRUG DELIVERY BY ORGANELLE FLOW CYTOMETRY

NOTE: Polymers used in this chapter were prepared with the help of Coralie M. Backlund and Miguel A. Franco. Preliminary delivery experiments were performed with the help of Miguel A. Franco.

5.1 Introduction

5.1.1 Summary

A simple approach for evaluating subcellular delivery is herein presented as an alternative to methods such as confocal microscopy, imaging flow cytometry, and bulk analysis of purified organelle fractions. In this workflow, intracellular delivery is followed by cell lysis and analysis at the single organelle level using a conventional flow cytometer. Intra-organelle delivery can thus be quantified for statistically powerful sample sizes in a high-throughput and objective manner unattainable by confocal microscopy, the gold standard for examining subcellular distribution. This approach is particularly advantageous when accumulation in the organelle of interest is considerably lower than in other subcellular compartments (e.g., endosomes), causing intra-organelle fluorescence to be prohibitively obscured during whole-cell imaging. In the present study, the utility of this new method is exemplified through evaluation of polymeric cell-penetrating peptide mimics (CPPMs) for their ability to non-covalently transport an antibody cargo into the mitochondria of HeLa cells. Consistent with reports of structurally-similar mitochondria penetrating peptides, delivery with CPPMs containing significant hydrophobic content yielded enhanced intramitochondrial localization of both carrier and cargo. Importantly,

antibody detection within the mitochondria implies that such non-covalent carriers are capable of trafficking their cargoes subcellularly prior to release.

5.1.2 Background

Subcellular-targeted therapeutics are expected to be a critical thrust of next-generation therapeutics.[1–4] Organelle-selective delivery enables significant increases in potency, thereby reducing both the required dosage and incidence of off-target effects.[5–7] By far the most popular strategy for measuring intracellular drug distribution is confocal microscopy, in which a drug's overlap with the target organelle is visualized using appropriate chromophores.[7] However, it was recently found that over three-quarters of such reports include only qualitative data.[8] This lack of quantitative analysis is alarming, particularly given the countless sophisticated techniques available for calculating colocalization.[9,10] When used appropriately, confocal microscopy can be an unrivaled and powerful tool; however, it can sometimes be impractical or better suited in combination with another complementary technique. Such situations might include analysis of subcellular compartments with relatively low fluorescence in comparison with other regions of the cell and delivery to suspension cells.

An increasingly popular alternative to microscopy is multispectral imaging flow cytometry (IFC). IFC couples the detailed imagery of microscopy with the high-throughput, unbiased, and statistically powerful nature of flow cytometry (FCM).[11–14] Although not quite as spatially resolved as confocal, IFC generally enables satisfactory determination of subcellular localization. At present, imaging flow cytometers are less accessible than confocal microscopes, but this is rapidly changing. Mass spectrometry

(MS) is an emerging tool for mapping tissue and subcellular distributions of small molecules. Distinct advantages of MS over fluorescence-based techniques include higher sensitivity and detection of unmodified drugs, thus eliminating the risk of fluorophore-driven changes in biological activity. Widespread adoption of MS for subcellular detection is currently limited by its specialized instrumentation and inferior resolution as compared to confocal microscopy and IFC (~1 μm at best). Nonetheless, this technology is in its infancy, and these barriers are expected to be overcome in the near future.[7] Finally, subcellular delivery can be quantified through analysis of organelle-enriched fractions from cell lysates. These protocols are quite laborious and purity is vital to obtaining accurate results, though even the most rigorous protocols rarely yield complete separation.[15] Furthermore, the many wash steps required increase the risk of drug leakage out of the organelle being studied.[7] In lieu of traditional differential centrifugation, subcellular fractionation can also be performed by immunoisolation (e.g., antibody-coated magnetic beads), flow electrophoresis, or fluorescence-activated organelle sorting (FAOS).[15–18] Intra-organelle concentrations of small molecules, nucleic acids, and proteins can then be directly quantified by techniques such as chromatography, spectrophotometry, MS, PCR, and western blotting, as appropriate.[7]

In the present study, we introduce a hybrid technique that combines the precision and ease of FCM with analysis at the single-organelle level while simultaneously bypassing the need for organelle purification. Though FCM is often regarded as a tool for analyzing eukaryotic cells, it has also been used to characterize smaller particles, bacteria, extracellular vesicles, organelles, and even viruses.[15,16,18–27] Unlike other assays involving isolated organelles, organelle FCM does not require physical separation to obtain purified

fractions. Instead, separation is accomplished during the data analysis stage by use of an appropriate subcellular stain. Despite the extensive utilization of FCM to study organellular populations for various applications, to our knowledge, this is the first example of organelle FCM applied to drug delivery.[7,15,20–22,28] Accordingly, we herein present a case study involving intramitochondrial antibody delivery to exemplify the potential of organelle FCM in the field of subcellular-targeted therapies.

After the cytoplasm and nucleus, the mitochondrion is the most frequently-targeted subcellular compartment.[8,29] Due to their essential roles in energy production and programmed cell death, dysfunction of the mitochondria has been implicated in a number of diseases ranging from neurological disorders to cancer.[30] The mitochondria additionally contain their own set of DNA (mtDNA), offering opportunities for gene regulation and therapy.[31] However, the mitochondrion's highly hydrophobic double membrane structure and negative membrane potential add significant impediments to delivery, particularly the delivery of macromolecular cargoes.[30,32,33] Recently, Kelley and coworkers have reported an extensive library of specialized cell-penetrating peptides (CPPs) which actively accumulate in the mitochondria.[34] The cationic charge, hydrophobicity, length, and sequence of these mitochondria penetrating peptides (MPPs) were comprehensively optimized for either transduction or disruption of the mitochondrial membrane, depending on the application.[35–37] Most notably, **$(F_x r)_3$**, an alternating hexapeptide of $_L$-cyclohexylalanine and $_D$-arginine, has been used to covalently deliver a variety of small molecule drugs into the mitochondria.[38–42] Several other groups have reported structurally-similar molecules with impressive mitochondrial localization (see Scheme 5.1 in Section 5.3.1 Non-Covalent Carrier Design).[43,44]

Synthetic CPP mimics (CPPMs) recently developed in our group share strikingly similar cationic and hydrophobic constituents with MPPs. These CPPMs have been extensively studied for non-covalent delivery of functional proteins and nucleic acids to nuclear and cytosolic targets, though structural optimization for mitochondrial penetration has yet to be explored.[45–50] In this report, we compare previously developed CPPMs to newly synthesized polymers containing quasi-alternating cyclohexyl and guanidine groups, in direct mimicry of $\mathbf{(F_xr)_3}$. Given previous confocal observations of CPPM distribution throughout many parts of the cell, relatively low mitochondrial specificity was expected for most of the CPPMs studied here.[51,52] Accordingly, low intramitochondrial fluorescence relative to the rest of the cell was expected, making this system an ideal candidate for analysis at the single-mitochondrion level after eliminating extramitochondrial fluorescence. In the case study presented here, we seek to understand how CPPM structure influences mitochondrial localization of both the carrier and its non-covalently complexed antibody cargo.

5.2 Materials and Methods

5.2.1 Materials

5.2.1.1 Synthetic Materials

Chemicals and solvents were obtained as reagent grade from Millipore Sigma, Alfa Aesar, Fisher Scientific, Fluka, BDH, or Acros Organics and used as received unless otherwise noted. Grubbs 3rd generation catalyst (Dichloro-di(3-bromopyridino)-N,N'-Dimesitylenoimidazolino-Ru=CHPh; G3) was synthesized as described previously.[53] Deuterated NMR solvents were obtained from Cambridge Isotope Laboratories. Polymers

were fluorescently labelled using fluorescein-5-thiosemicarbazide (FITC) purchased from ThermoFisher Scientific (product number F121). Polymers were dialyzed using Spectra/Por® dialysis membranes with molecular weight cutoffs (MWCOs) ranging from 0.5-1 kDa.

5.2.1.2 Biological Materials

Cross-adsorbed goat anti-rabbit immunoglobulin G, fluorescently labelled with Alexa Fluor 647 (herein referred to as "IgG-AF647"), was purchased from ThermoFisher Scientific (product number A-21244) and stored in the dark at 4 ºC upon receipt, per manufacturer recommendations. Goat Immunoglobin G (IgG) from serum (herein referred to as "unlabeled IgG" or simply "IgG") was purchased from Millipore Sigma (product number I5256) and stored at 4 °C upon receipt. Prior to delivery experiments, a 2 mg/mL solution in 1x PBS was prepared and stored at 4 °C.

CellLight™ Mitochondria-RFP, BacMam 2.0 ("MitoRFP") was purchased from ThermoFisher Scientific (product number C10601) and stored in the dark at 4 °C upon receipt, per manufacturer recommendations. This reagent is a fusion construct of the leader sequence of E1 alpha pyruvate dehydrogenase and TagRFP packaged in packaged in a baculovirus. Upon transduction of mammalian cells, red fluorescent protein (RFP) DNA is expressed and trafficked to the mitochondria. Because baculoviruses are unable to replicate in mammalian cells, this process only achieves transient labelling.[54,55]

The Mitochondria Isolation Kit for Cultured Cells was purchased from ThermoFisher Scientific (product number 89874) and stored in the dark at 4 °C upon receipt, per manufacturer recommendations.

MitoTracker™ Red CMXRos and LysoTracker Red DND-99 were purchased from ThermoFisher Scientific (product numbers M7521 and L7528, respectively) and stored in the dark at -20 °C upon receipt, per manufacturer recommendations. Prior to use, reagents were reconstituted to in DMSO to 1 mM and aliquoted. Unused reagent was returned to -20 °C for storage.

Carbonylcyanide-3-chlorophenylhydrazone (CCCP) was purchased from VWR/Alfa Aesar (product number AAAL06932-MC) and stored at 4 °C upon receipt per manufacturer recommendations.

HeLa cells were cultured in Gibco™ DMEM High Glucose GlutaMAX™ Supplement (ThermoFisher Scientific), supplemented with 10% (v/v) EquaFETAL (Atlas Biologicals), 1% (v/v) 100 mM Sodium Pyruvate Solution (Lonza) or 100 mM HyClone™ Sodium Pyruvate Solution (Fisher Scientific), 1% (v/v) 100x MEM Non-Essential Amino Acid Solution (Lonza) or 100x HyClone™ Non-Essential Amino Acids NEAA (Fisher Scientific), 1% (v/v) HEPES (1 M) (Thermo Fisher Scientific), and 1% (v/v) Penicillin-Streptomycin Mixture (10K/10K) (Lonza). Gibco™ 10X phosphate-buffered saline (PBS), pH 7.4 was diluted to 1X prior to use. Gamma sterilized 0.22 µm poly(ethersulfone) Millex-GP syringe filters were purchased from Millipore Sigma (product number SLGPR33RS) and used to filter particles from solutions used prior to organelle flow cytometry (FCM). Heparin sodium salt from porcine intestinal mucosa (≥100 IU/mg) (Alfa Aesar/VWR) was used to remove extracellular complexes from the cell surfaces. Zombie Violet Fixable Viability Kit (BioLegend) was used to assess cellular viability in FCM cytometry experiments.

5.2.2 Instrumentation and Software

^{1}H nuclear magnetic resonance spectra were recorded for all monomers and polymers at 500 MHz using a Bruker Ascend Nuclear Magnetic Resonance Spectrometer retrofitted with a cryoprobe. Chemical shifts (δ) are listed in ppm and coupling constants (*J*) in Hz. Splitting patterns were described as either s, singlet; d, doublet; dd, doublet of doublets; t, triplet; tt triplet of triplets; dt, doublet of triplets; q, quartet; or m, multiplet; or br, broad. Analysis of NMR spectra was performed using MestReNova v. 6.1.0-6224 (Mestrelab Research).

Mass spectra were obtained at the University of Massachusetts Mass Spectrometry Center and recorded using a Bruker MicroTOF-II Mass Spectrometer.

Gel permeation chromatography (GPC) chromatograms were recorded for all polymers using an Agilent Technologies 1260 Infinity series system equipped with refractive index (RI) and ultraviolet (UV) detectors, a PL Gel 5 μm guard column, two PL Gel 5 μm analytical Mixed-C columns, and a PL Gel 5 μm analytical Mixed-D column. These columns were connected in series and incubated at 40 °C. THF was used as the eluent at a flow rate of 1 mL/min. Toluene was used as the flow marker. The instrument was calibrated with both poly(methyl methacrylate) and polystyrene standards. All samples were prepared at ~3 mg/mL and filtered into Agilent Technologies autosampler vials using 0.45 μm PTFE syringe filters prior to injection.

Confocal images were obtained using a Nikon scanning confocal microscope at the University of Massachusetts Amherst Light Microscopy Facility. HeLa cells were transduced in tissue-culture treated 8-well μ-slides purchased from Ibidi (product number

80826) and visualized using a 60x objective with immersion oil. FITC, MitoTracker Red/LysoTracker Red, and AF647 were excited with 488 nm, 561 nm, and 640 nm lasers, respectively. Confocal microscopy data was analyzed to obtain fluorophore correlation coefficients using the JACoP plugin[9] v. 2.1.1 in ImageJ v. 1.53c.

FCM experiments were conducted using a BD Dual LSRFortessa™ flow cytometer and FACSDiva as the acquisition software. Zombie Violet, FITC, RFP, MitoTracker Red, and AF647 were excited with 405 nm, 488 nm, 561 nm, 561 nm, and 640 nm lasers, respectively. Fluorescence emission for the dyes were collected using 450/50, 530/30, 585/15, 610/20, and 670/30 band pass filters, respectively. Fluorescence signals of 10,000 cells or (at minimum) ~2,000 mitochondria were collected for every sample. Multicolor compensation and data analysis were performed using FlowJo v. 10.0.7r2 (Tree Star).

FITC fluorescence emission curves were collected for all carriers using a BioTek Instruments Synergy Mx plate reader and Gen5 1.10 as the acquisition software. Samples were measured at 25 °C in Ultra Cruz 96 well sterile poly(styrene) black tissue culture plates with clear flat bottoms purchased from Santa Cruz Biotechnology, Inc.

5.2.3 Methods

5.2.3.1 Synthesis

The following FITC-labelled polymeric carriers were characterized in previous reports: **dG$_{10}$-FITC**, **PGON$_{20}$-FITC**, **MeG$_{10}$-FITC**, and **MePh$_{10}$-*b*-dG$_5$-FITC**.[45,51] The **CyG** monomer and its three resulting polymers, **CyG$_5$-FITC**, **CyG$_{10}$-FITC**, and **CyG$_{10}$-EVE** (quenched with ethyl vinyl ether, no fluorescent label) are reported here for the first time.

5.2.3.1.1 Monomer Synthesis

In general, the **CyG** monomer was prepared following previously reported procedures.[56,57] A brief overview is provided here (Figure 5.1).

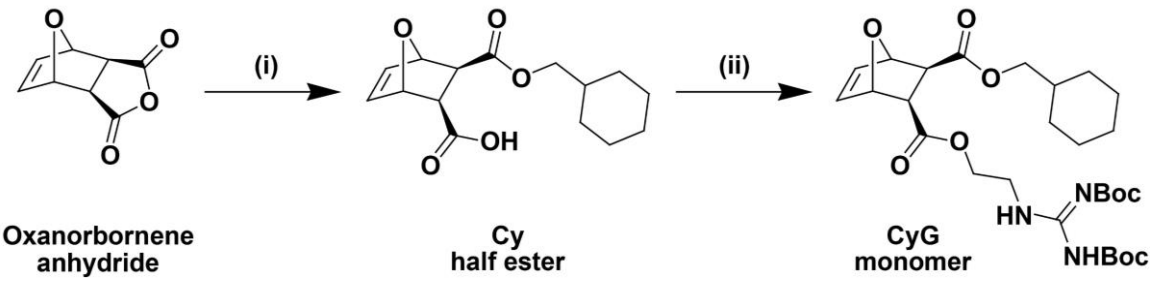

Figure 5.1: Synthesis of the asymmetric **CyG** monomer. (i) Cyclohexane methanol, DMAP, CH_2Cl_2, room temperature, overnight; (ii) 1,3,-di-boc-2-(2-hydroxyethyl)guanidine, DMAP, EDC, CH_2Cl_2, 0 °C to room temperature, overnight.

Cy half ester: One molar equivalent of **oxanorbornene anhydride** and 0.1 molar equivalents of 4-dimethylaminopyridine (DMAP) were added to an oven dried two-neck round bottom flask (RBF) under nitrogen gas and dissolved in sufficient freshly distilled CH_2Cl_2 dried over CaH_2. 1.2 molar equivalents of cyclohexane methanol were added via syringe. The reaction was stirred overnight under nitrogen at room temperature. The reaction was then concentrated by rotary evaporation to remove CH_2Cl_2, and the product was subsequently recrystallized from a 1:1 (v/v) mixture of chloroform:hexanes. The pure product was then collected by vacuum filtration and dried under vacuum to obtain a white solid.

42% yield

^{1}H NMR (500 MHz, $CDCl_3$) δ 6.47 (d, *J* = 26.2 Hz, 1H), 6.47 (d, *J* = 14.7 Hz, 1H), 5.33 (s, 1H), 5.25 (s, 1H), 3.99 – 3.83 (m, 2H), 2.90 – 2.81 (m, 2H), 1.68 (comp, 6H), 1.20 (comp, 3H), 1.02 – 0.90 (m, 2H).

CyG monomer: One molar equivalent of the **Cy half ester**, 0.1 molar equivalents of DMAP, and 1.2 molar equivalents of 1,3,-di-boc-2-(2-hydroxyethyl)guanidine were added to an oven dried two-neck RBF under nitrogen gas and dissolved in sufficient freshly distilled CH_2Cl_2 dried over CaH_2. The solution was then cooled down to 0 °C in an ice bath and 1.2 molar equivalents of 1-ethyl-3-(3-dimethylaminopropyl)carbodiimide (EDC) were added. The solution was allowed to stir overnight under nitrogen and gradually return to room temperature. The diester product was isolated by normal phase flash chromatography with silica using a 90/10 (v/v) mixture of CH_2Cl_2/ethyl acetate (EtOAc) as the eluent. Pure fractions were combined and concentrated using rotary evaporation. The sample was dried under vacuum overnight at room temperature to obtain a white solid.

68% yield

^{1}H NMR (500 MHz, $CDCl_3$) δ 11.48 (s, 1H), 8.62 – 8.49 (m, 1H), 6.50 – 6.42 (m, 2H), 5.29 (s, 1H), 5.27 (s, 1H), 4.32 – 4.17 (m, 2H), 3.98 – 3.81 (m, 2H), 3.80 – 3.62 (m, 2H), 2.86 – 2.79 (m, 2H), 1.68 (comp, 6H), 1.56 (s, 9H), 1.50 (s, 9H), 1.19 (comp, 3H), 0.95 (comp, 2H).

HR-MS (FAB) m/z $[M+H]^+$: 566.3078 (calc.), 566.4246 (found)

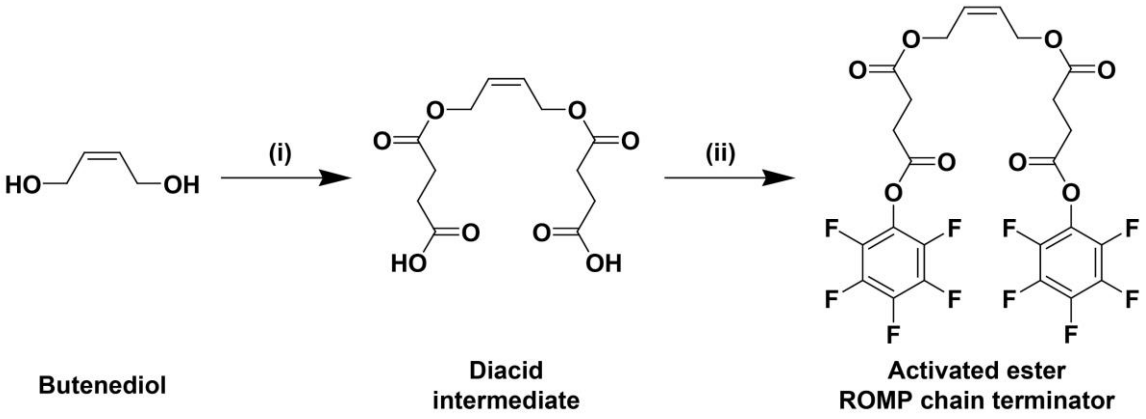

Figure 5.2: Synthesis of the activated ester ROMP chain terminator. (i) Succinic anhydride, DMAP, THF, 72 °C, reflux, overnight; (ii) pentafluorophenol, DMAP, EDC, CH_2Cl_2, 0 °C to room temperature, overnight.

5.2.3.1.2 Activated Ester Synthesis

The activated ester ROMP chain terminating agent (AE) was synthesized according to previously reported procedures.[45,51,58] The process is briefly outlined below (Figure 5.2).

Diacid intermediate: 2.1 molar equivalents of succinic anhydride were added to an oven-dried two-neck RBF and dissolved in sufficient tetrahydrofuran (THF) distilled from sodium/benzophenone under nitrogen. To this solution, 1 molar equivalent of *cis*-1,4-butenediol and 0.025 equivalents of DMAP were added. The reaction was run overnight at 72 °C under reflux. THF was then removed by rotary evaporation and the product was recrystallized from a mixture of 19:1 (v/v) diethyl ether:acetone. The pure product was then collected by vacuum filtration and dried overnight under vacuum to obtain a white solid.

63% yield

^{1}H NMR (500 MHz, CD_3CN) δ 5.72 (t, *J* = 4.3 Hz, 2H), 4.66 (d, *J* = 4.3 Hz, 4H), 2.55 (s, 8H).

Activated ester ROMP chain terminator: 1 molar equivalent of the diacid, 2.5 molar equivalents of pentafluorophenol, and 0.25 molar equivalents of DMAP were added to an oven-dried two-neck RBF and dissolved in sufficient freshly distilled CH_2Cl_2 dried over CaH_2. The solution was then cooled down to 0 °C in an ice bath and 2.5 molar equivalents of EDC were added. The solution was allowed to stir overnight under nitrogen and gradually return to room temperature. The reaction mixture was then sequentially washed with a 10 wt. % $KHSO_4$ solution, a saturated $NaHCO_3$ solution, and a saturated NaCl solution (brine). The product was then dried using anhydrous Na_2SO_4, filtered by gravity

filtration, and concentrated by rotary evaporation to remove most of the CH_2Cl_2. The concentrated solution was passed through a small neutral alumina column, using CH_2Cl_2 as the solvent, to remove impurities and concentrated once again by rotary evaporation to remove the CH_2Cl_2. The resulting pure product was dried under vacuum to obtain a white solid.

54% yield

^{1}H NMR (500 MHz, CD_3CN) δ 5.73 (t, *J* = 4.1 Hz, 2H), 4.70 (d, *J* = 4.9 Hz, 4H), 2.98 (t, *J* = 6.5 Hz, 4H), 2.73 (t, *J* = 6.5 Hz, 4H).

5.2.3.1.3 Polymer Synthesis

All polymers were prepared according to previously reported procedures (Figure 5.3).[51,56,58]

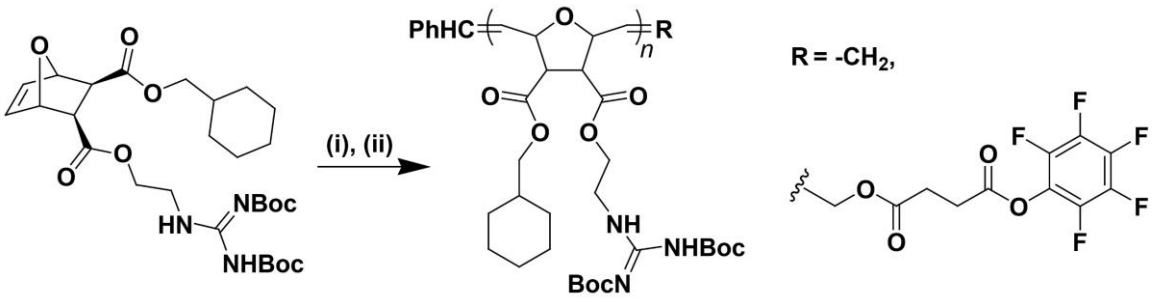

Figure 5.3: Synthesis of Boc-protected polymers used in Chapter 5, terminated with ethyl vinyl ether or an activated ester. (i) G3, CH_2Cl_2, room temperature, 90 min; (ii) ethyl vinyl ether or activated ester ROMP chain terminator, room temperature, overnight.

In brief, 1 molar equivalent of G3 and 5 or 10 molar equivalents the **CyG** monomer (depending on the targeted degree of polymerization) were each dissolved in separate oven-dried Schlenk flasks using freshly distilled CH_2Cl_2 dried over CaH_2. The contents of both Schlenk flasks were put through a minimum of 3 freeze, pump, thaw (FPT) cycles to rigorously degas the monomer and catalyst solutions. After the final FPT cycle, the

contents of the flask containing the monomer were cannulated into the flask containing the stirring G3 solution. This monomer was allowed to polymerize for about 90 minutes. Upon completion, ~20 molar equivalents of AE dissolved in minimal CH_2Cl_2 were injected into the Schlenk flask to terminate the polymerization. In the case of **CyG$_{10}$**, half of the reaction volume was terminated with AE, while the other half was terminated with ~3 mL of ethyl vinyl ether (EVE). This unlabeled analog of the polymer, **CyG$_{10}$-EVE**, was used as a control polymer to investigate the effect of the fluorescent label on delivery outcomes. Upon addition of AE or EVE, a crude aliquot was taken and dried using compressed air for analysis by ^{1}H NMR and THF GPC. This NMR spectrum was used to confirm complete consumption of the monomer. The GPC chromatogram was used to confirm the estimated target molecular weight and narrow dispersity. After stirring overnight with AE or EVE, the crude reaction mixture was concentrated to a solid using rotary evaporation. At this point, each polymer was dissolved in minimal CH_2Cl_2 and loaded onto a small (~15 mL) silica plug column. First, ~25 column volumes of 100% CH_2Cl_2 were eluted and discarded, to remove excess AE (R_f ~ 0.5-0.7). Next, the solvent was switched to 100% EtOAc and ~10 column volumes were eluted to collect the polymer (R_f = 1). The product was then collected by rotary evaporation to remove EtOAc and dried under vacuum overnight to obtain a brown solid. At this point, the polymers were again characterized by ^{1}H NMR and THF GPC to confirm purity, molecular weight, and dispersity of each sample (Table 5.1).

The ^{1}H NMR chemical shifts for each precipitated, Boc-protected polymer are below. The three GPC chromatograms (**CyG$_5$-AE**, **CyG$_{10}$-AE**, and **CyG$_{10}$-EVE**) can be found in Figure 5.4.

Table 5.1: Characterization summary for CPPMs used in Chapter 5 based on THF GPC analysis.

Polymer	Theoretical MW (g/mol)[a]	M_p (g/mol)[b]	M_n (g/mol)[b]	M_w (g/mol)[b]	Đ[b]
CyG$_5$-AE	2,817.86	3,028	2,784	3,051	1.1
CyG$_{10}$-AE	5,235.42	6,305	5,749	6,189	1.1
CyG$_{10}$-EVE	4,939.27	5,465	4,834	5,234	1.1

[a]Theoretical molecular weight based on polymer structure shown in Figure 5.3. [b]Calculated by GPC in THF, 40ºC, flow rate 1 mL/min with polystyrene standards and toluene as the flow marker.

CyG$_5$-AE: ^{1}H NMR (500 MHz, CD_2Cl_2) δ 11.50 (s, 5H), 8.49 (br, 5H), 7.33 (comp, 5H), 5.90 (t*rans*) and 5.72 (*cis*) (br, 12H total), 5.13 (*cis*) and 4.68 (*trans*) (br, 12H total), 4.24 (br, 10H), 3.88 (br, 10H), 3.64 (br, 10H), 3.25 (br, 10H), 2.99 (br, 2H), 2.77 (br, 2H), 1.63 (br, 30H), 1.48 (s, 45H), 1.45 (s, 45H), 1.20 (br, 15H), 0.87 (br, 10H).

CyG$_{10}$-AE: ^{1}H NMR (500 MHz, CD_3CN) δ 11.55 (br, 10H), 8.37 (br, 10H), 7.33 (comp, 5H), 5.85 (*trans*) and 5.66 (*cis*) (br, 22H total), 5.03 (*cis*) and 4.66 (*trans*) (br, 22H total), 4.14 (br, 20H), 3.84 (br, 20H), 3.61 (br, 20H), 3.24 (br, 20H), 2.99 (br, 2H), 2.74 (br, 2H), 1.61 (br, 60H), 1.47 (s, 90H), 1.42 (s, 90H), 1.19 (br, 30H), 0.92 (br, 20H).

CyG$_{10}$-EVE: ^{1}H NMR (500 MHz, CD_3CN) δ 11.53 (br, 10H), 8.37 (br, 10H), 7.33 (comp, 5H), 5.87 (*trans*) and 5.65 (*cis*) (br, 23H total), 5.03 (*cis*) and 4.72 (*trans*) (br, 20H total),

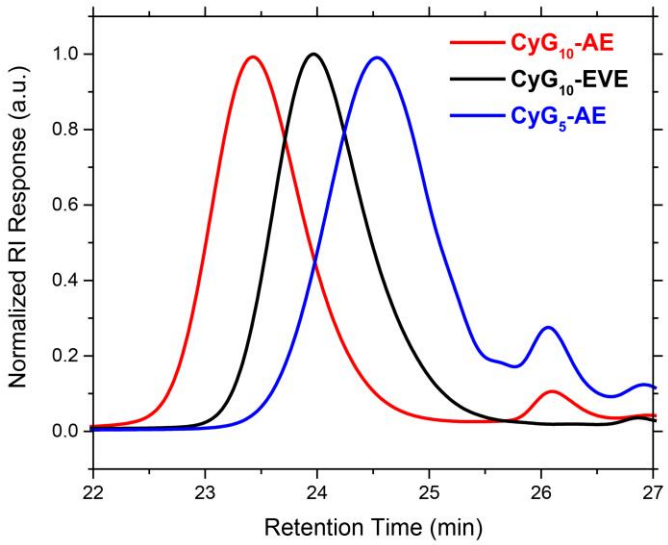

Figure 5.4: GPC traces comparing the molecular weight distributions of the activated ester-terminated, Boc-protected polymers, **CyG$_5$-AE** and **CyG$_{10}$-AE**, and the ethyl vinyl ether-terminated, Boc-protected control polymer, **CyG$_{10}$-EVE**.

4.18 (br, 20H), 3.83 (br, 20H), 3.55 (br, 20H), 3.24 (br, 20H), 1.59 (br, 60H), 1.47 (s, 90H), 1.42 (s, 90H), 1.20 (br, 30H), 0.93 (br, 20H).

5.2.3.1.4 Polymer Fluorescent Labelling

Fluorescent labelling of AE-terminated polymers was performed according to previously published procedures (Figure 5.5).[45,51] All steps were performed in the dark to minimize FITC photobleaching.

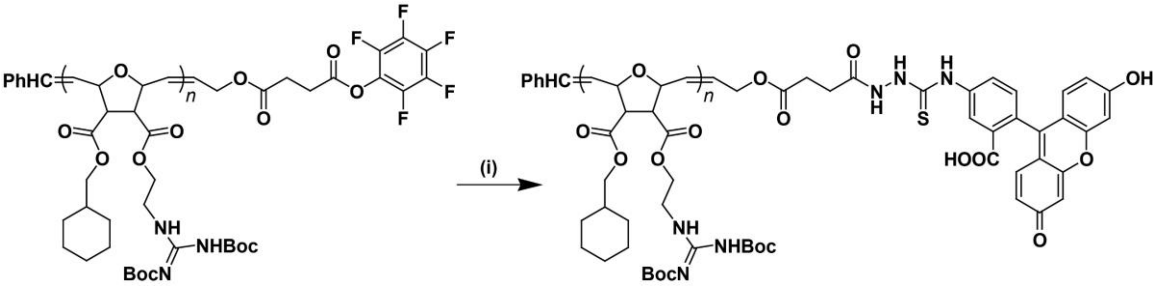

Figure 5.5: Synthesis of Boc-protected FITC-labelled CPPMs from activated ester-functionalized precursors. (i) Fluorescein-5-thiosemicarbazide, DMF, room temperature, 3 days, dark.

In general, 1 molar equivalent of AE-terminated polymer and 2 molar equivalents of FITC were dissolved in sufficient amine-free dimethylformamide (DMF). The reaction was allowed to stir at room temperature for three days. Reaction progress was monitored by ^{1}H NMR, as FITC conjugation could be observed by reductions in peak intensity at both ~9.39 ppm and ~8.85 ppm (in DMF-d_7). At this time, the reaction mixture was concentrated by rotary evaporation to remove DMF and then loaded onto a small silica plug column in 100% EtOAc. The first two column volumes were collected as the pure product, while excess FITC remained on the column. Removal of unreacted FITC was confirmed by the complete disappearance of the ^{1}H NMR peaks at ~9.39 and ~8.85 ppm. The product was then concentrated by rotary evaporation to remove EtOAc and dried under vacuum to obtain an orange solid. The ^{1}H NMR chemical shifts for both FITC-labelled, Boc-protected polymers are below.

CyG$_5$-FITC: ^{1}H NMR (500 MHz, DMF) δ 11.65 (br, 5H), 8.57 (br, 5H), 7.37 (comp, 6H), 6.71 (comp, 6H), 5.95 (*trans*) and 5.76 (*cis*) (br, 12H total), 5.12 (*cis*) and 4.73 (*trans*) (br, 22H total), 4.24 (br, 10H), 3.89 (br, 10H), 3.68 (br, 10H), 3.32 (br, 10H), 3.16 (br, 2H), 2.86 (br, 2H), 1.63 (br, 30H), 1.53 (s, 45H), 1.45 (s, 45H), 1.23 (br, 15H), 0.90 (br, 10H).

CyG$_{10}$-FITC: ^{1}H NMR (500 MHz, DMF) δ 11.66 (br, 10H), 8.55 (br, 10H), 7.44 (comp, 6H), 6.74 (comp, 6H), 5.95 (*trans*) and 5.77 (*cis*) (br, 22H total), 5.13 (*cis*) and 4.74 (*trans*) (br, 22H total), 4.25 (br, 20H), 3.89 (br, 20H), 3.65 (br, 20H), 3.32 (br, 20H), 3.17 (br, 2H), 2.89 (br, 2H), 1.67 (br, 60H), 1.55 (s, 90H), 1.46 (s, 90H), 1.20 (br, 30H), 0.93 (br, 20H).

5.2.3.1.5 Polymer Deprotection

The entire deprotection and purification process was done in the dark for each fluorescently-labelled sample. To remove the Boc protecting groups, each polymer was dissolved in a 4 mL solution of 1:1 CH_2Cl_2:trifluoroacetic acid (TFA) and stirred in a scintillation vial overnight (Figure 5.6). Removal of the Boc groups was confirmed by the disappearance of the two corresponding ^{1}H NMR peaks. The scintillation vials were then filled to halfway with methanol and concentrated using rotary evaporation. This process was repeated up to 7 times to remove traces of TFA by azeotropic distillation. The deprotected polymers were then dissolved in a minimal volume of methanol, diluted in

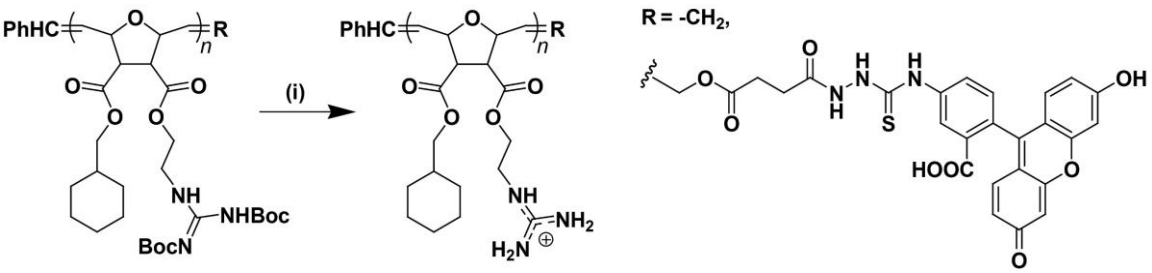

Figure 5.6: Deprotection of Boc-protected polymers used in Chapter 5 to yield cationic guanidinium groups. (i) TFA/CH_2Cl_2 (1:1), room temperature, overnight, dark.

approximately 10 mL of reverse osmosis (RO) water, and loaded into hydrated dialysis membrane tubing (MWCO = 500-1000 Da). All polymers were dialyzed against RO water until the conductivity of the solution outside the bag reached 0.3 µS or lower. Once dialysis was completed, polymer solutions were flash frozen in plastic cups by submerging them in liquid nitrogen. Frozen water was then removed by lyophilization *in vacuo* over the course of 3-5 days.

5.2.3.2 Characterization of Carrier-FITC Brightness

All fluorescent carriers were characterized for their relative FITC emission intensities in order to accurately compare their uptake into cells based on fluorescence. For example, a polymer with half the brightness of another would need to be corrected by a factor of 2 to fairly compare the amount of internalization in delivery experiments. Carriers were stored as 1 mM stock solutions in pure DMSO (**R_9-FITC**, **dG_{10}-FITC**, **$PGON_{20}$-FITC**, **CyG_5-FITC**, **$MePh_{10}$-*b*-dG_5-FITC**, and **CyG_{10}-EVE**) or DMSO with 1% (v/v) acetic acid (AcOH), if not readily soluble in pure DMSO (**MeG_{10}-FITC** and **CyG_{10}-FITC**). The stock solutions were stored in the dark at -20 °C or -80 °C (to minimize the risk of acid-catalyzed hydrolysis of the polymer ester bonds), respectively. All fluorescent carriers were diluted in H_2O (carriers stored in DMSO + AcOH) or H_2O spiked with AcOH (carriers stored in 100% DMSO) such that all carriers reached a final concentration of 2 µM in H_2O + 20 ppm AcOH (v/v). This was done to ensure equal pH among all samples, given the well-documented pH sensitivity of FITC emission.[59] 200 µL of each diluted polymer were pipetted into a 96-well plate and emission spectra were collected from 515-

545 nm (the range of the bandpass filter used for FCM) while exciting FITC at 488 nm. The overlaid spectra can be found in Figure 5.7.

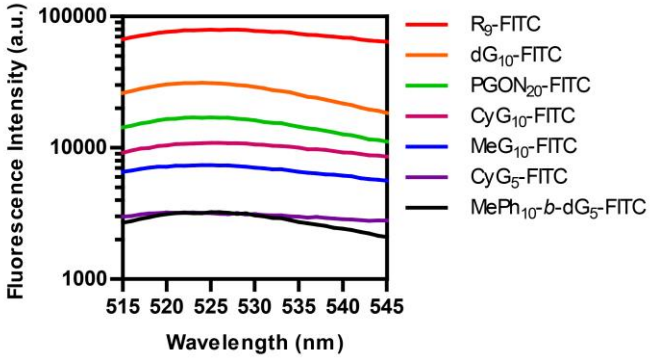

Figure 5.7: Emission spectra from 515 nm to 545 nm (range of flow cytometry FITC bandpass filter) for 2 µM solutions of all FITC-labelled carriers in PBS excited with 488 nm light.

Each emission curve was integrated to determine the total intensity over the measured range, and normalized to the brightest sample (**R_9-FITC**) to obtain the correction factors which account for differences in brightness at equal concentration. These correction factors are summarized in Table 5.2.

Table 5.2: Relative brightness for all FITC-labelled carriers and correction factors used in normalization of flow cytometry median fluorescence intensity (MFI) values.

Carrier	Total FITC Intensity (a.u.)[a]	Brightness Correction Factor[b]
R_9-FITC	2,282,884	1.00
dG_{10}-FITC	825,360	2.77
$PGON_{20}$-FITC	462,345	4.94
MeG_{10}-FITC	208, 921	10.93
$MePh_{10}$-*b*-dG_5-FITC	87,430	26.11
CyG_5-FITC	94,194	24.24
CyG_{10}-FITC	310,442	7.35

[a]Integration of emission spectrum between 515 nm and 545 nm (range of flow cytometry FITC bandpass filter) for a 2 µM solution in PBS of each FITC-labelled carrier. [b]Calculated by dividing total FITC intensity for each carrier by the total FITC intensity of the brightest carrier (R_9-FITC).

5.2.3.3 CPPM and CPPM:IgG Internalization

5.2.3.3.1 CPPM Subcellular Localization by Confocal Microscopy

All carriers were evaluated for colocalization with mitochondria using MitoTracker Red following their internalization into HeLa cells without cargo. In general, cells were

seeded 24 hours prior to delivery at a density of 8,000 cells/well in 8-well microscopy slides. On the day of the experiment, the medium was aspirated from each well and replaced with 200 µL fresh DMEM. 1 mM peptide and polymer stock solutions were diluted appropriately in sterile Milli-Q H_2O to achieve final volumes of 50 µL with concentrations of 10 µM **R_9-FITC**, 500 nM **dG_{10}-FITC**, 1000 nM **$PGON_{20}$-FITC**, 500 nM **MeG_{10}-FITC**, 250 nM **$MePh_{10}$-*b*-dG_5-FITC**, 1500 nM **CyG_5-FITC**, and 375 nM **CyG_{10}-FITC**. Importantly, these dilutions were spiked with appropriate volumes of DMSO and AcOH, such that all wells contained equivalent final concentrations of DMSO (0.2% v/v, dictated by the well with the highest DMSO concentration, **CyG_5-FITC**) and AcOH (1 ppm v/v, dictated by the well with the highest AcOH concentration, **MeG_{10}-FITC**) following addition to cell medium. The 50 µL polymer dilutions were then added dropwise to the wells containing cells to achieve final delivery volumes of 250 µL and carrier concentrations of 2 µM, 100 nM, 200 nM, 100 nM, 50 nM, 300 nM, and 75 nM, respectively. These concentrations were selected based on earlier optimization experiments in which FCM was used to determine conditions which led to roughly equivalent levels of uptake (i.e., intracellular FITC fluorescence) across all carriers (data not shown). The cells were incubated with the polymers in the dark for ~24 h at 37 °C in 5% CO_2, to allow sufficient time for both polymer internalization and any subsequent subcellular trafficking to occur. Following delivery, the medium was aspirated from each well and each sample was washed three times to remove extracellular polymer by incubating for 5 min each time with 250 µL heparin solution (20U/mL in PBS). After the final wash, each sample was incubated with 250 µL of 25 nM MitoTracker Red (diluted in DMEM) in the dark for 15 min at 37 °C and 5% CO_2. Following this incubation, the

staining solution was replaced with fresh medium and the cells were immediately imaged by the confocal microscopy.

CyG$_{10}$-FITC was also evaluated for colocalization with endo/lysosomes using LysoTracker Red. This experiment was carried out in an identical manner to the mitochondrial colocalization experiment, with the following major differences. Cells were seeded at a density of 12,000/well. On the day of the experiment, the medium was aspirated from each well and replaced with 400 µL fresh DMEM. **CyG$_{10}$-FITC** was diluted to 400 nM in H_2O to reach a volume of 100 µL and then added to cells. The final concentrations of DMSO and AcOH were 0.01 % (v/v) and 0.8 ppm (v/v), respectively, following addition to cell medium. The 100 µL polymer dilutions were then added dropwise to the wells containing cells to achieve final delivery volumes of 500 µL and a **CyG$_{10}$-FITC** concentration of 80 nM. Cells were incubated with the polymer for 16 h, after which they were immediately washed, stained (using 250 µL of 50 nM LysoTracker Red, diluted in DMEM), and imaged.

ImageJ was used to calculate the Pearson's Correlation Coefficient (PCC) and Manders's Coefficients (M_1 and M_2). Importantly, these coefficients were calculated following exclusion of background noise using thresholding tools in order to avoid artificially positive correlations which are known to otherwise arise.[9,10] The two micrographs to be compared (one from each fluorophore channel of interest) were imported into the software. The Pearson's coefficient, M_1 & M_2 coefficients, and Costes' automatic threshold analyses were then performed using the JACoP plugin.[9] During analysis of the first sample in each experimental set, the threshold value for each channel was manually increased from zero until all background noise was excluded from analysis. For

consistency, these same manual threshold values were applied during each subsequent analysis of images from the same experiment, (i.e., identical threshold values were set for all micrographs acquired with the same fluorophore and microscope settings). The calculated Pearson's Coefficient (using the Costes' automatic threshold) and Manders's Coefficients (using the manually-set threshold values) are reported in this chapter.

5.2.3.3.2 CPPM:IgG Subcellular Localization by Confocal Microscopy

To evaluate whether complexation with cargo altered mitochondrial localization of **CyG$_{10}$-FITC**, the CPPM was used to deliver IgG-AF647 into HeLa cells, which were subsequently imaged by confocal microscopy. This experiment was carried out in an identical manner to the CPPM-FITC mitochondrial colocalization experiments, with the following major differences. Cells were seeded at a density of 8,000/well 48 h in advance. Stock IgG-AF647 (2 mg/mL) was diluted 1:16 in H_2O to create a working solution. **CyG$_{10}$-FITC** stock solution was diluted 1:40 in H_2O to create a 25 µM working solution. Complexes were prepared by combining appropriate volumes of H_2O, IgG-AF647, and **CyG$_{10}$-FITC** (in that order) to make a 50 µL solution of 10 µM **CyG$_{10}$-FITC** and 250 nM IgG-AF647. The solution was vortexed briefly to mix and incubated 30 min in the dark at RT. The 50 µL solution was then added dropwise to a well containing cells and 200 µL DMEM to achieve a final delivery volume of 250 µL and concentrations of 2 µM **CyG$_{10}$-FITC** and 50 nM IgG-AF647 (1:40 ratio). The final concentrations of DMSO and AcOH were 0.2 % (v/v) and 20 ppm (v/v), respectively. Cells were incubated with the complexes for 4 h, after which they were immediately washed, stained, and imaged as described previously. Fluorophore colocalization coefficients (PCC, M_1, and M_2) were calculated for these experiments as described in the previous section.

5.2.3.3.3 CPPM:IgG Cellular Internalization by Flow Cytometry

To assess the ability of each carrier to internalize protein through the plasma membrane, IgG-AF647 delivery experiments were performed in HeLa cells and intact cells were analyzed by FCM. The impact of delivery on mitochondrial polarization was simultaneously assessed by staining samples with MitoTracker Red, whose fluorescence intensity is dependent on mitochondrial membrane potential.[28,60–63] HeLa cells were seeded in 12-well plates 24 hours prior to the start of the experiment at a density of 30,000 cells per well in 1 mL DMEM. On the day of the experiment, the medium was aspirated from each well and replaced with 0.8 mL fresh DMEM. Stock IgG-AF647 (2 mg/mL) was diluted 1:20 in H_2O to create a working solution. 1 mM carrier stock solutions were diluted 1:10 in H_2O to achieve 100 µM working solutions. Complexes were prepared by combining appropriate volumes of H_2O, IgG-AF647, and CPP(M)-FITC (in that order) to make a 200 µL solution of 10 µM CPP(M)-FITC and 250 nM IgG-AF647. The solutions were vortexed briefly to mix and incubated 30 min in the dark at RT. The 200 µL solutions were then added dropwise to wells containing cells in 0.8 mL DMEM to achieve final delivery volumes of 1 mL and concentrations of 2 µM CPP(M)-FITC and 50 nM IgG-AF647 (1:40 ratio). The final concentrations of DMSO and AcOH were 0.2 % (v/v) and 20 ppm (v/v), respectively. The cells were incubated with the complexes in the dark for 4 h at 37 °C in 5% CO_2. After the incubation period, the medium was aspirated from each well, and the cells were rinsed with PBS. The cells were then incubated with 500 µL of 25 nM MitoTracker Red solution (diluted in DMEM) in the dark for 15 min at 37 °C in 5% CO_2. Following this incubation, the medium was once again aspirated, the cells were again rinsed with PBS, and 200 µL 0.25% trypsin-EDTA solution was added to lift the cells from

the wells. After incubating with trypsin for 5 min, 1 mL DMEM was added to dilute and quench the trypsin and the cells were transferred to microcentrifuge tubes and collected by centrifugation at 400 x g. The samples were then washed 3 times with 800 μL of heparin (20 U/mL in PBS) to remove any extracellular or surface-bound complexes, in accordance with previously published procedures.[64] The cells were then resuspended in 100 μL Zombie Violet (diluted 1:1000 in PBS) and incubated in the dark for 15 minutes at room temperature. Following this incubation, 100 μL PBS was added to each sample dilute the dye, and the samples were centrifuged for 5 min at 400 x g. Finally, the samples were resuspended in 200 μL FACS buffer (0.2% by weight BSA in PBS) and analyzed by FCM, in which data for 10,000 cells were collected.

Fluorescence compensation between Zombie Violet, FITC, MitoTracker Red, and AF647 was performed using appropriate unstained and single stain (SS) samples. Gating was performed using untreated and fluorescence minus one (FMO) controls, in which all but one fluorophore were present. A summary of all controls and their treatment conditions is presented in Table 5.3. Samples were prepared as described above with the substitutions or omissions noted in the table. Cells in the Zombie SS (Dead) control were processed

Table 5.3: Treatment combinations of HeLa cells to achieve appropriate controls, including single stain (SS) and fluorescence minus one (FMO) controls for compensation and gating in whole-cell flow cytometry experiments.

Control Sample	CPPM	Cargo	Mito Labelling	Viability
Unstained	--	--	--	--
Untreated	--	--	MitoTracker	Zombie
Zombie SS (Live)	--	--	--	Zombie
Zombie SS (Dead)	--	--	--	Zombie (+Heat Shock)
FITC SS	CyG_{10}-FITC	IgG	--	--
MitoTracker Red SS	--	--	MitoTracker	--
FITC FMO	CyG_{10}-EVE	IgG-AF647	MitoTracker	Zombie
AF647 FMO	CyG_{10}-FITC	IgG	MitoTracker	Zombie

with an added heat shock step (2 min at 65 °C) immediately prior to staining with Zombie Violet.

The sensitivity of MitoTracker Red staining to mitochondrial membrane potential was tested in a separate control experiment in which cells were treated with 10 or 50 µM CCCP, a common mitochondrial uncoupling reagent, prior to staining with MitoTracker Red.[26,60,62,63,65–70] In this experiment, HeLa cells were seeded 24 h in advance in a 12-well plate at a density of 60,000 per well. CCCP was dissolved in PBS to make a 50 µM stock solution with pH = 7.5. On the day of the experiment, the medium was aspirated from each well and replaced with 1 mL of DMEM, 50 µM CCCP, or 10 µM CCCP (diluted in DMEM), depending on the condition to be tested. Cells were incubated with these solutions for 15 min at 4 °C, at which point the solution was aspirated and replaced with a 1 mL solution of 25 nM MitoTracker Red (diluted in DMEM). Cells were incubated with MitoTracker Red for 15 min at 4 °C, at which point they were rinsed with PBS and lifted by incubating 5 min with 200 µL of 0.25% trypsin-EDTA. At the end of the incubation, 1 mL DMEM was added to dilute and quench the trypsin and the cells were transferred to microcentrifuge tubes and collected by centrifugation at 400 x g. Pellets were resuspended in 200 µL FACS buffer and analyzed by FCM, in which data for 10,000 cells were collected.

5.2.3.3.4 CPPM:IgG Mitochondrial Internalization by Organelle Flow Cytometry (Freeze/Thaw Method)

To assess the ability of each carrier to transport cargo through the mitochondrial membrane following cellular internalization, IgG-AF647 delivery experiments were performed in HeLa cells and lysed cells were analyzed by organelle FCM. By transfecting

the cells with MitoRFP prior to performing the experiment, individual mitochondria could be distinguished from other organelles during FCM. IgG-AF647 delivery for mitochondrial internalization was performed in much the same way as IgG-AF647 delivery for cellular internalization, with the following exceptions.

HeLa cells were seeded in 24-well plates 48 hours prior to the start of the experiment at a density of 25,000 cells per well in 1 mL DMEM. 24 h later, the medium was aspirated and replaced with 200 μL fresh DMEM containing 6 μL of MitoRFP (~20 viral particles per cell). Wells were gently mixed by tilting the plate back and forth. The plate was returned to the incubator to allow the baculovirus to transduce the cells, causing them to express and traffic RFP to the mitochondria. After 24 h, the medium was aspirated from each well and replaced with 0.4 mL fresh DMEM. Complexes were prepared in 100 μL volumes in the manner described previously and added dropwise to cells to achieve final delivery volumes of 0.5 mL. After the 4 h incubation period, the medium was aspirated from each well, and the cells were rinsed with PBS (filtered through 0.22 μm PES membranes to reduce the risk of introducing small particles and improve visualization of organelles by FCM). The cells were then incubated with 100 μL filtered 0.25% trypsin-EDTA solution to lift the cells from the wells. After incubating with trypsin for 5 min, 0.5 mL filtered DMEM was added to dilute and quench the trypsin and the cells were transferred to microcentrifuge tubes and collected by centrifugation at 400 x g. The samples were then washed 3 times with 400 μL of heparin (20 U/mL in filtered PBS) to remove any extracellular or surface-bound complexes, in accordance with previously published procedures.[64] The cells were then resuspended in 500 μL filtered mitochondria isolation buffer (MIB, 250 mM sucrose, 1 mM EDTA, and 10 mM HEPES in H_2O, pH =

7.5) and transferred to cryotubes. The cryotubes were then subjected to three freeze/thaw cycles in liquid nitrogen (1 cycle = 1 min in liquid nitrogen followed by 1 min in RT water) to rupture the plasma membranes, releasing free subcellular components into solution, including intact mitochondria.[17,71,72] After the final freeze cycle, the cell solutions were allowed to fully thaw. From this point, all steps leading up to FCM were performed on ice (with the exception of centrifugation, which was done at 4 °C). The thawed cell lysates were transferred to microcentrifuge tubes and centrifuged 10 min at 700 x g to pellet any remaining intact cells and nuclei.[73,74] After centrifugation, the supernatants were transferred to FACS tubes and analyzed by FCM, in which data for a minimum of ~2,000 mitochondria were collected.

Fluorescence compensation between FITC, RFP, and AF647 was performed using appropriate unstained and single stain (SS) samples. Gating was performed using untreated and fluorescence minus one (FMO) controls, in which all but one fluorophore were present. A summary of all controls and their treatment conditions is presented in Table 5.4. Samples were prepared as described above with the substitutions or omissions noted in the table.

Table 5.4: Treatment combinations of HeLa cells to achieve appropriate controls, including single stain (SS) and fluorescence minus one (FMO) controls for compensation and gating in organelle flow cytometry experiments.

Control Sample	Mito Labelling	CPPM	Cargo
Unstained	--	--	--
FITC SS	--	CyG_{10}-FITC	IgG
RFP SS (Untreated)	MitoRFP	--	--
AF647 SS	--	CyG_{10}-EVE	IgG-AF647
FITC FMO	MitoRFP	CyG_{10}-EVE	IgG-AF647
RFP FMO	--	CyG_{10}-FITC	IgG-AF647
AF647 FMO	MitoRFP	CyG_{10}-FITC	IgG

5.2.3.3.5 CPPM:IgG Mitochondrial Internalization by Organelle Flow Cytometry (Reagent-Based Method).

To validate the mitochondrial internalization results from the previous experiment, IgG-AF647 delivery was repeated for the three most successful carriers (**MePh$_{10}$-*b*-dG$_5$-FITC**, **CyG$_5$-FITC**, and **CyG$_{10}$-FITC**) using a reagent-based cell lysis followed by differential centrifugation to obtain a purer population of mitochondria prior to organelle FCM. This experiment was performed in an identical manner to the previous mitochondrial internalization experiment with the following exceptions. 48 h prior to the experiment, cells were seeded in a 12-well plate at a density of 30,000/well in 1 mL DMEM. 24 h later, the medium was replaced with 500 µL DMEM containing 12 µL MitoRFP (~20 viral particles/cell). Another 24 h later, then medium was replaced once again with 0.8 mL fresh DMEM. Complexes were prepared in volumes of 200 µL and added to the 0.8 mL for final delivery volumes of 1 mL. Following the 4 h incubation, cells were rinsed with filtered PBS, lifted with 200 µL filtered trypsin, and washed 3 times with 800 µL filtered heparin solution. At this point, the Mitochondria Isolation Kit for Cultured Cells (ThermoFisher Scientific) was used following the reagent-based method. Briefly, pellets were resuspended in 200 µL filtered Reagent A and vortexed at medium speed for 5 s, followed by incubation on ice for 2 min. After the incubation, 2.5 µL Reagent B was added to each sample. The tubes were then incubated on ice for 5 min total, vortexing at maximum speed for 5 s every 1 min. Following this incubation, 200 µL filtered Reagent C was added to each sample and the tubes were inverted several times to mix. Next, the cells were centrifuged 10 min at 700 x g and 4 °C to pellet any remaining intact cells and nuclei. The supernatants were transferred to fresh microcentrifuge tubes and centrifuged 15 min at 3,000 x g and 4 °C to pellet a fraction of purified heavy

mitochondria (3,000 x g was used in lieu of 12,000 x g, which would pellet both heavy and light mitochondria but contain more lysosomal and peroxisomal contaminants[74]). The supernatants were discarded and the mitochondrial pellets were washed by resuspending with 200 µL filtered Reagent C and centrifuging again for 15 min at 3,000 x g and 4 °C. The pellets were resuspended in 400 µL filtered Reagent C, transferred to FACS tubes on ice, and immediately analyzed by organelle FCM, in which data for a minimum of ~2,000 mitochondria were collected. Fluorescence compensation between FITC, RFP, and AF647 was performed as described in the previous section using the same controls summarized in Table 5.4.

5.2.3.4 Gating Strategy for Organelle Flow Cytometry

The gating strategy used for quantifying intramitochondrial delivery by organelle FCM is illustrated in Figure 5.8. In brief, samples were first gated on a log-log side scatter (SSC) vs. forward scatter (FSC) plot to distinguish smaller organelles from nuclei and remaining intact cells. This was done by comparing an untreated sample to another untreated sample in which the 700 x g centrifugation step was omitted, such that the nuclei could be easily located and gated out. The RFP fluorescence minus one (FMO) control (containing all fluorophores except RFP) was then used to isolate mitochondria by subgating the subcellular, non-nuclear population on a SSC vs. compensated RFP fluorescence plot. Single mitochondria were differentiated from doublets by further subgating this mitochondrial population on a FSC-height vs. FSC-area plot.[75] Finally, mitochondria positive for polymer and cargo were identified by subgating the mitochondrial singlet population on both FITC and AF647 fluorescence histograms. In both cases, gating was performed using the appropriate FMO control samples.

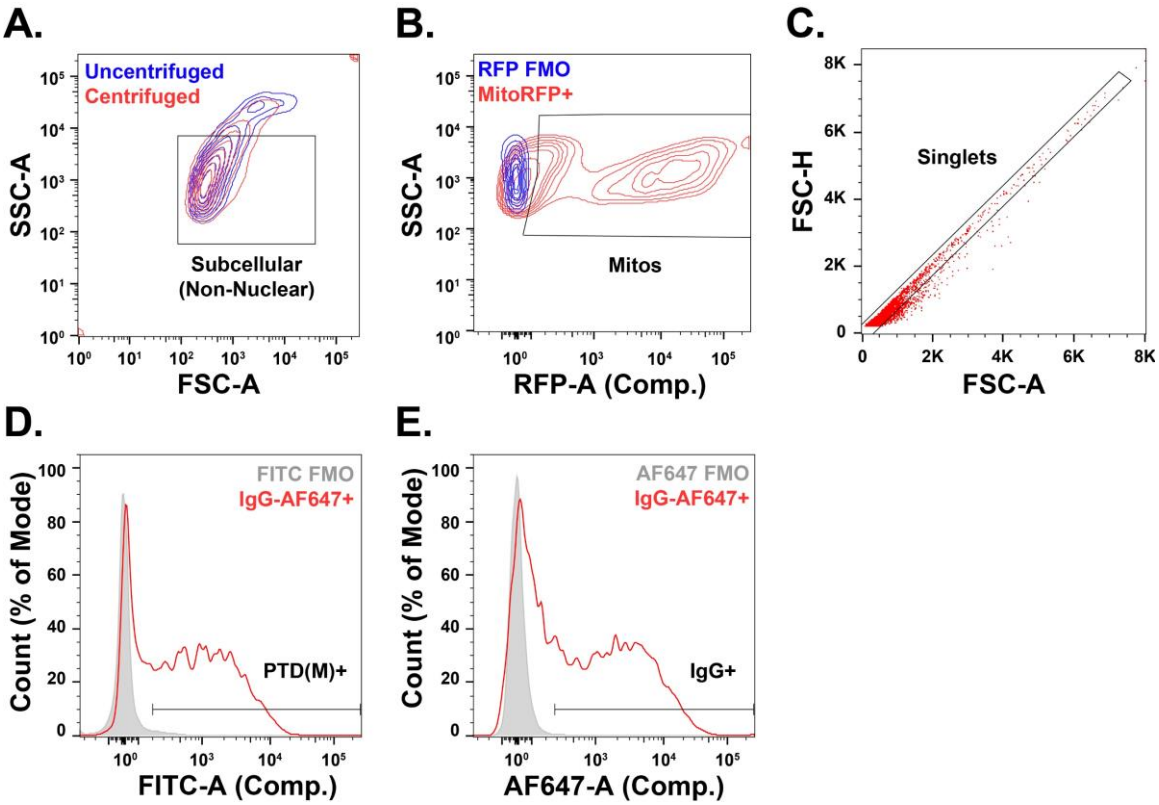

Figure 5.8: Flow cytometry gating strategy for evaluation of intramitochondrial delivery by organelle flow cytometry. (A) Discrimination of organelles smaller in size than nuclei based on the forward and side scatter of centrifuged and uncentrifuged samples. (B) Discrimination of mitochondria from other non-nuclear organelles based on side scatter and compensated RFP fluorescence of untreated and MitoRFP-transfected samples. (C) Discrimination of single mitochondria from doublets based on forward scatter signal area to height ratio. (D) Gating of CPP(M)+ mitochondria based on compensated FITC fluorescence of the FITC FMO and a delivery sample. (D) Gating of IgG+ mitochondria based on compensated AF647 fluorescence of the AF647 FMO and delivery sample.

5.3 Results and Discussion

5.3.1 Non-Covalent Carrier Design

A series of CPPM-fluorescein-5-thiosemicarbazide (CPPM-FITC) conjugates, including several previously reported CPP-inspired carriers (**dG$_{10}$-FITC**, **PGON$_{20}$-FITC**, **MeG$_{10}$-FITC**, and **MePh$_{10}$-*b*-dG$_5$-FITC**) and two new MPP-inspired carriers (**CyG$_5$-FITC** and **CyG$_{10}$-FITC**), were synthesized to contain systematic variations in length, cationic charge density, and hydrophobicity (Scheme 5.1). Details regarding the synthesis, labelling, and characterization of the two new cyclohexyl-guanidine carriers can be found

in Section 1.2 Materials and Methods. A common fluorescently-labelled CPP (**R$_9$-FITC**) and a CPPM with no fluorophore (**CyG$_{10}$-EVE**) were also included as control carriers.

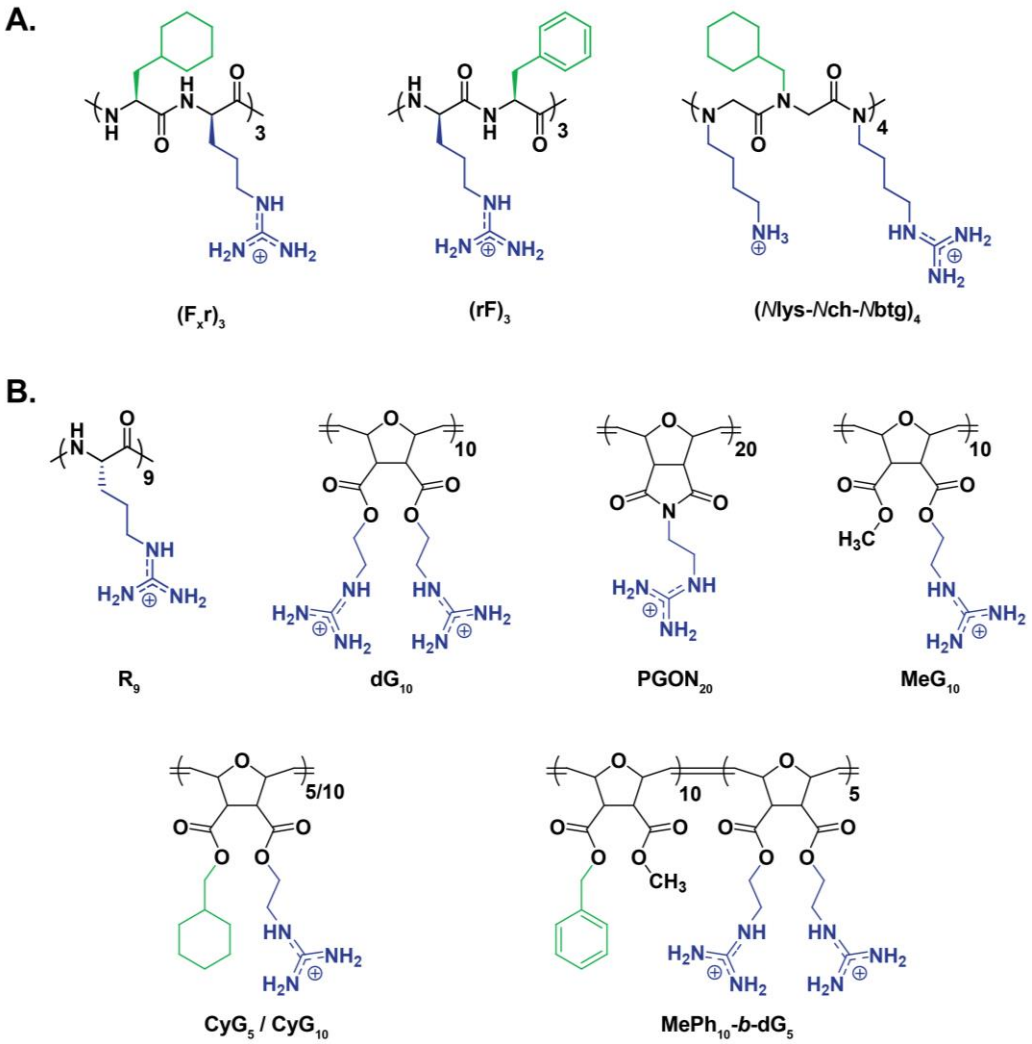

Scheme 5.1: Chemical structures of (A) several successful mitochondria penetrating peptides (MPPs) and (B) CPPMs selected for use in Chapter 5. The MPPs depicted here served as the direct inspiration for the cyclohexyl-guanidine (**CyG$_n$**) CPPMs used in this study.[34,43,44]

5.3.2 Cellular Internalization of CPPM:IgG Complexes

For any given carrier, intramitochondrial concentration is intrinsically linked to cytoplasmic concentration; thus, assessing cellular uptake is a critical prerequisite to understanding subcellular delivery. That is, disparities in mitochondrial delivery might be due to differences in ability to translocate the plasma membrane, the mitochondrial double membrane, or a combination of both. CPPM-FITC conjugates were incubated with

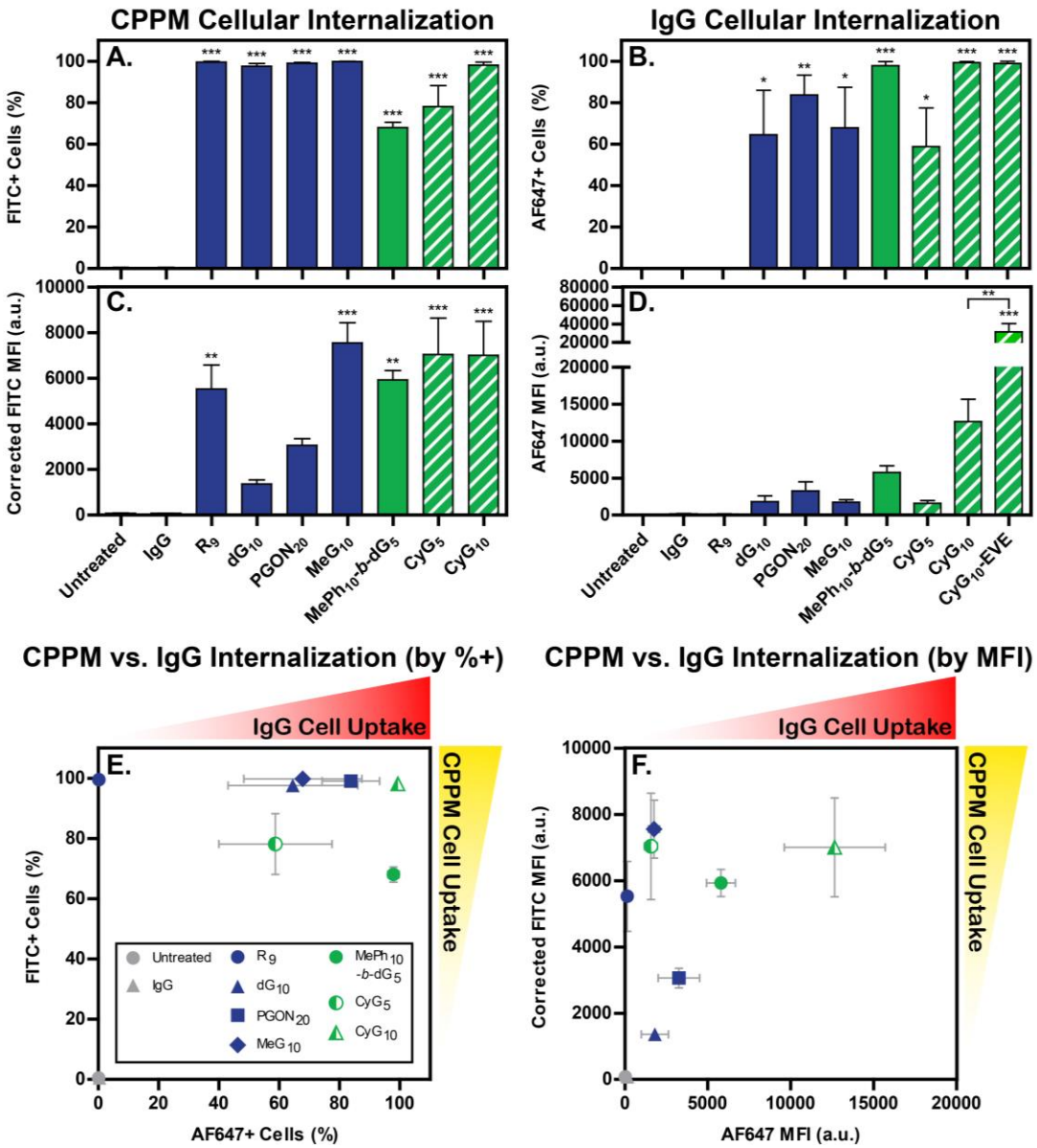

Figure 5.9: Uptake of CPPM-FITC:IgG-AF647 complexes into HeLa cells. Blue and green data represent delivery using CPPMs lacking and containing hydrophobic side-chains, respectively. Hatched green data indicate polymers with a pseudo-alternating side-chain arrangement (as opposed to a block architecture, indicated by solid green). Data are presented as: the percentage of live cells positive for FITC-conjugated CPPM or AlexaFluor (AF)647-conjugated IgG (A and B, respectively), the median FITC or AF647 fluorescence intensity (MFI) of the entire live-cell population, proportional to the quantity of carrier or cargo internalized (C and D, respectively), and the composite FITC and AF647 data, comparing cellular uptake of the carrier and cargo by percent positive or MFI (E and F, respectively). Relative carrier/cargo uptake provide important information regarding the carrier's ability to remain associated with its cargo, critical for its transport across the plasma membrane. Importantly, FITC MFI values have been corrected to account for differences in fluorophore brightness resulting from different degrees of polymer end-labeling efficiency (see Section 5.2.3.2 Characterization of Carrier-FITC Brightness for details). Additional IgG delivery with an unlabeled polymer (CyG10-EVE) has been included for evaluation of the impact of the fluorescent FITC end group on polymer performance (B, D). Data are displayed as the mean ± the standard error of the mean for three independent replicates of 10,000 cells each. Statistics indicate significance in comparison with the Untreated control (unless otherwise noted): * = $p < 0.05$, ** = $p < 0.01$, *** = $p < 0.001$, no symbol = no significance, as determined by one-way ANOVA followed by a Tukey post-test.

AlexaFluor 647-labelled IgG (IgG-AF647) for 30 minutes to form dual-labelled non-covalent complexes. HeLa cells were then incubated with the complexes for 4 hours at a concentration of 50 nM IgG and 2 μM CPPM (1:40 ratio). Following delivery, uninternalized complexes were washed from the cell surface and cells were assessed for both carrier and cargo internalization by flow cytometry (Figure 5.9). Delivery was quantified as percentage of positive cells and median fluorescence intensity (MFI) of the cellular population for each chromophore.

All carriers were able to permeate the plasma membrane at a high rate, with CPPM detected in > 60% of cells within each sample (Figure 5.9A). The concentration of successfully internalized carrier, proportional to the FITC MFI, however, was more dependent on carrier structure (Figure 5.9C). All of the hydrophobic carriers (**MePh$_{10}$-*b*-dG$_5$-FITC**, **CyG$_5$-FITC**, and **CyG$_{10}$-FITC**) were all internalized in significant quantities. **R$_9$-FITC** and **MeG$_{10}$-FITC** performed just as well as the hydrophobic carriers. While the former is well-documented to internalize within cells,[76] the latter's outperformance of **dG$_{10}$-FITC** and **PGON$_{20}$-FITC** is most likely due to the slight boost in hydrophobicity provided by its methyl substituent.[77,78]

Effective carrier internalization did not always translate to successful cargo delivery (Figure 5.9B and Figure 5.9D). For example, **R$_9$-FITC** was entirely incapable of delivering IgG-AF647. This is likely due to insufficient hydrophobicity for protein binding (see Chapter 3) and is consistent with its frequent use as a covalently-conjugated CPP.[79,80] The remainder of the carriers, which were all more hydrophobic than **R$_9$-FITC** due to both backbone and pendant group contributions, facilitated higher levels of IgG-AF647 internalization. The discrepancies between carrier and cargo internalization are highlighted

in the two-dimensional internalization plots (Figure 5.9E-F). It is important to note that, while data positioned high on the y-axis can appear impressive, increases along the x-axis are ultimately the more relevant outcome in non-covalent delivery.

In all fluorescence-based assays, it is important to understand the biological impact of the chromophore itself on the experiment. A common concern when using fluorescently-labelled probes is the influence of the label itself on the structure, properties, and localization of the probe, particularly when it comprises a significant fraction of the overall molecular weight.[7,81] To address this, IgG-AF647 was additionally delivered with an unlabeled analog of **CyG$_{10}$-FITC** (**CyG$_{10}$-EVE**). In this case, the unlabeled polymer delivered significantly more cargo, suggesting that FITC actually hindered CPPM internalization.

Lastly, high concentrations of cationic carriers can have negative effects on lipid membranes, inducing cellular toxicity or mitochondrial membrane depolarization.[35] Thus, samples were screened for cellular viability and mitochondrial membrane potential using

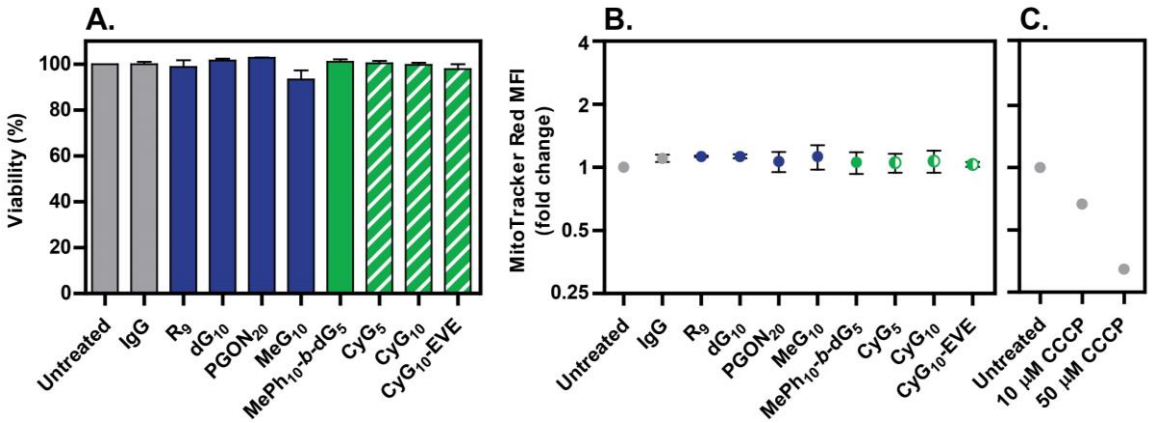

Figure 5.10: Analysis of (A) cellular viability and (B-C) mitochondrial membrane potential following (A-B) IgG delivery or (C) treatment with CCCP, a positive control for mitochondrial depolarization. Cationic homopolymers (blue), block copolymers (green), and cationic/hydrophobic homopolymers (hatched green) are shown alongside appropriate controls (grey). Data in (A-B) are displayed as the mean ± the standard error of the mean for one (C) or three (A-B) independent replicates consisting of 10,000 cells each. No samples treated with CPPM:IgG complexes were found to be statistically different ($p < 0.05$) from the untreated controls, as determined by one-way ANOVA followed by a Tukey post-test.

Zombie Violet and MitoTracker Red, a common mitochondrial stain whose fluorescence intensity is dependent on mitochondrial membrane potential,[28,60–63] respectively (Figure 5.10). These assays indicated that none of the carriers negatively impacted cellular or mitochondrial health.

5.3.3 Subcellular Localization of CPPMs by Confocal Microscopy

As previously stated, confocal microscopy is the dominant method for characterizing subcellular localization in the field of drug delivery. Success is typically associated with increased colocalization between the carrier (or cargo) being studied and its target organelle. Colocalization can be mathematically defined using a calculated coefficient, the most popular choices being the Pearson's Correlation Coefficient (PCC) and the Manders's Colocalization Coefficients (MCCs; M_1 and M_2). Importantly, these coefficients each utilize fundamentally different criteria to quantify colocalization. While the PCC seeks to describe the correlation of the two fluorophores, the MCCs quantify their co-occurrence. That is, the PCC probes whether a linear relationship (correlation) exists between the intensities of the two fluorophores, while the MCCs simply measure the spatial overlap between fluorophores, regardless of intensity. PCC values range from -1 (perfect negative correlation) to +1 (perfect positive correlation), with 0 representing complete absence of a relationship. M_1 values range from 0 (none of the pixels containing fluorophore 1 also containing fluorophore 2) to 1 (100% of the pixels containing fluorophore 1 also containing fluorophore 2). Likewise, M_2 is defined as proportion of fluorophore 2 pixels positive for fluorophore 1. Importantly, completely uncorrelated datasets (PCC ~ 0) could simultaneously exhibit high overlap (M_1 or M_2 ~ 1). Similarly,

no inherent relationship exists between the two MCC values; high M_1 overlap does not necessitate high M_2 overlap.[9,10]

In practicality, the PCC and MCCs are both useful in distinct biological contexts, depending on the question being asked, and attention must be paid to interpreting the results of each coefficient. In a mitochondrial delivery experiment containing carrier (fluorophore 1) and organelle (fluorophore 2) stains, for example, carriers which actively and selectively target the mitochondrion would be expected to exhibit PCC values near +1, making it a convenient metric. Conversely, carriers which distribute more broadly throughout cell would likely yield PCC and M_1 values closer to 0, but M_2 values near 1, since carrier would be present in virtually all mitochondria (albeit at low concentrations), but mitochondrial fluorescence would not be present in all pixels containing carrier. Therefore, for subcellular delivery with non-selective carriers, the MCCs will likely provide more resolution regarding differences in colocalization.

In a preliminary effort to quantify the ability of CPPMs to access the mitochondria, HeLa cells were treated with FITC-labelled carriers. The following carrier concentrations were selected in order to achieve roughly equal intracellular concentrations of FITC, since carriers were internalized with inequal efficiencies (data from optimization experiments not shown): 2 μM **R_9-FITC**, 100 nM **dG_{10}-FITC**, 200 nM **$PGON_{20}$-FITC**, 100 nM **MeG_{10}-FITC**, 50 nM **$MePh_{10}$-*b*-dG_5-FITC**, 300 nM **CyG_5-FITC**, 75 nM **CyG_{10}-FITC**. Cells were incubated with the polymers for 24 hours to allow sufficient time for intracellular trafficking, stained with MitoTracker Red, and visualized by confocal microscopy (Figure 5.11).

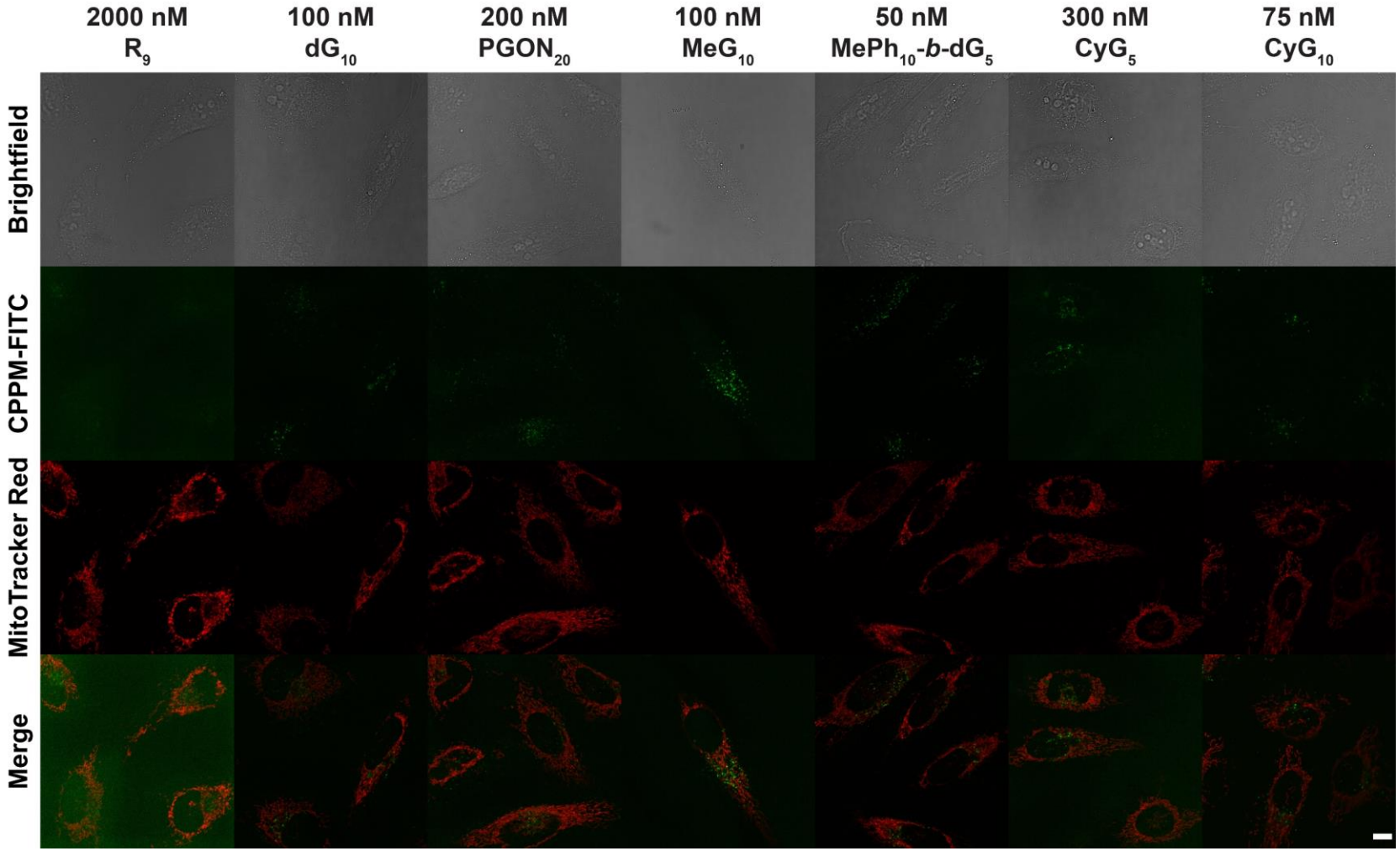

Figure 5.11: Representative confocal micrographs for HeLa cells treated with the indicated concentrations of FITC-labelled CPP(M)s and MitoTracker Red for evaluation of intramitochondrial localization. The brightness of each image has been autoscaled to the brightest pixel in each channel in order to visually highlight any differences in dye localization. As such, no conclusions based on relative color intensity should be drawn from the images as displayed here. Scale bar represents 10 μm.

Table 5.5: Colocalization of FITC-labelled carriers with mitochondria and endo/lysosomes as determined by confocal microscopy following a 24-hour incubation of HeLa cells with carriers (no cargo). Data represent analysis of either one representative micrograph (LysoTracker Red samples) or the average ± the standard deviation of two representative micrographs (MitoTracker Red samples) from a single biological replicate.

Fluorophore 1	Fluorophore 2	PCC[a]	M_1[b]	M_2[b]
R_9-FITC	MitoTracker Red	-0.011 ± 0.038	0.321 ± 0.083	0.355 ± 0.226
dG_{10}-FITC	MitoTracker Red	0.045 ± 0.070	0.230 ± 0.120	0.268 ± 0.061
$PGON_{20}$-FITC	MitoTracker Red	0.094 ± 0.019	0.821 ± 0.070	0.042 ± 0.012
MeG_{10}-FITC	MitoTracker Red	0.007 ± 0.001	0.574 ± 0.055	0.020 ± 0.004
$MePh_{10}$-*b*-dG_5-FITC	MitoTracker Red	-0.061 ± 0.009	0.698 ± 0.077	0.042 ± 0.007
CyG_5-FITC	MitoTracker Red	-0.014 ± 0.052	0.459 ± 0.095	0.006 ± 0.002
CyG_{10}-FITC	MitoTracker Red	0.015 ± 0.039	0.410 ± 0.005	0.009 ± 0.004
CyG_{10}-FITC	LysoTracker Red	0.693	0.477	0.819

[a]Pearson's Correlation Coefficient. [b]Manders's Colocalization Coefficients: M_1 = proportion of fluorophore 1 pixels also containing fluorophore 2, M_2 = proportion of fluorophore 2 pixels also containing fluorophore

Both the PCC and MCC values were calculated, definitively revealing that, while some CPPMs appeared to overlap more with the mitochondria (M_1 > 0.5 for **$PGON_{20}$-FITC**, **MeG_{10}-FITC**, and **$MePh_{10}$-*b*-dG_5-FITC**), none of the carriers appeared to wholly and selectively target the organelle (PCC ~ 0 for all carriers) in the way that their MPP counterparts have been reported to (Table 5.5). The lack of colocalization observed coupled with the punctate pattern of FITC fluorescence implied that the CPPMs may be trapped endosomes and lysosomes. To test this hypothesis, **CyG_{10}-FITC** and LysoTracker Red colocalization were assessed in a follow-up experiment (Figure 5.12). Bright, punctate FITC fluorescence patterns in confocal images were confirmed to largely represent endosomal/lysosomal polymer (PCC ~ 0.7) (Table 5.5).

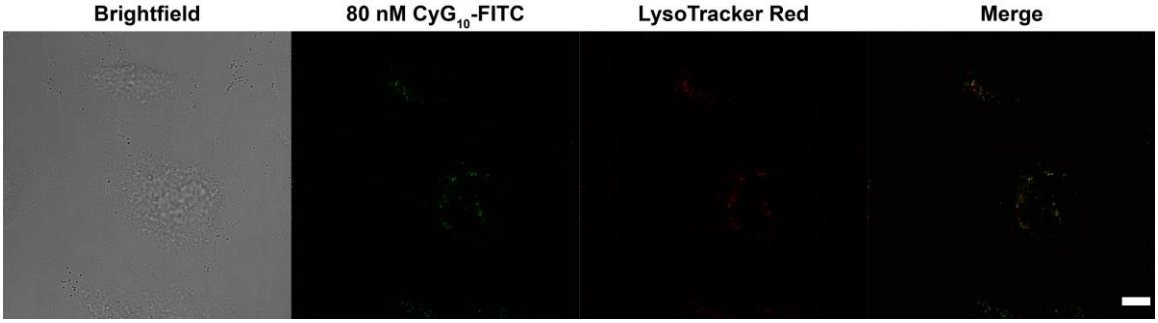

Figure 5.12: Representative confocal micrographs for HeLa cells treated with 80 nM **CyG_{10}-FITC** and LysoTracker Red for evaluation of endo/lysosomal colocalization. Scale bar represents 10 μm.

5.3.4 Subcellular Localization of Complexes by Confocal Microscopy

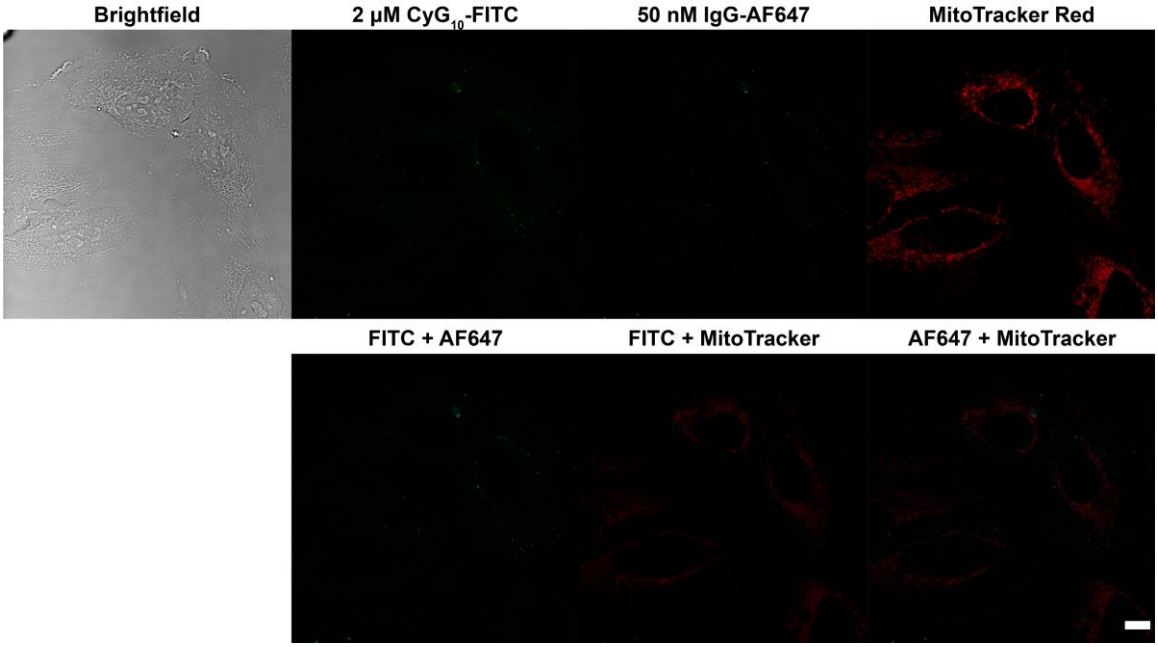

Figure 5.13: Representative confocal micrographs for HeLa cells treated with **CyG$_{10}$-FITC**:IgG-AF647 complexes and MitoTracker Red for evaluation of intramitochondrial localization. Scale bar represents 10 μm.

It was hypothesized that a polymer:protein complex may exhibit different localization than free polymer in solution. To investigate this, HeLa cells were incubated with **CyG$_{10}$-FITC**:IgG-AF647 complexes for 4 hours, stained with MitoTracker Red, and visualized by confocal microscopy (Figure 5.13). This time, PCC and MCC values were calculated for all three combinations of FITC, MitoTracker Red, and AF647 (Table 5.6). **CyG$_{10}$-FITC** and IgG-AF647 were found to be well-colocalized (PCC, M_1, and $M_2 > 0.5$), indicating that complexes do remain associated once inside cell, which is an important

Table 5.6: Colocalization of FITC-labelled carriers, IgG-AF467 cargo, and mitochondria as determined by confocal microscopy immediately following incubation of HeLa cells with carrier:cargo complexes for 4 hours. Data represent the average ± the standard deviation for analysis of three representative micrographs in a single biological replicate.

Fluorophore 1	Fluorophore 2	PCC[a]	M_1[b]	M_2[b]
CyG$_{10}$-FITC	IgG-AF647	0.609 ± 0.042	0.859 ± 0.038	0.607 ± 0.093
CyG$_{10}$-FITC	MitoTracker Red	-0.091 ± 0.007	0.637 ± 0.071	0.078 ± 0.027
IgG-AF647	MitoTracker Red	-0.162 ± 0.034	0.617 ± 0.054	0.125 ± 0.030

[a]Pearson's Correlation Coefficient. [b]Manders's Colocalization Coefficients: M_1 = proportion of fluorophore 1 pixels also containing fluorophore 2, M_2 = proportion of fluorophore 2 pixels also containing fluorophore 1.

prerequisite for subcellular delivery to any organelle. Furthermore, **CyG$_{10}$-FITC**:IgG-AF647 complexes were marginally more colocalized with mitochondria than **CyG$_{10}$-FITC** alone (M_1 ~ 0.6 vs. ~ 0.4). While complexes may have exhibited slight variations in internalization and trafficking in comparison with polymers alone, fundamentally different localization patterns were not observed.

Due to background noise, pixel values in each channel of an image are rarely equal to zero. Because MCCs consider any pixel with a nonzero value to be positive for the given fluorophore, setting accurate threshold values to exclude any background noise is critical to avoiding falsely high coefficients. This is particularly challenging when the signal in the region of interest is weak relative to the rest of the image, leaving even less margin for error between background and true signal.[9,10] Thus, despite our best efforts to fairly and accurately analyze mitochondrial uptake from confocal data, we hypothesized that the issue could be entirely circumvented by analyzing isolated mitochondria in statistically-relevant numbers using flow cytometry. By removing the overwhelming extramitochondrial (largely endosomal/lysosomal) fluorescence, more resolution and thus differentiation from the background noise could be obtained, enabling more robust conclusions to be drawn.

5.3.5 Mitochondrial Internalization by Organelle Flow Cytometry

The CellLight™ Mitochondria-RFP, BacMam 2.0 reagent ("MitoRFP") from ThermoFisher Scientific was selected to label mitochondria for organelle FCM. This reagent is a fusion construct of the leader sequence of E1 alpha pyruvate dehydrogenase and TagRFP packaged in a baculovirus. Upon transduction of mammalian cells, red

fluorescent protein (RFP) DNA is expressed and trafficked to the mitochondria. Because baculoviruses are unable to replicate in mammalian cells, this process only achieves transient labelling.[54,55] Since fluorescent protein is already contained within the mitochondria prior to cell lysis, this staining method is not dependent on the organelles retaining their activity and physical properties, which might be altered in this step. For this assay, cells were treated with MitoRFP 24 hours prior to incubation with CPPM-FITC:IgG-AF647 complexes.

Following delivery, cells were subjected to three freeze-thaw cycles in liquid nitrogen to accomplish lysis of the cellular membrane via ice crystal formation while leaving the mitochondrial membrane intact. This cell disruption method was selected for its speed and simplicity, given that no specialized equipment or reagents are required.[17,71,72] Finally, while a purified organellular fraction is not required for FCM, incomplete lysis or large aggregates of subcellular compartments could lead to detection of false positives, given that a particle could easily contain both RFP and FITC (or AF647) staining without being truly colocalized. For this reason, crude cell lysates were centrifuged for 10 min at 700 x g, pelleting intact cells, nuclei, and cellular debris which were subsequently discarded.[73,74] FCM data were also gated to include only particles smaller than nuclei based on centrifuged and non-centrifuged lysate controls. Finally, doublet discrimination was performed to ensure only single mitochondria were included in the analysis. That is, data resulting from two (or more) organelles passing through the lasers simultaneously in an aggregate have the potential to produce false positives, for example, in the case of a mitochondrion stuck to an endosome.[75] Further details regarding sample preparation, flow

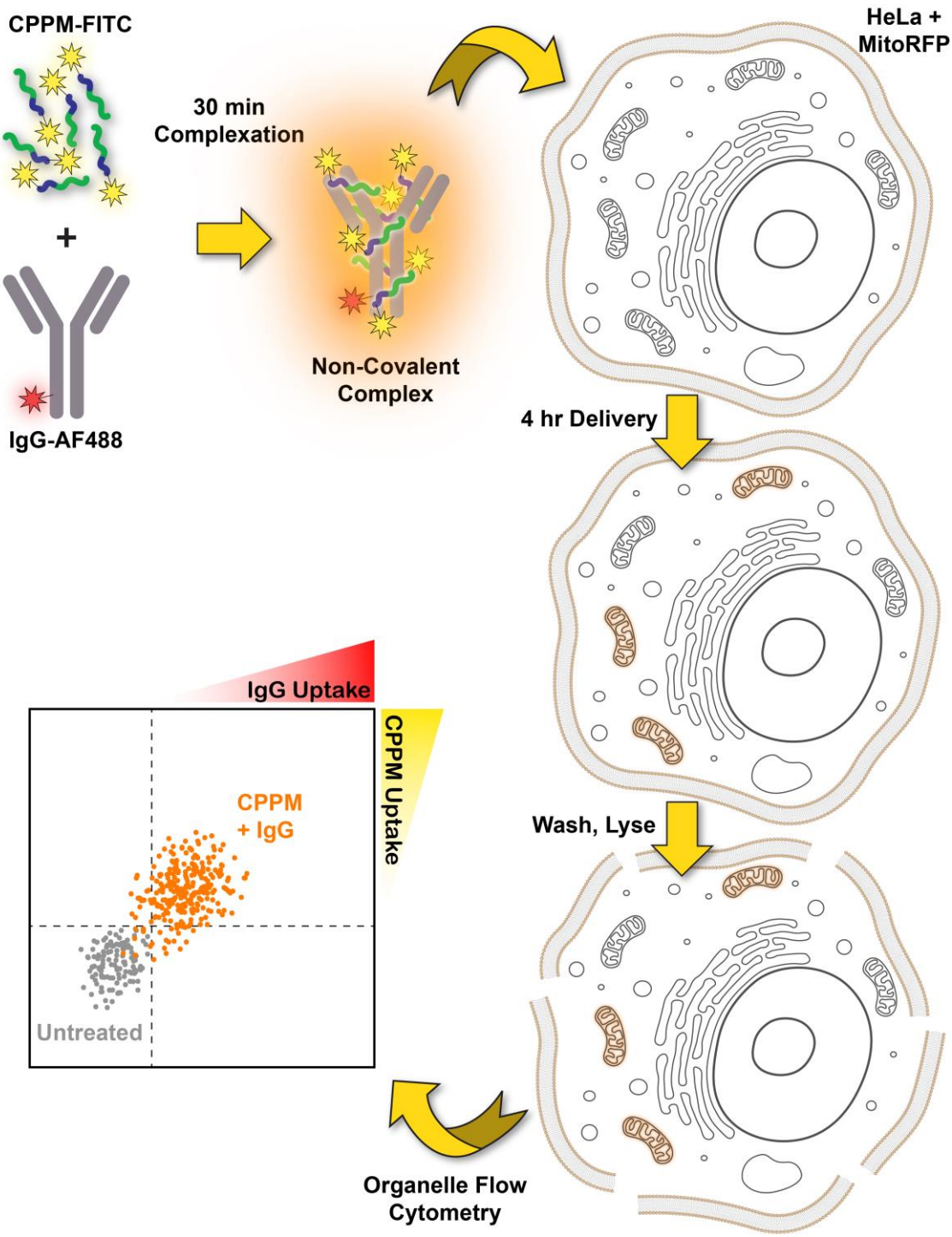

Figure 5.14: Workflow for evaluation of intramitochondrial carrier and cargo localization using organelle flow cytometry. FITC-labelled CPPMs (yellow) are incubated with an AF647-labelled antibody (red) for 30 min to form non-covalent complexes (orange). HeLa cells, treated with MitoRFP 24 hours in advance to yield RFP-stained mitochondria, are then incubated with the CPPM-FITC:IgG-AF647 complexes for 4 hours to allow for internalization and subcellular trafficking. Following delivery, cells are washed to remove extracellular complexes, lysed, and analyzed by organelle flow cytometry.

cytometry gating strategy, and data analysis can be found in Section 5.2.3.4 Gating Strategy for Organelle Flow Cytometry (Figure 5.8). The delivery workflow is illustrated in Figure 5.14.

HeLa cells treated with MitoRFP and CPPM-FITC:IgG-AF647 complexes were analyzed by organelle FCM to quantify carrier and cargo internalization (Figure 5.15). Despite the ability of all carriers to transduce the plasma membrane with ease (Figure 5.9), the most effective CPPMs for mitochondria penetration were only detected in half of the population. Interestingly, both cationic and hydrophobic polymers performed at similar levels for mitochondrial internalization, though, similar to cellular-level delivery, efficient carrier uptake did not necessitate robust cargo delivery. In particular, the two carriers with the most hydrophobic content (**MePh$_{10}$-*b*-dG$_5$-FITC** and **CyG$_{10}$-FITC**) were significantly more effective at facilitating intramitochondrial antibody transport. **CyG$_5$-FITC** was likely less effective simply because it wasn't able to deliver as much antibody intracellularly (Figure 5.9D). This may in turn be explained the presence of fewer hydrophobic groups per polymer, resulting in diminished polymer-protein and polymer-membrane intereactions.[77,82] As was done for cellular internalization, the effect of FITC on mitochondrial localization was assessed by delivering IgG-AF647 with the unlabeled CPPM **CyG$_{10}$-EVE**. Whereas the fluorophore had hampered cellular uptake of the antibody, there was no difference between mitochondrial delivery of the antibody with **CyG$_{10}$-FITC** and **CyG$_{10}$-EVE**.

In an effort to validate the protocol used to obtain mitochondrial delivery results, organelle FCM repeated following delivery with each of the three hydrophobic carriers, cell lysis by a reagent-based method, and purification of the heavy mitochondrial fraction

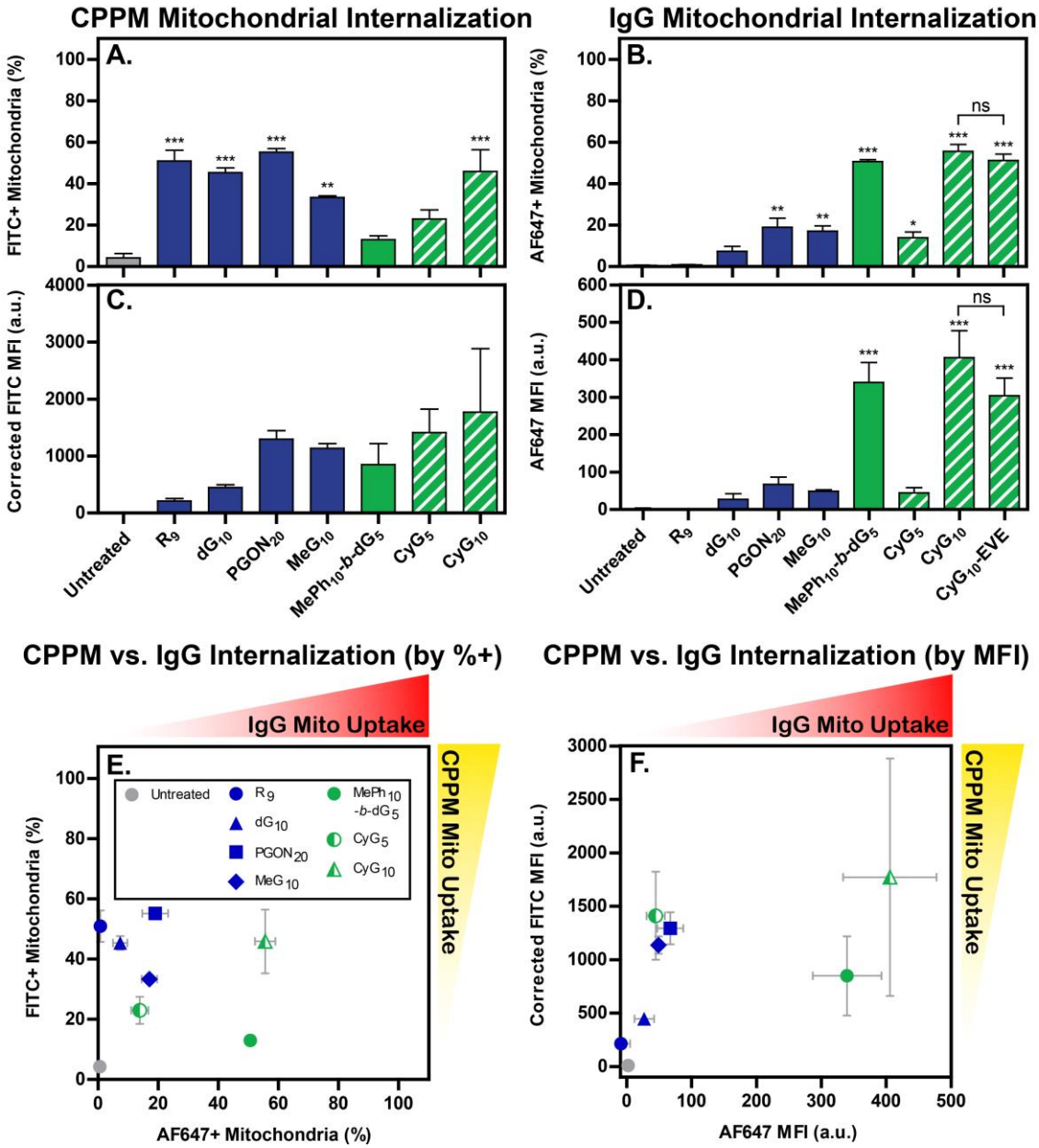

Figure 5.15: Uptake of CPPM-FITC:IgG-AF647 complexes into individual mitochondria, as determined by organelle flow cytometry after delivery to intact HeLa cells and subsequent cell lysis. Data are presented as: the percentage of mitochondria positive for FITC-conjugated CPPM or AF647-conjugated IgG (A and B, respectively), the FITC or AF647 MFI of the entire mitochondrial population, proportional to the quantity of carrier or cargo internalized (C and D, respectively), and the composite FITC and AF647 data, comparing mitochondrial uptake of the carrier and cargo by percent positive or MFI (E and F, respectively). Relative carrier/cargo uptake provide important information regarding the carrier's ability to remain associated with its cargo intracellularly, necessary for mitochondrial internalization of the cargo. Importantly, FITC MFI values have been corrected to account for differences in fluorophore brightness resulting from different degrees of polymer end-labeling efficiency (see Section 5.2.3.2 Characterization of Carrier-FITC Brightness for details). Additional IgG delivery with an unlabeled polymer (**CyG_{10}-EVE**) has been included for evaluation of the impact of the fluorescent FITC end group on polymer performance (B, D). Data are displayed as the mean ± the standard error of the mean for three independent replicates of at least 3,000 mitochondria each. Statistics indicate significance in comparison with the Untreated control (unless otherwise noted): * = $p < 0.05$, ** = $p < 0.01$, *** = $p < 0.001$, no symbol = no significance, as determined by one-way ANOVA followed by a Tukey post-test.

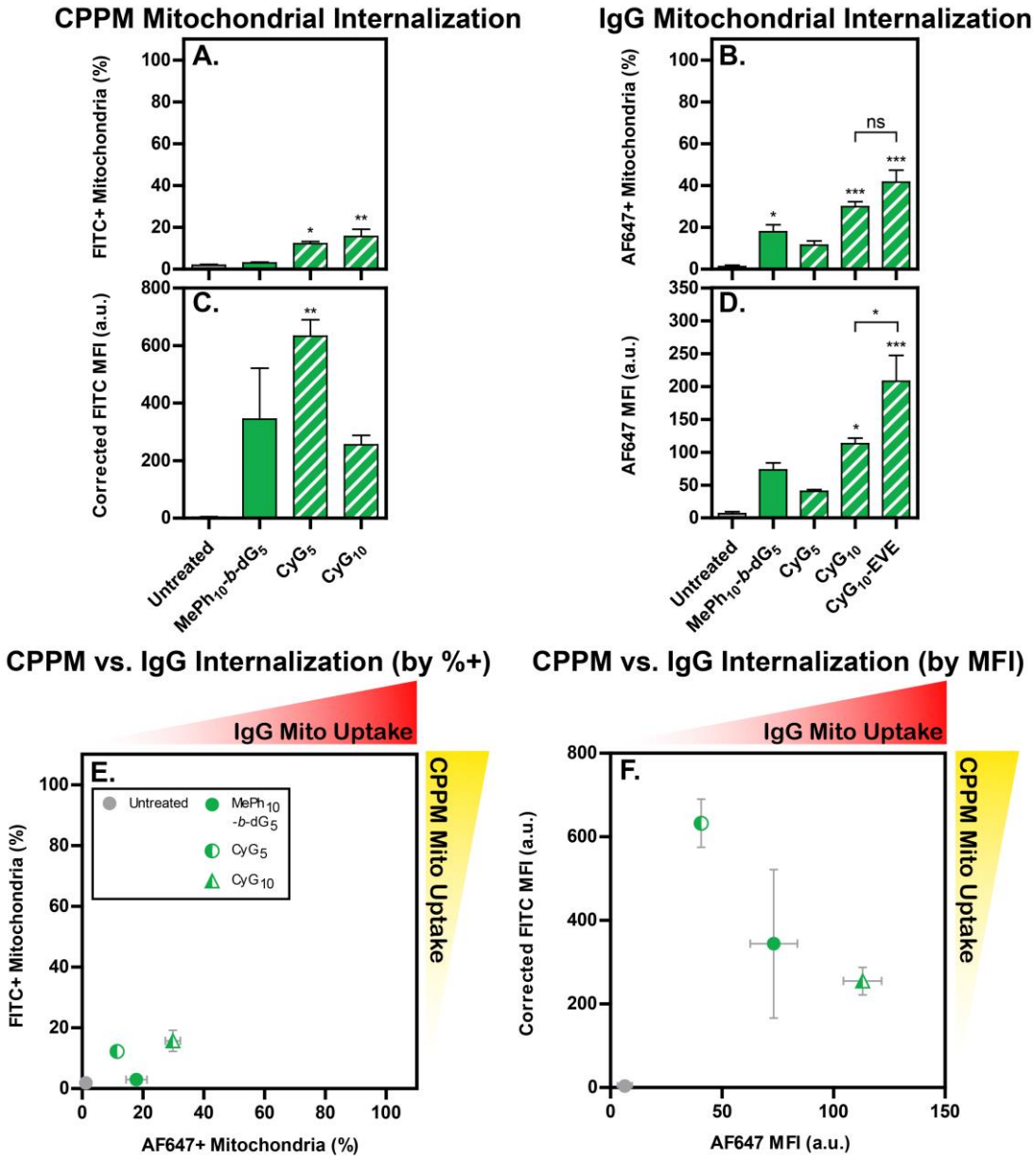

Figure 5.16: Uptake of CPPM-FITC:IgG-AF647 complexes into individual mitochondria, as determined by organelle flow cytometry after delivery to intact HeLa cells and subsequent processing via the reagent-based method in the Mitochondria Isolation Kit for Cultured Cells from ThermoFisher Scientific. Data are presented as: the percentage of mitochondria positive for FITC-conjugated CPPM or AF647-conjugated IgG (A and B, respectively), the FITC or AF647 MFI of the entire mitochondrial population, proportional to the quantity of carrier or cargo internalized (C and D, respectively), and the composite FITC and AF647 data, comparing mitochondrial uptake of the carrier and cargo by percent positive or MFI (E and F, respectively). Relative carrier/cargo uptake provide important information regarding the carrier's ability to remain associated with its cargo intracellularly, necessary for mitochondrial internalization of the cargo. Importantly, FITC MFI values have been corrected to account for differences in fluorophore brightness resulting from different degrees of polymer end-labeling efficiency. Additional IgG delivery with an unlabeled polymer (CyG10-EVE) has been included for evaluation of the impact of the fluorescent FITC end group on polymer performance (B, D). Data are displayed as the mean ± the standard error of the mean for three independent replicates of at least 3,000 mitochondria each. Statistics indicate significance in comparison with the Untreated control (unless otherwise noted): * = $p < 0.05$, ** = $p < 0.01$, *** = $p < 0.001$, no symbol = no significance, as determined by one-way ANOVA followed by a Tukey post-test.

by a more rigorous differential centrifugation process (Figure 5.16). Light mitochondria were specifically excluded during purification in favor of the higher-purity heavy mitochondrial fraction, as light mitochondria are more likely to contain lysosomal and peroxisomal contaminants.[74] While there were minor differences between the data obtained using different methods (most notably, lower apparent delivery when assessed via the reagent-based method), the overall trend in mitochondrial IgG localization remained the same: **CyG$_{10}$-FITC** > **MePh$_{10}$-*b*-dG$_5$-FITC** > **CyG$_5$-FITC**. Subtle differences in the absolute values by each method may be related to the inclusion of light mitochondria by the former method.

Two notable conclusions regarding CPPM behavior can be drawn from these studies. First, despite efforts to design CPPMs which structurally resemble MPPs, no carriers tested selectively accumulated in the mitochondria in the way that MPPs have been reported to. This suggests that the precise functional groups employed (i.e., alternating cyclohexyl and guanidine) are less important than the overall macromolecular properties of the carrier, such as hydrophobicity, charge, or three-dimensional structure. This is consistent with previous findings that protein delivery by CPPs and CPPMs was correlated with net hydrophobicity, rather than side-chain or backbone identity (see Chapter 3). Finally, detection of both carrier and cargo in the mitochondrion suggests that CPPMs, especially those incorporating more hydrophobicity, are capable of remaining non-covalently bound to proteins within the intracellular environment. While these complexes certainly remain intact long enough to traffic subcellularly, the kinetics of intracellular carrier-cargo dissociation remain an understudied, yet significant, subject for such non-covalent carriers.

5.4 Conclusions

Despite the prominence of flow cytometry in the field of intracellular delivery, colocalization by confocal microscopy remains the ubiquitous choice for evaluation of subcellar delivery. While the visual advantages of microscopy are unparalleled, analysis of individual organelles can nevertheless provide complementary information or offer compelling advantages depending on the circumstances. Microscopy can occasionally be insufficient or inaccurate, particularly when fluorescence is considerably dimmer in the region of interest than in other parts of the cell. Endosomal accumulation, a notorious issue in the delivery field, is a classic example of such a situation.[1,83–85] Meaningful colocalization data can likewise be difficult to accurately obtain for carriers which broadly permeate many regions of the cell rather than selectively accumulate in one organelle.[9,10] In this report, we have proposed the use of organelle flow cytometry as a simple, high-throughput, and statistically powerful method for single-organelle analysis. FCM provides data for up to thousands of particles per second, simultaneously increasing sample size and eliminating subjectivity associated with imaging.[14] Furthermore, the ever-growing array of organelle labeling probes, such as the CellLight™ reagents from ThermoFisher Scientific, enables significant flexibility in experimental design. Importantly, the ability to selectively label cellular structures such as mitochondria eliminates the need for time-intensive purification steps or specialized equipment to perform those separations.[17]

Organelle FCM was demonstrated by assessing mitochondrial localization of CPPM:IgG complexes. Despite their lack of selectivity for the mitochondria (yielding poorly resolved microscopy data), substantial differences in the activity of these carriers were nonetheless easily detected by this technique. Specifically, several polymers

delivered significantly more cargo into the mitochondria, quantities which may be biologically relevant. Although all carriers were able to access the mitochondria to similar extents, the longer and more hydrophobic carriers were superior in terms of cargo transport. This heavily implies that the binding interactions afforded by these CPPMs are necessary and sufficient to maintain complex integrity long enough for subcellular cargo trafficking. Finally, it is worth nothing that, while small molecule drugs are frequently targeted to the mitochondria, examples of macromolecular cargo delivery are surprisingly absent, despite the therapeutic opportunities this would present.[31,32] Future studies will be required to characterize the kinetics of intracellular cargo transport and release, as well as to determine whether CPPMs can deliver biologically-relevant quantities of functional cargo into the mitochondrion.

5.5 References

(1) Stewart, M. P.; Sharei, A.; Ding, X.; Sahay, G.; Langer, R.; Jensen, K. F. *In vitro* and *ex vivo* strategies for intracellular delivery. *Nature* **2016**, *538* (7624), 183–192.

(2) Qin, X.; Yu, C.; Wei, J.; Li, L.; Zhang, C.; Wu, Q.; Liu, J.; Yao, S. Q.; Huang, W. Rational Design of Nanocarriers for Intracellular Protein Delivery. *Adv. Mater.* **2019**, *31* (46), 1902791.

(3) Rajendran, L.; Knölker, H.-J.; Simons, K. Subcellular targeting strategies for drug design and delivery. *Nat. Rev. Drug Discov.* **2010**, *9* (1), 29–42.

(4) Chen, W. H.; Luo, G. F.; Zhang, X. Z. Recent Advances in Subcellular Targeted Cancer Therapy Based on Functional Materials. *Adv. Mater.* **2019**, *31* (3), 1–39.

(5) Nag, O. K.; Delehanty, J. B. Active cellular and subcellular targeting of nanoparticles for drug delivery. *Pharmaceutics* **2019**, *11* (10), 7–9.

(6) Ma, X.; Gong, N.; Zhong, L.; Sun, J.; Liang, X.-J. Future of nanotherapeutics: Targeting the cellular sub-organelles. *Biomaterials* **2016**, *97*, 10–21.

(7) Louzoun-Zada, S.; Jaber, Q. Z.; Fridman, M. Guiding Drugs to Target-Harboring Organelles: Stretching Drug-Delivery to a Higher Level of Resolution. *Angew. Chemie Int. Ed.* **2019**, *58* (44), 15584–15594.

(8) Maity, A. R.; Stepensky, D. Delivery of drugs to intracellular organelles using drug delivery systems: Analysis of research trends and targeting efficiencies. *Int. J. Pharm.* **2015**, *496* (2), 268–274.

(9) Bolte, S.; Cordelières, F. P. A guided tour into subcellular colocalization analysis in light microscopy. *J. Microsc.* **2006**, *224* (3), 213–232.

(10) Dunn, K. W.; Kamocka, M. M.; McDonald, J. H. A practical guide to evaluating colocalization in biological microscopy. *Am. J. Physiol. Physiol.* **2011**, *300* (4), C723–C742.

(11) Zuba-Surma, E. K.; Ratajczak, M. Z. Analytical Capabilities of the ImageStream Cytometer. In *Methods in Cell Biology*; Elsevier Inc., 2011; Vol. 102, pp 207–230.

(12) Zuba-Surma, E. K.; Kucia, M.; Abdel-Latif, A.; Lillard, J. W.; Ratajczak, M. Z. The ImageStream system: A key step to a new era in imaging. *Folia Histochem. Cytobiol.* **2007**, *45* (4), 279–290.

(13) Henriksen, M.; Miller, B.; Newmark, J.; Al-Kofahi, Y.; Holden, E. Laser Scanning Cytometry and Its Applications: A Pioneering Technology in the Field of Quantitative Imaging Cytometry. In *Methods in Cell Biology*; 2011; Vol. 102, pp 159–205.

(14) Basiji, D. A.; Ortyn, W. E.; Liang, L.; Venkatachalam, V.; Morrissey, P. Cellular Image Analysis and Imaging by Flow Cytometry. *Clin. Lab. Med.* **2007**, *27* (3), 653–670.

(15) Satori, C. P.; Kostal, V.; Arriaga, E. A. Review on recent advances in the analysis of isolated organelles. *Anal. Chim. Acta* **2012**, *753*, 8–18.

(16) Pasquali, C.; Fialka, I.; Huber, L. A. Subcellular fractionation, electromigration analysis and mapping of organelles. *J. Chromatogr. B Biomed. Sci. Appl.* **1999**, *722* (1–2), 89–102.

(17) Gauthier, D. J.; Lazure, C. Complementary methods to assist subcellular fractionation in organellar proteomics. *Expert Rev. Proteomics* **2008**, *5* (4), 603–617.

(18) Anand, R. K.; Chiu, D. T. Analytical tools for characterizing heterogeneity in organelle content. *Curr. Opin. Chem. Biol.* **2012**, *16* (3–4), 391–399.

(19) Degtyarev, M.; Reichelt, M.; Lin, K. Novel Quantitative Autophagy Analysis by Organelle Flow Cytometry after Cell Sonication. *PLoS One* **2014**, *9* (1), 87707.

(20) Böck, G.; Steinlein, P.; Huber, L. A. Cell biologists sort things out: Analysis and purification of intracellular organelles by flow cytometry. *Trends Cell Biol.* **1997**, *7* (12), 499–503.

(21) Lian, H.; He, S.; Chen, C.; Yan, X. Flow Cytometric Analysis of Nanoscale Biological Particles and Organelles. *Annu. Rev. Anal. Chem.* **2019**, *12* (1), 389–409.

(22) Demishtein, A.; Porat, Z.; Elazar, Z.; Shvets, E. Applications of flow cytometry for measurement of autophagy. *Methods* **2015**, *75*, 87–95.

(23) Stotland, A.; Gottlieb, R. A. α-MHC MitoTimer mouse: *In vivo* mitochondrial turnover model reveals remarkable mitochondrial heterogeneity in the heart. *J. Mol. Cell. Cardiol.* **2016**, *90*, 53–58.

(24) Lecoeur, H.; Langonné, A.; Baux, L.; Rebouillat, D.; Rustin, P.; Prévost, M. C.; Brenner, C.; Edelman, L.; Jacotot, E. Real-time flow cytometry analysis of permeability transition in isolated mitochondria. *Exp. Cell Res.* **2004**, *294* (1), 106–117.

(25) Radcliff, G.; Jaroszeski, M. J. Basics of flow cytometry. *Methods Mol. Biol.* **1998**, *91*, 1–24.

(26) Pickles, S.; Arbour, N.; Vande Velde, C. Immunodetection of Outer Membrane Proteins by Flow Cytometry of Isolated Mitochondria. *J. Vis. Exp.* **2014**, No. 91, 1–8.

(27) Zhang, S.; Zhu, S.; Yang, L.; Zheng, Y.; Gao, M.; Wang, S.; Zeng, J.-Z.; Yan, X. High-Throughput Multiparameter Analysis of Individual Mitochondria. *Anal. Chem.* **2012**, *84* (15), 6421–6428.

(28) Poot, M. Analysis of Intracellular Organelles by Flow Cytometry or Microscopy. *Curr. Protoc. Cytom.* **2000**, *14* (1), 1–24.

(29) Jhaveri, A.; Torchilin, V. Intracellular delivery of nanocarriers and targeting to subcellular organelles. *Expert Opin. Drug Deliv.* **2016**, *13* (1), 49–70.

(30) Hou, X.-S. S.; Wang, H.-S. S.; Mugaka, B. P.; Yang, G.-J. J.; Ding, Y. Mitochondria: Promising organelle targets for cancer diagnosis and treatment. *Biomater. Sci.* **2018**, *6* (11), 2786–2797.

(31) Muratovska, A.; Lightowlers, R. N.; Taylor, R. W.; Wilce, J. A.; Murphy, M. P. Targeting large molecules to mitochondria. *Adv. Drug Deliv. Rev.* **2001**, *49* (1–2), 189–198.

(32) Nurunnabi, M.; Khatun, Z.; Badruddoza, A. Z. M.; McCarthy, J. R.; Lee, Y. K.; Huh, K. M. Biomaterials and Bioengineering Approaches for Mitochondria and Nuclear Targeting Drug Delivery. *ACS Biomater. Sci. Eng.* **2019**, *5* (4), 1645–1660.

(33) Ma, C.; Xia, F.; Kelley, S. O. Mitochondrial Targeting of Probes and Therapeutics to the Powerhouse of the Cell. *Bioconjug. Chem.* **2020**, *31* (12), 2650–2667.

(34) Jean, S. R.; Ahmed, M.; Lei, E. K.; Wisnovsky, S. P.; Kelley, S. O. Peptide-Mediated Delivery of Chemical Probes and Therapeutics to Mitochondria. *Acc. Chem. Res.* **2016**, *49* (9), 1893–1902.

(35) Horton, K. L.; Pereira, M. P.; Stewart, K. M.; Fonseca, S. B.; Kelley, S. O. Tuning the activity of mitochondria-penetrating peptides for delivery or disruption. *ChemBioChem* **2012**, *13* (3), 476–485.

(36) Horton, K. L.; Stewart, K. M.; Fonseca, S. B.; Guo, Q.; Kelley, S. O. Mitochondria-Penetrating Peptides. *Chem. Biol.* **2008**, *15* (4), 375–382.

(37) Yousif, L. F.; Stewart, K. M.; Horton, K. L.; Kelley, S. O. Mitochondria-penetrating peptides: Sequence effects and model cargo transport. *ChemBioChem* **2009**, *10* (12), 2081–2088.

(38) Chamberlain, G. R.; Tulumello, D. V.; Kelley, S. O. Targeted delivery of doxorubicin to mitochondria. *ACS Chem. Biol.* **2013**, *8* (7), 1389–1395.

(39) Fonseca, S. B.; Pereira, M. P.; Mourtada, R.; Gronda, M.; Horton, K. L.; Hurren, R.; Minden, M. D.; Schimmer, A. D.; Kelley, S. O. Rerouting chlorambucil to mitochondria combats drug deactivation and resistance in cancer cells. *Chem. Biol.* **2011**, *18* (4), 445–453.

(40) Fonseca, S. B.; Kelley, S. O. Peptide-chlorambucil conjugates combat Pgp-dependent drug efflux. *ACS Med. Chem. Lett.* **2011**, *2* (6), 419–423.

(41) Lei, E. K.; Kelley, S. O. Delivery and Release of Small-Molecule Probes in Mitochondria Using Traceless Linkers. *J. Am. Chem. Soc.* **2017**, *139* (28), 9455–9458.

(42) Wisnovsky, S.; Jean, S. R.; Kelley, S. O. Mitochondrial DNA repair and replication proteins revealed by targeted chemical probes. *Nat. Chem. Biol.* **2016**, *12* (7), 567–573.

(43) Nam, H. Y.; Hong, J.-A.; Choi, J.; Shin, S.; Cho, S. K.; Seo, J.; Lee, J. Mitochondria-Targeting Peptoids. *Bioconjug. Chem.* **2018**, *29* (5), 1669–1676.

(44) Zhao, T.; Liu, X. X.; Singh, S.; Liu, X. X.; Zhang, Y.; Sawada, J.; Komatsu, M.; Belfield, K. D. Mitochondria Penetrating Peptide-Conjugated TAMRA for Live-Cell Long-Term Tracking. *Bioconjug. Chem.* **2019**, *30* (9), 2312–2316.

(45) Backlund, C. M.; Parhamifar, L.; Minter, L.; Tew, G. N.; Andresen, T. L. Protein Transduction Domain Mimics Facilitate Rapid Antigen Delivery into Monocytes. *Mol. Pharm.* **2019**, *16* (6), 2462–2469.

(46) Tezgel, A. Ö.; Jacobs, P.; Backlund, C. M.; Telfer, J. C.; Tew, G. N. Synthetic Protein Mimics for Functional Protein Delivery. *Biomacromolecules* **2017**, *18* (3), 819–825.

(47) Ozay, E. I.; Shanthalingam, S.; Torres, J. A.; Osborne, B. A.; Tew, G. N.; Minter, L. M. Protein Kinase C Theta Modulates PCMT1 through hnRNPL to Regulate FOXP3 Stability in Regulatory T Cells. *Mol. Ther.* **2020**, *28* (10), 1–17.

(48) Ozay, E. I.; Shanthalingam, S.; Sherman, H. L.; Torres, J. A.; Osborne, B. A.; Tew, G. N.; Minter, L. M. Cell-Penetrating Anti-Protein Kinase C Theta Antibodies Act Intracellularly to Generate Stable, Highly Suppressive Regulatory T Cells. *Mol. Ther.* **2020**, *28* (8), 1987–2006.

(49) Ozay, E. I.; Gonzalez-Perez, G.; Torres, J. A.; Vijayaraghavan, J.; Lawlor, R.; Sherman, H. L.; Garrigan, D. T.; Burnside, A. S.; Osborne, B. A.; Tew, G. N.; Minter, L. M. Intracellular Delivery of Anti-pPKCθ (Thr538) via Protein Transduction Domain Mimics for Immunomodulation. *Mol. Ther.* **2016**, *24* (12), 2118–2130.

(50) Tezgel, A. Ö.; Gonzalez-Perez, G.; Telfer, J. C.; Osborne, B. A.; Minter, L. M.; Tew, G. N. Novel Protein Transduction Domain Mimics as Nonviral Delivery Vectors for siRNA Targeting *NOTCH1* in Primary Human T cells. *Mol. Ther.* **2013**, *21* (1), 201–209.

(51) Backlund, C. M.; Takeuchi, T.; Futaki, S.; Tew, G. N. Relating structure and internalization for ROMP-based protein mimics. *Biochim. Biophys. Acta - Biomembr.* **2016**, *1858* (7), 1443–1450.

(52) Tezgel, A. O.; Telfer, J. C.; Tew, G. N. De Novo Designed Protein Transduction Domain Mimics from Simple Synthetic Polymers. *Biomacromolecules* **2011**, *12* (8), 3078–3083.

(53) Love, J. A.; Morgan, J. P.; Trnka, T. M.; Grubbs, R. H. A Practical and Highly Active Ruthenium-Based Catalyst that Effects the Cross Metathesis of Acrylonitrile. *Angew. Chemie Int. Ed.* **2002**, *41* (21), 4035–4037.

(54) Ames, R. S.; Kost, T. A.; Condreay, J. P. BacMam technology and its application to drug discovery. *Expert Opin. Drug Discov.* **2007**, *2* (12), 1669–1681.

(55) Dolman, N. J.; Kilgore, J. A.; Davidson, M. W. A Review of Reagents for Fluorescence Microscopy of Cellular Compartments and Structures, Part I: BacMam Labeling and Reagents for Vesicular Structures. *Curr. Protoc. Cytom.* **2013**, *65* (1).

(56) Lienkamp, K.; Madkour, A. E.; Musante, A.; Nelson, C. F.; Nüsslein, K.; Tew, G. N. Antimicrobial Polymers Prepared by ROMP with Unprecedented Selectivity: A Molecular Construction Kit Approach. *J. Am. Chem. Soc.* **2008**, *130* (30), 9836–9843.

(57) deRonde, B. M.; Posey, N. D.; Otter, R.; Caffrey, L. M.; Minter, L. M.; Tew, G. N. Optimal Hydrophobicity in Ring-Opening Metathesis Polymerization-Based Protein Mimics Required for siRNA Internalization. *Biomacromolecules* **2016**, *17* (6), 1969–1977.

(58) Madkour, A. E.; Koch, A. H. R.; Lienkamp, K.; Tew, G. N. End-Functionalized ROMP Polymers for Biomedical Applications. *Macromolecules* **2010**, *43* (10), 4557–4561.

(59) Chen, A. K.; Cheng, Z.; Behlke, M. A.; Tsourkas, A. Assessing the sensitivity of commercially available fluorophores to the intracellular environment. *Anal. Chem.* **2008**, *80* (19), 7437–7444.

(60) Dolman, N. J.; Chambers, K. M.; Mandavilli, B.; Batchelor, R. H.; Janes, M. S. Tools and techniques to measure mitophagy using fluorescence microscopy. *Autophagy* **2013**, *9* (11), 1653–1662.

(61) Doherty, E.; Perl, A. Measurement of Mitochondrial Mass by Flow Cytometry during Oxidative Stress. *React. Oxyg. Species* **2017**, *4* (10), 275–283.

(62) Lin, H.-C. C.; Liu, S.-Y. Y.; Lai, H.-S. S.; Lai, I.-R. R. Isolated mitochondria infusion mitigates ischemia-reperfusion injury of the liver in rats. *Shock* **2013**, *39* (3), 304–310.

(63) Poot, M.; Zhang, Y. Z.; Krämer, J. A.; Wells, K. S.; Jones, L. J.; Hanzel, D. K.; Lugade, A. G.; Singer, V. L.; Haugland, R. P. Analysis of mitochondrial morphology and function with novel fixable fluorescent stains. *J. Histochem. Cytochem.* **1996**, *44* (12), 1363–1372.

(64) McNaughton, B. R.; Cronican, J. J.; Thompson, D. B.; Liu, D. R. Mammalian cell penetration, siRNA transfection, and DNA transfection by supercharged proteins. *Proc. Natl. Acad. Sci.* **2009**, *106* (15), 6111–6116.

(65) Hornig-Do, H. T.; Günther, G.; Bust, M.; Lehnartz, P.; Bosio, A.; Wiesner, R. J. Isolation of functional pure mitochondria by superparamagnetic microbeads. *Anal. Biochem.* **2009**, *389* (1), 1–5.

(66) Chinnery, P. F.; Taylor, R. W.; Diekert, K.; Lill, R.; Turnbull, D. M.; Lightowlers, R. N. Peptide nucleic acid delivery to human mitochondria. *Gene Ther.* **1999**, *6* (12), 1919–1928.

(67) Reers, M.; Smiley, S. T.; Mottola-Hartshorn, C.; Chen, A.; Lin, M.; Chen, L. B. Mitochondrial membrane potential monitored by JC-1 dye. *Methods Enzymol.* **1995**, *260* (C), 406–414.

(68) Shapiro, H. M. Membrane potential estimation by flow cytometry. *Methods* **2000**, *21* (3), 271–279.

(69) Chen, L.; Ma, K.; Han, J.; Chen, Q.; Zhu, Y. Monitoring Mitophagy in Mammalian Cells. *Methods Enzymol.* **2017**, *588*, 187–208.

(70) Douglas, M. G.; McCammon, M. T.; Vassarotti, A. Targeting proteins into mitochondria. *Microbiol. Rev.* **1986**, *50* (2), 166–178.

(71) Chaiyarit, S.; Thongboonkerd, V. Comparative analyses of cell disruption methods for mitochondrial isolation in high-throughput proteomics study. *Anal. Biochem.* **2009**, *394* (2), 249–258.

(72) Bodzon-Kulakowska, A.; Bierczynska-Krzysik, A.; Dylag, T.; Drabik, A.; Suder, P.; Noga, M.; Jarzebinska, J.; Silberring, J. Methods for samples preparation in proteomic research. *J. Chromatogr. B Anal. Technol. Biomed. Life Sci.* **2007**, *849* (1–2), 1–31.

(73) Graham, J. M. Isolation of Lysosomes from Tissues and Cells by Differential and Density Gradient Centrifugation. *Curr. Protoc. Cell Biol.* **2000**, *7* (1).

(74) Pallotti, F.; Lenaz, G. Isolation and subfractionation of mitochondria from animal cells and tissue culture lines. In *Methods in Cell Biology*; 2001; pp 1–35.

(75) Staats, J.; Divekar, A.; McCoy, J. P.; Maecker, H. T. Guidelines for Gating Flow Cytometry Data for Immunological Assays. In *Methods in Molecular Biology*; Humana Press Inc., 2019; Vol. 2032, pp 81–104.

(76) Wender, P. A.; Mitchell, D. J.; Pattabiraman, K.; Pelkey, E. T.; Steinman, L.; Rothbard, J. B. The design, synthesis, and evaluation of molecules that enable or enhance cellular uptake: Peptoid molecular transporters. *Proc. Natl. Acad. Sci.* **2000**, *97* (24), 13003–13008.

(77) Posey, N. D.; Caffrey, L. M.; Minter, L. M.; Tew, G. N. Protein Mimic Hydrophobicity Affects Intracellular Delivery but not Cargo Binding. *ChemistrySelect* **2016**, *1* (19), 6146–6150.

(78) Backlund, C. M.; Sgolastra, F.; Otter, R.; Minter, L. M.; Takeuchi, T.; Futaki, S.; Tew, G. N. Increased hydrophobic block length of PTDMs promotes protein internalization. *Polym. Chem.* **2016**, *7* (48), 7514–7521.

(79) deRonde, B. M.; Tew, G. N. Development of protein mimics for intracellular delivery. *Biopolymers* **2015**, *104* (4), 265–280.

(80) Posey, N. D.; Tew, G. N. Associative and Dissociative Processes in Non-Covalent Polymer-Mediated Intracellular Protein Delivery. *Chem. - An Asian J.* **2018**, *13* (22), 3351–3365.

(81) Bechara, C.; Sagan, S. Cell-penetrating peptides: 20 years later, where do we stand? *FEBS Lett.* **2013**, *587* (12), 1693–1702.

(82) Posey, N. D.; Hango, C. R.; Minter, L. M.; Tew, G. N. The Role of Cargo Binding Strength in Polymer-Mediated Intracellular Protein Delivery. *Bioconjug. Chem.* **2018**, *29* (8), 2679–2690.

(83) Esquivel, R. N.; Patel, A.; Kudchodkar, S. B.; Park, D. H.; Stettler, K.; Beltramello, M.; Allen, J. W.; Mendoza, J.; Ramos, S.; Choi, H.; Borole, P.; Asija, K.; Bah, M.; Shaheen, S.; Chen, J.; Yan, J.; Durham, A. C.; Smith, T. R. F.; Broderick, K.; et al. *In Vivo* Delivery of a DNA-Encoded Monoclonal Antibody Protects Non-human Primates against Zika Virus. *Mol. Ther.* **2019**, *27* (5), 974–985.

(84) Selby, L. I.; Cortez-Jugo, C. M.; Such, G. K.; Johnston, A. P. R. Nanoescapology: progress toward understanding the endosomal escape of polymeric nanoparticles. *Wiley Interdiscip. Rev.: Nanomed. Nanobiotechnol.* **2017**, *9* (5), e1452.

(85) Smith, S. A.; Selby, L. I.; Johnston, A. P. R. R.; Such, G. K. The Endosomal Escape of Nanoparticles: Toward More Efficient Cellular Delivery. *Bioconjug. Chem.* **2019**, *30* (2), 263–272.

CHAPTER 6

6 PERSPECTIVES AND FUTURE DIRECTIONS

6.1 Summary

This dissertation has considered four distinct examples in which polymer structure profoundly influenced various aspects of the protein delivery process. In Chapter 2, performance of a variety of non-covalent carriers was observed to be cell line- and serum-dependent, though **MePh$_{10}$-*b*-dG$_5$** facilitated significant payload internalization in even the most challenging situations. Importantly, this CPPM was able to deliver both EGFP and IgG into neurons, a cell type for which effective carriers are greatly needed.[1]

Chapter 3 aimed to translate the success of CPPMs back to CPPs, that is, to reverse-engineer novel block copolypeptides capable of non-covalent protein delivery. While CPP(M) structures containing the same pendant group configurations did not perform similarly, this was attributed to the added hydrophobicity afforded by the ROMP backbone. When taken into account, it was revealed that overall carrier hydrophobicity was a much better predictor cargo internalization, activity, and intracellular availability (IA).

CPPM length was explored in relation to protein delivery for the first time in Chapter 4. Cargo internalization and function exhibited an unintuitive and competing relationship, with longer carriers facilitating significantly activity despite reduced uptake. Increased carrier molecular weight was also linked to smaller nanoparticle size, and potentially formation mechanism, hinting at mechanistic explanations for differences in cargo IA.

Finally, in Chapter 5, relationships between CPPM structure and mitochondrial localization were studied. Attempts to quantify mitochondrial uptake by confocal microscopy were impeded by bright endosomal fluorescence, a notoriously common issue in intracellular delivery.[2] For this reason, mitochondria were analyzed in isolation, necessitating the development of a new organelle flow cytometry method which can be easily and broadly applied to a variety of intra-organellular drug delivery studies in the future. These experiments revealed increased hydrophobicity to correlate with increased intramitochondrial cargo transport. However, it is worth noting that none of these carriers displayed the same level of mitochondrial selectivity characteristic of molecularly-similar mitochondria-penetrating peptides.[3]

Perhaps the most significant finding from the work presented here is that, even within the same synthetic delivery platform, minor changes in polymer structure can have complex consequences on resultant cargo intracellular availability. That is, cargo activity is not straightforwardly related to internalization, and the two can even be inversely related. Furthermore, dramatic differences in complex size, likely driven by changes in formation mechanism, were reported.

6.2 Functional Delivery Applications

Although the results from intraneuronal delivery were incredibly promising, delivery of functional proteins should next be confirmed in order to position this technology as a useful tool for basic neuroscience research. Additionally, it remains to be seen whether the quantities of antibody delivered to the mitochondria are biologically relevant.

6.3 CPPM Self-Assembly and Complex Structure

MePh$_{10}$-*b*-dG$_5$ has been extensively characterized for potential self-assembly in solution, producing no evidence of this phenomenon.[4] However, the remarkably small size and stability exhibited by **MePh$_{80}$-*b*-dG$_{40}$**:IgG complexes, even upon increase of polymer:protein ratio, suggests that these complexes may be formed by a fundamentally different mechanism than **MePh$_{10}$-*b*-dG$_5$**:IgG complexes. Additionally, preliminary transmission electron microscopy (TEM) and dynamic light scattering (DLS) data of these longer CPPMs alone have indicated that the longer block copolymers tested in Chapter 4 may self-assemble (data not shown). Assuming this is true, these self-assembled structures should be thoroughly characterized to determine whether they from polymeric micelles or some other ordered structure. If there is a critical micelle concentration above which these carriers perform more effectively, that would be good to know too. Complexes should be characterized by TEM to determine where protein is located in these assembled structures (e.g., adsorbed on the surface or contained within the core). Contrast between the polymer and protein material might be achieved by complexation with a metalloprotein, such as hemoglobin (containing iron), which could circumvent the need for complicated staining or labelling procedures.

6.4 Cargo Denaturation

The increased IA of Cre recombinase when delivered with **MePh$_{80}$-*b*-dG$_{40}$** suggests that stronger, more surfactant-like amphiphiles do not denature proteins, at least not to a higher degree than shorter CPPMs. A preliminary circular dichroism (CD) spectroscopy experiment indicated no difference in BSA or IgG secondary structure before and after complexation with **MePh$_{10}$-*b*-dG$_5$** (data not shown). Given that CD spectroscopy

appears to be a viable tool for quantifying integrity of complexed proteins, measurements should be taken for a broader range of carriers, cargoes, and binding strengths to determine whether denaturation is a concern for this delivery platform.

6.5 Endosomal Escape

Given the relatively high degree of endo/lysosomal colocalization for CPPM:antibody complexes found in Chapter 5, quantifying and improving upon complex endosomal escape efficiency seems to be a fruitful path forward. This could be studied in both simple cell-free assays as well as with *in vitro* delivery experiments. Leakage from dye-loaded vesicles, a standard assay in our group, could be employed to model polymer-membrane disruption. *In vitro*, the split GFP-complementation assay could be employed, in which a fragment of GFP is delivered and must successfully enter the cytoplasm to fuse with its complement (expressed by the cell line) to become fluorescent. Alternatively, complexes could be dual-labelled with a pH-sensitive fluorophore on the carrier and a pH-insensitive fluorophore on the cargo (or vice-versa).[5] In this way, the ratio of fluorophore brightness would correlate with the pH experienced by the nanoparticles, indirectly providing information regarding endo/lysosomal localization or escape.

6.6 Cargo Release Kinetics

Organelle flow cytometry data in Chapter 5 demonstrated that both polymer and protein are able to enter the mitochondrion, provided that the polymer contains adequate hydrophobicity. This lack of complex dissociation prior to mitochondrial entry is intriguing, indicating that cargo release may be slow or even nonexistent, and proteins may remain active while complexed. Moreover, cargo release kinetics and activity in the

complexed state may be highly dependent on both polymer and protein identity. Elucidation of such relationships might provide significant insights into IA discrepancies, enabling educated design of better CPPMs.

Cargo release remains an understudied aspect of CPPM-mediated delivery. Ongoing competition assays, in which complexes are challenged with serum proteins, appear to indicate that at least some level of unbinding can be achieved at very high competitor concentrations (data not shown). Such high concentrations attempt to mimic the highly crowded intracellular environment and suggest that protein release via this mechanism is a reasonable assumption. These assays should be continued with various polymer-protein binding pairs and competitors.

Initial attempts to establish a Förster resonance energy transfer (FRET)-based reporter system to evaluate intracellular carrier-cargo association degree were unsuccessful (data not shown). FRET is a non-radiative energy transfer process sensitive to distance between the donor and acceptor molecules. In close proximity, FRET pairing occurs, and acceptor fluorescence is observed when the donor is excited. At distances greater than ~10 nm, no FRET pairing occurs, resulting in the observation of donor fluorescence. FRET is utilized extensively to characterize intracellular protein-protein interactions,[6–8] and was expected to be useful in both cell-free and *in vitro* delivery assays to probe degree carrier-cargo association over time. Fluorescent proteins (blue fluorescent protein [BFP] and IgG-AF405) were utilized as the donors while labelled CPPM (**MePh$_{10}$-*b*-dG$_5$-FITC**) was chosen to be the acceptor (Figure 6.1). In these preliminary experiments, no FRET pairing was observed upon cargo binding—only quenching of protein fluorescence, as is typically observed in standard binding assays. While it is unclear why this is the case, there may be

alternative strategies to achieve a FRET-based (or non-FRET-based) reporter system to study cargo release.

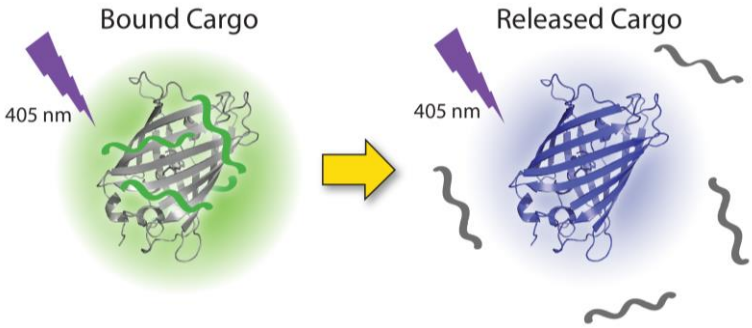

Figure 6.1: FRET-based carrier-cargo reporter system, in which blue fluorescent protein (BFP) and CPPM-FITC function as the donor and acceptor fluorophores, respectively. Upon excitation with 405 nm light, FITC emission indicates bound cargo, whereas BFP emission indicates released cargo.

It will be equally important to understand whether CPPM-protein complex dissociation is required for protein function. Cell-free colorimetric assays involving enzymes with small molecule substrates would be an excellent preliminary study to address these questions. In these experiments, a model enzyme such as β-galactosidase (β-gal) could be straightforwardly utilized. β-gal can enzymatically cleave the small molecule X-gal to produce a bright blue compound, providing a simple readout for activity.[9] β-gal's low isoelectric point (similar to that of BSA) suggests it would be tightly bound by CPPMs. Enzymatic activity could be monitored along the binding curve by increasing CPPM:protein ratio, while effects of binding strength could be probed by modifications in CPPM architecture.[10] Furthermore, these assays could be coupled with competition assays in order to model the intracellular environment and probe the proposed model of cargo release by protein displacement. Results from this cell-free activity assay could be directly replicated in delivery experiments, since X-gal (but not β-gal) is readily cell-permeable. If β-gal is inactive when complexed with CPPM, any intracellular activity would be indicative of at least minimal protein release. Provided that release is sufficiently slow,

kinetics of cargo release, assumed to correlate with protein activity, could perhaps be extracted from these assays as well.

The ability of complexed proteins to interact with macromolecular substrates should likewise be investigated. In these experiments, the ability of enzymes to degrade biopolymers might be investigated, with readouts in molecular weight reductions quantified using GPC or mass spectrometry. Alternatively, the ability of antibody cargoes to bind their antigens could be studied using an ELISA-like flow cytometry assay (Figure 6.2). CPPMs could be complexed with antibodies immobilized on beads, followed by sequential exposure to the antigen and a dye-labeled secondary antibody. Beads would then be analyzed by flow cytometry, in which differences in binding ability would manifest as variations in fluorescence intensity. Since on-target delivery of functional antibodies has already been demonstrated in our group, impaired activity in these assays would suggest that complexes dissociate upon delivery.

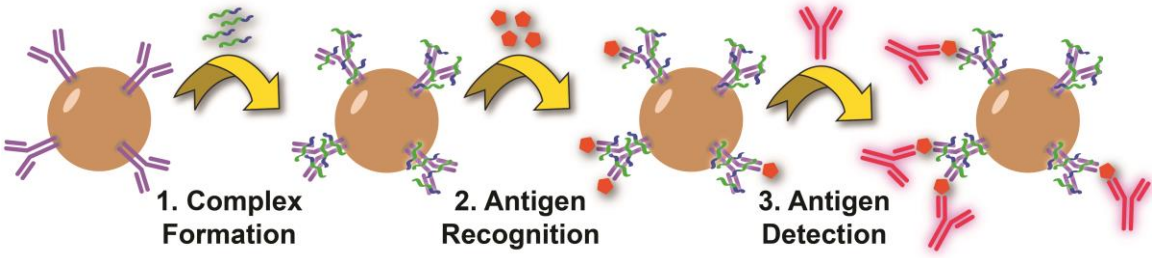

Figure 6.2: Proposed workflow for evaluating antibody function while complexed using a bead-based flow cytometry assay. (1) Complex formation between polymers and antibodies immobilized on flow cytometry beads. (2) Beads are incubated with antigen to probe antibody activity. (3) Beads are incubated with a fluorescently-tagged secondary antibody to enable detection of bound antigen prior to flow cytomery.

6.7 Subcellular Delivery

Carrier-cargo association within the cell, at least long enough to traffic intracellularly, validates the strategy of modifying CPPM structure to influence cargo localization (as an alternative to engineering protein cargoes to contain appropriate

localization signals). If future delivery to specific subcellular compartments (e.g., the nucleus) is desired, it may be more straightforward and effective to conjugate peptide localization sequences to the end of ROMP polymers, in the same manner that CPPMs were fluorescently labelled in Chapter 5. In this way, highly the selective subcellular targeting characteristic of these peptide sequences could potentially be achieved without compromising CPPM structure, binding, or internalization activity.

6.8 Outlook

The future of CPPM development for functional protein delivery lies in better understanding the mechanisms underlying enhanced intracellular availability. In particular, characterization and optimization of polymer-protein interactions, self-assembled structures, endosomal escape, subcellular targeting, and ultimate cargo release provide exciting opportunities for improvement of these uniquely effective non-covalent delivery vehicles.

6.9 References

(1) Stewart, M. P.; Sharei, A.; Ding, X.; Sahay, G.; Langer, R.; Jensen, K. F. *In vitro* and *ex vivo* strategies for intracellular delivery. *Nature* **2016**, *538* (7624), 183–192.

(2) Shete, H. K.; Prabhu, R. H.; Patravale, V. B. Endosomal Escape: A Bottleneck in Intracellular Delivery. *J. Nanosci. Nanotechnol.* **2014**, *14* (1), 460–474.

(3) Jean, S. R.; Ahmed, M.; Lei, E. K.; Wisnovsky, S. P.; Kelley, S. O. Peptide-Mediated Delivery of Chemical Probes and Therapeutics to Mitochondria. *Acc. Chem. Res.* **2016**, *49* (9), 1893–1902.

(4) Posey, N. D.; Tew, G. N. Protein Transduction Domain Mimic (PTDM) Self-Assembly? *Polymers* **2018**, *10* (9), 1039.

(5) Smith, S. A.; Selby, L. I.; Johnston, A. P. R. R.; Such, G. K. The Endosomal Escape of Nanoparticles: Toward More Efficient Cellular Delivery. *Bioconjug. Chem.* **2019**, *30* (2), 263–272.

(6) Ryu, J.-H.; Chacko, R. T.; Jiwpanich, S.; Bickerton, S.; Babu, R. P.; Thayumanavan, S. Self-Cross-Linked Polymer Nanogels: A Versatile Nanoscopic Drug Delivery Platform. *J. Am. Chem. Soc.* **2010**, *132* (48), 17227–17235.

(7) Lu, J.; Owen, S. C.; Shoichet, M. S. Stability of self-assembled polymeric micelles in serum. *Macromolecules* **2011**, *44* (15), 6002–6008.

(8) Keum, J.-W.; Bermudez, H. DNA-based delivery vehicles: pH-controlled disassembly and cargo release. *Chem. Commun.* **2012**, *48* (99), 12118.

(9) González-Toro, D. C.; Ryu, J. H.; Chacko, R. T.; Zhuang, J.; Thayumanavan, S. Concurrent binding and delivery of proteins and lipophilic small molecules using polymeric nanogels. *J. Am. Chem. Soc.* **2012**, *134* (16), 6964–6967.

(10) Sgolastra, F.; Backlund, C. M.; Ilker Ozay, E.; deRonde, B. M.; Minter, L. M.; Tew, G. N. Sequence segregation improves non-covalent protein delivery. *J. Control. Release* **2017**, *254*, 131–136.

BIBLIOGRAPHY

Åmand, H. L.; Fant, K.; Nordén, B.; Esbjörner, E. K. Stimulated endocytosis in penetratin uptake: Effect of arginine and lysine. *Biochem. Biophys. Res. Commun.* **2008**, *371* (4), 621–625.

Ames, R. S.; Kost, T. A.; Condreay, J. P. BacMam technology and its application to drug discovery. *Expert Opin. Drug Discov.* **2007**, *2* (12), 1669–1681.

Anand, R. K.; Chiu, D. T. Analytical tools for characterizing heterogeneity in organelle content. *Curr. Opin. Chem. Biol.* **2012**, *16* (3–4), 391–399.

Backlund, C. M.; Hango, C. R.; Minter, L. M.; Tew, G. N. Protein and Antibody Delivery into Difficult-to-Transfect Cells by Polymeric Peptide Mimics. *ACS Appl. Bio Mater.* **2020**, *3* (1), 180–185.

Backlund, C. M.; Parhamifar, L.; Minter, L.; Tew, G. N.; Andresen, T. L. Protein Transduction Domain Mimics Facilitate Rapid Antigen Delivery into Monocytes. *Mol. Pharm.* **2019**, *16* (6), 2462–2469.

Backlund, C. M.; Sgolastra, F.; Otter, R.; Minter, L. M.; Takeuchi, T.; Futaki, S.; Tew, G. N. Increased hydrophobic block length of PTDMs promotes protein internalization. *Polym. Chem.* **2016**, *7* (48), 7514–7521.

Backlund, C. M.; Takeuchi, T.; Futaki, S.; Tew, G. N. Relating structure and internalization for ROMP-based protein mimics. *Biochim. Biophys. Acta - Biomembr.* **2016**, *1858* (7), 1443–1450.

Bang, E.-K.; Gasparini, G.; Molinard, G.; Roux, A.; Sakai, N.; Matile, S. Substrate-Initiated Synthesis of Cell-Penetrating Poly(disulfide)s. *J. Am. Chem. Soc.* **2013**, *135* (6), 2088–2091.

Basiji, D. A.; Ortyn, W. E.; Liang, L.; Venkatachalam, V.; Morrissey, P. Cellular Image Analysis and Imaging by Flow Cytometry. *Clin. Lab. Med.* **2007**, *27* (3), 653–670.

Bechara, C.; Pallerla, M.; Zaltsman, Y.; Burlina, F.; Alves, I. D.; Lequin, O.; Sagan, S. Tryptophan within basic peptide sequences triggers glycosaminoglycan-dependent endocytosis. *FASEB J.* **2013**, *27* (2), 738–749.

Bechara, C.; Sagan, S. Cell-penetrating peptides: 20 years later, where do we stand? *FEBS Lett.* **2013**, *587* (12), 1693–1702.

Bechinger, B. Membrane Insertion and Orientation of Polyalanine Peptides: A ^{15}N Solid-State NMR Spectroscopy Investigation. *Biophys. J.* **2001**, *81* (4), 2251–2256.

Bekale, L.; Agudelo, D.; Tajmir-Riahi, H. A. The role of polymer size and hydrophobic end-group in PEG–protein interaction. *Colloids Surfaces B Biointerfaces* **2015**, *130*, 141–148.

Bekale, L.; Agudelo, D.; Tajmir-Riahi, H. A. Effect of polymer molecular weight on chitosan–protein interaction. *Colloids Surfaces B Biointerfaces* **2015**, *125*, 309–317.

Böck, G.; Steinlein, P.; Huber, L. A. Cell biologists sort things out: Analysis and purification of intracellular organelles by flow cytometry. *Trends Cell Biol.* **1997**, *7* (12), 499–503.

Bodzon-Kulakowska, A.; Bierczynska-Krzysik, A.; Dylag, T.; Drabik, A.; Suder, P.; Noga, M.; Jarzebinska, J.; Silberring, J. Methods for samples preparation in proteomic research. *J. Chromatogr. B Anal. Technol. Biomed. Life Sci.* **2007**, *849* (1–2), 1–31.

Bolte, S.; Cordelières, F. P. A guided tour into subcellular colocalization analysis in light microscopy. *J. Microsc.* **2006**, *224* (3), 213–232.

Caffrey, L. M.; deRonde, B. M.; Minter, L. M.; Tew, G. N. Mapping Optimal Charge Density and Length of ROMP-Based PTDMs for siRNA Internalization. *Biomacromolecules* **2016**, *17* (10), 3205–3212.

Carter, P. J. Introduction to current and future protein therapeutics: A protein engineering perspective. *Exp. Cell Res.* **2011**, *317* (9), 1261–1269.

Chaiyarit, S.; Thongboonkerd, V. Comparative analyses of cell disruption methods for mitochondrial isolation in high-throughput proteomics study. *Anal. Biochem.* **2009**, *394* (2), 249–258.

Chamberlain, G. R.; Tulumello, D. V.; Kelley, S. O. Targeted delivery of doxorubicin to mitochondria. *ACS Chem. Biol.* **2013**, *8* (7), 1389–1395.

Chan, D. I.; Prenner, E. J.; Vogel, H. J. Tryptophan- and arginine-rich antimicrobial peptides: Structures and mechanisms of action. *Biochim. Biophys. Acta - Biomembr.* **2006**, *1758* (9), 1184–1202.

Chang, A. B.; Miyake, G. M.; Grubbs, R. H. Sequence-Controlled Polymers by Ruthenium-Mediated Ring-Opening Metathesis Polymerization. *ACS Symp. Ser.* **2014**, *1170*, 161–188.

Chen, A. K.; Cheng, Z.; Behlke, M. A.; Tsourkas, A. Assessing the sensitivity of commercially available fluorophores to the intracellular environment. *Anal. Chem.* **2008**, *80* (19), 7437–7444.

Chen, L.; Ma, K.; Han, J.; Chen, Q.; Zhu, Y. Monitoring Mitophagy in Mammalian Cells. *Methods Enzymol.* **2017**, *588*, 187–208.

Chen, W. H.; Luo, G. F.; Zhang, X. Z. Recent Advances in Subcellular Targeted Cancer Therapy Based on Functional Materials. *Adv. Mater.* **2019**, *31* (3), 1–39.

Chinnery, P. F.; Taylor, R. W.; Diekert, K.; Lill, R.; Turnbull, D. M.; Lightowlers, R. N. Peptide nucleic acid delivery to human mitochondria. *Gene Ther.* **1999**, *6* (12), 1919–1928.

Chung, L. A.; Thompson, T. E. Design of Membrane-Inserting Peptides: Spectroscopic Characterization with and without Lipid Bilayers. *Biochemistry* **1996**, *35* (35), 11343–11354.

Cleland, J. L.; Daugherty, A.; Mrsny, R. Emerging protein delivery methods. *Curr. Opin. Biotechnol.* **2001**, *12* (2), 212–219.

Cokca, C.; Zartner, L.; Tabujew, I.; Fischer, D.; Peneva, K. Incorporation of Indole Significantly Improves the Transfection Efficiency of Guanidinium-Containing Poly(Methacrylamide)s. *Macromol. Rapid Commun.* **2020**, *41* (6), 1900668.

Cooley, C. B.; Trantow, B. M.; Nederberg, F.; Kiesewetter, M. K.; Hedrick, J. L.; Waymouth, R. M.; Wender, P. A. Oligocarbonate Molecular Transporters: Oligomerization-Based Syntheses and Cell-Penetrating Studies. *J. Am. Chem. Soc.* **2009**, *131* (45), 16401–16403.

Coulpier, M.; Anders, J.; Ibáñez, C. F. Coordinated activation of autophosphorylation sites in the RET receptor tyrosine kinase: Importance of tyrosine 1062 for GDNF mediated neuronal differentiation and survival. *J. Biol. Chem.* **2002**, *277* (3), 1991–1999.

Crombez, L.; Aldrian-Herrada, G.; Konate, K.; Nguyen, Q. N.; McMaster, G. K.; Brasseur, R.; Heitz, F.; Divita, G. A New Potent Secondary Amphipathic Cell–penetrating Peptide for siRNA Delivery Into Mammalian Cells. *Mol. Ther.* **2009**, *17* (1), 95–103.

Dalle-Donne, I.; Aldini, G.; Carini, M.; Colombo, R.; Rossi, R.; Milzani, A. Protein carbonylation, cellular dysfunction, and disease progression. *J. Cell. Mol. Med.* **2006**, *10* (2), 389–406.

Degtyarev, M.; Reichelt, M.; Lin, K. Novel Quantitative Autophagy Analysis by Organelle Flow Cytometry after Cell Sonication. *PLoS One* **2014**, *9* (1), 87707.

Delaroche, D.; Aussedat, B.; Aubry, S.; Chassaing, G.; Burlina, F.; Clodic, G.; Bolbach, G.; Lavielle, S.; Sagan, S. Tracking a New Cell-Penetrating (W/R) Nonapeptide, through an Enzyme-Stable Mass Spectrometry Reporter Tag. *Anal. Chem.* **2007**, *79* (5), 1932–1938.

Demishtein, A.; Porat, Z.; Elazar, Z.; Shvets, E. Applications of flow cytometry for measurement of autophagy. *Methods* **2015**, *75*, 87–95.

deRonde, B. M.; Birke, A.; Tew, G. N. Design of Aromatic-Containing Cell-Penetrating Peptide Mimics with Structurally Modified π Electronics. *Chem. - A Eur. J.* **2015**, *21* (7), 3013–3019.

deRonde, B. M.; Posey, N. D.; Otter, R.; Caffrey, L. M.; Minter, L. M.; Tew, G. N. Optimal Hydrophobicity in Ring-Opening Metathesis Polymerization-Based Protein Mimics Required for siRNA Internalization. *Biomacromolecules* **2016**, *17* (6), 1969–1977.

deRonde, B. M.; Tew, G. N. Development of protein mimics for intracellular delivery. *Biopolymers* **2015**, *104* (4), 265–280.

deRonde, B. M.; Torres, J. A.; Minter, L. M.; Tew, G. N. Development of Guanidinium-Rich Protein Mimics for Efficient siRNA Delivery into Human T Cells. *Biomacromolecules* **2015**, *16* (10), 3172–3179.

Derossi, D.; Joliot, A. H.; Chassaing, G.; Prochiantz, A. The third helix of the Antennapedia homeodomain translocates through biological membranes. *J. Biol. Chem.* **1994**, *269* (14), 10444–10450.

Deshayes, S.; Heitz, A.; Morris, M. C.; Charnet, P.; Divita, G.; Heitz, F. Insight into the Mechanism of Internalization of the Cell-Penetrating Carrier Peptide Pep-1 through Conformational Analysis. *Biochemistry* **2004**, *43* (6), 1449–1457.

Deshayes, S.; Morris, M.; Heitz, F.; Divita, G. Delivery of proteins and nucleic acids using a non-covalent peptide-based strategy. *Adv. Drug Deliv. Rev.* **2008**, *60* (4–5), 537–547.

Doherty, E.; Perl, A. Measurement of Mitochondrial Mass by Flow Cytometry during Oxidative Stress. *React. Oxyg. Species* **2017**, *4* (10), 275–283.

Dolman, N. J.; Chambers, K. M.; Mandavilli, B.; Batchelor, R. H.; Janes, M. S. Tools and techniques to measure mitophagy using fluorescence microscopy. *Autophagy* **2013**, *9* (11), 1653–1662.

Dolman, N. J.; Kilgore, J. A.; Davidson, M. W. A Review of Reagents for Fluorescence Microscopy of Cellular Compartments and Structures, Part I: BacMam Labeling and Reagents for Vesicular Structures. *Curr. Protoc. Cytom.* **2013**, *65* (1).

Douglas, M. G.; McCammon, M. T.; Vassarotti, A. Targeting proteins into mitochondria. *Microbiol. Rev.* **1986**, *50* (2), 166–178.

Du, J.; Jin, J.; Yan, M.; Lu, Y. Synthetic Nanocarriers for Intracellular Protein Delivery. *Curr. Drug Metab.* **2012**, *13* (1), 82–92.

Dunn, K. W.; Kamocka, M. M.; McDonald, J. H. A practical guide to evaluating colocalization in biological microscopy. *Am. J. Physiol. Physiol.* **2011**, *300* (4), C723–C742.

El-Andaloussi, S.; Johansson, H. J.; Holm, T.; Langel, Ü. A Novel Cell-penetrating Peptide, M918, for Efficient Delivery of Proteins and Peptide Nucleic Acids. *Mol. Ther.* **2007**, *15* (10), 1820–1826.

Elmquist, A.; Lindgren, M.; Bartfai, T.; Langel, Ü. VE-Cadherin-Derived Cell-Penetrating Peptide, pVEC, with Carrier Functions. *Exp. Cell Res.* **2001**, *269* (2), 237–244.

Esquivel, R. N.; Patel, A.; Kudchodkar, S. B.; Park, D. H.; Stettler, K.; Beltramello, M.; Allen, J. W.; Mendoza, J.; Ramos, S.; Choi, H.; Borole, P.; Asija, K.; Bah, M.; Shaheen, S.; Chen, J.; Yan, J.; Durham, A. C.; Smith, T. R. F.; Broderick, K.; et al. *In Vivo* Delivery of a DNA-Encoded Monoclonal Antibody Protects Non-human Primates against Zika Virus. *Mol. Ther.* **2019**, *27* (5), 974–985.

Farkhani, S. M.; Johari-ahar, M.; Zakeri-Milani, P.; Shahbazi Mojarrad, J.; Valizadeh, H. Enhanced cellular internalization of CdTe quantum dots mediated by arginine- and tryptophan-rich cell-penetrating peptides as efficient carriers. *Artif. Cells, Nanomedicine, Biotechnol.* **2015**, 1–5.

Fenton, M.; Bone, N.; Sinclair, A. J. The efficient and rapid import of a peptide into primary B and T lymphocytes and a lymphoblastoid cell line. *J. Immunol. Methods* **1998**, *212* (1), 41–48.

Fonseca, S. B.; Pereira, M. P.; Mourtada, R.; Gronda, M.; Horton, K. L.; Hurren, R.; Minden, M. D.; Schimmer, A. D.; Kelley, S. O. Rerouting chlorambucil to mitochondria combats drug deactivation and resistance in cancer cells. *Chem. Biol.* **2011**, *18* (4), 445–453.

Fonseca, S. B.; Kelley, S. O. Peptide-chlorambucil conjugates combat Pgp-dependent drug efflux. *ACS Med. Chem. Lett.* **2011**, *2* (6), 419–423.

Frankel, A. D.; Pabo, C. O. Cellular uptake of the tat protein from human immunodeficiency virus. *Cell* **1988**, *55* (6), 1189–1193.

Frokjaer, S.; Otzen, D. E. Protein drug stability: A formulation challenge. *Nat. Rev. Drug Discov.* **2005**, *4* (4), 298–306.

Fu, A.; Tang, R.; Hardie, J.; Farkas, M. E.; Rotello, V. M. Promises and Pitfalls of Intracellular Delivery of Proteins. *Bioconjug. Chem.* **2014**, *25* (9), 1602–1608.

Futaki, S.; Nakase, I.; Suzuki, T.; Youjun, Z.; Sugiura, Y. Translocation of branched-chain arginine peptides through cell membranes: Flexibility in the spatial disposition of positive charges in membrane-permeable peptides. *Biochemistry* **2002**, *41* (25), 7925–7930.

Gan, Q.; Wang, T. Chitosan nanoparticle as protein delivery carrier—Systematic examination of fabrication conditions for efficient loading and release. *Colloids Surfaces B Biointerfaces* **2007**, *59* (1), 24–34.

Gasparini, G.; Bang, E. K.; Montenegro, J.; Matile, S. Cellular uptake: lessons from supramolecular organic chemistry. *Chem. Commun.* **2015**, *51* (52), 10389–10402.

Gauthier, D. J.; Lazure, C. Complementary methods to assist subcellular fractionation in organellar proteomics. *Expert Rev. Proteomics* **2008**, *5* (4), 603–617.

Geihe, E. I.; Cooley, C. B.; Simon, J. R.; Kiesewetter, M. K.; Edward, J. A.; Hickerson, R. P.; Kaspar, R. L.; Hedrick, J. L.; Waymouth, R. M.; Wender, P. A. Designed guanidinium-rich amphipathic oligocarbonate molecular transporters complex, deliver and release siRNA in cells. *Proc. Natl. Acad. Sci.* **2012**, *109* (33), 13171–13176.

Gill, S. C.; von Hippel, P. H. Calculation of protein extinction coefficients from amino acid sequence data. *Anal. Biochem.* **1989**, *182* (2), 319–326.

Gilleron, J.; Querbes, W.; Zeigerer, A.; Borodovsky, A.; Marsico, G.; Schubert, U.; Manygoats, K.; Seifert, S.; Andree, C.; Stöter, M.; Epstein-Barash, H.; Zhang, L.; Koteliansky, V.; Fitzgerald, K.; Fava, E.; Bickle, M.; Kalaidzidis, Y.; Akinc, A.; Maier, M.; et al. Image-based analysis of lipid nanoparticle–mediated siRNA delivery, intracellular trafficking and endosomal escape. *Nat. Biotechnol.* **2013**, *31* (7), 638–646.

Gong, Y.; Leroux, J. C.; Gauthier, M. A. Releasable Conjugation of Polymers to Proteins. *Bioconjugate Chemistry*. 2015, pp 1179–1181.

González-Toro, D. C.; Ryu, J. H.; Chacko, R. T.; Zhuang, J.; Thayumanavan, S. Concurrent binding and delivery of proteins and lipophilic small molecules using polymeric nanogels. *J. Am. Chem. Soc.* **2012**, *134* (16), 6964–6967.

González-Toro, D. C.; Thayumanavan, S. Advances in polymer and polymeric nanostructures for protein conjugation. *Eur. Polym. J.* **2013**, *49* (10), 2906–2918.

Graham, J. M. Isolation of Lysosomes from Tissues and Cells by Differential and Density Gradient Centrifugation. *Curr. Protoc. Cell Biol.* **2000**, *7* (1).

Green, M.; Loewenstein, P. M. Autonomous functional domains of chemically synthesized human immunodeficiency virus tat trans-activator protein. *Cell* **1988**, *55* (6), 1179–1188.

Gu, Z.; Biswas, A.; Zhao, M.; Tang, Y. Tailoring nanocarriers for intracellular protein delivery. *Chem. Soc. Rev.* **2011**, *40* (7), 3638.

Gump, J. M.; June, R. K.; Dowdy, S. F. Revised Role of Glycosaminoglycans in TAT Protein Transduction Domain-mediated Cellular Transduction. *J. Biol. Chem.* **2010**, *285* (2), 1500–1507.

Guo, F.; Gopaul, D. N.; Van Duyne, G. D. Structure of Cre recombinase complexed with DNA in a site-specific recombination synapse. *Nature* **1997**, *389* (6646), 40–46.

Guo, X.; Wei, X.; Chen, Z.; Zhang, X.; Yang, G.; Zhou, S. Multifunctional nanoplatforms for subcellular delivery of drugs in cancer therapy. *Prog. Mater. Sci.* **2020**, *107*, 100599.

Guo, Z.; Kong, Z.; Wei, Y.; Li, H.; Wang, Y.; Huang, A.; Ma, L. Effects of gene carrier polyethyleneimines on the structure and binding capability of bovine serum albumin. *Spectrochim. Acta - Part A Mol. Biomol. Spectrosc.* **2017**, *173*, 783–791.

Hamid Akash, M. S.; Rehman, K.; Chen, S. Natural and Synthetic Polymers as Drug Carriers for Delivery of Therapeutic Proteins. *Polym. Rev.* **2015**, *55* (3), 371–406.

Hamilton, J. G. The determination and interpretation of tacticity in ring-opening metathesis polymerization. *Polymer* **1998**, *39* (8–9), 1669–1689.

Hamm, A.; Krott, N.; Breibach, I.; Blindt, R.; Bosserhoff, A. K. Efficient Transfection Method for Primary Cells. *Tissue Eng.* **2002**, *8* (2), 235–245.

Hanson, J. A.; Chang, C. B.; Graves, S. M.; Li, Z.; Mason, T. G.; Deming, T. J. Nanoscale double emulsions stabilized by single-component block copolypeptides. *Nature* **2008**, *455* (7209), 85–88.

Hasadsri, L.; Kreuter, J.; Hattori, H.; Iwasaki, T.; George, J. M. Functional protein delivery into neurons using polymeric nanoparticles. *J. Biol. Chem.* **2009**, *284* (11), 6972–6981.

Heitz, F.; Morris, M. C.; Divita, G. Twenty years of cell-penetrating peptides: from molecular mechanisms to therapeutics. *Br. J. Pharmacol.* **2009**, *157* (2), 195–206.

Henriksen, M.; Miller, B.; Newmark, J.; Al-Kofahi, Y.; Holden, E. Laser Scanning Cytometry and Its Applications: A Pioneering Technology in the Field of Quantitative Imaging Cytometry. In *Methods in Cell Biology*; 2011; Vol. 102, pp 159–205.

Herrera Estrada, L. P.; Champion, J. A. Protein nanoparticles for therapeutic protein delivery. *Biomater. Sci.* **2015**, *3* (6), 787–799.

Hoffman, A. Pharmacodynamic aspects of sustained release preparations. *Adv. Drug Deliv. Rev.* **1998**, *33* (3), 185–199.

Holowka, E. P.; Pochan, D. J.; Deming, T. J. Charged Polypeptide Vesicles with Controllable Diameter. *J. Am. Chem. Soc.* **2005**, *127* (35), 12423–12428.

Holowka, E. P.; Sun, V. Z.; Kamei, D. T.; Deming, T. J. Polyarginine segments in block copolypeptides drive both vesicular assembly and intracellular delivery. *Nat. Mater.* **2007**, *6* (1), 52–57.

Hornig-Do, H. T.; Günther, G.; Bust, M.; Lehnartz, P.; Bosio, A.; Wiesner, R. J. Isolation of functional pure mitochondria by superparamagnetic microbeads. *Anal. Biochem.* **2009**, *389* (1), 1–5.

Horton, K. L.; Pereira, M. P.; Stewart, K. M.; Fonseca, S. B.; Kelley, S. O. Tuning the activity of mitochondria-penetrating peptides for delivery or disruption. *ChemBioChem* **2012**, *13* (3), 476–485.

Horton, K. L.; Stewart, K. M.; Fonseca, S. B.; Guo, Q.; Kelley, S. O. Mitochondria-Penetrating Peptides. *Chem. Biol.* **2008**, *15* (4), 375–382.

Hou, X.-S. S.; Wang, H.-S. S.; Mugaka, B. P.; Yang, G.-J. J.; Ding, Y. Mitochondria: Promising organelle targets for cancer diagnosis and treatment. *Biomater. Sci.* **2018**, *6* (11), 2786–2797.

Ilker, M. F.; Nüsslein, K.; Tew, G. N.; Coughlin, E. B. Tuning the Hemolytic and Antibacterial Activities of Amphiphilic Polynorbornene Derivatives. *J. Am. Chem. Soc.* **2004**, *126* (48), 15870–15875.

Jain, S.; Bates, F. S. On the origins of morphological complexity in block copolymer surfactants. *Science* **2003**, *300* (5618), 460–464.

Janes, K. A.; Alonso, M. J. Depolymerized chitosan nanoparticles for protein delivery: Preparation and characterization. *J. Appl. Polym. Sci.* **2003**, *88* (12), 2769–2776.

Jean, S. R.; Ahmed, M.; Lei, E. K.; Wisnovsky, S. P.; Kelley, S. O. Peptide-Mediated Delivery of Chemical Probes and Therapeutics to Mitochondria. *Acc. Chem. Res.* **2016**, *49* (9), 1893–1902.

Jhaveri, A.; Torchilin, V. Intracellular delivery of nanocarriers and targeting to subcellular organelles. *Expert Opin. Drug Deliv.* **2016**, *13* (1), 49–70.

Jiang, T.; Zhang, Z.; Zhang, Y.; Lv, H.; Zhou, J.; Li, C.; Hou, L.; Zhang, Q. Dual-functional liposomes based on pH-responsive cell-penetrating peptide and hyaluronic acid for tumor-targeted anticancer drug delivery. *Biomaterials* **2012**, *33* (36), 9246–9258.

Joliot, A.; Pernelle, C.; Deagostini-Bazin, H.; Prochiantz, A. Antennapedia homeobox peptide regulates neural morphogenesis. *Proc. Natl. Acad. Sci.* **1991**, *88* (5), 1864–1868.

Jordan, E. T.; Collins, M.; Terefe, J.; Ugozzoli, L.; Rubio, T. Optimizing electroporation conditions in primary and other difficult-to-transfect cells. *J. Biomol. Tech.* **2008**, *19* (5), 328–334.

Karra, D.; Dahm, R. Transfection Techniques for Neuronal Cells. *J. Neurosci.* **2010**, *30* (18), 6171–6177.

Katayama, S.; Hirose, H.; Takayama, K.; Nakase, I.; Futaki, S. Acylation of octaarginine: Implication to the use of intracellular delivery vectors. *J. Control. Release* **2011**, *149* (1), 29–35.

Kettler, K.; Veltman, K.; van de Meent, D.; van Wezel, A.; Hendriks, A. J. Cellular uptake of nanoparticles as determined by particle properties, experimental conditions, and cell type. *Environ. Toxicol. Chem.* **2014**, *33* (3), 481–492.

Keum, J.-W.; Bermudez, H. DNA-based delivery vehicles: pH-controlled disassembly and cargo release. *Chem. Commun.* **2012**, *48* (99), 12118.

Khalil, I. A.; Kogure, K.; Akita, H.; Harashima, H. Uptake Pathways and Subsequent Intracellular Trafficking in Nonviral Gene Delivery. *Pharmacol. Rev.* **2006**, *58* (1), 32–45.

Kim, T.; Ou, M.; Lee, M.; Kim, S. W. Arginine-grafted bioreducible poly(disulfide amine) for gene delivery systems. *Biomaterials* **2009**, *30* (4), 658–664.

Kolonko, E. M.; Kiessling, L. L. A Polymeric Domain That Promotes Cellular Internalization. *J. Am. Chem. Soc.* **2008**, *130* (17), 5626–5627.

Koren, E.; Torchilin, V. P. Cell-penetrating peptides: breaking through to the other side. *Trends Mol. Med.* **2012**, *18* (7), 385–393.

Kowalski, P. S.; Bhattacharya, C.; Afewerki, S.; Langer, R. Smart Biomaterials: Recent Advances and Future Directions. *ACS Biomater. Sci. Eng.* **2018**, *4* (11), 3809–3817.

Kozlowski, L. P. IPC – Isoelectric Point Calculator. *Biol. Direct* **2016**, *11* (1), 55.

Krejsa, C.; Rogge, M.; Sadee, W. Protein therapeutics: new applications for pharmacogenetics. *Nat. Rev. Drug Discov.* **2006**, *5* (6), 507–521.

Kurzawa, L.; Pellerano, M.; Morris, M. C. PEP and CADY-mediated delivery of fluorescent peptides and proteins into living cells. *Biochim. Biophys. Acta - Biomembr.* **2010**, *1798* (12), 2274–2285.

Lampariello, F. Ratio analysis of cumulatives for labeled cell quantification from immunofluorescence histograms derived from cells expressing low antigen levels. *Cytom. Part A* **2009**, *75A* (8), 665–674.

Leader, B.; Baca, Q. J.; Golan, D. E. Protein therapeutics: A summary and pharmacological classification. *Nat. Rev. Drug Discov.* **2008**, *7* (1), 21–39.

Lecoeur, H.; Langonné, A.; Baux, L.; Rebouillat, D.; Rustin, P.; Prévost, M. C.; Brenner, C.; Edelman, L.; Jacotot, E. Real-time flow cytometry analysis of permeability transition in isolated mitochondria. *Exp. Cell Res.* **2004**, *294* (1), 106–117.

Lécorché, P.; Walrant, A.; Burlina, F.; Dutot, L.; Sagan, S.; Mallet, J.-M.; Desbat, B.; Chassaing, G.; Alves, I. D.; Lavielle, S. Cellular uptake and biophysical properties of galactose and/or tryptophan containing cell-penetrating peptides. *Biochim. Biophys. Acta - Biomembr.* **2012**, *1818* (3), 448–457.

Lei, E. K.; Kelley, S. O. Delivery and Release of Small-Molecule Probes in Mitochondria Using Traceless Linkers. *J. Am. Chem. Soc.* **2017**, *139* (28), 9455–9458.

Lian, H.; He, S.; Chen, C.; Yan, X. Flow Cytometric Analysis of Nanoscale Biological Particles and Organelles. *Annu. Rev. Anal. Chem.* **2019**, *12* (1), 389–409.

Lienkamp, K.; Madkour, A. E.; Musante, A.; Nelson, C. F.; Nüsslein, K.; Tew, G. N. Antimicrobial Polymers Prepared by ROMP with Unprecedented Selectivity: A Molecular Construction Kit Approach. *J. Am. Chem. Soc.* **2008**, *130* (30), 9836–9843.

Lin, H.-C. C.; Liu, S.-Y. Y.; Lai, H.-S. S.; Lai, I.-R. R. Isolated mitochondria infusion mitigates ischemia-reperfusion injury of the liver in rats. *Shock* **2013**, *39* (3), 304–310.

Lindgren, M.; Hällbrink, M.; Prochiantz, A.; Langel, Ü. Cell-penetrating peptides. *Trends Pharmacol. Sci.* **2000**, *21* (3), 99–103.

Long, J.; Xu, E.; Li, X.; Wu, Z.; Wang, F.; Xu, X.; Jin, Z.; Jiao, A.; Zhan, X. Effect of chitosan molecular weight on the formation of chitosan-pullulanase soluble complexes and their application in the immobilization of pullulanase onto Fe_3O_4-κ-carrageenan nanoparticles. *Food Chem.* **2016**, *202*, 49–58.

Louzoun-Zada, S.; Jaber, Q. Z.; Fridman, M. Guiding Drugs to Target-Harboring Organelles: Stretching Drug-Delivery to a Higher Level of Resolution. *Angew. Chemie Int. Ed.* **2019**, *58* (44), 15584–15594.

Love, J. A.; Morgan, J. P.; Trnka, T. M.; Grubbs, R. H. A Practical and Highly Active Ruthenium-Based Catalyst that Effects the Cross Metathesis of Acrylonitrile. *Angew. Chemie Int. Ed.* **2002**, *41* (21), 4035–4037.

Lu, J.; Owen, S. C.; Shoichet, M. S. Stability of self-assembled polymeric micelles in serum. *Macromolecules* **2011**, *44* (15), 6002–6008.

Lu, Y. M. Src Activation in the Induction of Long-Term Potentiation in CA1 Hippocampal Neurons. *Science* **1998**, *279* (5355), 1363–1368.

Luedtke, N. W.; Carmichael, P.; Tor, Y. Cellular Uptake of Aminoglycosides, Guanidinoglycosides, and Poly-arginine. *J. Am. Chem. Soc.* **2003**, *125* (41), 12374–12375.

Ma, C.; Xia, F.; Kelley, S. O. Mitochondrial Targeting of Probes and Therapeutics to the Powerhouse of the Cell. *Bioconjug. Chem.* **2020**, *31* (12), 2650–2667.

Ma, X.; Gong, N.; Zhong, L.; Sun, J.; Liang, X.-J. Future of nanotherapeutics: Targeting the cellular sub-organelles. *Biomaterials* **2016**, *97*, 10–21.

Madani, F.; Lindberg, S.; Langel, Ü.; Futaki, S.; Gräslund, A. Mechanisms of Cellular Uptake of Cell-Penetrating Peptides. *J. Biophys.* **2011**, *2011*, 1–10.

Madkour, A. E.; Koch, A. H. R.; Lienkamp, K.; Tew, G. N. End-Functionalized ROMP Polymers for Biomedical Applications. *Macromolecules* **2010**, *43* (10), 4557–4561.

Maeder, M. L.; Gersbach, C. A. Genome-editing Technologies for Gene and Cell Therapy. *Mol. Ther.* **2016**, *24* (3), 430–446.

Magenau, A. J. D.; Richards, J. A.; Pasquinelli, M. A.; Savin, D. A.; Mathers, R. T. Systematic Insights from Medicinal Chemistry To Discern the Nature of Polymer Hydrophobicity. *Macromolecules* **2015**, *48* (19), 7230–7236.

Mai, Y.; Eisenberg, A. Self-assembly of block copolymers. *Chem. Soc. Rev.* **2012**, *41* (18), 5969.

Maiolo, J. R.; Ferrer, M.; Ottinger, E. A. Effects of cargo molecules on the cellular uptake of arginine-rich cell-penetrating peptides. *Biochim. Biophys. Acta - Biomembr.* **2005**, *1712* (2), 161–172.

Maiti, K. K.; Jeon, O.-Y.; Lee, W. S.; Kim, D.-C.; Kim, K.-T.; Takeuchi, T.; Futaki, S.; Chung, S.-K. Design, Synthesis, and Membrane-Translocation Studies of Inositol-Based Transporters. *Angew. Chemie Int. Ed.* **2006**, *45* (18), 2907–2912.

Maity, A. R.; Stepensky, D. Delivery of drugs to intracellular organelles using drug delivery systems: Analysis of research trends and targeting efficiencies. *Int. J. Pharm.* **2015**, *496* (2), 268–274.

Marschall, A. L. J.; Frenzel, A.; Schirrmann, T.; Schüngel, M.; Dübel, S. Targeting antibodies to the cytoplasm. *mAbs* **2011**, *3* (1), 3–16.

Martin, L.; Peltier, R.; Kuroki, A.; Town, J. S.; Perrier, S. Investigating Cell Uptake of Guanidinium-Rich RAFT Polymers: Impact of Comonomer and Monomer Distribution. *Biomacromolecules* **2018**, *19* (8), 3190–3200.

Matsumoto, R.; Okochi, M.; Shimizu, K.; Kanie, K.; Kato, R.; Honda, H. Effects of the properties of short peptides conjugated with cell-penetrating peptides on their internalization into cells. *Sci. Rep.* **2015**, *5* (1), 12884.

McNaughton, B. R.; Cronican, J. J.; Thompson, D. B.; Liu, D. R. Mammalian cell penetration, siRNA transfection, and DNA transfection by supercharged proteins. *Proc. Natl. Acad. Sci.* **2009**, *106* (15), 6111–6116.

Milletti, F. Cell-penetrating peptides: classes, origin, and current landscape. *Drug Discov. Today* **2012**, *17* (15–16), 850–860.

Mitchell, D. J.; Steinman, L.; Kim, D. T.; Fathman, C. G.; Rothbard, J. B. Polyarginine enters cells more efficiently than other polycationic homopolymers. *J. Pept. Res.* **2000**, *56* (5), 318–325.

Mitragotri, S.; Burke, P. A.; Langer, R. Overcoming the challenges in administering biopharmaceuticals: Formulation and delivery strategies. *Nat. Rev. Drug Discov.* **2014**, *13* (9), 655–672.

Moloney, M.; Shreffler, W. G. Basic science for the practicing physician: flow cytometry and cell sorting. *Ann. Allergy, Asthma Immunol.* **2008**, *101* (5), 544–549.

Morris, M. C.; Vidal, P.; Chaloin, L.; Heitz, F.; Divita, G. A new peptide vector for efficient delivery of oligonucleotides into mammalian cells. *Nucleic Acids Res.* **1997**, *25* (14), 2730–2736.

Morris, M. C.; Deshayes, S.; Heitz, F.; Divita, G. Cell-penetrating peptides: from molecular mechanisms to therapeutics. *Biol. Cell* **2008**, *100* (4), 201–217.

Morris, M. C.; Depollier, J.; Mery, J.; Heitz, F.; Divita, G. A peptide carrier for the delivery of biologically active proteins into mammalian cells. *Nat. Biotechnol.* **2001**, *19* (12), 1173–1176.

Mulgrew-Nesbitt, A.; Diraviyam, K.; Wang, J.; Singh, S.; Murray, P.; Li, Z.; Rogers, L.; Mirkovic, N.; Murray, D. The role of electrostatics in protein–membrane interactions. *Biochim. Biophys. Acta - Mol. Cell Biol. Lipids* **2006**, *1761* (8), 812–826.

Muratovska, A.; Lightowlers, R. N.; Taylor, R. W.; Wilce, J. A.; Murphy, M. P. Targeting large molecules to mitochondria. *Adv. Drug Deliv. Rev.* **2001**, *49* (1–2), 189–198.

Nag, O. K.; Delehanty, J. B. Active cellular and subcellular targeting of nanoparticles for drug delivery. *Pharmaceutics* **2019**, *11* (10), 7–9.

Nam, H. Y.; Hong, J.-A.; Choi, J.; Shin, S.; Cho, S. K.; Seo, J.; Lee, J. Mitochondria-Targeting Peptoids. *Bioconjug. Chem.* **2018**, *29* (5), 1669–1676.

Nongkhlaw, R.; Patra, P.; Chavrasiya, A.; Jayabalan, N.; Dubey, S. Biologics: Delivery options and formulation strategies. In *Drug Delivery Aspects*; Elsevier, 2020; pp 115–155.

Nozaki, Y.; Tanford, C. The solubility of amino acids and two glycine peptides in aqueous ethanol and dioxane solutions: establishment of a hydrophobicity scale. *J. Biol. Chem.* **1971**, *246* (7), 2211–2217.

Nurunnabi, M.; Khatun, Z.; Badruddoza, A. Z. M.; McCarthy, J. R.; Lee, Y. K.; Huh, K. M. Biomaterials and Bioengineering Approaches for Mitochondria and Nuclear Targeting Drug Delivery. *ACS Biomater. Sci. Eng.* **2019**, *5* (4), 1645–1660.

Oehlke, J.; Scheller, A.; Wiesner, B.; Krause, E.; Beyermann, M.; Klauschenz, E.; Melzig, M.; Bienert, M. Cellular uptake of an α-helical amphipathic model peptide with the potential to deliver polar compounds into the cell interior non-endocytically. *Biochim. Biophys. Acta - Biomembr.* **1998**, *1414* (1–2), 127–139.

Ozay, E. I.; Shanthalingam, S.; Sherman, H. L.; Torres, J. A.; Osborne, B. A.; Tew, G. N.; Minter, L. M. Cell-Penetrating Anti-Protein Kinase C Theta Antibodies Act Intracellularly to Generate Stable, Highly Suppressive Regulatory T Cells. *Mol. Ther.* **2020**, *28* (8), 1987–2006.

Ozay, E. I.; Shanthalingam, S.; Torres, J. A.; Osborne, B. A.; Tew, G. N.; Minter, L. M. Protein Kinase C Theta Modulates PCMT1 through hnRNPL to Regulate FOXP3 Stability in Regulatory T Cells. *Mol. Ther.* **2020**, *28* (10), 1–17.

Ozay, E. I.; Gonzalez-Perez, G.; Torres, J. A.; Vijayaraghavan, J.; Lawlor, R.; Sherman, H. L.; Garrigan, D. T.; Burnside, A. S.; Osborne, B. A.; Tew, G. N.; Minter, L. M. Intracellular Delivery of Anti-pPKCθ (Thr538) via Protein Transduction Domain Mimics for Immunomodulation. *Mol. Ther.* **2016**, *24* (12), 2118–2130.

Pack, D. W.; Hoffman, A. S.; Pun, S.; Stayton, P. S. Design and development of polymers for gene delivery. *Nat. Rev. Drug Discov.* **2005**, *4* (7), 581–593.

Pallotti, F.; Lenaz, G. Isolation and subfractionation of mitochondria from animal cells and tissue culture lines. In *Methods in Cell Biology*; 2001; pp 1–35.

Pasquali, C.; Fialka, I.; Huber, L. A. Subcellular fractionation, electromigration analysis and mapping of organelles. *J. Chromatogr. B Biomed. Sci. Appl.* **1999**, *722* (1–2), 89–102.

Pasupuleti, M.; Chalupka, A.; Mörgelin, M.; Schmidtchen, A.; Malmsten, M. Tryptophan end-tagging of antimicrobial peptides for increased potency against Pseudomonas aeruginosa. *Biochim. Biophys. Acta - Gen. Subj.* **2009**, *1790* (8), 800–808.

Pasupuleti, M.; Schmidtchen, A.; Chalupka, A.; Ringstad, L.; Malmsten, M. End-Tagging of Ultra-Short Antimicrobial Peptides by W/F Stretches to Facilitate Bacterial Killing. *PLoS One* **2009**, *4* (4), e5285.

Pasut, G. Polymers for Protein Conjugation. *Polymers* **2014**, *6* (1), 160–178.

Peer, D. A daunting task: Manipulating leukocyte function with RNAi. *Immunol. Rev.* **2013**, *253* (1), 185–197.

Pickles, S.; Arbour, N.; Vande Velde, C. Immunodetection of Outer Membrane Proteins by Flow Cytometry of Isolated Mitochondria. *J. Vis. Exp.* **2014**, No. 91, 1–8.

Pooga, M.; Hällbrink, M.; Zorko, M.; Langel, Ü. Cell penetration by transportan. *FASEB J.* **1998**, *12* (1), 67–77.

Poot, M.; Zhang, Y. Z.; Krämer, J. A.; Wells, K. S.; Jones, L. J.; Hanzel, D. K.; Lugade, A. G.; Singer, V. L.; Haugland, R. P. Analysis of mitochondrial morphology and function with novel fixable fluorescent stains. *J. Histochem. Cytochem.* **1996**, *44* (12), 1363–1372.

Poot, M. Analysis of Intracellular Organelles by Flow Cytometry or Microscopy. *Curr. Protoc. Cytom.* **2000**, *14* (1), 1–24.

Posey, N. D.; Caffrey, L. M.; Minter, L. M.; Tew, G. N. Protein Mimic Hydrophobicity Affects Intracellular Delivery but not Cargo Binding. *ChemistrySelect* **2016**, *1* (19), 6146–6150.

Posey, N. D.; Hango, C. R.; Minter, L. M.; Tew, G. N. The Role of Cargo Binding Strength in Polymer-Mediated Intracellular Protein Delivery. *Bioconjug. Chem.* **2018**, *29* (8), 2679–2690.

Posey, N. D.; Tew, G. N. Associative and Dissociative Processes in Non-Covalent Polymer-Mediated Intracellular Protein Delivery. *Chem. - An Asian J.* **2018**, *13* (22), 3351–3365.

Posey, N. D.; Tew, G. N. Protein Transduction Domain Mimic (PTDM) Self-Assembly? *Polymers* **2018**, *10* (9), 1039.

Qin, X.; Yu, C.; Wei, J.; Li, L.; Zhang, C.; Wu, Q.; Liu, J.; Yao, S. Q.; Huang, W. Rational Design of Nanocarriers for Intracellular Protein Delivery. *Adv. Mater.* **2019**, *31* (46), 1902791.

Radcliff, G.; Jaroszeski, M. J. Basics of flow cytometry. *Methods Mol. Biol.* **1998**, *91*, 1–24.

Raffa, P.; Wever, D. A. Z.; Picchioni, F.; Broekhuis, A. A. Polymeric Surfactants: Synthesis, Properties, and Links to Applications. *Chem. Rev.* **2015**, *115* (16), 8504–8563.

Rajendran, L.; Knölker, H.-J.; Simons, K. Subcellular targeting strategies for drug design and delivery. *Nat. Rev. Drug Discov.* **2010**, *9* (1), 29–42.

Rao, J. P.; Geckeler, K. E. Polymer nanoparticles: Preparation techniques and size-control parameters. *Prog. Polym. Sci.* **2011**, *36* (7), 887–913.

Ray, M.; Lee, Y. W.; Scaletti, F.; Yu, R.; Rotello, V. M. Intracellular delivery of proteins by nanocarriers. *Nanomedicine* **2017**, *12* (8), 941–952.

Raz-Prag, D.; Grimes, W. N.; Fariss, R. N.; Vijayasarathy, C.; Campos, M. M.; Bush, R. A.; Diamond, J. S.; Sieving, P. A. Probing potassium channel function *in vivo* by intracellular delivery of antibodies in a rat model of retinal neurodegeneration. *Proc. Natl. Acad. Sci.* **2010**, *107* (28), 12710–12715.

Reers, M.; Smiley, S. T.; Mottola-Hartshorn, C.; Chen, A.; Lin, M.; Chen, L. B. Mitochondrial membrane potential monitored by JC-1 dye. *Methods Enzymol.* **1995**, *260* (C), 406–414.

Reynhout, I. C.; Cornelissen, J. J. L. M.; Nolte, R. J. M. Synthesis of Polymer−Biohybrids: From Small to Giant Surfactants. *Acc. Chem. Res.* **2009**, *42* (6), 681–692.

Rodriguez, A. R.; Choe, U.-J.; Kamei, D. T.; Deming, T. J. Blending of Diblock and Triblock Copolypeptide Amphiphiles Yields Cell Penetrating Vesicles with Low Toxicity. *Macromol. Biosci.* **2015**, *15* (1), 90–97.

Rydberg, H. A.; Carlsson, N.; Nordén, B. Membrane interaction and secondary structure of *de novo* designed arginine-and tryptophan peptides with dual function. *Biochem. Biophys. Res. Commun.* **2012**, *427* (2), 261–265.

Rydberg, H. A.; Matson, M.; Åmand, H. L.; Esbjörner, E. K.; Nordén, B. Effects of Tryptophan Content and Backbone Spacing on the Uptake Efficiency of Cell-Penetrating Peptides. *Biochemistry* **2012**, *51* (27), 5531–5539.

Ryu, J.-H.; Chacko, R. T.; Jiwpanich, S.; Bickerton, S.; Babu, R. P.; Thayumanavan, S. Self-Cross-Linked Polymer Nanogels: A Versatile Nanoscopic Drug Delivery Platform. *J. Am. Chem. Soc.* **2010**, *132* (48), 17227–17235.

Sabnis, S.; Block, L. H. Chitosan as an enabling excipient for drug delivery systems I. Molecular modifications. *Int. J. Biol. Macromol.* **2000**, *27*, 181–186.

Sahay, G.; Alakhova, D. Y.; Kabanov, A. V. Endocytosis of nanomedicines. *J. Control. Release* **2010**, *145* (3), 182–195.

Salmaso, S.; Caliceti, P. Self assembling nanocomposites for protein delivery: Supramolecular interactions of soluble polymers with protein drugs. *Int. J. Pharm.* **2013**, *440* (1), 111–123.

Sarapas, J. M.; Backlund, C. M.; DeRonde, B. M.; Minter, L. M.; Tew, G. N. ROMP- and RAFT-Based Guanidinium-Containing Polymers as Scaffolds for Protein Mimic Synthesis. *Chem. - A Eur. J.* **2017**, *23* (28), 6858–6863.

Satori, C. P.; Kostal, V.; Arriaga, E. A. Review on recent advances in the analysis of isolated organelles. *Anal. Chim. Acta* **2012**, *753*, 8–18.

Schmidt, N. W.; Lis, M.; Zhao, K.; Lai, G. H.; Alexandrova, A. N.; Tew, G. N.; Wong, G. C. L. Molecular Basis for Nanoscopic Membrane Curvature Generation from Quantum Mechanical Models and Synthetic Transporter Sequences. *J. Am. Chem. Soc.* **2012**, *134* (46), 19207–19216.

Schmidt, S.; Adjobo-Hermans, M. J. W.; Kohze, R.; Enderle, T.; Brock, R.; Milletti, F. Identification of Short Hydrophobic Cell-Penetrating Peptides for Cytosolic Peptide Delivery by Rational Design. *Bioconjug. Chem.* **2017**, *28* (2), 382–389.

Schmidtchen, A.; Pasupuleti, M.; Mörgelin, M.; Davoudi, M.; Alenfall, J.; Chalupka, A.; Malmsten, M. Boosting Antimicrobial Peptides by Hydrophobic Oligopeptide End Tags. *J. Biol. Chem.* **2009**, *284* (26), 17584–17594.

Selby, L. I.; Cortez-Jugo, C. M.; Such, G. K.; Johnston, A. P. R. Nanoescapology: progress toward understanding the endosomal escape of polymeric nanoparticles. *Wiley Interdiscip. Rev.: Nanomed. Nanobiotechnol.* **2017**, *9* (5), e1452.

Selby, L. I.; Kongkatigumjorn, N.; Such, G. K.; Johnston, A. P. R. HD Flow Cytometry: An Improved Way to Quantify Cellular Interactions with Nanoparticles. *Adv. Healthc. Mater.* **2016**, *5* (18), 2333–2338.

Sgolastra, F.; Backlund, C. M.; Ilker Ozay, E.; deRonde, B. M.; Minter, L. M.; Tew, G. N. Sequence segregation improves non-covalent protein delivery. *J. Control. Release* **2017**, *254*, 131–136.

Sgolastra, F.; deRonde, B. M.; Sarapas, J. M.; Som, A.; Tew, G. N. Designing mimics of membrane active proteins. *Acc. Chem. Res.* **2013**, *46* (12), 2977–2987.

Sgolastra, F.; Kuksin, C. A. A.; Gonzalez-Perez, G.; Minter, L. M.; Tew, G. N. Enhanced TAT-Cre Protein Transduction for Efficient Gene Recombination in T cells. *ACS Appl. Bio Mater.* **2018**, *1*, 444–451.

Sgolastra, F.; Minter, L. M.; Osborne, B. A.; Tew, G. N. Importance of Sequence Specific Hydrophobicity in Synthetic Protein Transduction Domain Mimics. *Biomacromolecules* **2014**, *15* (3), 812–820.

Shalek, A. K.; Gaublomme, J. T.; Wang, L.; Yosef, N.; Chevrier, N.; Andersen, M. S.; Robinson, J. T.; Pochet, N.; Neuberg, D.; Gertner, R. S.; Amit, I.; Brown, J. R.; Hacohen, N.; Regev, A.; Wu, C. J.; Park, H. Nanowire-mediated delivery enables functional interrogation of primary immune cells: Application to the analysis of chronic lymphocytic leukemia. *Nano Lett.* **2012**, *12* (12), 6498–6504.

Shapiro, H. M. Membrane potential estimation by flow cytometry. *Methods* **2000**, *21* (3), 271–279.

Shea, T. B.; Perrone-Bizzozero, N. I.; Beermann, M. L.; Benowitz, L. I. Phospholipid-mediated delivery of anti-GAP-43 antibodies into neuroblastoma cells prevents neuritogenesis. *J. Neurosci.* **1991**, *11* (6), 1685–1690.

Shete, H. K.; Prabhu, R. H.; Patravale, V. B. Endosomal Escape: A Bottleneck in Intracellular Delivery. *J. Nanosci. Nanotechnol.* **2014**, *14* (1), 460–474.

Simeoni, F.; Morris, M. C.; Heitz, F.; Divita, G. Insight into the mechanism of the peptide-based gene delivery system MPG: Implications for delivery of siRNA into mammalian cells. *Nucleic Acids Res.* **2003**, *31* (11), 2717–2724.

Smith, S. A.; Selby, L. I.; Johnston, A. P. R. R.; Such, G. K. The Endosomal Escape of Nanoparticles: Toward More Efficient Cellular Delivery. *Bioconjug. Chem.* **2019**, *30* (2), 263–272.

Som, A.; Tezgel, A. Ö.; Gabriel, G. J.; Tew, G. N. Self-Activation in De Novo Designed Mimics of Cell-Penetrating Peptides. *Angew. Chemie Int. Ed.* **2011**, *50* (27), 6147–6150.

Song, S. J.; Lee, S.; Ryu, K.-S.; Choi, J. S. Amphiphilic Peptide Nanorods Based on Oligo-Phenylalanine as a Biocompatible Drug Carrier. *Bioconjug. Chem.* **2017**, *28* (9), 2266–2276.

Staats, J.; Divekar, A.; McCoy, J. P.; Maecker, H. T. Guidelines for Gating Flow Cytometry Data for Immunological Assays. In *Methods in Molecular Biology*; Humana Press Inc., 2019; Vol. 2032, pp 81–104.

Stewart, M. P.; Sharei, A.; Ding, X.; Sahay, G.; Langer, R.; Jensen, K. F. *In vitro* and *ex vivo* strategies for intracellular delivery. *Nature* **2016**, *538* (7624), 183–192.

Stotland, A.; Gottlieb, R. A. α-MHC MitoTimer mouse: *In vivo* mitochondrial turnover model reveals remarkable mitochondrial heterogeneity in the heart. *J. Mol. Cell. Cardiol.* **2016**, *90*, 53–58.

Strömstedt, A. A.; Pasupuleti, M.; Schmidtchen, A.; Malmsten, M. Oligotryptophan-tagged antimicrobial peptides and the role of the cationic sequence. *Biochim. Biophys. Acta - Biomembr.* **2009**, *1788* (9), 1916–1923.

Sun, J.; Chen, X.; Deng, C.; Yu, H.; Xie, Z.; Jing, X. Direct Formation of Giant Vesicles from Synthetic Polypeptides. *Langmuir* **2007**, *23* (16), 8308–8315.

Takayama, K.; Hirose, H.; Tanaka, G.; Pujals, S.; Katayama, S.; Nakase, I.; Futaki, S. Effect of the Attachment of a Penetration Accelerating Sequence and the Influence of Hydrophobicity on Octaarginine-Mediated Intracellular Delivery. *Mol. Pharm.* **2012**, *9* (5), 1222–1230.

Tezgel, A. Ö.; Gonzalez-Perez, G.; Telfer, J. C.; Osborne, B. A.; Minter, L. M.; Tew, G. N. Novel Protein Transduction Domain Mimics as Nonviral Delivery Vectors for siRNA Targeting *NOTCH1* in Primary Human T cells. *Mol. Ther.* **2013**, *21* (1), 201–209.

Tezgel, A. Ö.; Jacobs, P.; Backlund, C. M.; Telfer, J. C.; Tew, G. N. Synthetic Protein Mimics for Functional Protein Delivery. *Biomacromolecules* **2017**, *18* (3), 819–825.

Tezgel, A. O.; Telfer, J. C.; Tew, G. N. De Novo Designed Protein Transduction Domain Mimics from Simple Synthetic Polymers. *Biomacromolecules* **2011**, *12* (8), 3078–3083.

Thorén, P. E. G.; Persson, D.; Esbjörner, E. K.; Goksör, M.; Lincoln, P.; Nordén, B. Membrane Binding and Translocation of Cell-Penetrating Peptides. *Biochemistry* **2004**, *43* (12), 3471–3489.

Thorén, P. E. G.; Persson, D.; Isakson, P.; Goksör, M.; Önfelt, A.; Nordén, B. Uptake of analogs of penetratin, Tat(48–60) and oligoarginine in live cells. *Biochem. Biophys. Res. Commun.* **2003**, *307* (1), 100–107.

Todorova, R. Estimation of methods of protein delivery into mammalian cells--a comparative study by electroporation and bioporter assay. *Appl. Biochem. Microbiol.* **2009**, *45* (4), 493–496.

Treat, N. J.; Smith, D.; Teng, C.; Flores, J. D.; Abel, B. A.; York, A. W.; Huang, F.; McCormick, C. L. Guanidine-Containing Methacrylamide (Co)polymers via a RAFT: Toward a Cell-Penetrating Peptide Mimic. *ACS Macro Lett.* **2012**, *1* (1), 100–104.

Umezawa, N.; Gelman, M. A.; Haigis, M. C.; Raines, R. T.; Gellman, S. H. Translocation of a β-Peptide Across Cell Membranes. *J. Am. Chem. Soc.* **2002**, *124* (3), 368–369.

Vaishya, R.; Khurana, V.; Patel, S.; Mitra, A. K. Long-term delivery of protein therapeutics. *Expert Opin. Drug Deliv.* **2015**, *12* (3), 415–440.

Varkouhi, A. K.; Scholte, M.; Storm, G.; Haisma, H. J. Endosomal escape pathways for delivery of biologicals. *J. Control. Release* **2011**, *151* (3), 220–228.

Verdurmen, W. P. R.; Mazlami, M.; Plückthun, A. A quantitative comparison of cytosolic delivery via different protein uptake systems. *Sci. Rep.* **2017**, *7* (1), 13194.

Vezenkov, L. L.; Martin, V.; Bettache, N.; Simon, M.; Messerschmitt, A.; Legrand, B.; Bantignies, J.-L.; Subra, G.; Maynadier, M.; Bellet, V.; Garcia, M.; Martinez, J.; Amblard, M. Ribbon-like Foldamers for Cellular Uptake and Drug Delivery. *ChemBioChem* **2017**, *18* (21), 2110–2114.

Vivès, E.; Brodin, P.; Lebleu, B.; Vivè, E.; Brodin, P.; Lebleu, B. A Truncated HIV-1 Tat Protein Basic Domain Rapidly Translocates through the Plasma Membrane and Accumulates in the Cell Nucleus. *J. Biol. Chem.* **1997**, *272* (25), 16010–16017.

Wadia, J. S.; Stan, R. V; Dowdy, S. F. Transducible TAT-HA fusogenic peptide enhances escape of TAT-fusion proteins after lipid raft macropinocytosis. *Nat. Med.* **2004**, *10* (3), 310–315.

Walrant, A.; Bauzá, A.; Girardet, C.; Alves, I. D.; Lecomte, S.; Illien, F.; Cardon, S.; Chaianantakul, N.; Pallerla, M.; Burlina, F.; Frontera, A.; Sagan, S. Ionpair-π interactions favor cell penetration of arginine/tryptophan-rich cell-penetrating peptides. *Biochim. Biophys. Acta - Biomembr.* **2020**, *1862* (2), 183098.

Walrant, A.; Correia, I.; Jiao, C.-Y.; Lequin, O.; Bent, E. H.; Goasdoué, N.; Lacombe, C.; Chassaing, G.; Sagan, S.; Alves, I. D. Different membrane behaviour and cellular uptake of three basic arginine-rich peptides. *Biochim. Biophys. Acta - Biomembr.* **2011**, *1808* (1), 382–393.

Wang, F.; Mo, J.; Huang, A.; Zhang, M.; Ma, L. Effects of interaction with gene carrier polyethyleneimines on conformation and enzymatic activity of pig heart lactate dehydrogenase. *Spectrochim. Acta - Part A Mol. Biomol. Spectrosc.* **2018**, *204*, 217–224.

Wang, Y.; Yang, Y.; Yan, L.; Kwok, S. Y.; Li, W.; Wang, Z.; Zhu, X.; Zhu, G.; Zhang, W.; Chen, X.; Shi, P. Poking cells for efficient vector-free intracellular delivery. *Nat. Commun.* **2014**, *5*, 1–9.

Washbourne, P.; McAllister, A. K. Techniques for gene transfer into neurons. *Curr. Opin. Neurobiol.* **2002**, *12* (5), 566–573.

Wender, P. A.; Mitchell, D. J.; Pattabiraman, K.; Pelkey, E. T.; Steinman, L.; Rothbard, J. B. The design, synthesis, and evaluation of molecules that enable or enhance cellular uptake: Peptoid molecular transporters. *Proc. Natl. Acad. Sci.* **2000**, *97* (24), 13003–13008.

Wender, P. A.; Galliher, W. C.; Goun, E. A.; Jones, L. R.; Pillow, T. H. The design of guanidinium-rich transporters and their internalization mechanisms. *Adv. Drug Deliv. Rev.* **2008**, *60* (4–5), 452–472.

Wender, P. A.; Kreider, E.; Pelkey, E. T.; Rothbard, J.; VanDeusen, C. L. Dendrimeric Molecular Transporters: Synthesis and Evaluation of Tunable Polyguanidino Dendrimers That Facilitate Cellular Uptake. *Org. Lett.* **2005**, *7* (22), 4815–4818.

Wender, P. A.; Rothbard, J. B.; Jessop, T. C.; Kreider, E. L.; Wylie, B. L. Oligocarbamate Molecular Transporters: Design, Synthesis, and Biological Evaluation of a New Class of Transporters for Drug Delivery. *J. Am. Chem. Soc.* **2002**, *124* (45), 13382–13383.

Wimley, W. C.; White, S. H. Experimentally determined hydrophobicity scale for proteins at membrane interfaces. *Nat. Struct. Mol. Biol.* **1996**, *3* (10), 842–848.

Wisnovsky, S.; Jean, S. R.; Kelley, S. O. Mitochondrial DNA repair and replication proteins revealed by targeted chemical probes. *Nat. Chem. Biol.* **2016**, *12* (7), 567–573.

Witte, K.; Olausson, B. E. S.; Walrant, A.; Alves, I. D.; Vogel, A. Structure and dynamics of the two amphipathic arginine-rich peptides RW9 and RL9 in a lipid environment investigated by solid-state NMR and MD simulations. *Biochim. Biophys. Acta - Biomembr.* **2013**, *1828* (2), 824–833.

Xiang, S.; Tong, H.; Shi, Q.; Fernandes, J. C.; Jin, T.; Dai, K.; Zhang, X. Uptake mechanisms of non-viral gene delivery. *J. Control. Release* **2012**, *158* (3), 371–378.

Xu, Y.; Du, Y. Effect of molecular structure of chitosan on protein delivery properties of chitosan nanoparticles. *Int. J. Pharm.* **2003**, *250* (1), 215–226.

Yameen, B.; Choi, W. Il; Vilos, C.; Swami, A.; Shi, J.; Farokhzad, O. C. Insight into nanoparticle cellular uptake and intracellular targeting. *J. Control. Release* **2014**, *190*, 485–499.

Yoo, J.; Sanoj Rejinold, N.; Lee, D.; Jon, S.; Kim, Y.-C. Protease-activatable cell-penetrating peptide possessing ROS-triggered phase transition for enhanced cancer therapy. *J. Control. Release* **2017**, *264*, 89–101.

Yousif, L. F.; Stewart, K. M.; Horton, K. L.; Kelley, S. O. Mitochondria-penetrating peptides: Sequence effects and model cargo transport. *ChemBioChem* **2009**, *10* (12), 2081–2088.

Yus, C.; Irusta, S.; Sebastian, V.; Arruebo, M. Controlling Particle Size and Release Kinetics in the Sustained Delivery of Oral Antibiotics Using pH-Independent Mucoadhesive Polymers. *Mol. Pharm.* **2020**, *17* (9), 3314–3327.

Zhang, S.; Zhu, S.; Yang, L.; Zheng, Y.; Gao, M.; Wang, S.; Zeng, J.-Z.; Yan, X. High-Throughput Multiparameter Analysis of Individual Mitochondria. *Anal. Chem.* **2012**, *84* (15), 6421–6428.

Zhao, H.; Lin, Z. Y.; Yildirimer, L.; Dhinakar, A.; Zhao, X.; Wu, J. Polymer-based nanoparticles for protein delivery: design, strategies and applications. *J. Mater. Chem. B* **2016**, *4* (23), 4060–4071.

Zhao, T.; Liu, X. X.; Singh, S.; Liu, X. X.; Zhang, Y.; Sawada, J.; Komatsu, M.; Belfield, K. D. Mitochondria Penetrating Peptide-Conjugated TAMRA for Live-Cell Long-Term Tracking. *Bioconjug. Chem.* **2019**, *30* (9), 2312–2316.

Zhou, P.; Wang, M.; Du, L.; Fisher, G. W.; Waggoner, A.; Ly, D. H. Novel Binding and Efficient Cellular Uptake of Guanidine-Based Peptide Nucleic Acids (GPNA). *J. Am. Chem. Soc.* **2003**, *125* (23), 6878–6879.

Zhu, Z.; Tian, D.; Gao, P.; Wang, K.; Li, Y.; Shu, X.; Zhu, J.; Zhao, Q. Cell-Penetrating Peptides Transport Noncovalently Linked Thermally Activated Delayed Fluorescence Nanoparticles for Time-Resolved Luminescence Imaging. *J. Am. Chem. Soc.* **2018**, *140* (50), 17484–17491.

Zorko, M.; Langel, Ü. Cell-penetrating peptides: mechanism and kinetics of cargo delivery. *Adv. Drug Deliv. Rev.* **2005**, *57* (4), 529–545.

Zuba-Surma, E. K.; Kucia, M.; Abdel-Latif, A.; Lillard, J. W.; Ratajczak, M. Z. The ImageStream system: A key step to a new era in imaging. *Folia Histochem. Cytobiol.* **2007**, *45* (4), 279–290.

Zuba-Surma, E. K.; Ratajczak, M. Z. Analytical Capabilities of the ImageStream Cytometer. In *Methods in Cell Biology*; Elsevier Inc., 2011; Vol. 102, pp 207–230.